Investigations of Intercellular Mitochondrial Transfer in Neural Cells by Applied Single Molecule Genotyping

By

Matthew Richard Rowe

A thesis

Submitted to the Victoria University of Wellington

in fulfilment of the requirements for the degree of

Doctor of Philosophy

Victoria University of Wellington

2019

Abstract

Over the past decade and a half, evidence for transfer of whole mitochondria between mammalian cells has emerged in the literature. The notion that mitochondria are restricted to the cell of origin has been overturned by this curious phenomenon, yet the physiological relevance of these transfer events remains unclear.

This thesis investigates intercellular mitochondrial transfer in co-cultures of neural cells *in vitro*, to understand whether neural cells placed under stress demonstrate an enhanced rate of intercellular mitochondrial transfer. This would implicate the phenomenon as a cellular response to stress.

Reliable techniques for quantitative study of intercellular mitochondrial transfer are limited so far in this field. To address this, a novel quantitative approach was developed to detect intercellular mitochondrial transfer, based on single molecule genotyping by target-primed rolling circle amplification. This enabled imaging of individual mitochondrial DNA molecules *in situ*, to detect those molecules which had moved between cells. Through this strategy, intercellular mitochondrial transfer was detected in new *in vitro* co-culture models.

Primary murine pericytes derived from brain microvessels, were found to readily transfer mitochondria to a murine astrocyte cell line *in vitro*. Cisplatin, a DNA damaging agent; and chloramphenicol, a mitochondrial ribosome inhibitor, used to induce acute cellular injuries in the murine astrocyte cell line. These injuries were characterised and found to induce apoptosis, cause changes in growth characteristics, mitochondrial gene expression, and alter the metabolic phenotype of the cells. A derivative of the astrocyte cell line which completely lacks mitochondrial respiration, was found to model a chronic metabolic injury.

As pericytes are prevalent throughout the brain, the pericyte/astrocyte co-culture model was selected to evaluate how the rate of intercellular mitochondrial transfer was altered, when the astrocytes were injured prior to co-culture. Through *in situ* single molecule genotyping and high throughput confocal microscopy, quantitative data was produced on how the rate of intercellular mitochondrial transfer was altered by injury in these models. The rate of intercellular mitochondrial transfer remained unaltered by chloramphenicol, however both cisplatin and the chronic metabolic injury model demonstrated reduced numbers of pericyte mitochondrial DNAs transferred into the injured astrocytes.

These studies demonstrate successful application of a novel approach to study intercellular mitochondrial transfer and enable quantitative studies of this phenomenon.

Acknowledgements

The journey taken to compile this body of work was not one I took alone. Through each success, and perhaps even more so each challenge, walked alongside me a number of wonderful, talented and/or people who are very dear to me. I would like to acknowledge all of those who made this PhD come to fruition. Though it is not possible to include each and every one of you by name, I sincerely thank you all.

I recognise with utmost gratitude the role the Neurological Foundation played in enabling my PhD research. Thank you for placing faith in me through award of the W&B Miller Scholarship. The financial support provided to me by the foundation represents support from thousands of Kiwi donors, for which I will be forever grateful. In return, this thesis presents another small (but not insignificant) piece of the neurological puzzle, from which to build future knowledge. It is only from all of these small pieces, that we may one day assemble new treatments for neurological disease.

Alongside me, and most connected to my PhD journey, my supervisor and mentor Dr. Melanie McConnell deserves more thanks than I could possibly give her on this page. Over these past years, she has shaped my thinking and helped to hone my scientific skills more-so than any other. Working with her taught me things I would never have predicted to be a part of the PhD journey. I wish to thank her for trusting me to execute a project that manifested differently from initial expectation. It was a privilege of the highest order to have been her student. From her I have derived incredible value, and I hope that her investment in me continues to provide value to her research programme in future.

Through an unanticipated yet invaluable mentorship, Dr. Patries Herst contributed enormously to my journey. Her advice, guidance and independent opinions provided critical fuel for me while traveling to reach our destination. Her generous provision of time for review of my work during the writing up stages was incredible. Our discussions on science and science adjacent PhD life will be remembered fondly. I cannot provide adequate thanks for her contribution to my journey.

The ideas behind this arch of research in the McConnell lab were seeded by Professor Michael Berridge. I wish to thank him for encouraging our research in this area, and for following us down entirely new, unexpected directions during the course of this work. It was from Professor Berridge that I have learned so much about the 'P' part of a PhD, through in-depth discussion of biological philosophy related to our projects. I sincerely appreciated his enthusiasm and willingness to discuss this project at great length.

Though not entirely sure exactly what I have been doing the last few years, my incredible family came along vicariously on the PhD journey. Richard, Paula and Anna, thank you for your incredible and infinite support, which came in forms too numerous to list. I wouldn't have made it without this, so success in completing this work is in a large part, also yours. Thanks for listening to any PhD induced venting I had to do, and helping me to slog through the rough parts!

I wish to extend a huge thanks to Remy Schneider, from whom I collected the baton in this research. Remy provided huge doses of enthusiasm on which I fed. From our many late night discussions came experimental ideas which I eventually executed to create a good chunk of the work in this thesis. Our science and banter were incredibly valuable and will remain some of the best memories I have from this time. I couldn't pass by this paragraph without also including Remy's right hand man – Dinindu Senanayake. Dini was a huge source of support for me during this PhD. Thank you for following alongside my challenges and providing ample encouragement.

A source of valuable humour and scientific input in equal amounts, Vimal Patel gets a huge shutout in these acknowledgements. You kept my perspective in line and a smile on my face, and for that I am truly grateful.

To three of my most favourite fellow PhDs, Nicole Stanton, Nikki Templeton and Georgia Carson, thank you for being memorable and colourful components of my PhD journey. I will never forget this time with each of you as we constantly crashed headfirst into this wall called 'research'. Thanks for putting up with my inane but sometimes useful banter. I hold each of you in the highest regard and can't wait to see where the future takes you.

To all those on the Alan MacDiarmid third floor, thank you for creating a pleasant environment in which to carry out this work. I find it hard to imagine a better set of people to have had around me day to day, for the last however many years. This thanks is of course, intended equally to the students and the senior academics.

Finally, to the support staff in SBS and the faculty of science, I would like to acknowledge how hugely helpful you have all been during my PhD. Thank for you for sorting out any and all my admin problems over the years.

Once more, to all those who have been a part of my PhD journey, I would like to thank you for wherever the scientific future takes me.

Table of contents

Table of figures

Table of tables

List of abbreviations

Acetyl-CoA	Acetyl Coenzyme A
ATP	Adenosine Triphosphate
BFP	Blue Fluorescent Protein
BMSC	Bone Marrow Stromal Cell Line
bp	Base Pair
BSA	Bovine Serum Albumin
CFSE	5(6)-Carboxyfluorescein Diacetate Succinimidyl Ester
CMP	Chloramphenicol
COX1	Cytochrome C Oxidase
COX4	Cytochrome Oxidase Subunit 4
COX8A	cytochrome C Oxidase Subunit 8A
Ct	Cycle Threshold (qPCR)
CSP	Cisplatin
CytB	Cytochrome B
DAPI	4′,6-diamidino-2-phenylindole
DIC	Differential Interference Contrast
DiD	1,1'-Dioctadecyl-3,3,3',3'-Tetramethylindodicarbocyanine Perchlorate
DIV	Days *In Vitro*
DMEM	Dulbecco's Modified Eagle's Medium
DMSO	Dimethyl Sulfoxide
DNA	Deoxyribonucleic Acid
dsDNA	Double Stranded DNA
E. coli	Escherichia Coli
ECAR	Extracellular Acidification Rate
EDTA	Ethylenediaminetetraacetic Acid
eGFP	Enhanced Green Fluorescent Protein
EtBr	Ethidium Bromide
ETC	Electron Transport Chain
EtOH	Ethanol
FACS	Fluorescence-Activated Cell-Sorting
FBS	Foetal Bovine Serum
FP(s)	Fluorescent Protein(s)
FSA	Forward Scatter Area
FSC	Forward Scatter
FSH	Forward Scatter Height
FSW	Forward Scatter Width
GBM	Glioblastoma
G418	Geneticin
gDNA	Genomic DNA
GFP	Green Fluorescent Protein
h	Hour(s)
HCl	Hydrochloric Acid
HSP	Heavy Strand Promotor
HTCM	High throughput Confocal Microscopy
IMT	Intercellular Mitochondrial Transfer

KDE	Kernel Density Estimate
LB	Luria-Bertani
LSCM	Laser Scanning Confocal Microscopy
LSP	Light Strand Promotor
min	Minute(s)
mito-FP(s)	Mitochondrial Targeted Fluorescent Protein(s)
mKO2	Monomer Kusabira Orange 2
ms	Millisecond
MSC(s)	Mesenchymal Stem Cell(s)
mtDNA(s)	Mitochondrial DNA(s)
mtSSB	Mitochondrial Single Stranded Binding Protein
mtR	Mitochondrial Ribosome
NuMT	Nuclear mitochondrial DNA
OCR	Oxygen Consumption Rate
OXPHOS	Oxidative Phosphorylation
PBS	Phosphate Buffered Saline
PCR	Polymerase Chain Reaction
PI	Propidium Iodide
POLMRT	Mitochondrial RNA Polymerase
POLγ	Polymerase Gamma
RCA	Rolling Circle Amplification
RCP(s)	Rolling Circle Product(s)
ROS	Reactive Oxygen Species
RTS	Rémy Treillat Schneider – McConnell Laboratory Member
s	Second(s)
SD	Standard Deviation
SEM	Standard Error of Means
SNV	Single Nucleotide Variant
SSA	Side Scatter Area
SSC	Side Scatter
ssDNA	Single Stranded DNA
SSH	Side Scatter Height
SSW	Side Scatter Width
TBS	Tris buffered Saline
TBST	Tris buffered Saline with Tween-20
TCA	Tricarboxylic Acid Cycle
TEM	Transmission Electron Microscopy
TFAM	Mitochondrial Transcription Factor A
TFB2M	Mitochondrial Transcription Factor B2
TNT	Tunneling Nanotubule
TRIS	Tris(hydroxymethyl)aminomethane
WT	Wild Type

Nomenclature for modified oligonucleotides

3Phos	3’ Phosphorylation
5Phos	5’ Phosphorylation
5Alex405N	5’ Alexafluor dye series 405
5ATTO647	5’ Atto dye series 647
6FAM	6-Carboxyfluorescein

BHQ	Black Hole Quencher
Zen	Proprietary Zen Internal Quencher
mA	2′-O-methyl-adenine

Thesis outline

This thesis is comprised of seven chapters.

Chapter 1 is a general introduction. This chapter provides background information on mitochondrial biology and intercellular mitochondrial transfer. A context for this research is established, and unanswered questions in the field of intercellular mitochondrial transfer are introduced. The chapter concludes with an outline of the aims of this thesis.

Chapter 2 describes the materials and methods used in this research.

The experimental results of this thesis are presented in chapters 3-6. Each chapter includes an introduction which covers specific background information, in addition to a discussion or summary of the results. Chapter 2 is a combined method development/results chapter and as such, additional background information is introduced as the chapter progresses. Chapter 6 is separated into two separate results sections, based on the models used. Each figure presented in chapters 3-6 appears with a figure legend either below, or on the page opposite the figure.

Chapter 7 is an overall discussion of this project and includes an outline of potential future research directions.

1 General Introduction

Roughly 2.7 billion years ago, our planet surface, and much of life thereon, underwent major compositional change. Oxygenic photosynthesis by cyanobacteria began to accumulate molecular oxygen in the earth's atmosphere [1-3], which trickled down into the planet's surface oceans [4, 5]. Another two billion years or so later and even the earths deepest oceans contained dissolved oxygen [6-8]. Both causative of, and consequential to these changes, adaptation drove metabolic evolution in primordial microbes, towards oxygen use in energy-transducing reactions [9, 10]. At least once over the aeons, an event of principle significance occurred between archaea and proteobacteria. A free-living protobacterial ancestor was taken up by an ancestral archaeon, ultimately resulting in an obligate form of endosymbiosis [11, 12]. Whether a singular event or just one of many, a genetic memory of this event persists, and can be traced back from all modern eukaryotic cells. The protomitochondrion, a symbiont within these primitive eukaryotes, facilitated aerobic respiration. This allowed life not only to adapt to, but begin to thrive in oxygen-rich environments.

Fast forward 2 billion years and the modern mitochondrion not only persists, but is critical to normal eukaryotic cell function. Mitochondrial activities are highly intertwined with multiple well understood cellular processes, and yet this curious component of the cell continues to surprise. Somewhat reminiscent of its movement into its ancient host, emergent research suggests mitochondria are not strictly confined to a host cell.

Intercellular mitochondrial transfer (IMT) between mammalian cells has recently been discovered to occur, both *in vitro* and *in vivo*. The physiological relevance of, and signal(s) which may drive IMT events remain poorly characterised.

The demands placed on mitochondrial function are among their highest in brain tissue. Neurodegenerative and neurological diseases share a commonality in that mitochondrial dysfunction is a core component of the disease phenotypes. Cancers of the brain, particularly glioblastoma, exhibit therapy resistance and rapid disease recurrence after therapy.

Given mitochondria influence numerous cellular processes, IMT is likely to have both purpose and consequence in normal and disease biology. This thesis examines IMT in co-culture models of neural cells *in vitro*, in efforts to understand what this novel biology may contribute to cell survival in the brain. If the transfer of mitochondria from healthy cells into diseased neural cells enhances survival, understanding this phenomenon represents a context dependent therapeutic target to promote or prevent cell survival.

1.1 The mitochondrion

Mammalian cells contain numerous mitochondria; the number of which is tightly coupled to the bioenergetic demands of the specific cell type [13-16]. While it is convenient to think of mitochondria as individual units, together they form a dynamic networked structure. The entire structure is fluid; constant mitochondrial mobility, fusion and fission processes regulate metabolic functions, mitochondrial quality control and response to stressors [17, 18]. In the majority of somatic cells, mitochondrial biomass equates to roughly 80-2000 individual granular mitochondria [19]. This is however, difficult to determine experimentally due to the continuous spatio-temporal rearrangement of the organelles [17, 19]. Mitochondrial mass is tightly coupled to cell cycle stage [20, 21], likely to ensure daughter cells are produced with sufficient mitochondrial function.

1.1.1 Organelle structure

A mitochondrion is a double-membraned structure, comprised of specialised compartments. The inner mitochondrial membrane is highly folded into tubular or lamellar structures known as cristae [22, 23]. Contained within the inner membrane, the mitochondrial matrix supports mitochondrial ribosomes (mtR), mitochondrial DNA (mtDNA), and mitochondrial RNA granules [23-25]. The matrix is the site of protein biosynthesis, mtDNA replication, transcription and numerous enzyme catalysed reactions such as those of the tricarboxylic acid cycle (TCA) as well as a number of biosynthetic pathways [26, 27]. Embedded in the inner mitochondrial membrane are numerous mitochondrial protein complexes: the five complexes of the respiratory chain; transport inner membrane complex; contact site complex; calcium uniporter complex and the nucleoid complex [28]. The inner membrane is strictly impermeable to ions and proteins, which must be transported through dedicated transporters to reach the matrix [26]. Under normal conditions, the pH within the matrix rests at 7.9-8.0 [29]. This elevated pH is generated as protons are pumped into the intermembrane space; a compartment between the inner and outer mitochondrial membranes with an approximate depth of 20 nm [26]. An electrochemical gradient of approximately 180 mV is formed across the inner membrane and drives activity of the adenosine triphosphate (ATP) synthase complex [30]. The outer mitochondrial membrane separates the inner compartments of the mitochondrion from the cytosol. It is permeable to small uncharged molecules and ions. Larger protein components required for mitochondrial function are imported via dedicated translocases [26].

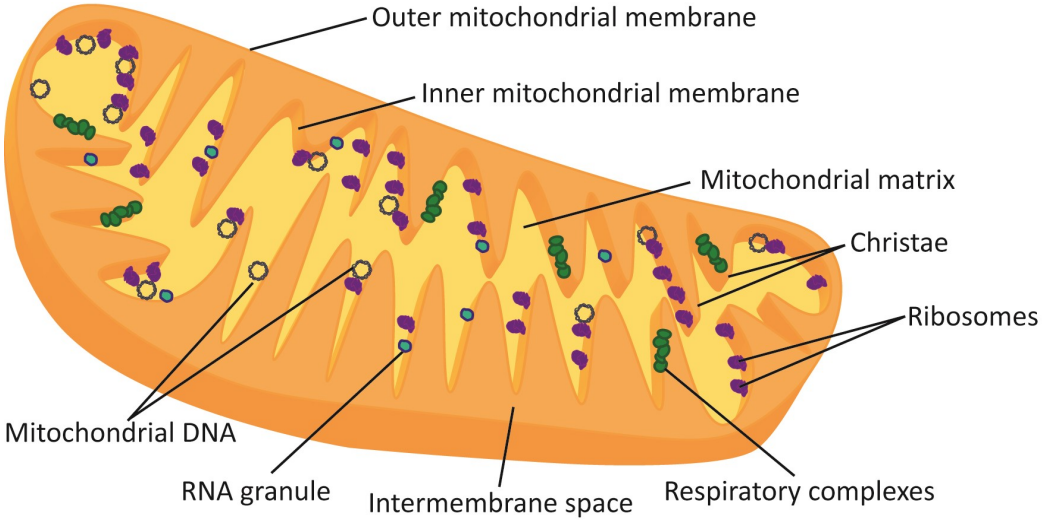

Figure 1.1.1. Mitochondrial structure
Graphical representation of basic mitochondrial structure. Ribosomes, RNA granules and mtDNA are located on the inner mitochondrial membrane, while the respiratory complexes are embedded into the inner mitochondrial membrane.

1.1.2 The mitochondrial genome

The theory of an endosymbiotic origin for the protomitochondrion cells is most readily evidenced by the presence of mtDNA, found within the mitochondrial matrix. Each eukaryotic cell carries numerous copies of mtDNA. Modern mammalian mtDNA is a gene dense, circular dsDNA (double stranded DNA) molecule approximately 16.6 kb in size. Each strand of the dsDNA mtDNA molecule is identified as the heavy or light strand respectively; terms derived from the ability to separate each strand by density centrifugation, in an alkaline cesium chloride gradient [31]. Over the course of evolutionary time, human mtDNA has become highly simplified; just 11 messenger RNAs which 13 proteins, 22 transfer RNAs and 2 ribosomal RNAs are encoded by the genome [32]. Additional small polypeptides known as mito-peptides are also encoded by mtDNA [33-36]. Given the mitochondrial proteome consists of 1158 proteins as described in the most recent revision of MitoCarta, the overwhelming majority of genes required for complete mitochondrial function are encoded by the nuclear genome [37]. Interestingly, extensive fragments of mtDNA sequence can be found integrated throughout the nuclear genome as transcriptionally inactive pseudogenes termed NuMTs (nuclear mtDNAs) [38-41]. The mtDNA molecules are localised to structures approximately 100 nm in size termed mtDNA nucleoids. These are anchored to the inner mitochondrial membrane, within the matrix [42, 43]. A mtDNA nucleoid frequently contains a singular mtDNA copy [15, 44].

Approximately 90 mitochondrial proteins form complexes made up of sub-units expressed from both nuclear and mitochondrial genomes [32]. Those genes which do remain in mtDNA encode essential sub-units of the respiratory complexes and machinery required for protein synthesis within the mitochondrion. While it is unclear why such a small complement of mitochondrial gene products remain encoded by mtDNA, it is possible that localised expression is regulated by transcriptional machinery which is responsive to the redox state or membrane potential of the mitochondria [32]. This may facilitate rapid adjustments in gene expression, to meet dynamic requirements in the organelle.

Because the mitochondrial genome has become highly optimised over evolutionary time, many mutations in mtDNA are poorly tolerated. The genome is intron free, thus most perturbations to the mtDNA sequence readily alter function of the transcribed RNA. Fortunately, as mtDNA is present as multiple copies per cell, a low level of mutant copies does not cause a pathogenic phenotype [45]. A threshold ratio of mutant/normal mtDNA copies must be crossed to influence the global respiratory function of a cell. In any given cell, mtDNA sequence can be homoplasmic, or exist in a state of heteroplasmy with two or more mtDNA sequences carried. Different cells from the same individual can exhibit widely varied levels of heteroplasmy, due to random segregation of mtDNA during somatic

cell division [46]. Because mammalian mtDNA is maternally inherited, pathogenic heteroplasmy in the maternal germline can lead to transmission of high levels of dysfunctional mtDNA to the progeny. This manifests as mitochondrial disease; a name given to various diseases driven by mutations in mtDNA or nuclear genes which encode mitochondrial-related proteins. The level of respiratory deficiency and thus disease severity is dependent on both mutation load and which specific tissues are effected in the individual [47]. Fortunately, there is evidence for selective pressure against nonsynonymous mutations in the germline [38, 48]. Tolerated or synonymous mutations inherited through the maternal lineage gives rise to mtDNA haplotypes carried by individuals [49, 50]. The clonal nature of many model organisms or cell lines used *in vitro* means a relatively stable haplotype, derived from the maternal organism, is reflected in the mtDNA sequence of these models.

1.1.3 Replication of mitochondrial DNA

The mtDNA of mammalian cells is maintained by a dedicated complement of proteins, distinct from those involved the replication of nuclear DNA. Replication of mtDNA is carried out by protein machinery similar to that of bacteriophages, preserved from the endosymbiotic origin [51]. Replication of mtDNA occurs in all mitochondria, regardless of subcellular localization. It is asynchronous to nuclear DNA replication and occurs throughout the cell cycle [52].

The principal replicatory polymerase of mtDNA is DNA polymerase gamma (POLγ); a heterotrimeric protein comprised of a catalytic POLγA subunit and 2 POLγB accessory subunits [53-55]. Four other DNA polymerases (DNA polymerases β, θ, ζ and PrimPol) have been described that act in the mitochondria, however the specific role of each is not well understood [56-59]. It is likely these are instead used in mtDNA repair as opposed to replication. Replication of mtDNA occurs at high fidelity due to the 3'-5' exonuclease domain of POLγ; the excision of misincorporated bases occurs before synthesis continues [55, 60]. Synthesis of the heavy and light strands of mtDNA is thought to occur simultaneously in a model known as strand displacement [61]. As POLγ cannot act on dsDNA as a template, a DNA helicase known as TWINKLE acts ahead of POLγ to unwind mtDNA for the polymerase [62-64]. Two further proteins, mitochondrial single stranded binding protein (mtSSB) and mitochondrial RNA polymerase (POLMRT) are required to protect, stabilise and enhance (mtSSB), and to synthesise an RNA primer [65-67]. As TWINKLE and POLγ initiate synthesis from the heavy mtDNA strand at the heavy strand origin of replication, mtSSB prevents random priming on the light strand by POLMRT. Synthesis along occurs the heavy strand until the light strand origin of replication is reached, whereby a stem-loop secondary structure is formed; this prevents

effective binding of mtSSB to the light strand and allows POLMRT to bind and synthesise an RNA primer on the light strand [61, 65-67]. Synthesis from the light strand is initiated from this primer for synthesis of the 'lagging' strand by POLγ. Very few replication events continue to completion, with 95 % of events initiated from the heavy strand origin of replication terminated by approximately 650 nucleotides. A short DNA fragment known as 7S DNA is produced by these early termination events and remains bound to the parental light strand. This produces a triple stranded region known as the D-Loop. The precise purpose and function of the D-loop remain unclear, however the switch between abortive and complete replicatory events may be interconnected with regulation of mtDNA copy number [68].

1.1.4 Mitochondrial gene expression

Similar to replication, transcription from mtDNA requires a distinct set of machinery from nuclear gene transcription. To transcribe from mtDNA, just three principal proteins are necessary; POLRMT, mitochondrial transcription factor A (TFAM) and mitochondrial transcription factor B2 (TFB2M) [69]. Some controversy persists around the necessity of TFAM for transcription *in vivo*, as it appears to enhance rather than enable transcription *in vitro* [70-73], however TFAM knockout mice are embryonic lethal prior to day 10.5 of development [72].

As mammalian mtDNA encodes gene products on both heavy and light strands, an independent promoter sequence is required to drive transcription from each. A single light strand promotor (LSP) is known to drive transcription from the mtDNA light strand, however the precise nature of promotors on the heavy strand are less well understood [69]. There is evidence to suggest that the heavy strand contains two promotor sites, termed HSP1 and HSP2 [69, 74-76].

Because the precise role of TFAM in transcription is not yet fully elucidated, this protein is included in the current 3 stage model of mitochondrial transcription. TFAM associates upstream of HSP1/2 and the LSP with high affinity, which distorts the shape of the promotor regions. A pre-initiation complex is then formed by recruitment of POLRMT to the mtDNA bound TFAM. Finally TFB2M is recruited to the complex and correctly positions the ssDNA relative to the catalytic subunit of POLRMT [69]. Synthesis of the transcript proceeds until a structural element of mtDNA known as the conserved sequence block II is reached [77]. This sequence forms a G-quadruplex and is thought to facilitate formation of the RNA primers required in mtDNA replication. The presence of an additional protein, mitochondrial transcription elongation factor (TEFM), is required for POLRMT to produce full length, polycistronic transcript [77, 78].

Full length mitochondrial transcripts from HSP2 and LSP are almost genome length, however exactly how termination of transcription occurs is poorly understood [69]. Steady state levels of full length transcript are low relative to mature RNAs, which suggests that processing of full length transcript into mature mRNA, rRNA and tRNA species occurs co-transcriptionally [32].

1.1.5 Mitochondrial proteins and translation

While the vast majority of proteins required for mitochondrial function are encoded in the nuclear genome, 13 respiratory complex subunits are encoded by mtDNA and are translated directly within the mitochondrial matrix. Primary transcripts are processed in the mitochondrial RNA granules by endonucleolytic processing [79], before maturation by post-transcriptional modification and stabilisation [80]. The 12S and 16S rRNAs undergo extensive modification before assembly into the mtR; a complex composed of the 28S small subunit, 39S large subunit, 12S a 16S rRNAs [81-84]. The specialised mtR differs significantly from cytosolic ribosomes; it must function in concert with each of the 22 mitochondrial tRNAs. Mitochondrial tRNAs utilise an alternative codon structure from the canonical system of mammalian cells, and thus require a specialised ribosome for translation [85]. The mammalian mtR shares ancestral homology with prokaryotic ribosomes though the structure has diverged significantly [86]. Mitochondrial function remains susceptible to inhibition by antibiotics which target prokaryotic ribosomes [87].

As each respiratory complex subunit is translated at the mtR, it is inserted into the inner mitochondrial membrane by two major systems; the Sec complex and the YidC/Oxa/Alb3 insertases [87, 89-95]. These nuclear encoded proteins facilitate insertion of the respiratory subunits into the inner mitochondrial membrane, through mechanisms shared with their action on membranes accessed directly from the cytosol.

The respiratory chain of mammalian mitochondria consists of 5 complexes, together termed the respirasome. The thirteen essential subunits translated within the mitochondrial matrix associate with approximately 77 nuclear encoded subunits to form a fully functional respiratory chain [32]. Intriguingly, complexes I, III, IV and V include a substantial number of subunits encoded by mtDNA, whereas all subunits required to form complex II are encoded by the nuclear genome. Members of the complexes either self-assemble after importation into the mitochondrion, or require facilitated assembly by chaperones [88]. Additionally, the complexes form spatially integrated supercomplexes, to facilitate electron transport chain (ETC) function. Formation of a fully functional respirasome requires extreme co-ordination [89-91].

1.2 Glycolysis and oxidative phosphorylation

Life requires energy. Metabolism in the cell transfers the chemical potential energy stored in organic compounds to ATP; a universal energy carrier which drives almost all cellular chemistry. In mammalian cells, ATP is regenerated from ADP through two major pathways; glycolysis and oxidative phosphorylation (OXPHOS).

1.2.1 Glycolysis and the fates of pyruvate

Mammalian metabolism of glucose to pyruvate takes place in the cytoplasm. This occurs through 10 enzymatic catalysed reactions [92-94]. One molecule of glucose is converted to 2 glyceraldehyde 3-phosphate molecules in five initial reactions, which requires the hydrolysis of 2 molecules of ATP to ADP. The second five reactions generate 4 ATP molecules and two pyruvate molecules, whilst 2 nicotinamide adenine dinucleotide (NADH) are generated through co-reduction of 2 NAD^+. The net yield of energy carriers from glycolysis is +2 ATP and +2 NADH. Under aerobic conditions, the NAD^+ deficit created through glycolysis is recovered by mitochondrial respiration [95, 96].

Under anaerobic conditions where mitochondrial respiration is not available, the NAD^+ deficit created in glycolysis must be regenerated by fermentation of pyruvate to lactic acid. Here, 2 molecules of pyruvate are reduced to lactic acid by lactate dehydrogenase, simultaneously regenerating 2 NAD^+. This provides the 2 NAD^+ required for subsequent cycles of glycolysis. The net yield of energy carriers from glycolysis followed by fermentation of pyruvate is +2 ATP [95, 96].

1.2.2 Mitochondrial respiration and metabolism

Under aerobic conditions, pyruvate may be transported into the mitochondrial matrix where it is converted to acetyl-CoA and CO_2 by pyruvate dehydrogenase. Acetyl-CoA is a major bio-synthetic intermediate able to enter the TCA cycle. Stepwise decarboxylation of acetyl-CoA through the TCA cycle is carried out in a series of enzyme catalysed redox reactions, which generate 3 NADH, 1 flavin adenine dinucleotide ($FADH_2$) and 1 guanosine-5'-triphosphate (GTP) per molecule of pyruvate completely oxidised. Intermediates produced in the TCA cycle at various stages are shunted into other biosynthetic pathways, thus global metabolic flux in the cell determines exactly how many energy carriers in the form of NADH, $FADH_2$ and GTP are produced [95, 96]. These intermediates are utilised to synthesise the fundamental building blocks for cell function which include fatty acids, amino acids and nucleotides [27]. The use of glucose to sustain production of intermediates for use in TCA is termed glucose anaplerosis [97]. Oxidation of pyruvate by pyruvate dehydrogenase in the mitochondria provides acetyl-CoA, which is

subsequently converted to citrate, to fuel the TCA cycle, or alternatively transported out of the mitochondria by ATP citrate lyase; this is a key substrate for acetylation as well as *de novo* lipogenesis [27]. Production of α-ketoglutarate in the TCA cycle enables synthesis of glutamate by transamination. Together, α-ketoglutarate and glutamate are key precursors for synthesis of many non-essential amino acids which include glutamine, alanine, proline and aspartate. Additionally, oxaloacetate produced by TCA activity enables synthesis of asparagine, lysine, threonine and isoleucine [27].

The NADH and $FADH_2$ generated through both glycolysis and the TCA cycle are a source of high energy electrons that drive mitochondrial respiration. Together, respiratory complexes I, II, III and IV of the mitochondrial electron transport chain (ETC), catalyse the transfer of electrons from these carrier molecules [27, 95]. Respiratory complex I, NADH:ubiquinone oxidoreductase, mediates the reduction of ubiquinone by catalysing the transfer of two electrons from NADH. Electrons are shuttled across the inner mitochondrial membrane via a series of iron sulphur redox centres which simultaneously drive the translocation of four protons (H^+) across the inner mitochondrial membrane [98]. Free ubiquinone accepts these electrons and is reduced by two protons to form ubiquinol. Complex II, known as succinate:quinone oxidoreductase catalyses the conversion of succinate to fumarate in the TCA cycle. This generates $FADH_2$; the electron source for reduction of further ubiquinone by complex II [99]. Unlike complexes I, III and IV, complex II Is not directly involved in translocation of protons to the intermembrane space. Complex III, known as ubiquinol-cytochrome C oxidoreductase, catalyses the transfer of electrons from the ubiquinol formed by complexes I and II, to cytochrome C, in a process known as the Q cycle [100-102]. A complete Q cycle drives 4 protons into the inter membrane space. Complex IV, known as cytochrome C oxidase, accepts electrons from reduced cytochrome C. Electron transfer across complex IV occurs through a number of iron and copper redox centres, where molecular oxygen acts as a final acceptor molecule, forming water [95, 96, 103]. This process drives four additional protons into the intermembrane space. Molecular oxygen is required as the final acceptor of electrons from the ETC, giving the process its name: aerobic respiration.

Protons translocated into the intermembrane space by complexes I, III and IV establish a membrane potential across the inner membrane. This electrochemical gradient drives formation of ATP from ADP + inorganic phosphate at complex V, known as ATP synthase. This complex engages a unique mechanism known as rotary catalysis, to drive regeneration of ATP [30, 104, 105]. The proton motive force of H^+ ions moving in a tightly controlled fashion through the ATP synthase complex into the mitochondrial matrix drives rotation of the central shaft of the complex. Conformational changes in the structure force

ADP and organic phosphate into proximity whereby the formation of ATP is thermodynamically favoured [104, 106]. For each molecule of glucose completely metabolised by glycolysis followed by oxidative phosphorylation, approximately 32 ATP are generated. This is lower than the theoretical ATP yield for various reasons; transport processes deplete energy carriers; protons leak back into the matrix independent of ATP synthase; free radicals are generated by electron leak from respiratory complexes [107].

1.2.3 Metabolic phenotypes and flexibility

Cells exist in a constant state of metabolic adaptation; responses to continuous changes in resource availability, biosynthetic demand or cellular proliferation state drive changes in metabolic flux. Under favourable conditions, a normal cell uses glucose anaplerosis to sustain biosynthesis from TCA intermediates, whilst simultaneously producing ATP via oxidative phosphorylation [27]. Conversely, under hypoxic conditions most normal cells are limited in their ability to engage oxidative phosphorylation and adopt metabolic profiles which favour glycolysis.

1.2.4 Extracellular flux of O_2 and H^+

The balance between ATP production by oxidative phosphorylation or glycolysis provides great insight into the state of cells health or metabolic activity. Traditionally, monitoring activity in these pathways relied on functional assessment of individual enzymes in the pathways [108-110]. As cells engage in oxidative phosphorylation, molecular oxygen is depleted by conversion to H_2O at complex IV. For this reason, the oxygen consumption rate (OCR) of cells describes the level of mitochondrial respiration which occurs in a discrete increment of time.

As cells engage glycolytic metabolism, conversion of pyruvate to lactic acid regenerates NAD^+ to sustain glycolysis. Under physiological conditions, lactic acid dissociates into lactate and H^+. Free protons generated in this process are readily monitored in the form of a decrease in extracellular pH; the extracellular acidification rate (ECAR) is coupled to the level of lactic acid production over a discrete time increment, and thus is a proxy for glycolytic rate [108, 109, 111].

When oxidative phosphorylation is inhibited by pharmacological means, cells are forced to rely on glycolytic derivation of ATP. The changes in OCR and ECAR which result from this inhibition are valuable in understanding the bioenergetic status of cells or tissues [112].

1.3 The ρ^0 phenotype

Cells which completely lack the capacity to engage in mitochondrial respiration are a powerful research tool. Mammalian cells like this do not exist naturally, however they may be derived from a parental cell line by complete ablation of the mtDNA; these are known as ρ^0 cells. In ρ^0 cells, the mtDNA encoded proteins necessary for ETC function are no longer synthesised in the matrix, thus oxidative phosphorylation is absent [113].

To generate cells with the ρ^0 phenotype, ethidium bromide is added to culture medium at low concentration for an extended period of time. Ethidium bromide intercalates with mtDNA and interferes with its replication [114-117]. Serial mitosis of the cells causes dilution of mtDNA molecules and ultimately results in a complete loss across the population given sufficient sub-cloning. More recently, enzymatic strategies which employ a mitochondrial targeting sequence fused to one of exonuclease III, endonuclease EcoRI, mutant Y147A uracil-N-glycosylase or herpes simplex virus protein UL12.5M185, have been used to directly degrade mtDNA in pursuit of generating ρ^0 cells [118-120].

In order to survive with complete loss of mitochondrial respiratory function, the medium used to culture ρ^0 cells during and after mtDNA ablation must be supplemented with pyruvate and uridine. The majority of pyruvate will be used by ρ^0 cells to produce lactate and regenerate NAD^+ necessary to sustain glycolytic derivation of ATP [120]. As such, pyruvate availability for conversion to acetyl-CoA is restricted and cells are no longer able to engage TCA to produce biosynthetic precursors. Medium supplemented with high concentration pyruvate ameliorates this constraint.

Because ρ^0 cells are not able to carry out mitochondrial electron transport, de novo pyrimidine biosynthesis is impossible. The enzyme dihydroorotate dehydrogenase catalyses the transfer of electrons from dihydroorotate to ubiquinone, at the interface of the inner mitochondrial membrane and matrix [121]. This reaction generates orotate; an essential precursor in pyrimidine biosynthesis [122-124]. The absence of electron transport at complex III prevents replenishment of the ubiquinone pool in ρ^0 cells, the activity of dihydroorotate dehydrogenase stalls along with production of the orotate necessary for pyrimidine biosynthesis [125, 126]. Uridine supplementation provides pyrimidines for nucleic acid synthesis, to sustain DNA replication and repair. This enables ρ^0 cells to proliferate.

When deprived of pyruvate and uridine, ρ^0 cells cease proliferation and die soon after. For this reason, restriction of pyruvate and/or uridine can be considered a severe form of chronic metabolic injury for ρ^0 cells.

1.4 Mitochondria in health and disease

Given the multiple essential functions of mitochondria, it is unsurprising that the organelle is implicated in, or the central cause of multiple disease phenotypes. Mutations in mitochondrial proteins (both mitochondrial and nuclear) lead to defects in bioenergetics, metabolic signalling, reactive oxygen species (ROS) generation, calcium homeostasis and activation of cell death pathways [127]. Clinical presentations of disease manifest in tissues which are heavily reliant on mitochondrial function. Common disease phenotypes include endocrine disorders, neuropathies, nephropathies, myopathies, aging and cancer [128].

1.4.1 Mitochondria in neurodegenerative disease

Mitochondrial dysfunction is heavily implicated in neurodegenerative or neurological diseases. These include ischemic stroke, Alzheimer's disease, Parkinson's disease, Huntington's disease, amyotrophic lateral sclerosis and psychiatric disorders (depression, bipolar disorder and schizophrenia) [129]. While these diseases are not known to be caused directly by mutations in mtDNA, a combination of environmental and nuclear genome effects result in disrupted mitochondrial function [129, 130]. Mutations in nuclear genes associated with mtDNA replication, stability or nucleotide metabolism do however, cause mutations in mtDNA [131]. Somatic mtDNA mutations are elevated in the brain tissues of patients effected with Parkinson's [132], Huntington's [133] or Alzheimer's diseases [134-136]. These tissues bear heteroplasmic mtDNA mutations; sequence deletions appear to be a common element. It is theorised that these, when coupled with the distinct mtDNA haplotypes carried by the human population, result in the differential susceptibility of individuals to develop an age related neurological disorder [137].

The specific causes of each of these diseases is variable, however each share a commonality; cells with dysfunctional mitochondria die [129, 130, 132, 134]. Progressive loss of neurons leads to a devastating disease phenotype for individuals afflicted with these diseases.

1.4.2 Mitochondria in cancer biology

Curiously, cancer cells or cells which require the capacity to proliferate rapidly (e.g. T-cells and progenitor cells) exhibit increased reliance on glycolytic metabolism [27, 138-148]. This is counter-intuitive at face value, given production of ATP via oxidative phosphorylation produces upwards of 30 ATP per glucose, compared to the 2 ATP produced in glycolysis. This effect, first described by Otto Warburg [149] is often referred to as the 'Warburg' effect, or aerobic glycolysis. Nevertheless, the increased lactate production of highly proliferative cells in aerobic conditions demonstrates that to sustain this

phenotype, major metabolic remodelling has occurred [150]. Current understanding proposes that cells adopt aerobic glycolysis to accumulate glycolytic intermediates as precursors. These feed directly into metabolic pathways other than TCA/OXPHOS, which include the pentose phosphate pathway, synthesis of phospholipids or serine [146, 151-153]. The final glycolytic reaction which forms pyruvate is catalysed by pyruvate kinase. To slow the rate of oxidative phosphorylation and enhance the accumulation of glycolytic intermediates, cancers or rapidly proliferating cells demonstrate altered pyruvate kinase balance or other mutations in the glycolytic pathway [154-160]. This reduces the availability of pyruvate to the mitochondria. The 2 ATP produced by glycolysis, while inefficient, can be generated rapidly under high glucose concentrations and glycolytic activity, to sustain cellular proliferation providing glucose is available [161-163]. In glycolytic metabolism, a cell preserves carbon for macromolecular synthesis through formation of lactate, whereas production of acetyl-CoA and subsequent TCA activity results in loss of carbon as CO_2.

Additionally, oxidative phosphorylation generates ROS which are known to be elevated in many cancers [164]. Signalling mediated by ROS drives tumorigenesis through pathways which impact metabolism, cellular proliferation and angiogenesis. The level of ROS generation must not exceed the cell's capacity for antioxidant defence or the cell instead risks an oxidative stress-driven pro-apoptotic response [164]. The limited rate of OXPHOS in cancer cells is thought to limit ROS generation, to maintain a tumorigenic signalling program.

While extensive metabolic reprogramming in cancer cells favours glycolysis [165-167], mitochondrial respiration remains essential for tumorigenesis. In ρ^0 cancer cells, where mtDNA has been completely ablated, xenograft or syngeneic transplant models reveal that respiration deficient cells lack the ability to form tumours [167-172]. It is conceivable that for this reason, extensive damage to mtDNA or to nuclear genes required for mtDNA replication, transcription, respiration and protein synthesis, could contribute significantly to therapeutic efficacy.

1.5 Intercellular mitochondrial transfer

1.5.1 Origins and current state of knowledge

The first report of organelle transfer between mammalian cells appeared in 2004 from the Gerdes lab with Rustom et al. documenting thin 50-200 nm membrane protrusions which bridged between rat pheochromocytoma PC12 cells *in vitro* [173]. Membrane vesicles and lysosomes were found to be transported between cells by these conduits, which the group termed tunneling nanotubules (TNTs) [173]. Within months, a report was published which detailed similar structures between immune cells from human peripheral blood, inclusive of NK, macrophages, and Epstein-Barr virus transformed B cells [174].

The first report of mitochondrial transfer between cells came in 2006 from Spees et al. [175]. In this seminal study, a ρ^0 derivative of human A549 lung cancer was generated and subsequently shown to take up mitochondria from both human skin fibroblasts and non-hematopoietic stem/progenitor cells isolated from human bone marrow. Spees et al. demonstrated recovery of both respiratory function and mtDNA in the ρ^0 A549 after mitochondrial transfer had occurred. Importantly, the recovered cells were shown to carry the mtDNA sequence consistent with the donor cell mitochondria, through restriction fragment length polymorphism analysis. The recovered cells were no longer auxotrophic for pyruvate and uridine; a significant functional advantage imbued by uptake of exogenous mitochondria [175].

Together, these early studies had revealed a completely new mode of intercellular communication; cells also communicate through the transfer of intracellular macro-structures. With great interest in the purpose and consequences of this phenomenon, multiple groups published accounts of IMT in new cellular contexts [176-192]. Cell types from neuronal, epithelial and mesenchymal lineages; both malignant and benign; had been shown to engage in IMT. The phenomenon however, is not universal among all mammalian cell types [193]; unknown regulatory mechanisms enable certain cell types to act as mitochondrial 'donor' or 'recipient'. This remains a major unknown in the field of IMT research. Likewise, elements of this potential regulatory mechanism may contribute to upregulation or downregulation of IMT activity in response to external stimulus or cell states.

In 2015, Tan et al. published the first report of IMT involved in tumorigenesis *in vivo* [167]. When ρ^0-B16 murine melanoma or ρ^0-4T1 murine breast carcinoma cells were injected subcutaneously, a significant lag period was observed in the development of the primary tumour, compared to injection of the parental B16 or 4T1 cells [167]. Cultures established

from the tumours revealed that these cells had acquired mtDNA from the host animal and recovered respiratory capacity, which eventually restored tumourigenicity. The host origin of the mtDNA in the recovered cells was confirmed by Sanger sequencing of target mtDNA polymorphisms, which differed between host animal and parental cell line [167]. This publication spurred great interest in the field for two major reasons. Firstly, doubts were cleared about whether IMT was simply a potential artefact of *in vitro* culture, with no physiological equivalent. Secondly, tumourigenicity of the ρ^0 cells was restored only upon reacquisition of mtDNA; this confirmed mitochondrial respiration was essential for cancer cell proliferation.

From 2015 to the present, studies of IMT have continued to emerge in the literature [194-211]. Typically, each study describes a known 'donor' cell type engaging in IMT with a 'recipient' cell type; the recipient cell usually models a disease phenotype or is exposed to exogenous injury. These papers describe rescue effects or improved cell survival in recipient cells, which are then attributed to IMT. Just two notable studies describe an alternative context for IMT; Davis et al. describe an instance of retinal ganglion cells engaged in IMT with astrocytes, to outsource mitophagy [211]. Similarly, Phinney et al. describe mitochondria exported from mesenchymal stem cells (MSCs) for purposes of degradation [196]. As it stands, the overwhelming majority of studies published on IMT describe MSCs as effective mitochondrial 'donor' cells [175, 176, 186, 188, 195, 196, 199-203, 205, 207, 208, 212, 213].

1.5.2 Mitochondrial transfer in health and disease

Because normal mitochondrial function is critical to the maintenance of multiple cellular processes, the overall physiological health of an organism is greatly affected by mitochondrial defects. For this reason, the newly recognised phenomenon of mitochondria transferring between cells is likely to represent a new component of mitochondrial maintenance and homeostasis. By understanding the processes surrounding IMT in more detail, we may begin to realise whether or not defects in this phenomenon contribute to the presentation of a disease phenotype in neurodegenerative disease, or whether mitochondrial transfer enhances cell survival in situations where cells are damaged intentionally, such as chemotherapy. If these links are established, the potential exists for therapeutic intervention in mitochondrial or neurodegenerative disease, by enhancing the transfer of functional mitochondria into defective cells, or by disrupting the process to reduce cell survival for cancer cells. For these reasons, it is important to first understand where IMT may occur and what drives the process.

1.5.3 Mechanisms of intercellular mitochondrial transfer

1.5.3.1 Tunneling nanotubules

The first reported instances of IMT were associated with TNTs. These specialised structures have been found between multiple cell types including stem, immune, neuronal and cancer cells *in vitro* [214]. A TNT forms an open ended tubular contact with another cell, which allows cytoplasmic continuity and exchange of intracellular contents [215]. The internal structure of a TNT consists predominantly of F-actin [173] and other cytoskeletal elements. Astrocytes, neuronal cells and immune cells may produce TNTs with a larger diameter, which are known to include microtubules [180, 215, 216].

Several proteins involved in the transfer of organelles via TNTs have been elucidated since their discovery. These include: Miro1 and Miro2, calcium dependent Rho-GTPases [217, 218]; TRAK1 and TRAK2, trafficking kinesin-binding proteins [219, 220]; Myo 10 and Myo 19, actin-based motor proteins [221]; and KLF5, a microtubule modulating motor protein [222]. Perhaps unsurprisingly, these proteins share a conserved role in the intracellular transport of mitochondria over long distances, such as for axonal transport in neurons [223].

The mechanisms behind how a developing TNT enters or integrates with a 'recipient' cell membrane has not yet been fully characterised. Tunneling nanotubule formation is known to be responsive to external signals, such as cytokines, serum starvation or oxygen radicals [189, 202]. This was found to be mediated through p53, EGFR, Akt, PI3K, and mTOR pathways in astrocytes [189]. M-sec, the protein previously known as TNFaip2, is also known to be involved in TNT formation [224-226].

1.5.3.2 Extracellular vesicles

As an umbrella descriptor, the term 'extracellular vesicle' encompasses secreted lipid-bilayer particles broadly categorised as microvesicles or exosomes, which originate from the cell membrane or endosome respectively [227]. These are shed from the cell to exchange proteins, lipids and genetic information between cells as a contact independent form of intercellular communication. The cellular origin and cargo of extracellular vesicles is highly variable, thus categorisation by size is a useful means of classification: 50-500 nm for exosomes; 1-10 μm for microvesicles.

Islam et al. first described IMT mediated through extracellular vesicles [186]. In this report, MSCs were found to secrete extracellular vesicles which contained functional mitochondria. These were shown to impart a protective effect to murine pulmonary alveoli against acute lung injury [186]. Soon after, macrophages were also demonstrated to take up

mitochondria via MSC derived microvesicles by Phinney et al. [196]. These were shown to enhance oxidative phosphorylation in the 'recipient' cells.

Of particular relevance to this thesis, Hayakawa et al. also described transfer of mitochondria from astrocytes to neurons, mediated by extracellular particles *in vitro*. This was found to be dependent on cyclic ADP ribose hydrolase (CD38) and cyclic ADP ribose signalling [198]. Uptake of mitochondria via these particles was associated with improved survival outcomes for neurons following oxygen-glucose deprivation. Additionally, when astrocyte derived EVs were injected into ischaemic brain regions, the improved survival outcome for neurons was recapitulated [198]. This study highlights a new mechanism through which astrocytes support neurons. Similarly, in the work of Davis et al., outsourcing of mitophagy from neurons to astrocytes was mediated through extracellular vesicles [211]. Together, these studies begin to explore the idea that damaged or dysfunctional mitochondria may be exported from neurons, while a parallel replacement occurs via exogenous mitochondria. This may be particularly relevant for mitochondria located far from the cell body in axons or synaptic regions, such as in peripheral nerves where the synapse can be up to a meter away from the cell body. Perhaps under certain circumstances a mechanism like this could be bioenergetically favourable over mitochondrial biogenesis.

While not IMT, mitochondria purified from MSCs and other cells and delivered as free isolates can be taken up by cells, by a process called mitochondrial transplantation [228-230]. Using mitochondria isolated from MSCs, Cho et al. demonstrated that the free organelles could restore respiratory function to ρ^0-143B cells, but this was not recapitulated when mtDNA molecules alone were provided to the cells [176]. A series of publications from the McCully lab provide compelling evidence that uptake of free mitochondria increases tissue ATP content, high energy synthesis, replaces damaged mtDNA and enhances proteomic pathways in cardiac tissues [231-234]. In particular, Cowan et al. demonstrate endolysosomal involvement in the uptake of free mitochondria by IPS-derived cardiomyocytes and primary cardiac fibroblasts [234], however exactly how free mitochondria escape lysosomal degradation remains unknown.

1.5.3.3 Cell fusion

Perhaps the least elegant of described mechanisms for mitochondrial transfer is by partial or complete cell fusion. The vast majority of cells are individually compartmentalised; however it is well understood that specific cell types are capable of cell fusion. Fusion between two or more cells of the same type leads to the formation of syncytia; well characterised multinucleated cells such as osteoclasts in bone, chondroblasts in cartilage,

trophoblasts in placenta or myoblasts in muscle [235]. Fusion between cells of distinct types yields heterokaryons; these were initially experimental creations [236], thought to occur by artificial means [235]. However, a precedence for cells to fuse spontaneously both *in vitro* and *in vivo* is now well established [235, 237-240]. Fusion events which involve MSCs in particular, have been documented with both normal and malignant cells of numerous types [235, 241-245]. Syncytial-like structures have also been described in gliomas, with contiguous intercellular communication mediated by connexin 43 gap junctions and tumour microtubes [246, 247]. These observations have recently been extended further to include direct tumour network coupling with neurons [248-250].

Of particular relevance to this thesis, Alvarez-Dolado et al. demonstrated that intravenous administration of bone marrow derived cells which expressed Cre-recombinase, to recipient animals with Lox P sites regulating LacZ expression in the Purkinje neurons, resulted in low levels of multinucleated Purkinje neurons that could be visualised with X-gal [238]. This elegant study demonstrated that it was possible for bone marrow derived cells administered systemically to cross the blood-brain barrier and engage in cell fusion with neurons. Further work in this area established that this phenomenon occurred more regularly under inflammatory conditions, which increase blood-brain barrier permeability to cell migration [251-253].

Given the numerous studies which explore MSCs as IMT 'donor' cells, it is not surprising that partial or complete cell fusion provides copious opportunity for IMT to occur, in addition to the transfer of all other cellular contents. Cell fusion equally results in what can be described as IMT and could explain the data in many published reports. Very few studies of IMT provide evidence to exclude cell fusion as a potential mechanism for IMT [175, 200].

1.6 Aims of this research

If IMT is involved in cell survival *in vivo*, we must progress our understanding of how the process is regulated, and which cell types are involved. Knowledge gained in these areas may provide an opportunity to improve existing cancer therapies, or to identify new molecular targets to treat neurological disease. Numerous reports of IMT are now published, and regularly describe functional benefits for cells which have taken up or exported mitochondria. Unfortunately, these reports include little quantitative data to support conclusions on how acute or chronic injuries influence the rate of IMT. This is in part, because the existing tools to measure this are limited.

If the rate of IMT is responsive to specific cellular stressors, we may gain insight into the molecular mechanisms which regulate IMT using stress models. Additionally, what characterises a cell as able to act as 'donor' or 'recipient' in IMT remains poorly understood. We need to discover IMT in new biological contexts to uncover shared features between cells which are capable of IMT. The research presented in this thesis progressed understanding in these two key areas through experiments which addressed the following aims:

1. Apply existing methodologies used to study IMT, to determine if these are appropriate for quantitative studies of IMT in neural cell models.

2. Develop a novel quantitative approach to study IMT.

3. Identify cell types within the brain microenvironment which engage in IMT *in vitro*.

4. Apply a novel quantitative approach to study how acute or chronic injury alters the rate of IMT, in an appropriate neural cell model.

2 Materials and Methods

2.1 Materials

12 Well Clear Cell Culture Treated Microplates	Corning, USA
150 x 25mm Cell Culture Treated Dish	Corning, USA
24 Well Clear Cell Culture Treated Microplates	Corning, USA
25 mm diameter, No. 1.5 coverslips	ThermoFisher, USA
6 Well Clear Cell Culture Treated Microplates	Corning, USA
60 x 15mm Cell Culture Treated Dish	Corning, USA
9 cm Bacteriological Petri	TechnoPlas, Australia
96 Well Clear Flat Bottom Cell Culture Treated Microplates	Corning, USA
Adhesive seal tabs for SecureSeal™ chambers	Grace Bio-Labs, USA
Agilent Seahorse XFe96 Cell Culture Microplates	ThermoFisher, USA
Agilent XFe96 Sensor Cartridge	ThermoFisher, USA
Cryo.s™ 1 mL cryovials	Greiner bio-one, Austria
CultureWell™ Reusable Gaskets 4 x 9 mm diameter	Grace Bio-Labs, USA
Eppendorf™ DNA LoBind 1.5mL Tubes	ThermoFisher, USA
Falcon™ 15 mL tubes	ThermoFisher, USA
Falcon™ 50 mL tubes	ThermoFisher, USA
HybriSlip™ 22 mm x 60 mm hybridisation covers	Grace Bio-Labs, USA
MicroAmp® Fast Optical 96-Well Reaction Plate, 0.1 mL	ThermoFisher, USA
MicroAmp® Optical Adhesive Film	ThermoFisher, USA
Millex GP33 0.22um 33 mm PES express syringe filter	ThermoFisher, USA
Minisart® NML, 1.2 um syringe filter	Sartorius, USA
Pyrex® cloning cylinder 6 mm × 8 mm	Merck, USA
SecureSeal™ 8 x hybridisation chambers 9 mm diameter	Grace Bio-Labs, USA
Snap Strip 8 PCR Tubes 200 µL	SSIBio, USA
Superfrost Plus microscope slides	ThermoFisher, USA
T25 Flask Tissue Culture Treated	Corning, USA
T75 Flask Tissue Culture Treated	Corning, USA

2.2 Reagents

10 x Annexin V Binding Buffer	Biolegend, USA
Accutase™	STEMCELL Technologies, Canada
Annexin V	Biolegend, USA
Anti-Mouse CD16/CD32 clone 2.4G2 (Mouse BD Fc Block™)	BD, USA
ApogeeMix	Apogee Flow Systems, United Kingdom
BD™ CS&T Beads	BD, USA
SPHERO™ Ultra Rainbow Fluorescent Particles	Spherotech, USA
Big Dye® V3.1	ThermoFisher, USA
Bovine Serum Albumin	ICP Biologicals, New Zealand
Cell-Tak™ Cell and Tissue Adhesive	ThermoFisher, USA

2.2 Reagents (continued)

Collagen I, Rat Tail	ThermoFisher, USA
Dulbecco's Modified Eagle Medium	ThermoFisher, USA
DNA Clean & Concentrator™	Zymo Research, USA
Dulbecco's phosphate-buffered saline, no calcium, no magnesium	ThermoFisher, USA
DraI restriction enzyme	New England Biolabs, USA
NdeI restriction enzyme	New England Biolabs, USA
BsaBI restriction enzyme	New England Biolabs, USA
T7 exonuclease	New England Biolabs, USA
10 x Cutsmart digest buffer	New England Biolabs, USA
T4 DNA Ligase	ThermoFisher, USA
10 x T4 DNA Ligation buffer	ThermoFisher, USA
Foetal Bovine Serum	ThermoFisher, USA
FluoroBright DMEM Media	ThermoFisher, USA
GELRED® Nucleic Acid Stain	Biotium, USA
GlutaMAX™	ThermoFisher, USA
Hank's Balanced Salt Solution	ThermoFisher, USA
HyAgraose LE Agarose (Multi-purpose)	HydraGene, USA
KAPA HiFi Hotstart ReadyMix	KAPA Biosystems, USA
KAPA SYBR® Fast Universal Master Mix	KAPA Biosystems, USA
Luria Broth Base (Miller's LB Broth Base), powder	ThermoFisher, USA
MitoTracker® Green FM	ThermoFisher, USA
MitoTracker® Red CMXRos	ThermoFisher, USA
Penicillin-Streptomycin	ThermoFisher, USA
Pericyte Growth Medium	Sciencell, USA
Pericyte Growth Supplement	Sciencell, USA
PrimeScript™ RT Master Mix	TaKaRa Bio, Japan
Pepsin (Porcine, 2500 U/mg)	Merck, USA
Propidium Iodide (PI)	Biolegend, USA
QuantiTect primer assay (Mm_Rn18s_3_SG)	Qiagen, Netherlands
Quick-gDNA™ MiniPrep	Zymo Research, USA
Richard-Allan Scientific™ Histoplast PE Paraffin	ThermoFisher, USA
RNeasy® Mini Kit	Qiagen, Netherlands
Seahorse XF Base medium without phenol red	ThermoFisher, USA
Seahorse XF Calibration Solution	ThermoFisher, USA
VectaShield ™ Antifade Mounting Medium with DAPI	Vector Laboratories, United Kingdom
VectaShield ™ Antifade Mounting Medium	Vector Laboratories, United Kingdom
Trypsin-EDTA 0.05%	ThermoFisher, USA
Vaseline®	Unilever, United Kingdom
Viafect™	Promega, USA
Zombie NIR™ Fixable dye	Biolegend, USA

Note: All oligonucleotides used in this thesis were purchased from IDT, USA.

Nomenclature for modified oligonucleotides follows the standard IDT system.

2.3 Kits

Agilent XF Glycolytic Rate Assay Kit	ThermoFisher, USA
CellTrace™ CFSE Cell Proliferation Kit	ThermoFisher, USA
CellTrace™ Violet Cell Proliferation Kit	ThermoFisher, USA
CellTrace™ Yellow Cell Proliferation Kit	ThermoFisher, USA
e-Myco™ Mycoplasma PCR Detection Kit	iNtRON Biotechnology, South Korea
Epoxy Embedding Medium kit	Merck, USA
PureLink™ HiPure Plasmid Maxiprep Kit	ThermoFisher, USA
PureLink™ HiPure Precipitator Module	ThermoFisher, USA
Qubit™ dsDNA BR Kit	ThermoFisher, USA
TURBO DNA-free™ Kit	ThermoFisher, USA

2.4 Chemicals

(3-Aminopropyl)triethoxysilane	Merck, USA
7-Aminoactinomycin D	ThermoFisher, USA
Acetic acid	Merck, USA
Acetone	ThermoFisher, USA
Ampicillin, sodium salt, irradiated	ThermoFisher, USA
ATP	ThermoFisher, USA
Boric Acid	Merck, USA
Chloramphenicol	PanReac AppliChem, USA
Cisplatin	Cayman Chemical, USA
Dimethyl Sulfoxide (DMSO)	ThermoFisher, USA
EDTA	Merck, USA
Ethidium Bromide	Bio-Rad Laboratories, USA
Formamide	ThermoFisher, USA
Geneticin® Selective Antibiotic (G418 Sulfate)	ThermoFisher, USA
Glucose	Merck, USA
Glutamine	ThermoFisher, USA
Glutaraldehyde Solution, 25%	Merck, USA
HEPES	ThermoFisher, USA
Hoechst 33342	ThermoFisher, USA
Kanamycin Sulfate	ThermoFisher, USA
Molecular grade ethanol	ThermoFisher, USA
Nitric Acid	ThermoFisher, USA
Osmium Tetroxide	Merck, USA
Sodium Bicarbonate	Merck, USA
Sodium Chloride	Merck, USA
Sodium Hydroxide (Pellets)	Merck, USA
Sodium Pyruvate	ThermoFisher, USA
Sucrose	ThermoFisher, USA
SYBR® Green I	ThermoFisher, USA
Tris-HCL	Merck, USA

2.4 Chemicals (continued)

Trizma® base	Merck, USA
Trypan blue 0.04%	ThermoFisher, USA
Tween-20	Merck, USA
UltraPure™ DEPC-Treated Water	ThermoFisher, USA
Uranyl Acetate	Merck, USA

2.5 Antibodies

AN2-PE Clone 1E6.4	Miltenyi Biotech, Germany
Anti-Mouse CD16/CD32 clone 2.4G2 (Mouse BD Fc Block™)	BD, USA
CD105-APC-Vio770 Clone REA794	Miltenyi Biotech, Germany
CD140b-APC Clone APB5	Miltenyi Biotech, Germany
CD146-PerCP-Vio700 Clone ME-9F1	Miltenyi Biotech, Germany
CD73-FITC Clone TY/11.8	Miltenyi Biotech, Germany
CD90.2-VioBlue Clone 30-H12	Miltenyi Biotech, Germany

2.6 Equipment

BD FACSCanto II™	BD, USA
BD Influx™	BD, USA
Bioline Shaking Incubator	Edwards Instrument Company, Australia
CoolCell® LX	BioCision, USA
Coverslip Cell Chamber	Aireka Scientific Company, China
Dumont #5/45 Forceps	Fine Science Tools, USA
FV1200 Laser Scanning Confocal Microscope	Olympus Scientific, USA
IN Cell Analyzer 6500 HS	GE Healthcare Life Sciences, USA
IncuCyte® S3 Live-Cell Analysis System	Essen BioScience, USA
JEOL2010 Transmission electron microscope	JEOL, USA
Locator 6 Liquid Nitrogen Storage	ThermoFisher, USA
Logic Labconco® Purifier® Biological Safety Cabinet	Total Lab Systems Ltd, New Zealand
NanoDrop™ One	ThermoFisher, USA
prime-G thermocycler	Techne, United Kingdom
QuantStudio™ 7	Applied Biosystems, USA
SANYO MCO-20AIC humidified incubator	SANYO Electric Company, Japan
Seahorse XFe96 Analyzer	Agilent, USA
SORVALL RC6+ ultrafuge	ThermoFisher, USA
Tecan Infinite M1000 Pro Plate Reader	Tecan, Switzerland

2.7 Cell culture

2.7.1 Cell types

Multiple cell types were utilised in this research, including both primary cells and immortalised cell lines.

Table 1. Cell types cultured in this research

Line Name	Origin	Strain	Status	Tissue Type	Source
LN18	Human	-	Immortalised	Glioblastoma	ATCC
SH-SY5Y	Human	-	Immortalised	Neuroblastoma	ATCC
SVGp12	Human	-	Immortalised	Astroglia, foetal	ATCC
T98-G	Human	-	Immortalised	Glioblastoma	ATCC
U87-MG	Human	-	Immortalised	Glioblastoma	ATCC
WI-38	Human	-	Primary	Lung fibroblast	ATCC
3T3	Murine	NIH Swiss	Immortalised	Fibroblast	ATCC
B16	Murine	C57BL/6	Immortalised	Melanoma	ATCC
Bone marrow stromal cell (BMSC)	Murine	BALB/CJ	Immortalised		Primary Tissue
C8D1A	Murine	C57BL/6	Immortalised	Astrocyte	ATCC
eGFP-astrocyte (C57A)	Murine	eGFP-C57BL/6	Immortalised	Astrocyte	Primary Tissue
GL261	Murine	C57BL/6	Immortalised	Glioma	ATCC
Murine pericyte	Murine	C57BL/6 x mito-DsRed: BCF1, BCF7	Primary	Pericyte	Primary Tissue
Murine pericyte	Murine	BALB/cByJ	Primary	Pericyte	Primary Tissue
NE-4C	Murine	BALB/cByJ	Immortalised	Neuro-ectodermal	ATCC
ρ^0-eGFP-astrocyte	Murine	eGFP-C57BL/6	Immortalised	Astrocyte	Primary Tissue

2.7.2 Cell culture media

All cell lines used in this research were cultured in DMEM medium, high glucose medium supplemented with 10% FBS (foetal bovine serum) (v/v) and 2 μM Glutamax™ (complete media), unless otherwise specified. Primary murine pericytes were cultured in Pericyte Growth Medium supplemented with 1 x Pericyte Growth Supplement, 100 U/mL penicillin, 100 μg/mL streptomycin (Life Technologies), 2% (v/v) FBS (PCGM). All FBS used in this research was first heat inactivated by incubation at for 30 m at 56 °C.

2.7.3 Culture method

All cell lines used in this research were maintained as adherent cultures unless otherwise stated. To culture cells as 3D aggregates, cells were seeded at low density in uncoated 10 cm plates. All cells were maintained at 37 °C in a 5% CO_2 atmosphere within a humidified incubator. Cells were maintained by subculture at approximately 75-85% confluence, under sterile conditions in a biosafety cabinet. To harvest cells, culture media was first aspirated and cells rinsed briefly with DPBS. Cells were coated briefly with a thin layer of trypsin-EDTA 0.05% before aspiration of this solution. Cells were incubated for 5 min at 37 °C, 5% CO_2, or until complete dissociation of the cell monolayer was observed. Cells were washed from the vessel surface with complete medium, to inactivate residual trypsin. Cells were pelleted by centrifugation for 5 min at 400 g before suspension in DPBS or complete medium, ready for downstream use. Cells were prepared for cryostorage by addition of 10% DMSO (v/v) to 1 x 10^6 cells in a 1 mL volume within Cryo.s™ 1 mL cryovials and cooled to -80 °C at a rate of 1 °C /m in a CoolCell® LX controlled rate cooler. Cells were placed in vapour phase liquid nitrogen for long term storage within one week. All cell counts were carried out by addition of 1 volume 0.4% (v/v) Trypan Blue to determine cell viability alongside count by haemocytometer. To ensure cell cultures were free from mycoplasma contamination, all cell lines were subject to regular (approximately 3 monthly) PCR screens by e-Myco™ Mycoplasma PCR Detection Kit as directed by the manufacturers protocol. Cell lines were renewed from cryopreserved stocks within 15 subcultures to reduce genetic drift.

2.7.4 Drug treatment of eGFP-astrocytes

Cisplatin was dissolved in normal saline (0.9% NaCl w/v) at 1 mg/mL, sterile filtered and stored protected from light. The solution was disposed of within two weeks of preparation and a fresh stock prepared to avoid loss of drug activity. Chloramphenicol was dissolved at 30 mg/mL in molecular grade EtOH, sterile filtered and stored at -20 °C. For experiments in which cisplatin or chloramphenicol were used as cellular injuries, cells were treated as follows. Three hundred thousand cells were seeded in 75 cm^2 culture flasks in 15 mL of

complete medium which contained the compound of interest. Additional flasks remained untreated as an untreated control. Cells were incubated for 48 h at 37 °C, 5% CO_2 in the presence of drug.

2.8 Primary murine brain pericytes

2.8.1 Mouse strains

This research made use of cell lines or primary cells derived from animals in the Berridge or McConnell laboratories at Malaghan Institute of Medical Research, New Zealand or Victoria University of Wellington, New Zealand, respectively. The transgenic eGFP-C57/B6 were generated from a cross between C57B/6J and C3H/He mice, back-crossed onto a C57B/6J background. These transgenic mice express ubiquitous cytosolic eGFP driven by a chicken beta-actin promoter (CAG) and cytomegalovirus enhancer [254]. Transgenic mito-DsRed2 (unpublished) were generated by the Neuzil lab (Institute of Biotechnology, Czech Academy of Sciences, Prague, Czech Republic) with genetic resources from the Okabe lab [255]. These transgenic mice express ubiquitous DsRed2 conjugated to the ATP synthase F_0 complex subunit 9 mitochondrial import sequence, driven by a CAG promoter. Female BALB/cByJ were bred with male mito-DsRed2 mice to produce a BALB/cByJ x mito-DsRed2 first generation hybrid pups (BC-F1). The BC-F1 animals were back-crossed onto a C57B/6J background by sequential breeding of female, transgene positive progeny with male C57B/6J. This was carried out for 7 generations to produce C57BL/6J x mito-dsRed BC-F7 animals used in this research, and continued for 9 generations to produce a final C57BL/6J x mito-dsRed BC-F9 animal. The purpose of this was to produce a mouse strain with fluorescent DsRed2 mitochondria that carried the mitochondrial DNA sequence of the BALB/cByJ strain, on a C57BL/6J background. Both transgene-positive and negative BCF1 and BCF7 animals were used, in addition to BALB/cByJ animals for the preparation of primary pericyte cultures in this research.

2.8.2 Brain microdissection

Murine brain was used as a source of primary pericytes, from adult animals approximately 6 weeks of age. Each animal was euthanised by CO_2, before the head was removed and placed in an individual 50 mL tube. The tubes were kept on ice while each brain was retrieved by microdissection. Using microdissection scissors, a cut was made to the skin at the base of the skull and extended coronally to the maxilla. The frontal bone was gripped by tweezers placed into the orbital sockets, to steady the skull. A cut was made through the occipital bone and extended coronally along the sagittal suture line and approximately 50%

of the way through the frontal bone. Two further cuts were made horizontally through the each side of the occipital bone towards the orbital sockets. Each half of the skull plate structures were gently lifted from the brain surface using tweezers to separate meningeal tissue from the inner surface of the bone. Tweezers were used to cut through the medulla oblongata and spinal cord as they were inserted gently towards the olfactory bulbs along the underside of the brain. A gentle upwards pressure was applied to the brain to lift the entire structure away from the animal, intact. The olfactory bulbs and residual hindbrain structures were removed with microdissection scissors, with care taken to avoid damage to the cerebellum. The brain was placed into a 10 cm glass dish which contained ice-cold HBSS with 100 U/mL penicillin, 100 µg/mL streptomycin, 1 mM sodium pyruvate and 10 mM HEPES. The dish was placed on ice on the stage of a 4 x objective dissection microscope. Easily accessed meningeal tissue was teased away from the surface of the brain using fine grade surgical tweezers. This was to reduce the presence of fibroblasts in the downstream isolation. The brains were rinsed briefly and placed into fresh buffer on ice.

2.8.3 Isolation of murine brain microvessels

To prepare whole brains for isolation of microvessels, buffer was aspirated and a sterile scalpel used to finely dice the tissue. The combined tissue from all animals was resuspended in 4 mL of cold HBSS with 100 U/mL penicillin, 100 µg/mL streptomycin, 1 mM sodium pyruvate and 10 mM HEPES and moved into a 15 mL tube . The tissue was centrifuged for 4 m at 400 x g at room temperature and the buffer aspirated. To dissociate tissue, the Neural Tissue Dissociation Kit (T) (Miltenyi Biotech) was used with a modified version of the manufacturer's manual dissociation protocol. After enzymatic dissociation of the tissue as described by the manufacturer, the crude tissue digest was pelleted by centrifugation for 5 m at 500 x g. No physical trituration was applied to the crude tissue digestion. The tissue was washed twice in a solution of HBSS which contained 5% FBS (v/v). The tissue suspension was gently resuspended in 8 mL filter sterilised solution of DMEM basal medium, 5% FBS (v/v) and 22% BSA (w/v). To remove myelin, the tissue was centrifuged for 10 m at 1000 x g. The high density BSA solution allowed myelin to be aspirated as a separated layer from the cell pellet and microvasculature fragments. The remaining BSA solution was aspirated and the pelleted material washed twice with HBSS.

2.8.4 Primary pericyte culture

Prior to isolation of microvessels, a 25 cm^2 tissue culture flask was prepared with a 7.5 µg/cm^2 rat collagen I coating. Briefly, 125 µL of 3 mg/mL Collagen I, Rat Tail (Life Technologies) was resuspended to a final volume of 2 mL in filter sterilised 20 mM acetic acid in ddH_2O. The solution was transferred into a sterile 25 cm^2 tissue culture flask and incubated for 1 h at 37 °C. The collagen solution was aspirated and the flask rinsed twice with DPBS. The cells prepared as in section **2.8.3** were resuspended in 5 mL Pericyte Growth Medium supplemented with 100 U/mL penicillin, 100 µg/mL streptomycin and 2% FBS (PCGM). The cells were transferred into the collagen I coated flask and incubated at 37 °C, 5% CO_2 overnight. After 16-18 h, the culture medium was aspirated to remove all non-adherent cells and rinsed once gently with DPBS. Additional care was taken in this rinse to avoid disturbance of lightly adhered microvessel fragments. The medium was replenished with 5 mL PCGM and the cells incubated at 37 °C, 5% CO_2 until approximately 85% confluence (approximately 2 further days). Cells were harvested as described in section **2.7** and all cells transferred into a sterile 75 cm^2 tissue culture flask in 12 mL of PCGM. Cells were sub cultured twice further after each time 85% confluency was reached. For each vessel harvested, 50% of the culture was transferred into each of two sterile 75 cm^2 tissue culture flasks. After the third subculture, cells were harvested by Accutase™ as described by the manufacturer. This was to reduce the loss of surface protein epitopes by trypsin harvest before flow cytometry or co-culture.

2.9 Constructs and expression of transgenes

Table 2. Constructs used in this research

Name	Transgene	Fusion	Bacterial Resistance Cassette	Mammalian Resistance Cassette	Source
mKO2-Mito-7	Kusabira Orange	MTS of COX8A	Kanamycin	Neomycin	Addgene
Mito-BFP	Blue Fluorescent Protein	MTS of yeast COX4	Kanamycin	Neomycin	Addgene
GFP	Green Fluorescent Protein	-	Ampicillin	Neomycin	Addgene
mCherry2-N1	mCherry2	-	Kanamycin	Neomycin	Addgene

2.9.1 Preparation of plasmids

All plasmids were prepared from transformed *E. coli* in agar stabs received directly from the Addgene plasmid repository, or prepared from frozen glycerol stocks in the McConnell laboratory. A sterile wire loop was used to inoculate fresh Luria Bertani (LB) agar plates containing 50 µg/mL kanamycin (LB-Kan) or 100 µg/mL ampicillin (LB-Amp) dependent on the resistance cassette present within the transformed bacteria. Bacterial plates were cultured overnight at 37 °C to allow colony formation. A single colony with normal morphology was lifted by sterile wire loop and inoculated into 2 mL sterile liquid LB-Amp or LB-Kan in a 15 mL tube with a partially tightened cap. Cultures were incubated for 16 h at 37 °C under constant shaking. Five hundred microliters of this culture was used as inoculum for 400 mL of sterile liquid LB-Amp or LB-Kan in 1 L conical flasks. Cultures were incubated for 16 h at 37 °C under constant shaking to grow sufficient bacteria for plasmid extraction from the exponential phase of culture. Bacterial cultures were concentrated by ultrafugation at 5000 g for 10 min at 4 °C.

2.9.2 Plasmid isolation and concentration

To isolate high quality plasmid DNA suitable for transfection, the PureLink™HiPure Plasmid Maxiprep Kit and Purelink™ HiPure Precipitator module (ThermoFisher) were used as directed by the manufacturer. Briefly, bacterial pellets were suspended in a buffered glucose solution which included RNase A, then lysed with an alkaline lysis buffer. A homogenous lysate was produced by multiple gentle inversions, followed by a 5 min incubation at room temperature. Addition of a potassium acetate formulated buffer neutralised the lysates prior to clarification by gravity filtration through the inner cartridge of the PureLink™ Maxi column. Column flow through was collected and passed once more through the inner cartridge to maximise the yield of column bound plasmid. The design of the inner cartridge allows the vast majority of gDNA, protein and other cellular materials to be discarded after this step. The column was loaded with Wash Buffer and allowed to pass through the column by gravity, before the flow through was discarded. Elution Buffer was loaded onto the column, and the eluted plasmid collected. To precipitate plasmid DNA, Isopropanol was added to the elution and incubated for 2 min at room temperature. A PureLink™HiPure Precipitator Module was attached to a 30 mL syringe, and the precipitated DNA mixture loaded via the plunger end of the syringe barrel. Gently, the precipitated DNA solution was passed into the module and the flow through discarded. To purify plasmid DNA, 70% EtOH was added to the syringe and passed through the module and discarded as flow through. Air was passed through the module several times to evaporate residual EtOH and dry the resin. The module was then removed and reattached to a 5 mL syringe. One millilitre TE buffer was gently passed through the

module to elute purified plasmid DNA into a sterile 1.5 mL tube. Plasmids were assessed for integrity by electrophoretic separation in a 1.5% agarose gel run in 1 x TBE buffer at 10 v/cm for 1 h. Plasmid DNA concentration was quantified by Qubit™ Fluorometer using the Qubit™ dsDNA BR kit as directed by the manufacturers protocol.

2.9.3 Transfection

2.9.3.1 Transient transfection

All transfections in this research were mediated by cationic liposomal reagent Viafect™ based on the manufacturers protocol. Briefly, cells were seeded in 6-well tissue culture plates at a density which allowed cells to reach approximately 70% density by surface area overnight. For each of the wells to be transfected, 500 µL of DMEM basal medium was combined with 2 µg of the plasmid, before addition of 4 µL room-temperature Viafect™ reagent. The transfection mixture was incubated for 20 min at room temperature to allow formation of liposomal complexes. The complete transfection mixture was delivered to cells in complete medium and allowed to incubate overnight. Medium was aspirated and replaced by complete medium within 16 h of introduction of lipid complexes.

2.9.3.2 Stable selection and cloning

All constructs used in this research carried a neomycin resistance cassette driven by a mammalian promoter. This allowed for successfully transfected cells to be selected by addition of geneticin to culture medium. Appropriate geneticin concentrations were determined for each cell line based on daily visual assessment of cell morphology across a titration of drug concentrations. For SH-SY5Y cells (400 µg/mL), LN18 (500 µg/mL), NE-4C (300 µg/mL) and U87-MG (400 µg/mL), geneticin selective medium was replaced daily to maintain drug concentration. Cell death was monitored daily by visual inspection, and major selection events were observed approximately 5-7 days after transfection. At this time, a vast majority cells expressed the fluorescent reporter also encoded by the respective construct. To support cell health, culture vessel size was reduced upon sub-culture of colonies to maintain sufficient culture density. After approximately 12 days, if colonies were not seen to expand, the geneticin concentration was reduced by 100 µg/mL. If colonies appeared to be at risk of complete cell death, medium conditioned by the parental cell line was filtered through a 0.22 micron syringe filter and provided in support. After 3 weeks selection, cells were plated at extremely low density (approximately 5 cells/cm^2) in selective medium contained in 150 mm cell culture dishes to promote formation of colonies from single cells. Individual colonies which had reached approximately 20 cells were marked on the outside of the culture dish and the culture medium aspirated. One edge of a

sterile 6 mm × 8 mm Pyrex® cloning cylinder was coated with sterile Vaseline®, and sealed gently around the colony by sterile forceps. Selective medium was replaced and the colonies incubated for a further 3 days. To retrieve colonies, culture medium was aspirated, and the cloning ring filled with 5 µL .05% trypsin EDTA and incubated for 5 min. The trypsin solution was retrieved using a P10 pipette and each colony transferred to a single well of a 96 well tissue culture plate. One hundred and ninety five microliters of complete selective medium was added to each well and the clones incubated until approximately 85% density by surface area. Clones which exhibited a high degree of fluorescence from each desired fluorescent protein were expanded to 75 cm^2 culture flasks and preserved in liquid nitrogen for future use.

2.10 Live Cell Imaging

2.10.1 Imaging medium

To facilitate live cell imaging by laser scanning confocal (LSCM) or high throughput confocal microscopy (HTCM), all live cell imaging was carried out using FluoroBright DMEM supplemented with 2 µM GlutaMax™, 10% FBS and 1 mM sodium pyruvate (complete imaging medium) unless stated otherwise.

2.10.2 Preparation of coverslips

All coverslips used for live cell imaging were sterilised before use in cell culture. Briefly, singular 25 mm diameter, No. 1.5 coverslips were each placed into a well of a 6-well tissue culture plate which contained 1 mL of 100% EtOH, and incubated for 20 m at room temperature under UV light. Each coverslip was retrieved using flame-sterilised Dumont #5/45 Forceps (Fine Science Tools) and the excess EtOH allowed to drain before passing the coverslip quickly through a flame. Each coverslip was placed within a single well of a 6-well plate which contained DPBS.

2.10.3 Nitric acid etched microscope slides

Superfrost Plus microscope slides were placed within a stainless steel slide rack which was submerged in 70% nitric acid in a fume hood. The slides were incubated for 48 h at room temperature to allow for acid induced damage to the glass surface. This generates an enhanced surface for cell adhesion when used for cell culture. The slides were washed 3 times by immersion in a 1 L glass beaker filled with fresh ddH_2O, and placed into a second ddH_2O filled beaker to incubate overnight with constant orbital motion. The slides were

removed from the ddH_2O and sterilised using 10 cm tissue culture dishes as described 2.10.2.

2.10.4 Surface silanisation with (3-aminopropyl)triethoxysilane

To generate an enhanced positive surface charge on 25 mm coverslips or Superfrost Plus glass slides, surfaces were functionalised with (3-Aminopropyl)triethoxysilane (APTES). A 1:50 dilution of APTES was prepared in acetone in a 500 mL beaker. Coverslips or slides were submerged in the solution and incubated for 10 min at room temperature with orbital motion. The coverslips or slides were retrieved from the APTES solution and placed into a second beaker of acetone. The slides were incubated for 5 min at room temperature, rinsed twice with fresh acetone and placed in 100% EtOH for storage until use.

2.10.5 Preparation of glass-bottomed confocal plates

Optical plates were prepared for use in live cell imaging as follows. Briefly, standard 12-well tissue culture plates were laser cut with an 18 mm diameter circle removed from the centre of each well. A 3:1 liquid mixture (w/w) of Vaseline® and Richard-Allan Scientific™ Histoplast PE Paraffin was prepared by gentle heating of the solid materials in a glass dish on a 70 °C hot plate. The temperature was reduced if bubbles were seen to form. A basic, round-brushed artist's paintbrush was used to distribute an even layer of wax mixture around the periphery of each hole, on the underside of the 12-well plate, approximately 4 mm in width. Twenty five millimetre diameter No. 1.5 coverslips prepared as described in section **2.10.4**, were carefully placed upon the wax surface, centred precisely on the base of the well. The plates were incubated overnight at 65 °C on a tray placed within a drying incubator. This softened the wax layer and allowed coverslips to form a complete seal with the bottom of the tissue culture plate. The plates were tested for leaks by addition of approximately 500 µL of ddH_2O. To sterilise the plates, ddH_2O was aspirated and replaced with 70% EtOH. The plates were incubated for 20 min at room temperature while exposed to UV radiation within a biosafety cabinet. The ethanol solution was aspirated, and the wells washed once with DPBS. The plates were dried by aspiration of DPBS, and placed at 4 °C for storage before use.

2.10.6 Hoechst 33342 staining

To visualise the nuclei of cells in both LSCM and HTCM experiments, Hoechst 33342 was added directly to imaging medium at a final concentration of 5 µg/mL immediately prior to imaging.

2.10.7 Mitotracker® Red CMXRos staining

Stock solutions of MitoTracker® Red CMXRos were prepared from lyophilised reagent as directed by the manufacturer. Briefly, 50 µg of lyophilised MitoTracker® CMXRos was resuspended in sterile DMSO at a final concentration of 1 mM. The solution was vortexed vigorously for 30 s at room temperature to ensure complete resuspension. The reagent was then aliquoted and stored at -20 °C for use within two weeks of resuspension. To stain and visualise mitochondrial networks with a functional membrane potential, medium was aspirated from cells and replaced with 50 nM MitoTracker® CMXRos in complete medium. Cells were then incubated for 1 h at 37 °C, 5% CO_2 before the stain was aspirated. Cells were washed once in DPBS before replacement with complete imaging medium. Cells were imaged within 3 h of the introduction of MitoTracker® CMXRos, to minimise potential deterioration of cell health due to the presence of the dye.

2.10.8 Ethidium bromide staining

To visualise mitochondrial networks by LSCM or HTCM, cells were stained with ethidium bromide (EtBr). Medium was aspirated from the culture and replaced with 5 µg/mL EtBr in complete medium. Cells were incubated for 30 min at 37 °C, 5% CO_2, before the stain was aspirated. Cells were washed once in DPBS before replacement with complete imaging medium. Cells were imaged within 3 h of the introduction of EtBr to minimise potential deterioration of cell health due to the presence of the dye.

2.10.9 SYBR green I staining in BMSC cells

To visualise mitochondrial DNA by HTCM, BMSC cells were stained with SYBR Green I (ThermoFisher). At low concentration, this dye exhibits selectivity towards mitochondrial DNA over genomic DNA [43]. BMSC cells were seeded at 3 x 10^5 cells/well in 6-well tissue culture plates and allowed to incubate overnight. Medium was aspirated from the culture and replaced with a 1:100,000 dilution of SYBR Green I in complete medium and incubated for 5 min at 37 °C, 5% CO_2. Cells were washed once in DPBS before replacement with complete imaging medium. Cells were imaged within 3 h of the introduction of SYBR Green I to minimise potential deterioration of cell health due to the presence of the dye. Image analysis is described in detail in results section **4.3.11** of this thesis.

2.11 Imaging of extracellular vesicles

2.11.1 Transmission electron microscopy

Three 75 cm^2 tissue culture flasks were seeded each with 4 x 10^5 WI-38 cells in 15 mL of medium before incubating at 37 °C, 5% CO_2 for 3 days to secrete extracellular vesicles. Cells and debris were pelleted by centrifugation for 5 min at 700 x g. Supernatant was harvested from the culture and 24 mL aliquoted into each of two ultrafuge bottles before ultrafugation for 25 min at 16,000 x g at 4 °C. Medium was decanted from the bottles, and the sample resuspended in 1 mL of a 4% glutaraldehyde, 3% sucrose in DPBS solution. The samples were incubated overnight at 4 °C before centrifugation for 10 min at 10,000 x g at room temperature. Fixative was removed and the sample resuspended in 2% osmium tetroxide for 1 h at 4 °C. The samples were centrifuged for 10 min at 10,000 x g at room temperature. The osmium tetroxide solution was removed and the samples dehydrated through an acetone series. The samples were then embedded in epoxy resin and sectioned to 60 nM by ultravibratome. Sections were double stained with a 2% uranyl acetate solution for 20 min at room temperature with 3 rinses of CO_2 free ddH_2O after applications of stain. Sections were imaged by TEM using a JEOL2010 transmission electron microscope.

2.12 Endpoint PCR

All Endpoint PCR in this research was carried out using a prime-G thermocycler (Techne).

2.12.1 Endpoint PCR and Sanger sequencing of mtDNA

Genomic DNA was extracted from fewer than 5 x 10^6 cells using the Quick-gDNA™ MiniPrep as directed by the manufacturers' protocol and quantified by spectrophotometric analysis of absorbance at 260 nM using a NanoDrop spectrophotometer as described by the manufacturer. The 260/280 and 260/230 absorbance ratios were used to establish that sample purity was sufficient for endpoint PCR. To prepare mtDNA PCR products for sequencing, endpoint PCR was carried out with KAPA HiFi Hotstart ReadyMix. Reactions were setup as follows: 300 nM each of forward and reverse primer, 12.5 µL KAPA HiFi Polymerase Master Mix and 50 ng template gDNA and DEPC-treated ddH_2O to a final reaction volume of 25 µL. For sequencing from human cell lines, a 1021 bp fragment was amplified from the hypervariable D-Loop region of human mtDNA using the forward primer (5' CACCATTAGCACCCAAAGCT 3') and reverse primer (5' CTGTTAAAAGTGCATACCGCCA 3'). Amplification was achieved with the

thermocycling conditions as follows: Initial denaturation for 3 min at 95 °C, followed by 30 amplification cycles (95 °C for 15 s, 63 °C for 20 s, 72 °C for 30 s) and a final extension for 2 min at 72 °C. For mtDNA sequencing from mouse lines or primary cells, a 2,149 bp fragment was amplified using the forward primer (5' TCAGTACTTCTAGCATCA GGTGT 3') and reverse primer (5' GCTAGGCAGAATAGGAGTGATG 3'). This product was carefully selected to avoid amplification of genomic mitochondrial NuMT pseudogenes. Amplification was achieved with the following thermocycling conditions: Initial denaturation for 3 min at 95 °C, followed by 30 amplification cycles (95 °C for 15 s, 63 °C for 20 s, 72 °C for 30 s) and a final extension for 2 min at 72 °C. PCR products were analysed by gel electrophoresis on a 2% agarose gel run in 1 x TBE buffer at 10 v/cm for one h. PCR products were concentrated using a DNA Clean & Concentrator™ Kit as directed by the manufacturer, before quantification by NanoDrop spectrophotometer. To prepare templates for Sanger sequencing, 25.5 ng (human product) or 53.7 ng (mouse product) was combined with 4 pmol of either forward, or reverse primer in a final volume of 20 µL. For human PCR products, sequencing primers were equivalent to those used for initial amplification. For mouse PCR products, the forward sequencing primer was equivalent to that used for initial amplification, while a nested reverse primer (5' TGGGGATTGGTATGGAGCTT 3') was used for sequencing. Sanger sequencing was carried out using Big Dye® V3.1 chemistry by Massey Genome Services.

2.12.2 Endpoint PCR for confirmation of ρ^0 status

Genomic DNA was extracted from fewer than 5 x 10^6 cells using the Quick-gDNA™ MiniPrep as directed by the manufacturers' protocol and quantified by spectrophotometric analysis of absorbance at 260 nM using a NanoDrop spectrophotometer. The 260/280 and 260/230 absorbance ratios were used to establish sample purity was sufficient for endpoint PCR. Endpoint PCR was carried out with KAPA HiFi Hotstart ReadyMix. Reactions were setup as follows: 300 nM each of forward and reverse primer, 12.5 µL KAPA HiFi Polymerase Master Mix and 50 ng template gDNA and DEPC-treated ddH_2O to a final reaction volume of 25 µL. A 147 bp fragment of mitochondrial DNA was amplified using the forward primer (5' CTCCGTGCTACCTAAACACCTTATC 3') and reverse primer (5' GACCTAAGAAGATTGTGAAGTAGATGATG 3'). A 114 bp fragment of the apolipoprotein B gene was amplified as a nuclear control using the forward primer (5' TCACCAGTCATTTCTGCCTTTG 3') and reverse primer (5' CACGTGGGCT CCAGCATT 3'). Amplification was achieved with the following thermocycling conditions: Initial denaturation for 3 min at 95 °C, followed by 30 amplification cycles (95 °C for 15 s, 60 °C for 20 s, 72 °C for 30 s) and a final extension for 2 min at 72 °C. A no template control was carried out for each primer set alongside the experimental samples.

The PCR products were analysed by gel electrophoresis on a 2% agarose gel run in 1 x TBE buffer at 10 v/cm for 1 h.

2.13 Quantitative PCR

All qPCR and RT-qPCR in this research was carried out using the Quantstudio 7. All analysis of qPCR data was carried out using Quantstudio Real-Time PCR Software Version 1.2. All reactions in qPCR experiments were performed in technical triplicates. Primer efficiency for all primer pairs was evaluated by generation of a standard curve, before use of the primer pairs on experimental samples.

2.13.1 Quantitative PCR for cell free mitochondrial DNA

Three hundred thousand cells were seeded in T75 flasks in 15 mL of complete medium before incubating at 37 °C, 5% CO_2 for 3 days to secrete extracellular vesicles. Medium was collected and briefly centrifuged for 5 min at 700 x g to pellet dead cells and large debris. The top 12.5 mL of supernatant was collected with care taken to leave the remaining volume undisturbed. Three 4 mL aliquots of each sample were placed into an individual 5 mL syringe, and filtered by one of the conditions as follows: unfiltered, 1.2 micron filtered or 0.2 micron filtered. The filtrate was collected, and DNA extracted using the Quick-gDNA™ MiniPrep with a modified protocol. To each filtrate, an equivalent volume (4 mL) of lysis buffer was added before a vigorous 30 s vortex. The samples were then incubated at room temperature for 10 min. The whole 8 mL volume of each sample was then passed through a DNA binding column in sequential 1 mL aliquots, after which the protocol was continued as described by the manufacturer. DNA was eluted from the columns in a final volume of 40 µL TE buffer. Quantitative PCR was carried out using KAPA SYBR® FAST qPCR master mix with the following reaction conditions: 300 nM of each forward and reverse primer, 0.4 µL ROX low, 5 µL KAPA SYBR Fast Universal Master Mix, 2 µL DNA template and DEPC-treated ddH_2O to a final reaction volume of 10 µL. For detection of human extracellular mitochondrial DNA, a 152 bp fragment was amplified using the forward primer (5' CGAAAGGACAAGAGAAATAAGG 3') and reverse primer (5' CTGTAAAGTTTTAAGTTTTATGCG 3'). Amplification was achieved with the following thermocycling conditions: Initial denaturation for 3 min at 95 °C, followed by 40 amplification cycles (95 °C for 15 s, 54 °C for 20 s, 72 °C for 20 s). For detection of mouse mitochondrial DNA, a 147 bp fragment was amplified using the forward primer (5' CTCCGTGCTACCTAAACACCTTATC 3') and reverse primer (5' GACCTAA GAAGATTGTGAAGTAGATGATG 3'). Amplification was achieved with the following thermocycling conditions: Initial denaturation for 6 min at 95 °C, followed by 40 amplification cycles of 95 °C for 5 s, 60 °C for 25 s. A positive genomic DNA control from

the parental cell line, an unfiltered media control and a no template control were included for amplification. A melt curve analysis was carried out for all SYBR Green-based qPCR.

2.13.2 Quantitative reverse-transcription PCR

To examine mitochondrial gene expression, RNA was extracted from fewer than 4 x 10^6 cells using the RNeasy® Mini Kit as directed by the manufacturer. RNA was kept on ice for all downstream manipulations. The RNA was quantified by spectrophotometric analysis of absorbance at 260 nM using a NanoDrop spectrophotometer. The 260/280 and 260/230 absorbance ratios were used to establish sample purity was sufficient for cDNA synthesis. To ensure the samples were free from gDNA contamination, samples were treated with a hyperactive TURBO DNase™ using the TURBO DNA-free™ Kit rigorous DNase treatment as directed by the manufacturer. Briefly, less than 10 µg of total RNA was combined with 5 µL of 10 x TURBO DNase™ buffer and 2 units of TURBO DNase™ enzyme (2 U/µL) and DEPC-treated ddH_2O to a total reaction volume of 50 µL. Samples were then incubated at 37 °C for 30 min before addition of a further 2 units of TURBO DNase™. After a further incubation for 30 min at 37 °C, 5 µL of DNase Inactivation Reagent was added, and a further incubation for 5 min 24 °C was carried out. The reactions were agitated 4 times throughout this incubation to keep the slurry dispersed throughout the reaction. The samples were centrifuged at 10,000 x g for 5 min to pellet the DNase Inactivation Reagent and 40 µL of the RNA-containing supernatant was carefully removed, with care taken to avoid any disturbance of the pelleted DNase Inactivation Reagent. The RNA was again quantified by NanoDrop spectrophotometer. To Synthesise cDNA, 50 ng of total RNA was reacted with 2 µL 5X PrimeScript RT Master Mix and DEPC-treated ddH_2O to a final reaction volume of 10 µL. Reverse transcription was carried out for 15 min at 37 °C followed by a short 5 s incubation at 85 °C to inactivate the enzyme. Newly synthesised cDNA was kept on ice for all downstream manipulations. To prepare templates for qPCR, each 10 µL cDNA reaction was diluted with 190 µL DEPC-ddH_2O. For each mitochondrial gene to be examined by qPCR, 2 µL of cDNA template was added to 5 µL KAPA SYBR Fast Universal Master Mix, 400 nM of each forward and reverse primer, 0.2 µL ROX Low and DEPC-treated ddH_2O to a final reaction volume of 10 µL. A 150 bp fragment from mouse mitochondrial D-Loop cDNA was amplified using the forward primer (5' AGGTTTGGTCCTGGCCTTAT 3') and reverse primer (5' GTGGCTAGGC AAGGTGTCTT 3'). A 136 bp fragment from cytochrome B (CytB) cDNA was amplified using the forward primer (5' ACACGCAAACGGAGCCTCAA 3') and reverse primer (5' TGCTGTGGCTATGACTGCGAACA 3'). A 128bp fragment from mouse cytochrome C oxidase I (Cox1) was amplified using the forward primer (5' CCAGTGCTAGCCG CAGGCAT 3') and reverse primer (5' TCTGGGTGCCCAAAGAATCAGAACA 3'). To amplify mouse 18s as a housekeeping gene control, 2 µL of cDNA template was added to 5 µL KAPA SYBR Fast Universal

Master Mix, 0.5 µL of QuantiTect primer assay (Mm_Rn18s_3_SG) (Qiagen), 0.2 µL ROX Low and DEPC-treated ddH_2O to a final reaction volume of 10 µL.

2.14 Flow Cytometry

2.14.1 Small particle detection

To examine extracellular particles by flow cytometry, 3 x 10^5 cells were seeded in a 75 cm^2 flask in 15 mL of complete medium and incubated for 3 days at 37 °C, 5% CO_2 to condition the medium. The medium was collected and centrifuged briefly for 5 min at 400 x g at room temperature to pellet any cells or large debris. Conditioned medium was filtered through a 1.2 µM syringe filter before 2 mL aliquots were stained with each of MitoTracker® Red CMXRos at 5 µM, MitoTracker® Green FM at 50 nM or the lipophilic tracer 1,1'-Dioctadecyl-3,3,3',3'-tetramethylindodicarbocyanine perchlorate (DiD) at 12.5 µg/mL. Stains were added directly to culture medium and allowed to incubate for 30 min at 37 °C before the samples of conditioned medium were placed on ice. Samples were analysed using a BD Influx™ FACS instrument fitted with an enhanced forward scatter detector (Small Particle Option configuration). To approximate particle size, ApogeeMix (Apogee Flow Systems) and SPHERO™ Ultra Rainbow Fluorescent Particles were used. Gates were applied to cytometer events which corresponded to 0.5 µm, 1.3 µm and 3.2 µm to identify the region of interest in which extracellular vesicles were likely to be detected if present in the sample.

2.14.2 Fluorescence activated cell sorting

To separate cell populations after co-culture or for clonal isolation, FACS was carried out using a BD Influx™ Cell Sorter fitted with a 140 µm nozzle to facilitate accurate sorts for large cell types. Cytometer operation was facilitated by Hugh Green Cytometry Core staff at the Malaghan Institute of Medical Research, Wellington, New Zealand. Cells were harvested, washed once with DPBS and resuspended in FACS Sort buffer at a concentration not exceeding 1 x 10^6 cells/mL. The entire volume of sample was passed through a 35 µm filter cap into a 5 mL Round-Bottom Polystyrene Tube. Cells were stained with 4′,6-diamidino-2-phenylindole (DAPI) at 1 µg/mL directly in FACS Sort buffer and allowed to incubate for 20 min on ice before initiation of the FACS session. Cell populations of interest were identified by forward and side scatter profiles. A live cell inclusion gate was next placed on DAPI negative cells. Sort gates were determined based on signal intensity of fluorescent protein expressed by the target cells. An initial enrichment sort was performed, followed by two subsequent one-drop pure sorts of the co-culture. The final purity of the sorted sample was assessed before downstream experiments.

2.15 Analytical flow cytometry

A shared procedure to prepare cells for cytometry was common to all cytometry experiments in this research. Briefly, cells were harvested as described in section **2.7.3**, and washed twice with DPBS before resuspension in a stain-specific buffer as described in this section. For samples which required multiple reagents for the experiment, reagents were applied simultaneously where protocols were compatible. All analytical flow cytometry was performed using a BD FACSCanto II™ cytometer with a 4-2-2 laser configuration. CS&T performance calibrations of the FACSCanto II™ were carried out prior to each use using BD™ CS&T Beads.

2.15.1 Annexin V staining

Fewer than 1 x 10^6 cells were resuspended in 100 µL 1x Annexin V Binding Buffer. To detect externalised phosphatidyl serine as an early apoptotic marker, cells were stained with 5 µL APC Annexin V for 15 min at room temperature. After addition of APC Annexin V, samples were protected from light where possible for all downstream manipulations. The samples were then diluted in a further 400 µL of Annexin V binding buffer and placed on ice until analysis by flow cytometry.

2.15.2 Zombie live/dead staining

Lyophilised Zombie NIR™ Fixable dye was resuspended in 100 µL of DMSO and briefly vortexed to ensure the reagent was fully dissolved. Aliquots of stock solution were prepared and stored at -20 °C for use within 3 months. A 1:1,200 dilution of Zombie NIR™ Fixable dye was diluted in DPBS (Annexin V Binding Buffer for experiments together with Annexin V). Fewer than 1 x 10^6 cells were resuspended in 100 µL of freshly prepared dye solution and incubated for 15 min at room temperature. After addition of the dye, samples were protected from light where possible for all downstream manipulations. Samples were diluted by addition of 400 µL of DPBS (or Annexin V Binding Buffer when used in combination with Annexin V) and placed on ice until analysis by flow cytometry.

2.15.3 CellTrace™ dyes for cells in suspension

Lyophilised CellTrace™ dyes were resuspended in sterile DMSO to prepare 5 mM stock solutions as described by the manufacturer. To avoid degradation of the reagent, 5 µL aliquots were prepared and stored at -20 °C for use within one month. Cells were resuspended in DPBS at a concentration of 1 x 10^6 cells/mL and the volume required for the experiment was transferred to a sterile 15 mL tube. CellTrace™ dye was dispensed into the cap of the tube with a droplet volume sufficient to produce a 5 µM solution when mixed with a cell suspension. The tubes were sealed with care taken to avoid disturbance of the droplet. The tubes were inverted directly onto a vortex mixer for 20 s to facilitate rapid diffusion of the dye throughout the cell suspension. The cells were incubated for 20 min at 37 °C to allow the amine reactive dyes to bind to cellular proteins and undergo acetate hydrolysis. To remove residual unconjugated dye, the cells were pelleted by brief centrifugation for 4 min at 400 x g and the staining solution aspirated. The cells were then resuspended in pre-warmed complete medium equal to five times the volume of DPBS used during initial staining. The cells were incubated for a further 5 min at 37 °C to quench residual dye, then pelleted by brief centrifugation for 4 min at 400 x g. The medium was aspirated and the cells resuspended in a buffer or medium appropriate for the intended experimental use.

2.15.4 Cell cycle analysis by 7-Aminoactinomycin D

To evaluate cellular DNA content by flow cytometry, samples were stained with 7-Aminoactinomycin D (7-AAD) (ThermoFisher). Briefly, 1 x 10^6 cells were resuspended in 300 µL FACS staining buffer in a 15 mL tube to prepare for fixation. The tube was vortexed moderately while 700 µL of 100% EtOH was added dropwise using a P1000 pipette. The cell suspension, now in 70% EtOH, was incubated for 20 min at room temperature. Cells were pelleted by brief centrifugation for 4 min at 400 x g at room temperature, before the fixative was aspirated. The cells were resuspended in 500 µL of FACS buffer which contained 7-AAD at a concentration of 10 µg/mL and incubated for 60 min at room temperature, protected from light. The cells were centrifuged for 4 min at 400 x g at room temperature and the stain aspirated. Cells were washed twice in 500 µL FACS running buffer and resuspended in 500 µL FACS running buffer before cytometric analysis.

2.16 Immunophenotyping of primary cultures

The immunophenotype of primary cell cultures prepared in section **2.8.4** were characterised by flow cytometry. A 6 colour antibody panel was designed to label key surface antigens which would identify murine brain pericytes.

2.16.1 Antibodies and staining

Primary pericyte cultures were harvested by Accutase™ as described by the manufacturer, and washed twice with DPBS. Fewer than 1 x 10^6 cells were resuspended in 23 µL FACS staining buffer in 5 mL round bottomed polystyrene FACS tubes. For each sample to be stained, 250 µg of Purified Rat Anti-Mouse CD16/CD32 clone 2.4G2 (Mouse BD Fc Block™) was added and the samples incubated for 30 min at 37 °C, 5% CO_2. This antibody recognises epitopes present on FcγIII and FcγII, and possibly FcγI receptors and was used to block potential non-specific interactions between cells and the conserved Fc domain of antibodies. Fluorochrome conjugated primary antibodies were then used to label cell surface epitopes for CD90.2, CD73, AN2, CD146, CD140b and CD105. For each sample to be stained, 150 ng of each of the 6 primary antibodies were prepared as a mixture with a total volume of 26 µL. The antibody mixture was delivered to the cell suspensions, in final staining volume of 50 µL. the samples vortexed gently and incubated for 30 min on ice while protected from light. Cells were washed twice by centrifugation of the FACS tubes for 4 min at 700 x g and resuspended in 100 µL FACS running buffer, before a final resuspension in 500 µL of FACS running buffer. The stained samples were protected from light until analysed by flow cytometry as described in section **2.15**. Single stained controls were prepared and run alongside samples stained with the multicolour panel.

Table 3. Antibodies used for immunophenotyping of primary pericyte cultures

Epitope	Conjugate Fluorochrome	Laser Line	Ex_{max}/Em_{max}	Antibody Clone	Volume for 150 ng antibody (µL)
CD90.2	VioBlue	405	400/452	30-H12	5
CD73	FITC	488	495/520	TY/11.8	1
AN2	PE	488	565/578	1E6.4	5
CD146	PerCP-Vio700	488	482/704	ME-9F1	5
CD140b	APC	633	652/660	APB5	5
CD105	APC-Vio770	633	652/775	REA794	5

2.17 Seahorse extracellular flux

2.17.1 Cell-Tak™ extracellular matrix

In preparation for each Seahorse glycolytic rate assay, an Agilent Seahorse XFe96 Cell Culture Microplate was treated with Cell-Tak™ Cell and Tissue Adhesive. Due to the numerous buffer exchanges and wash procedures required to perform a Glycolytic Rate Assay, cells are prone to detachment from the glass surface of the XFe96 Cell Culture Microplate. The solubility of Cell-Tak™ is highly dependent on pH and is supplied in 5% acetic acid to remain soluble. Adsorption from a neutral solution is required to effectively coat a surface. A filter sterilised 0.1 M pH 8.0 $NaHCO_3$ (neutralisation buffer) buffer was prepared in ddH_2O for use in the process of Cell-Tak™ coating. To coat XFe96 microwell plates, a 22.88 µg/mL Cell-Tak™ coating solution was prepared in neutralisation buffer as described by the manufacturer. For each plate, 40 µL of Cell-Tak™ reagent supplied at 1.43 mg/mL was diluted in 2.44 mL neutralisation buffer and pH adjusted by addition of 20 µL 1M NaOH. The pH of this solution is approximately 8.0 and promotes spontaneous adsorption of Cell-Tak™ proteins onto the first surface contacted. Twenty-five microliters of Cell-Tak™ solution was quickly distributed to each microwell and the plate incubated at 37 °C for 30 min. The coating solution was aspirated and the plate washed twice with ddH_2O to remove residual bicarbonate. The theoretical protein mass adsorbed onto the each microwell surface was approximately 5.4 µg/cm^2. The coated plates were used immediately for cell culture, or placed at 4 °C for short term storage.

2.17.2 Glycolytic Rate Assay

To assess extracellular acidification rate, oxygen consumption and glycolytic rate, the Agilent Seahorse XF Glycolytic Rate Assay was performed using a Seahorse XF96 Extracellular Flux Analyser. Briefly, 3 x 10^5 C57 eGFP-astrocytes, ρ^0-eGFP- astrocytes or mitochondrial recovered-ρ^0-eGFP-astrocytes were seeded in 75 cm^2 tissue culture flasks. C57 eGFP-astrocytes were treated with 400 µg/mL chloramphenicol or 250 ng/mL as described in section 2.7.4. The cells were harvested as described in section **2.7.3** and 8 x 10^4 cells were seeded in complete medium into an Agilent Seahorse XFe96 Cell Culture Microwell Plate pre-coated with Cell-Tak™ as described in section **2.17.1**. The corners of the microplate were reserved for calculation of background as described by the manufacturer. The cells were incubated overnight at 37 °C, 50% CO_2 to allow for complete attachment to the microplate. An Agilent XFe96 Sensor Cartridge was hydrated in Seahorse XF Calibration Solution as described by the manufacturer and placed in a 37 °C non-CO_2 incubator overnight. The Seahorse XFe96 Analyzer was turned on and allowed to equilibrate overnight. Seahorse XF Base medium without phenol red was supplemented

with 2 mM glutamine, 10 mM glucose, 1 mM pyruvate and 5 mM HEPES (assay medium). The pH was carefully adjusted to 7.4 with NaOH and the medium filter sterilised, before it was placed at 37 °C in a non-CO_2 to pre-warm. The XFe96 Microwell Plate with the prepared cells was washed gently as described by the manufacturer, before 180 µL of assay medium was carefully added to each well. The cells were observed under a light microscope to ensure the monolayer had not been disturbed by the wash procedure. The cells were incubated in a non-CO_2 incubator at 37 °C for 1 h to allow metabolic adaptation to the new medium. The metabolic inhibitors rotenone/antimycin A (rot/AA) and 2-deoxyglucose (2-DG) supplied in an Agilent XF Glycolytic Rate Assay Kit were prepared as described by the manufacturer. The pre-hydrated Agilent XFe96 Sensor Cartridge was retrieved from the non-CO_2 incubator and ports A, B and C were sequentially loaded with of 20 µL of 5 µM rot/AA, 22 µL of 500 mM 2-deoxyglucose 2-DG and 25µL of 50 µg/mL Hoechst 33342 respectively. The loaded XFe96 Sensor cartridge was carefully placed into the XFe96 Analyzer and the plate calibration initiated. The cells were removed from the incubator and the medium exchanged with 180 µL of fresh, pre-warmed assay medium. Plate calibration results were examined for errors, and the XFe96 Sensor Cartridge retrieved. The sensor cartridge was then inserted into the XFe96 Microwell plate with care taken to avoid disturbing the loaded compounds, or the cells. The glycolytic rate assay was then initiated and allowed to proceed to completion. The plate was retrieved from the XFe96 Analyzer and the Hoechst 33342 fluorescence measured using a Tecan Infinite M1000 Pro Plate Reader. Data was normalised by Hoechst 33342 fluorescence to account for variation in cell density. All data analysis for Seahorse XFe96 experiments was carried out using Agilent Wave Version 2.6.0.31 and the Agilent™ Seahorse Glycolytic Rate Assay Multi-File XF Report Generator.

2.18 Cellular growth rates

2.18.1 IncuCyte S3™ for live-cell growth assays

To assess cellular growth rates, an IncuCyte® S3 Live-Cell Analysis System was used. Briefly, 5 x 10^5 cells were seeded in 6-well culture plates in complete medium and placed inside the IncuCyte® S3 system inside a 37 °C, 5% CO_2 incubator. Images were collected every 2 h from 32 individual fields per well using the 20 x objective. The inbuilt IncuCyte® S3 image processing tools were used to calculate percent confluence (area occupied by cells) for each field collected. To calculate doubling rates, percent confluence data was plotted against time as an X, Y scatter, and a non-linear regression calculated to model a population doubling rate.

2.19 Molecular methods for assays developed in this research

All methods detailed in the following section pertain to methods or assays developed in chapter 4 of this thesis.

2.19.1 ASB-qPCR for selective amplification of U87-MG from an LN18 gDNA background

Optimised reactions consisted of 200 nm of both forward and reverse primers, 1.2 µM blocker, 200 nm hydrolysis probe, 20 ng gDNA template, 1x HOT FIREPol® Probe Universal Master Mix and DECP treated ddH_2O to a final reaction volume of 10 µL. A positive control (100% U87-MG gDNA) and negative control (0% U87-MG gDNA) were included alongside the spike in conditions.

Table 4. Oligonucleotides for ASB-qPCR of U87-MG mtDNA_195 from an LN-18 background

Oligo Name	mtDNA Position	Sequence
Allele specific forward primer	241-259	5' GTGCAGACATTCAATTGT 3'
Common reverse primer	181-195	5' ACAGGCGAACATACC 3'
3' Phosphorylated blocker	186-208	5' CGAACATACTTACTAAA GTGTG/3Phos/ 3'
Hydrolysis probe (5' 6-Carboxyfluorescein modified (FAM), internal Zen quencher and 3' terminal Black Hole Quencher (BHQ)	204-234	5' /56-FAM/ATGTCCTAC/ZEN/AAGC ATTAATTAATTAACACA/3IABkFQ/ 3'

Table 5. Thermocycling parameters for ASB-qPCR of U87-MG mtDNA_195 from an LN-18 background

Thermocycling step:	Temperature (°C)	Time	Cycle Count
Initial Denaturation	95	12 min	1
Denaturation	95	15 s	
Annealing	53	30 s	40
Extension	60	30 s	

2.19.2 ASB-qPCR for selective amplification of WI-38 mtDNA_16114 from an SH-SY5Y gDNA background

Optimised reactions consisted of 800 nm of both forward and reverse primer, 3.6 µM blocker, 600 nm hydrolysis probe, 20 ng gDNA template, 1x HOT FIREPol® Probe Universal Master Mix and DECP treated ddH_2O to a final reaction volume of 10 µL. A positive control (100% WI-38 gDNA) and negative control (0% WI-38 gDNA) were included alongside the spike in conditions.

Table 6. Oligonucleotides for ASB-qPCR of WI-38 mtDNA_16114 from an SH-SY5Y background

Oligo Name	mtDNA Position	Sequence
Forward primer	16278-16261	5' GTATCCTAATGGGTGAGG 3'
Allele specific reverse primer	16100-16114	5' ATTACTGCCAGCCAA 3'
3' Phosphorylated blocker	16107-16122	5' CCAGCCACCATGAATA/3Phos/ 3'
Hydrolysis probe (5' FAM, internal Zen quencher and 3' BHQ	16178-16204	5' /56FAM/TCAAAACCC/ZEN/CCTCCT CATG CTTACAAG 3'

Table 7. Thermocycling parameters for ASB-qPCR of WI-38 mtDNA_16114 from an SH-SY5Y background

Thermocycling step:	Temperature (°C)	Time	Cycle Count
Initial Denaturation	95	12 min	1
Denaturation	95	16 s	40
Annealing/Extension	60	60 s	

2.19.3 *In situ* target-primed RCA by gap-fill ligation of mtDNA_9348 and 9461.

Table 8. Oligonucleotides for RCA by gap-fill ligation of mouse mtDNA_9348 and 9461

Oligo Name	mtDNA Position	Sequence
mtDNA_9348 gap-PDP	5' 9344-9323 3' 9351-9368	5'-/5Phos/GTCTACAAAATGTCAGTATCAT GTTCCTCTATGATTACTGACCTAAGTAGCCGT GACTATCGACTTCTTCGACGTATAGGAAAAG TCA 3'
mtDNA_9348 C57B/6J selective hexamer	5' 9350-9345	5'-/5Phos/GACTAC 3'
mtDNA_9348 BALB/CJ blocker	5' 9350-9345	5' GATTAC 3'
Alexafluor 405 (AF405) RCA detection probe	-	5'-/5Alex405N/AGTAGCCGTGACTATCGACT 3'
mtDNA_9461 gap-PDP	5' 9457-9436 3' 9464-9481	5'-/5Phos/ACTCTCTTCTGGGTTTATTCAG GTTCCTCTATGATTACTGACCTACCTCAATGC TGCTGCTGTACTACTCTTAAGATAACAGTGTA CAGG 3'
mtDNA_9461 BALB/CJ selective hexamer	5' 9463-9458	5'-/5Phos/TTGATT 3'
mtDNA_9461 C57B/6J blocker	5' 9463-9458	TTAATT 3'
Atto 647 (ATTO647) RCA detection probe	-	5'-/5ATTO647NN/CCTCAATGCTGCTGCTG TACTAC 3'

2.19.4 Finalised reaction method for target primed RCA by gap-fill ligation of mouse mtDNA_9348 and 9461

To establish *in situ* RCA by gap fill ligation, monocultures of either C57-eGFP-astrocytes (C57B/6J mtDNA genotype) or BMSC (BALB/CJ mtDNA genotype) cells were used. As depicted in **Figure 2.19.1A**, cells were seeded directly into 10 cm tissue culture plates which contained two sterilised Superfrost microscope slides. The cells were seeded at the density required to reach approximately 70% coverage by surface area, after an overnight incubation at 37 °C, 5% CO_2. The slides were retrieved from the culture vessel, rinsed with PBS and fixed in 70% EtOH for 15 min at room temperature. To assist in enzymatic access to the mtDNA, one sample at a time was digested in pre-warmed 1 µg/mL pepsin (2500 U/mg) in 0.1M HCL for 45 s at 37 °C, submerged in PBS for 30 s to dilute residual pepsin, then placed under fresh PBS while other samples were processed. The samples were dehydrated through a 70, 85, 100% EtOH series for 3 min at each exchange. Each slide was retrieved from the ethanol and allowed to dry with gentle airflow to assist evaporation.

Up to 8 Secure-seal™ 9 mm diameter hybridisation chambers (**Figure 2.19.1B**) were carefully fitted to dry slides. These chambers formed the reaction wells for all enzymatic/oligonucleotide reactions. Through the 1 mm reagent access ports in the Secure-Seal™ chambers depicted in (**Figure 2.19.1C**), samples were rehydrated through a 100, 85, 70% EtOH series for 3 min at each step before a final replacement with PBS.

To prepare mtDNA fragments *in situ*, restriction digest and exonucleolysis were performed in a single reaction which contained 0.5 u/µL of DraI restriction enzyme, 0.4 u/µl T7 exonuclease and 1 x NEB Cutsmart buffer with ddH_2O to a final volume of 50 µL per reaction well, and incubated for 30 min at 37 °C. After digestion, each chamber was rinsed gently with RCA wash buffer (0.1 M Tris-HCL pH 7.5, 0.15 M NaCl and 0.05% Tween-20).

PDP hybridisation and ligation reactions were prepared as a master reaction mixture which consisted of 0.1 µM of each PDP, 2 µM of each 5' phosphorylated gap-fill hexamer and 2 µM of each blocker hexamer for the desired reaction targets, 0.1 U/µL T4 DNA Ligase (ThermoFisher) in 1 x T4 DNA Ligation buffer (ThermoFisher). The reactions were supplemented with an additional 0.2 µg/µL BSA, 200 nM ATP and 200 mM NaCl in a final volume of 50 µL per reaction. After a 30 min incubation at 37 °C, each chamber was rinsed with RCA wash buffer. Fresh RCA wash buffer was supplied to each chamber and the samples were incubated for a further 5 min at 37 °C. Each chamber was rinsed 3 times with RCA wash buffer to remove unligated PDPs and hexamers.

To perform RCA from circularised PDPs, a master reaction mixture was prepared and consisted of 1 U/µL φ29 polymerase (Lucigen) 0.25 mM dNTPs, 0.2 µg/mL BSA, 5% glycerol and 1 x Phi29 reaction buffer (Lucigen) up to a final volume of 50 µL per reaction with ddH_2O. After the reagents were delivered to the reaction chambers, the reagent access ports were sealed with SecureSeal™ adhesive seal tabs to prevent evaporation. Samples were placed at 37 °C for 3 h for amplification of RCPs, after which each chamber was rinsed briefly with RCA wash buffer.

A fluorescent probe hybridisation mix of 200 nM of each PDP-paired fluorescent detection oligo was prepared in a 20% formamide, 2 x SSC solution and delivered to each reaction chamber. After 30 min hybridisation at 37 °C, the samples were washed briefly three times in RCA wash buffer and dehydrated through a 70%, 85% and 100% EtOH series for 3 min at each exchange. The samples were fitted with number 1.5 coverslips in VectaShield™ antifade mounting medium (with or without DAPI) and sealed with clear nail polish.

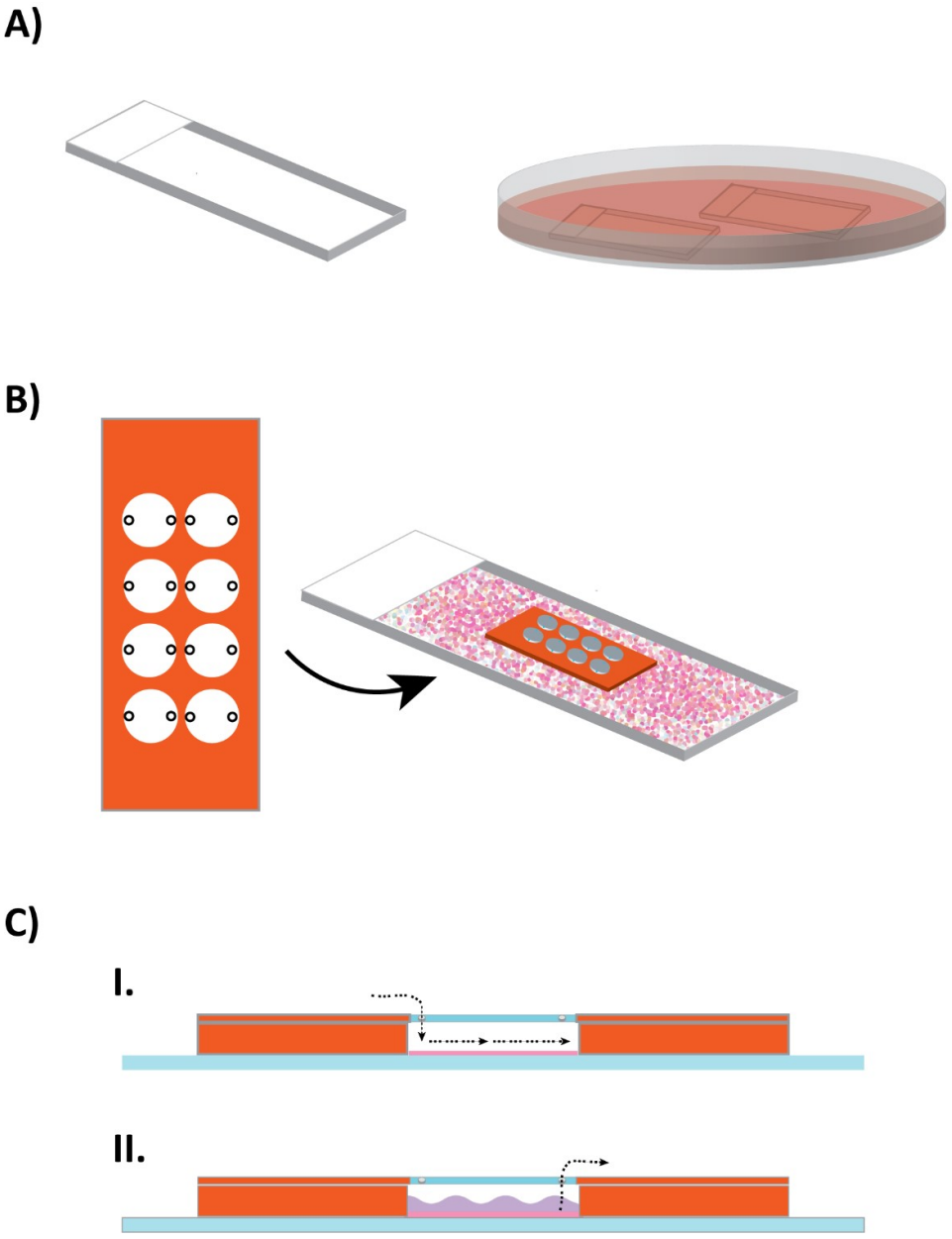

Figure 2.19.1. Schematic of culture method and reaction setup for *in situ* RCA
(A) Cells of interest are seeded into 10 cm dishes with sterilised glass slides and placed into culture. **(B)** The slides are removed, fixed and permeabilised before a SecureSeal™ hybridisation chamber is fitted to the slide. **(C, I.)** The chamber design allows addition of reagents through one of two 1 mm ports**. (C, II.)** Reagents are exchanged and the required wash steps performed throughout a multistage RCA protocol via these ports**.**

2.19.5 Finalised reaction method for target primed RCA with high fidelity ligases of mouse mtDNA_9348 and 9461

The RCA protocols used in combination with single ligation PDPs and high fidelity ligases were comparable those described in section **2.19.4**. The restriction digest and PDP hybridisation/ligation were modified as follows:

Restriction digest and exonucleolysis were carried out as two independent reactions due to the much higher digest temperature of BsaBI. Samples were treated with 0.5 U/µL BsaBI in 1 x NEB CutSmart™ buffer for 30 min at 64 °C. The reaction mix was aspirated and 0.4 u/µL T7 exonuclease in NEB 1 x CutSmart buffer and incubated for 30 min at 37 °C.

For PDP hybridisation and ligation with Taq HIFI Ligase™, 0.1 µM of each PDP, 1 µL of NEB Taq HiFi Ligase™ and 1 X Taq HIFI Ligation buffer were combined with ddH_2O in a final reaction volume of 50 µl per reaction. After addition of the reaction mixture to the chambers, samples were incubated for 30 min at 58 °C.

For PDP hybridisation and ligation with Ampligase™, 0.1 µM of each PDP, 0.5 U/µL Ampligase™ were combined with 1 x Ampligase™ reaction buffer supplemented with 0.2 µg/mL BSA and 125 mM KCL in a final reaction volume of 50 µL per reaction. After addition of the reaction mixture to the chambers, samples were incubated for 30 min at 45 °C.

Table 9. Oligonucleotides for target primed RCA of mouse mtDNA_9438 and 9461 in secondary reaction design

Oligo Name	mtDNA Position	Sequence
mtDNA_9348	5' 9347-9323 3' 9368-9348	5'-/5Phos/TACGTCTACAAAATGTCAGTA TCGTTCCTCTATGATTACTGACCTAAGTA GCCGTGACTATCGACTTCTTGACGTATAG GAAAAGTCAGAC 3'
Alexafluor 405 RCA detection probe	-	5'-/5Alex405N/AGTAGCCGTGACTA TCGACT 3'
mtDNA_9461	5' 9462-9483 3' 9439-9461	5'-/5Phos/ACCCTGTACACTGTTATCTT CAGTTCCTCTATGATTACTGACCTACCTC AATGCTGCTGCTGTACTACTCTTCAATAA ACCCAGAAGAGAGTAATC 3'
ATTO647 RCA detection probe	-	5'-/5ATTO647NN/CCTCAATGCTGCTGCT GTACTAC 3'
RCA compaction linker	-	5'-/TTCCTCTATGATTACTGACCTAAATT CCTCTATGATTACTGACCTmAmAmA 3'

Note: the compaction linker contains 3 sequential 2′-O-methyl-adenine (denoted by mA) residues at the 3' terminus to protect the oligo from φ29 polymerase 3' to 5' exonuclease activity.

2.20 Statistical Tests

All statistical tests performed in this research was carried out using GraphPad Prism™ version 5. Where averaged results are reported from individual measurements within a singular experimental repeat, results are reported as the mean ± standard deviation. Where the average of results are the mean of means generated from individual experimental repeats, results are reported as the mean ± standard error of means.

3 Early IMT models and assessment of present tools

3.1 Introduction

Literature published thus far in the field of IMT research relies heavily on qualitative, microscopic observations of the phenomenon. In the relevant literature, just two major methodologies enable researchers to fluorescently label mitochondria in live cells, to visualise IMT. The first of these consists of fluorescent labelling of mitochondria with MitoTracker® or similar dyes. Modified carbocyanine structures make up the FM class of MitoTracker® dyes. These molecules accumulate with a selective affinity for the mitochondrial membrane, but will label other lipid rich structures when used in excess. A second class of cationic dyes based on rosamine scaffolds, such as MitoTracker® Red CMXRos or MitoView™ Blue, exploit the electrochemical gradient present in live cells. These dyes accumulate in the negative mitochondrial matrix in response to the charge differential across both mitochondrial, and cell membranes. Both classes of dye represent a simple, cost effective solution for accurate labelling of mitochondria in live-cells.

When used appropriately at low nanomolar concentrations, the presence of either class of dye is tolerated by cells. This enables researchers to perform short and medium-term live cell IMT co-culture experiments under time-lapse microscopy. Dyes are available with a broad range of spectral properties, allowing assessment of mitochondrial morphology or membrane potential to be multiplexed with fluorophores reserved for additional experimental parameters. Due to the simplicity of their use, minimal training allows a researcher with any experimental background to produce beautiful images of mitochondrial networks in live cells. These properties make dyes an attractive candidate for use in co-culture models of IMT and explains much of their prevalence in the literature.

Unfortunately, mitochondrial labelling dyes are not without limitation. The dyes are well-known to impact cell function through photo-toxicity [256-258]. When a cell is under stress, the mitochondrial network fractures into a punctate arrangement through mitochondrial fission [17]. Images of fragmented mitochondrial networks like this are commonplace in the literature, likely due to overproduction of oxygen radicals such as hydroxyl radicals ($HO^{\bullet-}$), superoxide radicals ($O2^{\bullet-}$), or hydrogen peroxide (H_2O_2) after photo-stimulation. Oxygen radicals generated during imaging can exceed the cells capacity for antioxidant defence [259]. Damage to cellular proteins as a consequence of oxidation by free radicals places cells under stress, indicated by fission of the mitochondrial network [17]. Care must be taken to minimise both the intensity and duration of excitation under the microscope while live cell experiments are carried out.

Importantly, and of certain concern, is a lack of scrutiny directed towards the retention properties of these molecules in labelled mitochondria. For the vast majority of monoculture experiments, leakage of dyes from the target organelle is often not of particular concern. In IMT experiments however, dye retention is of critical importance to the experimental design. In an IMT co-culture model, only one of the two (or more) cell populations has labelled mitochondria. By design, the experiment requires that fluorescent signals which appear in the originally unlabelled population have occurred through transfer of labelled organelles. Disappointingly, dye retention and the possibility of direct leakage into the unlabelled cells is an aspect rarely discussed in the literature surrounding IMT.

Alongside mitochondrial dyes, the second major strategy relied on for models of IMT is the labelling of mitochondria through fluorescent proteins (FPs). Fusion of an FP to a mitochondrial protein, or more simply, a signal peptide for mitochondrial localisation, allows researchers to target FPs to the mitochondrion. Constructs expressing mito-FP are introduced by transfection of a plasmid, or through viral vectors. Both methods have been widely employed in IMT literature. Genomic integration of constructs produces cell lines which stably express the construct of interest, however transient expression models are equally prevalent in the literature.

Producing models of IMT with FPs is more involved than simple dye based labelling, however FPs provide advantages in co-culture models. Firstly, FPs are produced constitutively while a cell remains functional, enabling researchers to create longer-term models of IMT. Secondly, under a suitable promotor, expression of a fluorescent fusion protein is considered only a minor detriment to mitochondrial function and overall cell health [260]. Finally, FPs are retained by the cell in which they are expressed, unless the labelled protein is actively exported. In the context of IMT, this means any FP appearing within an un-labelled cell can more readily be accepted as exogenous material which originates from a transgenic cell.

There are disadvantages to the use of mito-FPs. Under active excitation, FPs are susceptible to phototoxic effects similarly to mitochondrial labelling dyes. Photo-oxidation of an FP chromophore and subsequent bleaching occurs much more rapidly than that of typical mitochondrial labelling dye. Alongside the respective cellular damage, this effect limits the total imaging time possible when using FPs to label mitochondria [259]. This is particularly relevant in the context of IMT experiments where FPs are intended to track labelled organelles. Once a labelled mitochondrion is outside its cell of origin, FPs are no longer replaced. This limits the time a researcher has to capture images of transferred organelles, as well as the intensity of imaging which can be carried out.

Many FPs were utilised in the initial stages of this research. To label mitochondria, the mammalian expression vectors mito-BFP and mKO2-Mito-7 were acquired from the Addgene plasmid repository. The mito-BFP construct is designed to produce a BFP fusion protein in frame with the mitochondrial targeting sequence of *Saccharomyces cerevisiae* cytochrome oxidase subunit 4 (COX4) [261]. mKO2-Mito-7 was selected as a second construct to label mitochondria with the extremely bright, photostable monomeric FP Kusabira-orange 2 (mKO2). This construct encodes mKO2 in frame with the MTS of human cytochrome C oxidase subunit 8A (COX8A).

A number of cell lines were utilised in exploratory co-culture models in the initial phases of this project. As the overarching aim of this research was to investigate how injury may alter the rate of IMT in the brain, cell lines of neural origin were selected as potential IMT 'recipient' cells. Human GBM cell lines LN18 and U87-MG were selected for their relevance to human disease, as I was interested in whether or not IMT would occur into cells with this disease state. Human neuroblastoma cell line SH-SY5Y was selected as a second cell line with disease characteristics, and for the ability to differentiate these cells into both neurons and astrocytes in future IMT models. In contrast, the human astroglial cell line SVGp12 was considered for IMT models as a cell line more characteristic of healthy astrocytes, which would be valuable to compare with IMT in diseased cells. The human lung fibroblast WI-38 was selected as a potential IMT 'donor', as fibroblasts had been demonstrated prior to act as IMT donor cells [175] and it was possible that other fibroblasts could act in a similar manner.

Three additional cell lines of murine origin were also selected for investigation as murine models would provide flexibility in future IMT co-culture experiments. Two astrocyte cell lines, C8D1A and eGFP-astrocytes were selected as models of healthy brain astrocytes to act as potential IMT 'recipient' cells. A immortalised cell line derived from mesenchymal bone marrow, BMSC cells, were selected as a potential IMT donor cell type, as it was thought that this cell line may behave similarly in IMT as other MSCs described as 'donor' cell types in the literature [175, 176, 186, 188, 195, 196, 199-203, 205, 207, 208, 212, 213].

3.2 Aims

The aim of this chapter was to establish initial co-culture models, and to assess existing methodologies used in intercellular mitochondrial transfer research, to evaluate their suitability for use in quantitative studies. Extracellular particles observed in these models were further explored to gain insight into why existing methodologies were not sufficient for quantitative studies in the field of IMT.

3.3 Results

3.3.1 Mitotracker® Red CMXRos leaks extensively from stained cells

Human SH-SY5Y neuroblastoma cells were selected as an initial candidate for investigations of IMT in neural cells. The prevalence of TNTs described in the IMT literature suggested that SH-SY5Y was an excellent candidate cell line - these cells have a propensity to develop a highly networked cellular projections which include thin TNT-like structures. These structures could potentially facilitate intercellular organelle transfer. MitoTracker Red™ CMXRos was selected to label the mitochondria of one cell population, before they were placed into co-culture with an unstained population.

Prior to use in co-culture experiments, the dye retention properties of MitoTracker Red™ CMXRos were assessed. Qualitative experiments were performed to evaluate the presence of free dye in the medium of cells stained with MitoTracker Red™ CMXRos after an extensive washout procedure. This experiment was designed to evaluate whether or not MitoTracker Red™ CMXRos would leak from stained cells into unstained cells, independent of IMT, to determine whether or not dyes such as these would be appropriate in this research.

In **Figure 3.3.1A**, Directly stained cells SH-SY5Y demonstrated bright, uniform signal when imaged by fluorescence microscope, albeit at a magnification where distinct mitochondrial networks were not resolved. The camera exposure time was locked, and unstained cells were imaged as depicted in **Figure 3.3.1B**, to evaluate the level of background signal in the culture. Under these conditions, autofluorescence was determined to be negligible. In order to wash out any leaking dye, an extensive washout procedure was carried out, and the conditioned medium collected. To ensure no transfer of detached cells or cellular components, the medium was passed through a 0.22 μM syringe filter. The contents of this medium represented the extracellular environment created by SH-SY5Y cells, 20 hours after co-culture. **Figure 3.3.1C** represents the fluorescent signal captured from unstained cells cultured in the harvested conditioned medium. Individual cells clearly stained with MitoTracker® CMXRos are visible, distributed throughout the culture. It was clear that even with the extensive wash procedure carried out, free dye present in the medium was sufficient to stain multiple cells. Upon closer examination by confocal microscopy as depicted in **Figure 3.3.1D**, it was clear that MitoTracker Red™ CMXRos was present throughout the culture at a low level. Punctate red signals were found associated with many of the nuclei. These signals were of lesser intensity and were not directly visible by fluorescent microscope, where only the most highly stained cells were detected. Together, these results indicated that MitoTracker Red™ CMXRos was

likely able to diffuse out from labelled organelles over an extended period, even when great care was taken to remove unbound dye at the time of staining. Free dye was present in the conditioned medium at a concentration sufficient to directly stain unlabelled cells. This suggests that stained cells in a co-culture scenario would be equally capable of passively labelling the unstained population. MitoTracker Red™ CMXRos would be an inappropriate tool for use in quantitative co-culture experiments, as dye diffusion and transfer would be inseparable from genuine organelle transfer into an unlabeled population. For this reason, MitoTracker™ or similar dyes found no further application to IMT models in this thesis.

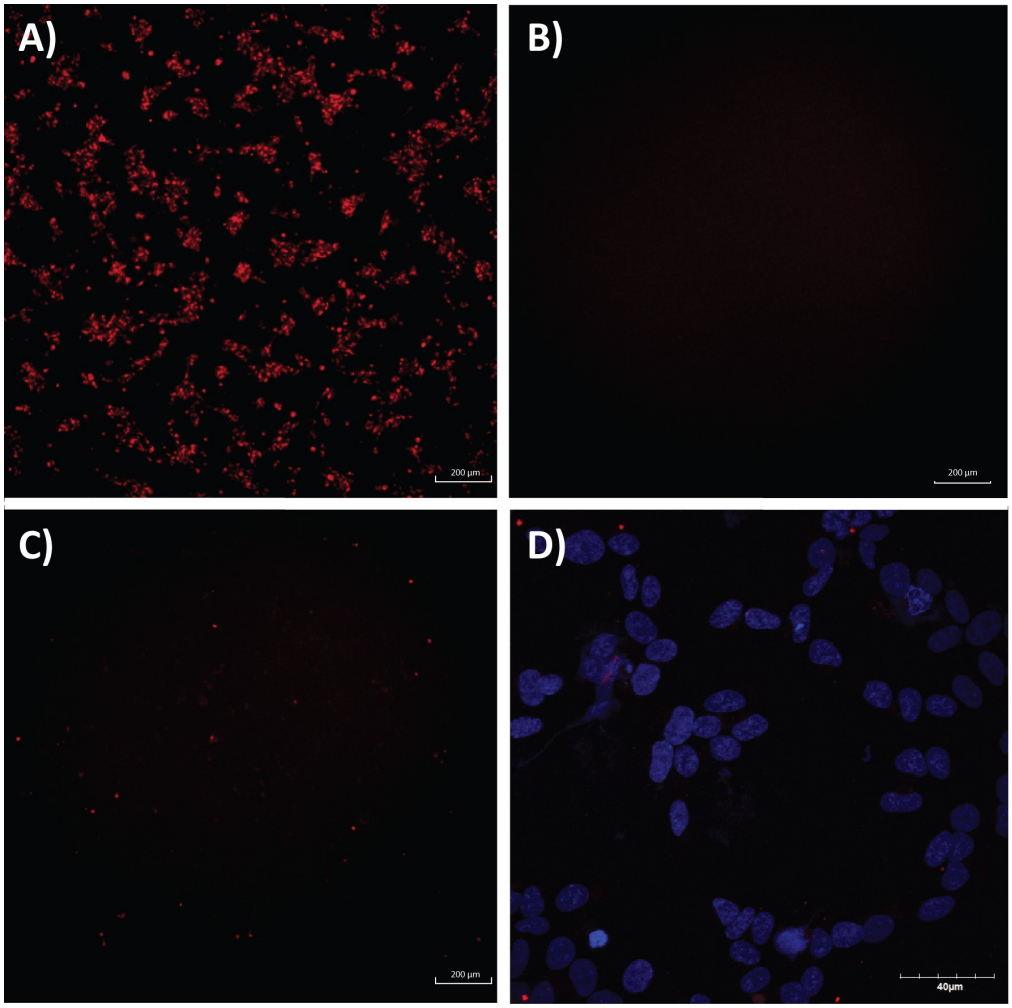

Figure 3.3.1. SH-SY5Y stained with MitoTracker® Red CMXRos or conditioned medium after extensive dye wash out

SH-SY5Y cells were stained with 50 nM MitoTracker® Red CMXRos for 1 h before dye washout. Cells were rinsed twice with DPBS followed by a 1 h incubation in complete medium. This wash procedure was repeated two further times, and the cells incubated for 20 h at 37°C, 5% CO_2 in complete medium. Conditioned media was then harvested and filtered through a 0.22 µM syringe filter. The conditioned medium was placed onto stain naive cells to examine dye carryover by fluorescent microscopy. **(A)** Direct staining of SH-SY5Y by 50 nM Mitotracker CMXRos at 24 h. **(B)** Unstained cells. **(C)** Conditioned medium of stained cells. **(D)** Conditioned medium stained SH-SY5Y visualised under LSCM. Blue = Hoechst 33342, red = MitoTracker® Red CMXRos.

3.3.2 Cells expressing mitochondrial targeted fluorescent proteins generate extracellular particles which contained the expressed transgenic protein

In an effort to avoid future experiments which involved the possibility of leaky mitochondrial labelling dyes, a FP strategy was adopted. It was hypothesised that by embedding the fluorophore as a structural component of the mitochondria, the system would show reduced false positive signals identified as 'transferred' mitochondria. Human glioblastoma (GBM) cell lines LN18 and U87 were selected alongside SH-SY5Y as candidate IMT donor/recipient neural cell lines, as any IMT interactions between these cell types could make a valuable model to study IMT in response to injury. In preparation for these co-cultures SH-SY5Y, LN18 and U87-MG were transfected with mitochondrial-targeted FPs. Stable clones were isolated using glass cylinders to produce lines with bright, stable expression of the chosen construct. The SH-SY5Y were transfected with one of each of mKO2-Mito-7, mito-BFP, cytosolic mCherry or cytosolic GFP to produce four lines suitable for co-culture experiments. U87-MG cells were transfected with either mito-BFP or GFP and stable clones were isolated. LN18 cells were transfected with mito-BFP or GFP and clones isolated to produce a further two lines.

As depicted in **Figure 3.3.2,** Initial experiments with FP models involved a one colour co-culture between mito-BFP-U87-MG and unlabelled LN18. Each line was prepared as described in **Figure 3.3.2A** and 24 h co-cultures carried out, to examine whether or not fluorescent-protein containing mitochondria could be detected after having transferred between cells. **Figure 3.3.2B** describes a representative field from these co-cultures. Though seeded in equal numbers, U87-MG appeared at much higher density after 24 h, and demonstrate brightly labelled mitochondrial networks. Sustained efforts were made to identify LN18 cells which contained FP from U87-MG. Panels **BI.** and **BII.** depict an isolated fluorescent signal in association with an unlabelled cell, an occurrence seen regularly in these cultures. These objects were only detected in the mito-BFP optical channel, and the signal of these objects decreased rapidly upon imaging, consistent with photobleaching. It was not possible to resolve these objects with sufficient fidelity to determine whether they were intracellular, or vesicle-like objects associated with the cell surface. As the model involved only a singular colour, it was not possible to identify LN18 cells with absolute certainty. Extensive IMT from U87-MG could not be identified in LN18 cells. For this reason, use of just a singular FP species was not sufficient for further co-culture experiments.

Figure 3.3.2. Extracellular mitochondrial proteins detected in mito-BFP-U87-MG and LN18 co-culture

Human glioblastoma U87-MG were transfected with Mito-BFP and cultured in selective medium. **(A)** A population of cells with stable expression of mito-BFP was cloned from the parental culture to generate the Mito-BFP-U87MG line, visualised by fluorescent microscopy. This newly created line was then co-cultured with LN18 glioblastoma cells. **(B)** After 24 h in a co-culture, fluorescent particles generated by mito-BFP-U87-MG cells were detected in association with LN18 cells as indicated by white arrows. Depicted is a single image field representative of a fluorescent particle associated with an unlabelled LN18 cell. The white square region within **BI.** and **BII.** Is magnified in the corresponding lower panels. A pseudocolour lookup table (LUT) has been applied to BFP to reflect the intensity of fluorescence with red, orange or white (low, medium or high intensity respectively).

A)

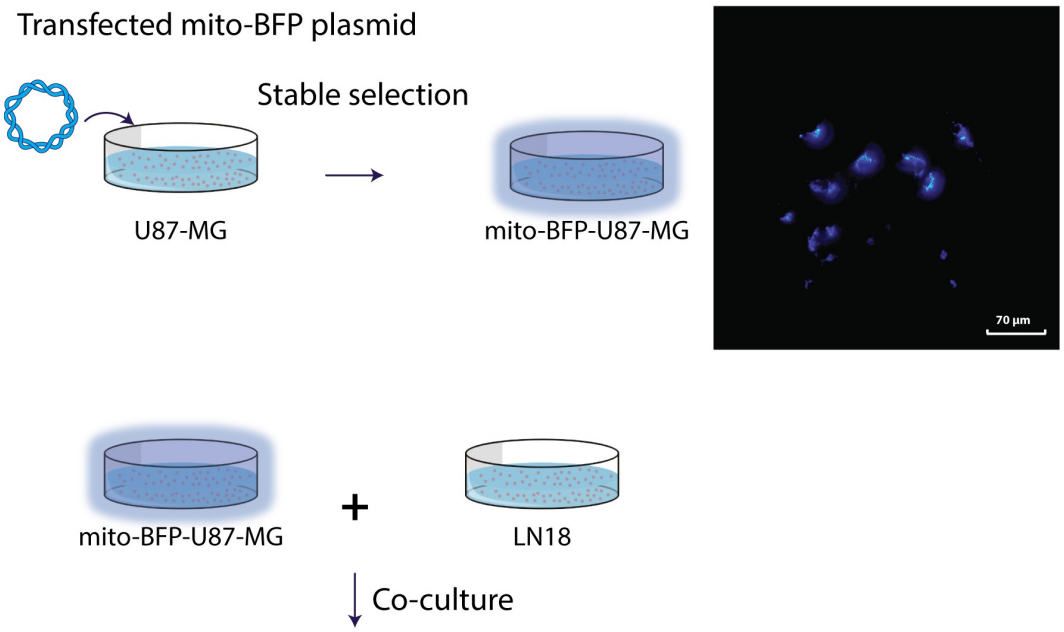
Transfected mito-BFP plasmid
Stable selection
U87-MG
mito-BFP-U87-MG
70 µm
mito-BFP-U87-MG
+
LN18
Co-culture

B)

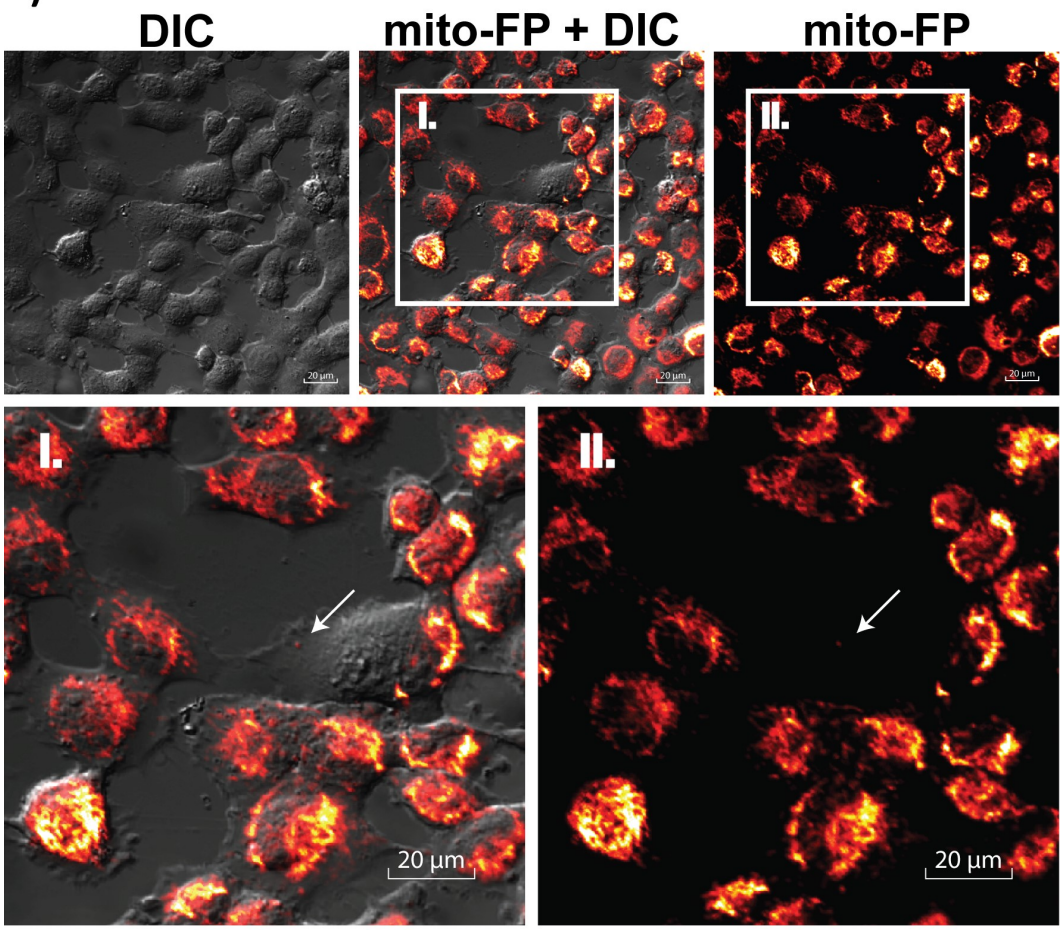
DIC
mito-FP + DIC
mito-FP
I.
II.
20 µm
20 µm

To improve these models of IMT, co-culture experiments with increased fluorescent complexity were carried out. Transgenic lines with clearly identifiable 'donor' and 'recipient' cells were established by inclusion of cytosolic FPs in the recipient population. **Figure 3.3.3A** describes the generation of three transgenic clones of SH-SY5Y, which were placed in co-culture in various combinations. By labelling the cytosol of one SH-SY5Y population with GFP, exogenous mitochondria would be more clearly identifiable. The cultures described in **Figure 3.3.3B** were established and IMT examined in more detail.

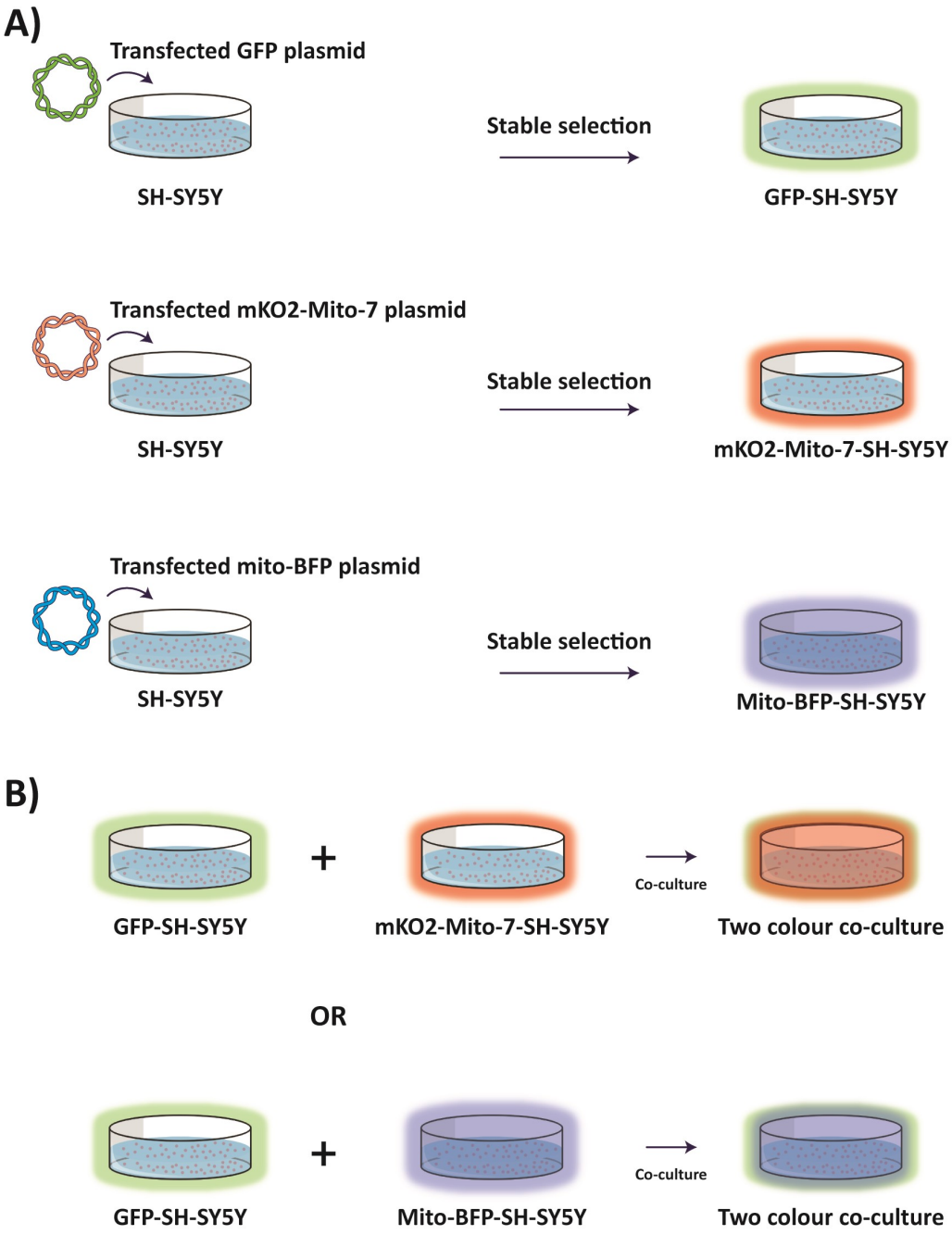

Figure 3.3.3. Establishment of two colour fluorescent protein models of mitochondrial transfer in SH-SY5Y

The human neuroblastoma cell line SH-SY5Y was transfected with one of GFP, Mito-BFP or mKO2-Mito-7 and cultured in selective medium. A population of cells with stable expression of each fluorescent protein was cloned from the parental culture to generate GFP-SH-SY5Y, Mito-BFP-SH-SY5Y and mKO2-Mito-7-SH-SY5Y lines as depicted in **(A)**. GFP-SH-SY5Y were cultured with either Mito-BFP-SH-SY5Y or mKO2-Mito-7-SH-SY5Y **(B)**. This allowed mito-FPs to be detected in association with GFP cells as a model of intercellular mitochondrial transfer.

Figure 3.3.4A represents a typical field of a GFP, mito-BFP SHSY5Y co-culture imaged by confocal microscopy. After 24 h in a 2D co-culture, extensive transfer of mito-BFP, or mKO2-Mito-7 into GFP-labelled 'recipient' SH-SY5Y cells was not readily observed. These style of co-culture were carried out 3 independent times, with many thousands of cells examined each time for any sign of organelle transfer between cells. Depicted in **Figure 3.3.4AI.**, SH-SY5Y did not appear to transfer mito-FPs labelled mitochondria between cells, but once more, small fluorescent objects present only in the mito-FP optical channels were visible throughout the cultures. Determining the precise spatial location of these objects was again difficult due to photo-bleaching effects, however the particles appeared more often to be associated with the outside of cells.

IMT between SH-SY5Y might be enhanced if interaction between each transgenic line was increased during co-culture. SH-SY5Y cells readily grow in 3D when cultured on an uncharged surface. 3D co-cultures were established and examined for evidence of IMT using the multicolour FP lines. As depicted in **Figure 3.3.4B**, after 72 h culture in 3D, SH-SY5Y co-cultures were disaggregated and cultured for a further 24 h as a monolayer. Three independent replicate co-cultures were examined and again, no evidence for extensive acquisition of FP labelled mitochondria by GFP SH-SY5Y cells was apparent.

Depicted in **Figure 3.3.4BII** and similar in appearance to the 2D culture condition, fluorescent objects in the FP optical channel were readily observed associated with the 3D cultured cells.

In an effort to understand the nature of these particles, images collected from each replicate of both 2D and 3D culture conditions and the fluorescent particles manually quantified. To compare each experiment and described in **Figure 3.3.5**, the number of 'recipient' GFP labelled cells in each image field (n = 11-15 fields per set) were counted alongside the observed particles and described as a ratio of particles per 'recipient' cell ±SEM. No significant difference was found in the number of particles detected between replicates, or between 2D and 3D culture conditions as tested by non-parametric one-way ANOVA ($p \geq 0.05$).

Figure 3.3.4. SH-SY5Y co-cultures generate extracellular particles which contain mitochondrial targeted fluorescent proteins.
Human Mito-BFP-SH-SY5Y cells or mKO2-Mito-7 transfected SH-SY5Y were co-cultured with GFP-SH-SY5Y cells. **(A)** After 24 h in a 2D co-culture, or 24 h after disaggregation of a 72 h, 3D culture **(B)**, fluorescent particles were observed associated with cells which also expressed GFP. Magnified image regions from each of **(A)** and **(B)** are represented in the lower panels **(A.I)** and **(B.II)**. A pseudocolor lookup table (LUT) has been applied to mKO2 or BFP to reflect the intensity of fluorescence with red, orange or white (low, medium or high intensity respectively). Blue = DAPI, Green = GFP.

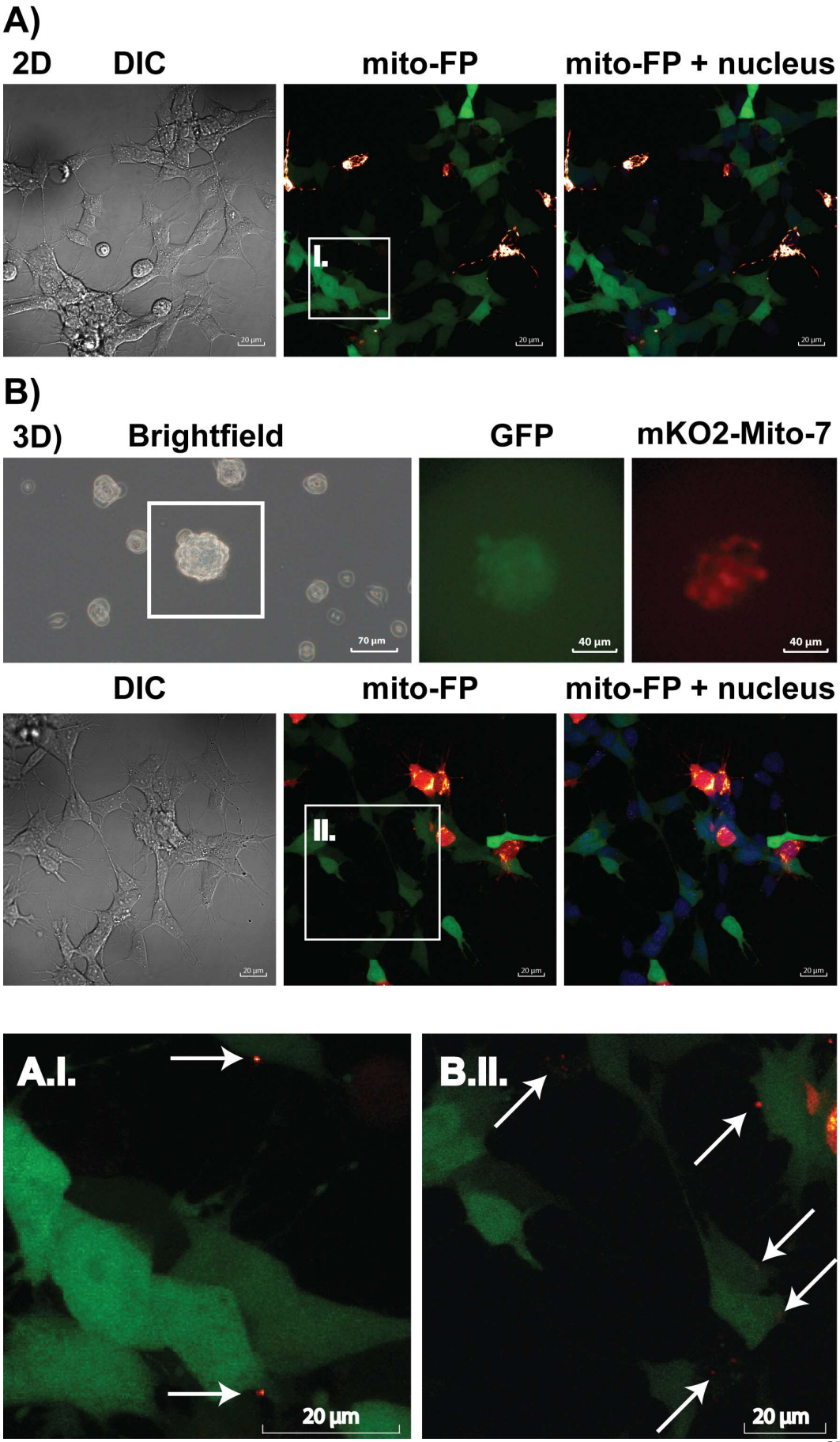
A)
2D
DIC
mito-FP
mito-FP + nucleus
I.
20 µm
B)
3D)
Brightfield
GFP
mKO2-Mito-7
70 µm
40 µm
DIC
mito-FP
mito-FP + nucleus
II.
A.I.
B.II.
20 µm

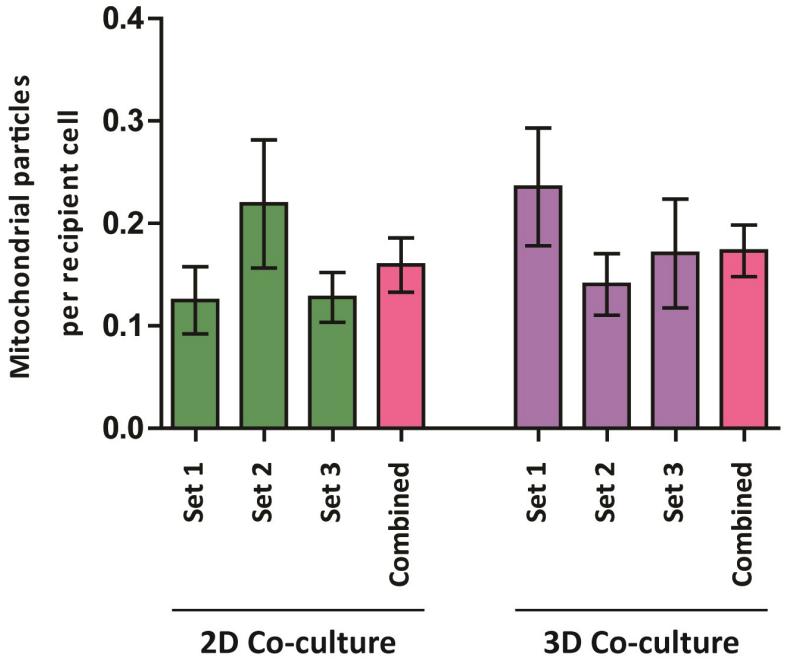

Figure 3.3.5. Quantification of mitochondrial particles detected in SH-SY5Y co-cultures

Particles detected in each image field were manually quantified and are presented as the average number of particles per cell ±SEM. The combined dataset columns represent the average of all observations for either 2D or 3D cultures ±SEM. (n = 11-15 image fields per set).

At the time SH-SY5Y co-culture experiments were carried out, members of the McConnell laboratory had made similar observations in alternate models of IMT. **Figure 3.3.6** describes work carried out by Rémy T. Schneider (RTS). Immortalised stromal cells derived from mouse bone marrow (BMSC) were transfected with mKO2-Mito-7 and co-cultured with mouse ρ^0-eGFP-astrocytes. In these experiments, RTS did not observe extensive IMT of complete mitochondrial networks from the BMSC cells by ρ^0-eGFP-astrocytes. Instead, as depicted in **Figure 3.3.6I.**, large particles which appeared to contain mitochondrial targeted FPs were regularly seen in association with ρ^0-eGFP-astrocytes. Due to the similar appearance of these particles to those in my own SH-SY5Y co-culture model, I designed further experiments which would generate insight into the nature of these objects.

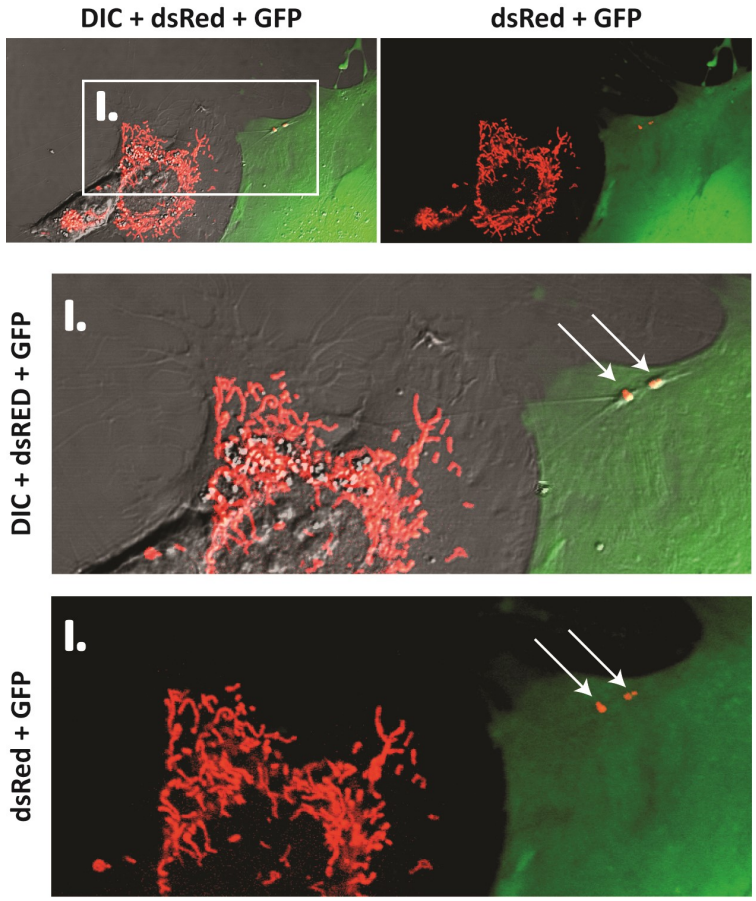

Figure 3.3.6. Transfected bone marrow derived stromal cells produce extracellular particles which contain mKO2-Mito-7

Immortalised bone marrow derived stromal cells (BMSC) in co-culture with ρ^0-eGFP-astrocytes. To model IMT, mitochondrial deficient ρ^0-eGFP-astrocytes were placed in co-culture with mKO2-Mito-7 transfected BMSC, and examined for evidence of mitochondrial transfer. The area within the white square is enlarged in the lower panels **(I.)**. Particles which appear to contain mitochondrial targeted fluorescent proteins appear to be associated with a ρ^0-eGFP-astrocyte, indicated by the white arrow. These experiments were conducted by McConnell laboratory member Remy T. Schneider [262] and reproduced with permission. Red = mKO2-Mito-7, Green = GFP.

3.3.3 Extracellular particles detected by analytical cytometry contain mitochondria

The fluorescent objects seen both SH-SY5Y and BMSC/ρ^0-eGFP-astrocyte co-culture models appeared to contain mitochondrial-targeted FPs. It was however, important to determine experimentally whether or not these objects actually contained mitochondria. It was plausible that these objects were instead excessive FPs generated by overexpression and secreted from the cell, or more simply auto-fluorescent artefacts.

To investigate, medium conditioned by BMSC cells was examined by analytical cytometry using a cytometer setup capable of resolving sub-micron sized particles. For small particle analysis, the BD Influx™ cytometer is fitted with a high numerical aperture microscope lens, a pinhole and a photomultiplier tube (PMT). These additional components of the detection system allow for accurate resolution of particles as small as 200 nm in size.

To detect and approximate the size of extracellular particles in the conditioned medium of BMSC cells, development of an appropriate reference scale was first required. **Figure 3.3.7** depicts how commercial microspheres of known sizes were used to develop an appropriate gating strategy, which could then be applied to BMSC conditioned medium. A discrete population of particles with high, uniform fluorescence appearing in the 520 nm/35 nm optical channel resolved by side scatter (SSC) were identified as green fluorescent 500 nm ApogeeMix microspheres (**Figure 3.3.7A**). A gate placed on this population enabled the corresponding signals to be identified within the forward scatter (FSC)/ SSC of the total population. ApogeeMix microspheres <500 nm in size were not well resolved in the sample, so I determined analysis of conditioned medium should be limited to particles >500 nm in size.

To determine an upper size reference, a sample SPHERO™ Ultra Rainbow Fluorescent Particles provided a clear, singular population resolved by FSC/SSC. A third reference population of 1.3 μM was identified as the population with the highest FSC/SSC properties within the ApogeeMix sample. To represent this lower limit, and middle and upper size reference scale, the microsphere populations of known size were overlaid (**Figure 3.3.7B**). A gate for analysis of conditioned medium was set along for all FSC values detected greater than those of the 500 nm population. The SSC value for this gate was reduced slightly from the value of the 500 nm population to allow for more generous collection of events. It was possible that biological particles could exhibit lesser SSC properties than the microspheres. This consideration would compensate somewhat for the unknown complexity of, and therefore light scattering properties for particles in conditioned medium. The 500 nm, 1.3 μm and 3.2 μm reference populations were overlaid with an ungated sample of BMSC

conditioned medium to demonstrate a likely range in which the biological particles of interest would fall. Extensive digital noise can be seen as events detected at low FSC/SSC values.

Figure 3.3.7. Gating strategy for approximation of extracellular particle size
To determine appropriate cytometer settings for the analysis of extracellular particles within conditioned medium, synthetic beads were used. A sample of ApogeeMix beads in 0.1 µm filtered sheath fluid was analysed to define a lower limit of detection for sub-micron sized particles of interest. **(A)** A 500 nm bead population was first identified by its strong green fluorescence detected in a 520 nm/35 nm band pass filter. The population with highest forward scatter was defined as 1.3 µm corresponding to the largest particle within ApogeeMix. A sample of 3.2 µm average SPHERO™ Ultra Rainbow Fluorescent Particles was analysed to provide an upper size reference for particles of interest. The populations identified within each bead sample were used to define a minimum forward scatter/side scatter gate suitable for analysis of extracellular particles in conditioned medium. **(B)** These populations have been overlaid with a sample of BMSC conditioned medium to approximate where biological particles of interest would likely be detected.

A)

ApogeeMix beads

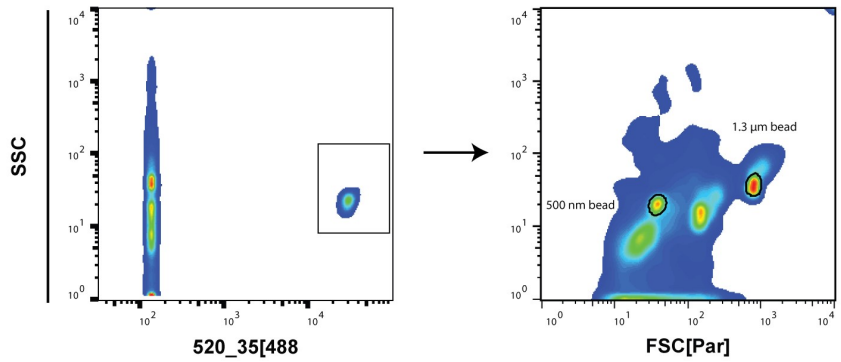

SPHERO™ Ultra Rainbow Fluorescent Particles

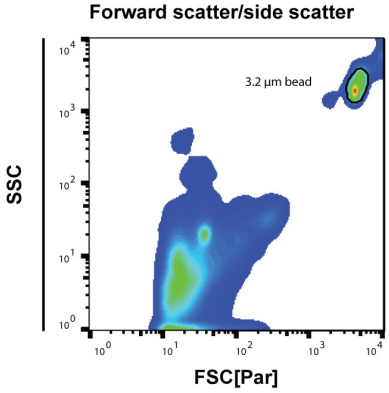

B)

Particle size approximation - foward scatter/side scatter

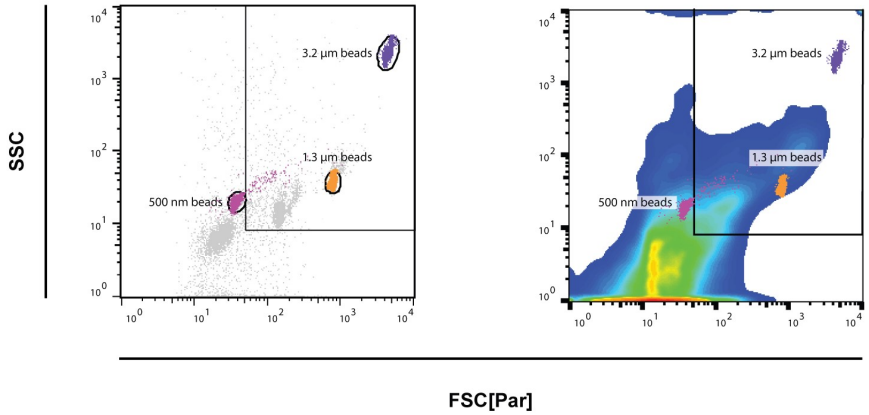

If the fluorescent objects appearing in microscopy of BMSC cells in fact contained mitochondria, it would be possible to detect them as events which fell within the determined FSC/SSC range. After large cell debris or intact cells were removed by filtration, particles in BSMC conditioned medium were stained and analysed as depicted in **Figure 3.3.8**. Complete medium contained two major populations by FSC/SSC, which diffuse gradually over a large radius. This suggests these particles exist in a range of sizes. As complete medium contains FBS, it is likely these particles are bovine in origin. The two populations may represent either exosomes or microvesicles. Curiously, the lipophilic stain DiD did not appear to stain these particles, indicating a low-lipid content, or perhaps a membrane structure to which DiD associates poorly. Particles in complete medium did not appear to be stained by MitoTracker™ Green FM or MitoTracker™ Red CMXRos which suggests that mitochondrial components were not present.

When medium conditioned by BMSC cells was analysed, an event profile distinct from complete medium was generated. The larger FSC/SCC population observed in complete medium appeared reduced in number relative to the smaller FSC/SSC population. Unfortunately, it was not possible to determine whether BMSC cells deplete this population during culture, or simply generate more of the smaller particles. Particles within the sample were however detected as positive for both DiD and MitoTracker™ Green FM. Similar to complete medium, particles did not exhibit distinct positivity for MitoTracker™ Red CMXRos. This indicated that a component of the total particles was lipid in nature, and potentially contained mitochondrial membranes. The MitoTracker™ Green positivity should be interpreted with restraint as the large shift in staining for the whole population may indicate non-specific interactions of the dye when detected at this small scale. It is important to note that the use of these dyes for staining sub-micron sized particles is not a typical application, so the dye properties and performance that could be expected with larger particles are not validated. The lack of MitoTracker™ Red CMXRos positivity suggested that any mitochondria lacked a membrane potential, or that the dye was simply not sensitive for detection at a sub-micron scale.

With these cautions in mind, it appeared that objects secreted by BMSC cells included microvesicle sized particles with staining characteristics which suggested the presence of mitochondria.

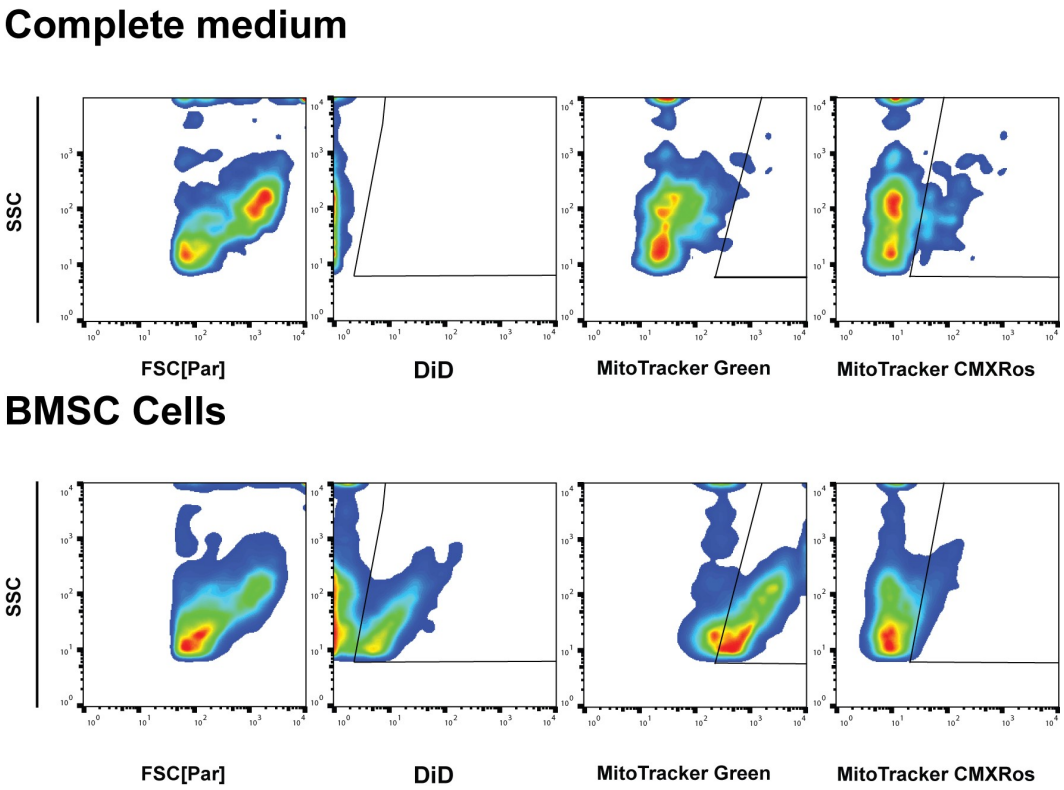

Figure 3.3.8. Extracellular Particles detected in medium conditioned by BMSC cells
Medium conditioned for approximately 3 days by BMSC lines was filtered through a 1.2 µm syringe filter and analysed by flow cytometry. Complete medium was analysed alongside samples of conditioned medium to evaluate particles above 500 nm present within serum-containing medium alone. Samples were stained with DiD, MitoTracker® Green FM and MitoTracker® Red CMXRos to assess whether detected events were particles likely to contain mitochondria. Events displayed are those which fell within the forward scatter/side scatter gate defined in **Figure 3.3.7**.

3.3.4 Extracellular particles contain mtDNA detectable by qPCR

To further understand whether or not the fluorescent particles secreted by BMSC were mitochondrial in nature, I investigated if a molecular signature could be detected in conditioned medium. By performing qPCR on conditioned medium harvested and filtered through membranes with various pore size, this experiment would enable identification of mtDNA contained within vesicles. The potential to establish future IMT co-culture models with murine cell lines lead to the inclusion of two murine astrocyte cell lines, C8D1A and eGFP-astrocytes, to determine whether or not these cells would also secrete mitochondrial containing vesicles. Additionally, the human lung fibroblast WI-38 cells were included for analysis as independent observations in the McConnell laboratory suggested they were high secretors of small vesicle-like structures and were considered a candidate 'donor' cell line for IMT models.

A method for detection of mitochondrial sequences from both mouse and human samples was designed and optimised by PCR, before adaptation to a qPCR format. Unlike PCR on genomic extracts, this assay was designed to isolate cell-free DNA from conditioned medium (**Figure 3.3.9A**). It was hypothesised that that both free, and vesicle bound mtDNA would be detected in the medium conditioned by cells. By processing the medium through either a 1.2 or 0.2 µm filter, the quantity of vesicle bound mtDNA molecules would be reduced. Filtration through a 1.2 µm pore size was likely to remove the majority of particles >1.2 µm in size –a candidate vesicle size to contain mitochondria. It was hypothesised that filtration through a 0.2 µm filter would further decrease the amplification if particles in the 0.2 to 1.2 µm size range contained mtDNA.

Depicted in **Figure 3.3.9B**, mtDNA was successfully amplified from medium conditioned by each of the cell lines tested. Amplification was significantly reduced by filtration through both 1.2 and 0.2 µm pore size relative to paired unfiltered conditioned medium. Amplification of mtDNA in medium conditioned by BMSC, C8D1A and EGFP-astrocytes (C57A) did not demonstrate a significant difference in the mean fold reduction when filtered through a 0.2 µm filter compared to 1.2 µm filter. This indicates that mtDNAs were associated with vesicles greater than 1.2 µm in diameter. Curiously, 0.2 µm filtered medium conditioned by WI-38 cells indicated instead that mtDNA was also present in vesicles smaller than 1.2 µm. This was apparent by a significant difference in mean fold reduction between each filter condition. This suggested the mitochondrial content of vesicles secreted by WI-38 were different in nature to those from the other assessed cell lines.

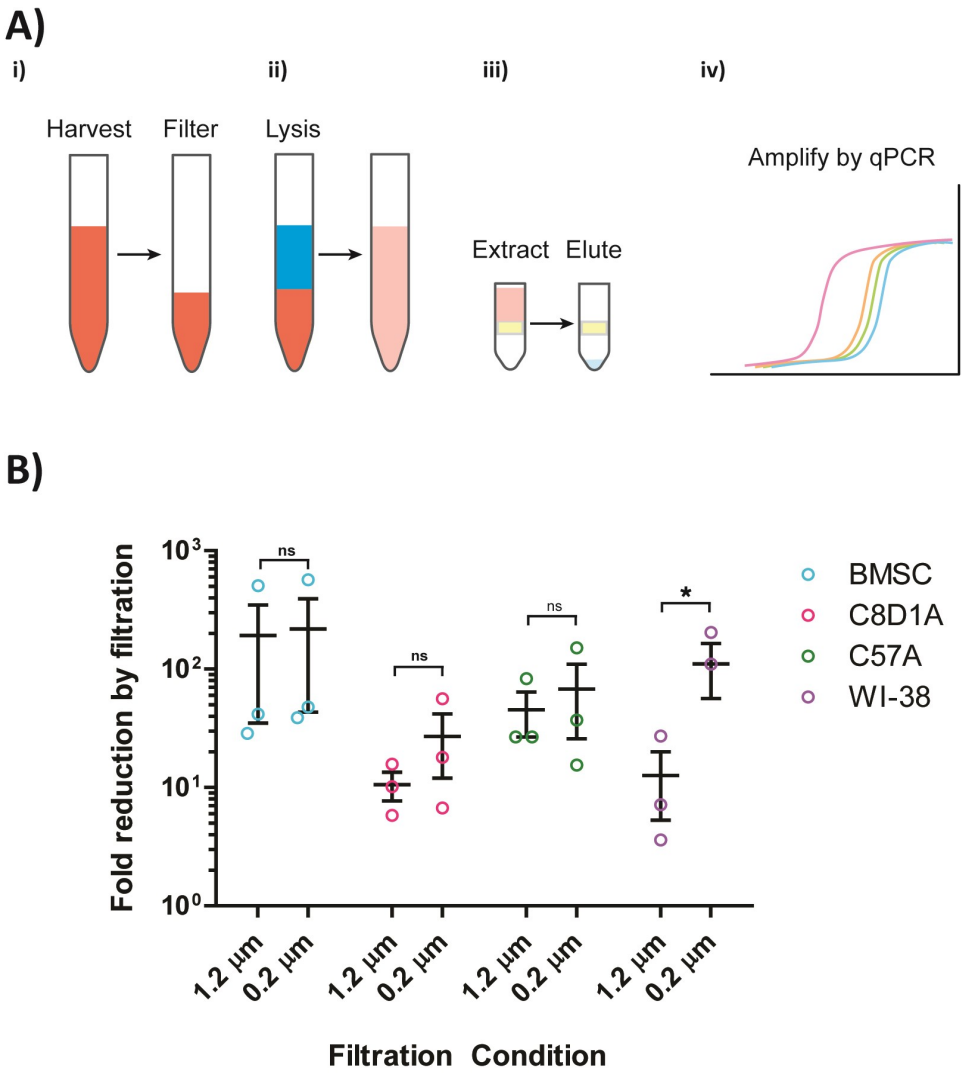

Figure 3.3.9. mtDNA is present in extracellular particles generated by BMSC, C8D1A, C57A and WI-38 cell lines

mtDNA was extracted from conditioned medium as illustrated in **(A).** A fixed volume of DNA extracted from conditioned medium was amplified by qPCR **(B)**. To delineate extracellular DNA present in medium from any DNA contained within extracellular vesicles, conditioned medium was filtered. A 1.2 µm filter or 0.2 µM filtration removed particles larger than the selected pore size. Data are presented as the mean fold reduction of mtDNA amplification ± SEM normalised to paired, unfiltered conditioned medium, to reflect the removal of extracellular particles during filtration. For all filtered samples, amplification of mtDNA was reduced by both 1.2 µm and 0.2 µm filtration, which suggests mtDNA was present within membrane bound particles. To evaluate if particles likely fell within the size range of 1.2 µm to 0.2 µm, the fold reduction of amplification for each sample was compared by unpaired student's t test. * $p<0.05$. n = 3 for each cell line assessed.

3.3.5 Human WI-38 lung fibroblasts secrete multiple classes of extracellular vesicle

Extracellular vesicles which appeared to contain mitochondria had now been detected by fluorescence in microscopy and cytometry, as well as extracellular mitochondria by a molecular signature, albeit in vesicles sourced from various cell lines. As an additional confirmation, I investigated whether or not mitochondrial structures could be observed within these extracellular vesicles by TEM, using extracellular vesicles secreted by WI-38 cells.

Figure 3.3.10 represents two major classes of extracellular vesicle detected in abundance in the prepared TEM grids. In **Figure 3.3.10A**, representative images of a larger vesicle type, approximately 1-3 μm in length are shown. These vesicles were consistent in size with objects widely described as microvesicles. The size of vesicles was consistent with what would be removed by filtration of the conditioned medium in **Figure 3.3.9**. Together, this indicated that the microvesicles were a likely candidate to contain mtDNA as detected by qPCR. The microvesicles consisted of an external membrane structure which appeared to contain multiple smaller, membrane bound compartments. Subtle differences in the stain intensity within these objects formed parallel structures reminiscent of mitochondrial cristae, however the detail captured was not sufficient to confirm this observation. Smaller objects with an intense staining profile were also present within the microvesicles. It is unclear what these objects were, but their appearance was distinct from the majority of the membrane-bound sub-components of the microvesicle. A second, smaller class of extracellular particle was detected, depicted in **Figure 3.3.10B**. These 400-600 nm particles consisted of a double membrane structure, but lacked other discernible characteristics. The observed particles were consistent with exosomes in size and appearance. The vesicles fell within a size range which would be excluded by filtration through a 0.2 μm filter, so it was plausible that a quantity of them may contain mtDNA as detected by qPCR in **Figure 3.3.9**.

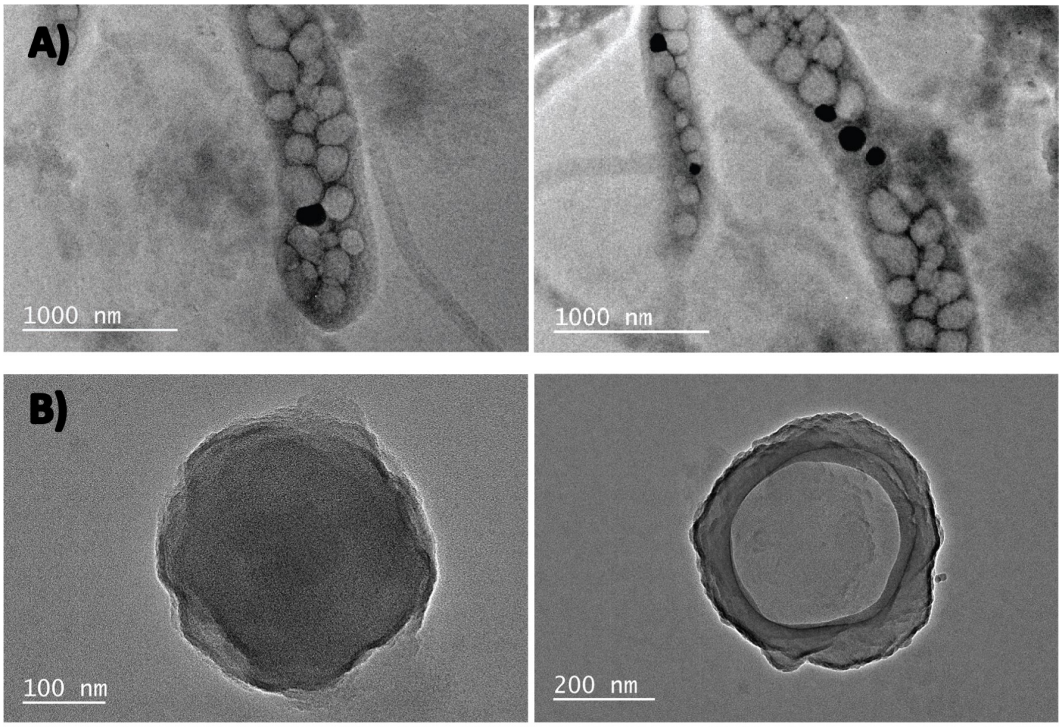

Figure 3.3.10. Transmission electron micrographs of extracellular vesicles secreted by WI-38 lung fibroblasts
Extracellular vesicles were collected from medium conditioned by WI-38 cells for 3 days and prepared for TEM. Large extracellular particles approximately 1-3 µm in length were highly abundant in samples **(A)**. These micro-vesicle sized particles appeared to contain multiple membrane bound components with faintly stained sub-structure, suggestive of mitochondrial cristae. Smaller extracellular particles approximately 400-600 nm in diameter were also identified in EM grids in high abundance **(B)**. These structures appeared to be consistent with exosomes seen by TEM.

3.3.6 SH-SY5Y and WI-38 lung fibroblast co-cultures demonstrate bi-directional transfer of mito-FPs as a complete mitochondrial network.

The qPCR and TEM results from WI-38 cells suggested these cells secreted extracellular vesicles, which could potentially contain mitochondria. To support this, co-cultures were established to examine if these particles would also contain mito-FPs, and whether or not they would be taken up by 'recipient cells'. There was already evidence in the literature to suggest fibroblasts could act as a mitochondrial donor in IMT [175]. These experiments were performed to determine whether or not fluorescently labeled mitochondria could be identified as transferring between WI-38 or SH-SY5Y cell lines.

WI-38 were transfected with mKO2-Mito-7 ('donor' cells) or cytosolic mCherry ('recipient cells') and placed into separate co-cultures with GFP-SHY5Y, or GFP-SHSY5Y-mito-BFP respectively. After 24 h in co-culture, the cells were examined by confocal microscopy for any signs of IMT or extracellular vesicles. Surprisingly, a low frequency of mCherry positive WI-38 cells were detected which appeared to contain a complete mitochondrial network, illuminated by mito-BFP (**Figure 3.3.11A**). In this condition, mito-BFP had been introduced only to GFP-SH-SY5Y through transfection. This suggested that extensive transfer of mitochondrial-FPs had occurred in a small number of WI-38 cells. This result was highly unanticipated in that no prior evidence for this type of interaction had been observed in the McConnell laboratory, across many varied cell types co-cultured. The directional transfer of fluorescent proteins suggested that SH-SY5Y had in fact 'donated' mitochondria to the WI-38 fibroblasts.

A second co-culture of transiently transfected mKO2-Mito-7-WI-38 with GFP-SH-SY5Y was examined and again, mitochondrial-FPs were detected at low frequency in GFP-SH-SY5Y cells (**Figure 3.3.11B**). These FPs were transfected only into WI-38, so the appearance of whole mitochondrial networks in very few SH-SY5Y indicated that IMT had occurred. Combined with the observations made in **Figure 3.3.11**A, it was apparent that in this model, IMT was able to occur bi-directionally. Both SH-SY5Y neuroblastoma and WI-38 lung fibroblasts were capable of acting as mitochondrial 'donor' and 'recipient' when co-cultured together. In addition, small clusters of SH-SY5Y cells with mitochondrial networks illuminated by mKO2-Mito-7 were detected (**Figure 3.3.11C**). Whether these cells had simply replicated following IMT, or multiple transfer events had occurred within proximity was not clear. Regardless, the observations made in this co-culture model were of great interest.

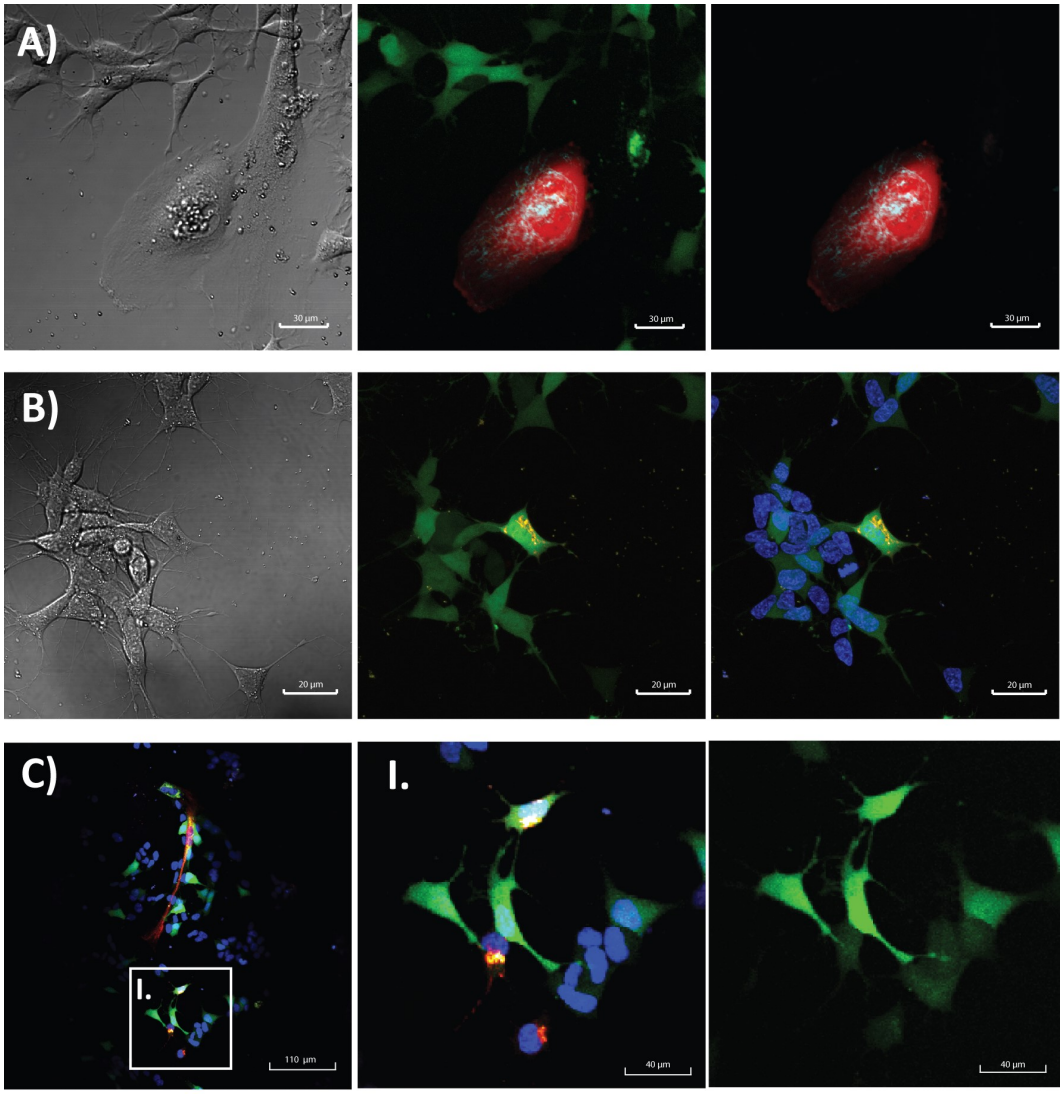

Figure 3.3.11. SH-SY5Y neuroblastoma and WI-38 lung fibroblasts show transfer of mito-FPs after 24 hours co-culture

Each image depicts a representative occurrence of mito-FPs detected within a non-transfected cell in 24 h co-cultures of WI-38 and SH-SY5Y cells. These events occurred at low abundance in co-culture. **(A)** WI-38 with transfected with cytosolic mCherry (red) were co-cultured with GFP-SH-SY5Y (green) transfected with mito-BFP (cyan). **(B, C)** GFP-SH-SY5Y (green) were co-cultured with WI-38 transfected with mKO2-Mito-7 (orange). Image **(C, I.)** represents a magnified region in which three SH-SY5Y cells are detected with mKO2-Mito-7.

3.4 Discussion

The methods applied in this chapter represent traditional experiments used to study IMT, as they appear regularly in the literature. A mitochondrial labelling dye and mitochondrial targeted FPs were evaluated in initial exploratory models of IMT. As a research field in its infancy, a precedent for the appropriate use of tools to study IMT is not strongly established [204]. No one co-culture model is robustly established as a positive control on which to benchmark detection techniques. To address the overarching questions of this thesis, absolute confidence in methods that would detect genuine IMT events was required.

MitoTracker™ CMXRos, while brilliant for its intended application, appeared completely unsuitable for use in IMT research. My own observations, along with others investigations of dye leakage in the McConnell laboratory provided a strong justification that MitoTracker™ or similar dyes should find no further application to IMT models. Indeed, a similar conclusion was reached by Cselenyák et al. for tests of dye leakage in the context of IMT [263]. The high likelihood of false positive observations was simply not conducive to the intended quantitative studies of the phenomenon.

To progress, mitochondrial targeted FPs were stably introduced into a number of cell lines, and clones isolated. These models allowed initial observation of extracellular vesicles which contained mitochondrial targeted FP. These vesicles seemed to associate with 'recipient' cells and the exogenous mitochondrial targeted FPs did not appear to integrate with the endogenous mitochondrial networks of 'recipient' cells. Furthermore, rapid photo-bleach of the vesicles when imaged by LSCM prevented accurate localisation of the signals. Rapid loss of fluorescence prevented accurate three dimensional imaging and deconvolution. For this reason, whether or not the FP-labelled mitochondria were internalised into 'recipient' cells could not be determined.

Observations of these fluorescent vesicles lead to many more questions – Did the vesicles actually contain mitochondria? Were these small vesicles likely to be auto fluorescence artefacts in LSCM? If these were examples of contact independent IMT, why were mito-FPs not detected within the 'recipient' cells? The mitochondrial network is a highly dynamic organelle – Would fluorescent proteins embedded in the membrane of exogenous mitochondria simply diffuse throughout the 'recipient' network upon integration into a foreign cell? This is plausible given the rapid diffusion properties of mitochondrial proteins [259]. Singular 'donated' mitochondria may simply integrate and their components diffuse throughout the endogenous network, alongside their fluorescent signal. Perhaps more simply, the cell types chosen for these models did not actually engage in IMT. Production

of stable mito-FP clones for each new model, only to reach this same conclusion would not be an effective approach in the longer term aims of this research.

Nevertheless, it was important to determine whether or not secreted vesicles did in fact contain mitochondrial components. This would provide insight into the effectiveness of mitochondrial targeted FPs for quantitative study of IMT in any given model. If the vesicles observed did in fact contain mitochondria, yet integration into 'recipient' cells was not always detected, mitochondrial targeted FPs were unlikely suitable to progress the intended aims of this research.

To address this, the nature of these extracellular vesicles was explored by a number of secondary techniques. A study published by Hayakawa et al. [198] proposed that primary rat cortical astrocytes produce extracellular vesicles 300 to 1100 nm in size which contain functional mitochondria. A component of this investigation made use of flow cytometry to characterise particles in medium conditioned by the astrocytes. This provided inspiration to characterise extracellular particles derived from BMSC conditioned medium similarly.

While Hayakawa et al. described vesicle bound, functional mitochondria derived from astrocyte conditioned medium [198], the vesicles generated by BMSC cells were not equivalent. Instead, vesicles positive for MitoTracker™ Green FM and DiD were detected, but did not stain with MitoTracker™ Red CMXRos. Together, these results identified membrane bound vesicles of a similar size and with possible mitochondrial membrane content, but a lack of mitochondrial membrane potential. The vesicles detected in this experiment were unlikely to contain active, respiratory competent mitochondria. If BMSC cells generated extracellular mitochondria that were not functional, perhaps a different cell line would produce a more similar result to the rat cortical astrocytes assessed by Hayakawa et al.

By extracting DNA from the extracellular environment of medium conditioned by BMSC, C8D1A, EGFP-astrocytes and WI-38 cells, the presence of mitochondrial DNA within filterable particles was assessed. A positive molecular signal indicated that mitochondrial DNA was present in particles generated by each of these lines. Perhaps secretion of these vesicles was complementary to larger global biological processes. Cells may simply dispose of regions of mitochondria and other cellular components by exocytosis-like mechanisms as opposed to autophagy. Whether these mitochondria are respiratory competent or taken up by other 'recipient' cells to some benefit remained unclear.

A subtle difference in the filterable, mtDNA content of particles generated by WI-38 lead to a closer examination by TEM. Here, I was able to confirm the presence of two vesicle-like structures in the medium by imaging. While the exact nature of the microvesicle sub-

structures was not determined, the presence of these objects identified WI-38 as a cell line that should be assessed for its ability to donate mitochondria in co-culture.

When placed into co-culture with SH-SY5Y cells, I detected complete and bidirectional IMT. While low in frequency, positive events were extremely obvious. To have occurred to this degree in a limited number of cells, a vesicle mediated mechanism alone was doubtful. Did this model simply involve the right cell types that would instead engage in IMT by contact-mediated mechanisms? Was there something inherently different about these few, select cells that took up mitochondria?

Perhaps the FP based model had not performed as expected. A critical difference in these co-cultures was the use of a primary cell type. WI-38 cells are one of a series of human primary lung fibroblasts isolated from a 3 month gestation foetus [264]. These cells are not immortalised, so transfection and selection of stable clones was not practical, as senescence would soon be inevitable with serial culture. To use these cells into a co-culture model, a transient transfection was used instead to introduce plasmids. In the same workflow, GFP-SHY5Y were transfected with a mito-FP. When co-cultures were established, were the transfected cells capable of sharing the plasmids directly into the partnered cell type?

If plasmid transfer occurred, it is plausible that 'non-transfected' cells would begin to transcribe their own intracellular mito-FP, and appear as a false positive result for IMT. I was unable to find any precedent for this in the literature, however this could be an interesting experimental scenario. It is not likely that plasmid transfer like this would impact the experimental design in other research applications, as it would in a IMT co-culture.

False positive detection of IMT by direct transfer of expression vector was a scenario that could have been explored further experimentally, however such investigations would have detracted from the purpose of this research. If I were to develop an IMT model in which to explore the effect of injury on the rate of IMT, it was clear that an alternative to mito-FPs, especially with transient vectors, would also be required. The signal generated by mito-FPs in secreted vesicles were dim and easily photo bleached; too fragile to approach with quantitative microscopy, especially if I were to confirm the objects as intracellular. The threat of vector transfer cast a large degree of doubt over my confidence in the existing methods applied thus far in IMT research.

In summary, the experiments presented in this chapter sought to address whether methods adapted from previously published IMT research were sufficient for a robust quantifiable detection of IMT in new models. To progress toward the key aims of this thesis and perform truly quantitative IMT research, a need to move past both mitochondrial labelling

dyes and mito-FPs was obvious. The development of novel methodologies which sought to advance this field of biology was prioritised for this thesis, based on the research presented in this chapter.

4 Molecular methods for investigation of IMT

4.1 Introduction

Current approaches to study IMT attempt to visualise the movement of mitochondria, or the organelles in their new destination, the recipient cell. The caveats of these approaches make quantitative studies of the IMT phenomenon a challenge [204]. To understand how cellular injury influences the rate of IMT for this research, it was essential that I develop a novel, quantitative alternative.

A molecular approach to detecting IMT requires the model to carry one or more unique, targetable elements which differ between 'donor' and 'recipient' mitochondria. The many mtDNAs carried by mitochondrial organelles were an obvious target biomolecule. Could mtDNA be used a trackable element in the context of IMT?

Few publications in this field have considered mtDNA as a measurable component of IMT. The closest examples of this come from studies in ρ^0 cells; cells devoid of endogenous mtDNA [113, 265]. Used in IMT models, these cells have been shown to take up mitochondria from 'donor' cells [167, 172, 175, 176, 212]. Because these cells undergo a binary transition from mtDNA null to mtDNA replete post-transfer, PCR can readily be used to detect mtDNA recovery. In addition, SNVs present in the 'donor' cell mtDNA can be sequenced to verify that ρ^0 cells have indeed, taken up exogenous mtDNA.

This approach, while an elegant piece of evidence to support transfer, becomes complicated outside of ρ^0 models. In normal cells, any transferred mtDNA molecules would now reside within tens, to potentially thousands of endogenous mtDNA copies. For this reason, a molecular approach toward detection of IMT in normal cells by mtDNA, is at its core, a challenge of low abundance SNV detection.

This chapter presents the development of a functional molecular method for quantitative study of IMT. This method enabled much of the downstream research presented in this thesis.

4.2 Aims

The aim of this chapter was to develop a novel strategy for robust, quantitative detection of IMT. Experiments presented in this chapter pertain to the design, optimisation and evaluation of novel molecular methods towards this aim.

4.3 Results:

4.3.1 Human and mouse mtDNA sequences contained variant bases valuable for molecular detection of IMT

Before a method based on molecular detection of mtDNA from individual IMT 'donor' cell lines could be developed, distinct SNVs within the mtDNA needed to be first identified. Sanger sequencing was performed on a range of cell lines which were considered candidate lines for IMT co-culture experiments.

An array of both mouse and human cell lines were available in the McConnell and Berridge laboratories, from which to survey mtDNA variation. Neural cell types; including GBM (LN18, 0809, 0906, 1003, DBTRG, U87, GL261), astrocyte (SVGp12, C8D1A, eGFP-astrocyte), neural progenitor (NE-4C) and neuroblastoma cells (SH-SY5Y) were selected as candidate 'recipient' cell types for mitochondrial transfer. Cells hypothesised to act as possible 'donor' cells included primary lung fibroblasts (WI-38, 3T3) and umbilical vein endothelial cells (HUVEC), alongside cancerous breast (4T1) and melanoma cell lines (B16). As a source of primary tissue, bloods were drawn from mouse strains C57BL/6, eGFP-C57/B6 and BALB/cByJ and included in the initial survey to ensure consistency with the publicly available reference sequences of each strain.

In **Figure 4.3.1A** Sanger sequencing revealed numerous SNVs across the hypervariable D-loop region of human mtDNA relative to the human genome reference sequence NC_012920. In the context of co-culture with these cell lines, a minimum of one SNV would be present between any pair when placed together into culture, with an exception of the LN-18/SH-SY5Y combination. It is however possible that a region outside of the depicted region would contain variation between LN-18 and SH-SY5Y cells. The variation discovered between the other cell line combinations was more than sufficient as a start point to select a target for a molecular assay. An overarching interest of the McConnell laboratory in co-cultures of GBM cell lines LN-18 and U87-MG led to selection of the SNV present at mtDNA_195 as the initial target for assay design.

In **Figure 4.3.1B** the mtDNA tRNA-Arg locus sequenced for the mouse-derived samples was also found to contain SNVs compared to murine reference sequence NC_005089.1. It was hypothesised that each cell line would share the majority of sequence homology to the parental mouse strain, however differences between strains were likely to be present. Three individual SNVs at mt_DNA9461, 9348 and 9820 were identified within the sequenced region. Relative to each other, C57BL/6 and BALB/cByJ mouse strains carried differences at each of these sites, consistent with publicly available data for each strain. The eGFP-C57BL/6 mouse strain was also consistent with its parental C57BL/6 genetic background at these loci. Curiously, all cell lines except in-house derived eGFP-astrocyte line differed from their parental background at mtDNA_9461 or 9820. The variation at mtDNA_9820 in all samples occurs in a poly-A tract. Here, sequences were found to carry an adenine count of 8, 9 and 10 bases. The SNVs at mtDNA_9348 and 9461 were selected as targets for molecular assays.

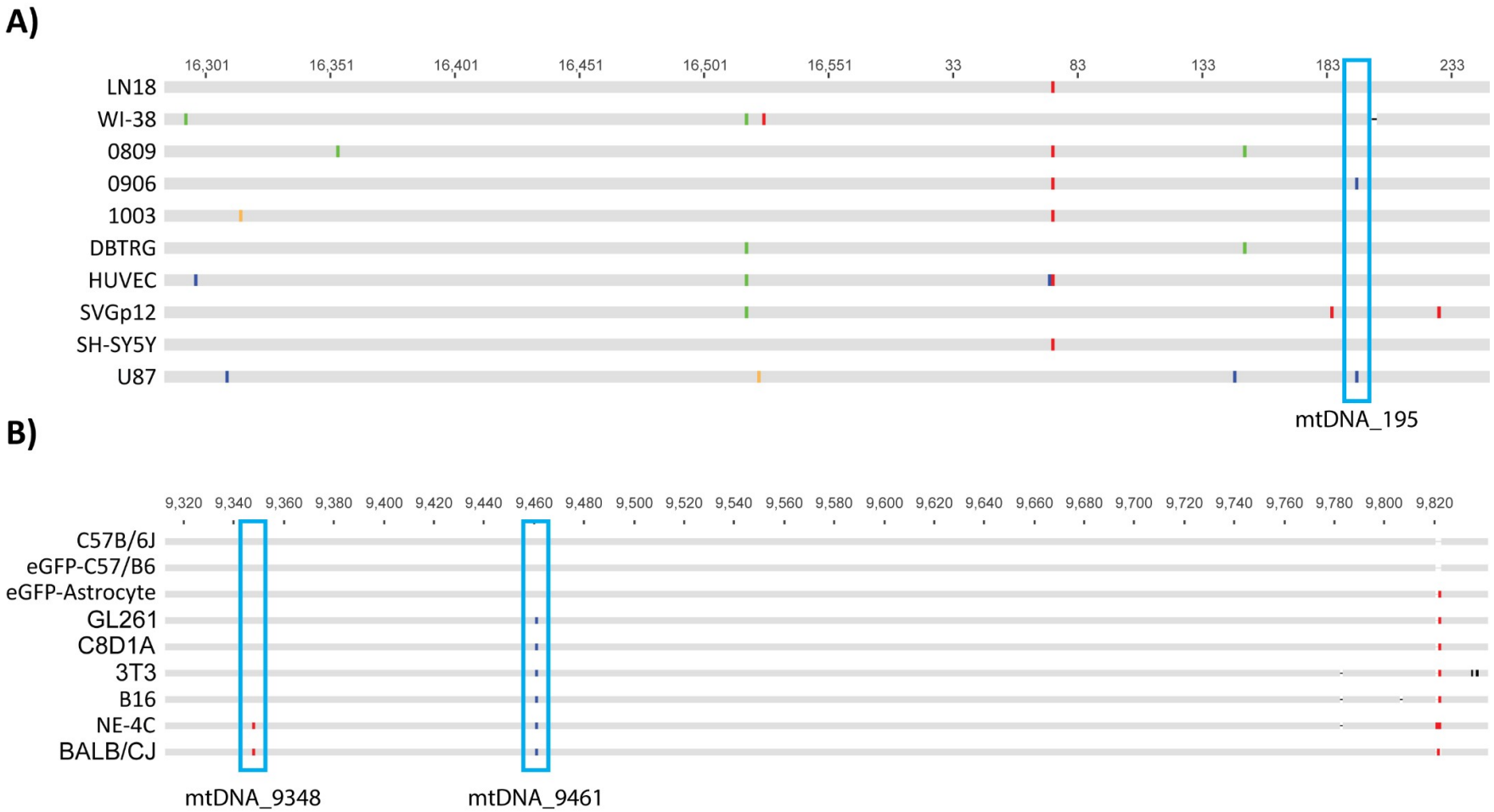
A)
16,301
16,351
16,401
16,451
16,501
16,551
33
83
133
183
233
LN18
WI-38
0809
0906
1003
DBTRG
HUVEC
SVGp12
SH-SY5Y
U87
mtDNA_195
B)
9,320
9,340
9,360
9,380
9,400
9,420
9,440
9,460
9,480
9,500
9,520
9,540
9,560
9,580
9,600
9,620
9,640
9,660
9,680
9,700
9,720
9,740
9,760
9,780
9,800
9,820
C57B/6J
eGFP-C57/B6
eGFP-Astrocyte
GL261
C8D1A
3T3
B16
NE-4C
BALB/CJ
mtDNA_9348
mtDNA_9461

Figure 4.3.1. Representative alignments of polymorphic mtDNA regions from human and mouse.

Human and mouse mtDNA was amplified by PCR and sequenced by chain termination. Here, a schematic representation of the consensus sequences obtained are presented for each species. Regions from the human hypervariable D-Loop (**A**) and mouse tRNA-Arg locus (**B**) from candidate cell lines or animal strains were amplified and sequenced. The sequences were aligned to reference sequences NC_012920 and NC_005089.1 for human and mouse mtDNA respectively. Variant bases are represented by a coloured bar at each position. Yellow = G, blue = C, red = A, green = T. Variant bases highlighted in blue rectangles represent those identified as suited to detection with molecular assays. For each sample, sequencing was targeted to both the forward and reverse strands of a PCR product, amplified each time from three independent biological samples.

4.3.2 Selective amplification of low abundance SNVs by allele-specific blocker qPCR

A technique known as allele-specific blocker qPCR (ASB-qPCR) [266] was identified as potentially useful for research in this thesis. If gDNA could be extracted from the IMT 'recipient' population, this sample could be interrogated for the presence of 'donor' mtDNA SNVs. To do this, 'donor' SNVs would need to be amplified from a vast excess of 'recipient' background sequence, based solely on minor variations in the form of SNVs, while surprising amplification of 'recipient' cell sequences. This amplification-based technique exploits two major features of DNA hybridisation; the thermodynamic properties of oligonucleotide interaction with DNA, and the diminished capacity of DNA polymerase to extend from a 3' mismatched oligonucleotide.

Figure 4.3.2 presents the finalised design of an ASB-qPCR assay targeted to U87-MG mtDNA_195 in an LN-18/U87-MG co-culture model. The 3' end of an allele-specific forward primer was designed to hybridise with the target U87-MG mtDNA SNV. This provides the first layer of template discrimination by DNA polymerase. A 3' phosphorylated blocking oligo is designed to match the 'off-target' template, with the SNV centrally located in the oligo. This position maximises the difference in T_m between matched and mismatched templates and implements a layer of thermodynamic discrimination to the assay. The phosphorylated 3' base prevents extension of the blocking oligo by DNA polymerase. Primers designed with 3' terminal purine-purine mismatches do not extend efficiently [267-269], as bases in this configuration produce maximum helical distortion in the 3' terminal region, preventing DNA polymerase activity. Unfortunately, a mismatch of this type was not available to target within the U87-MG and LN18 sequences obtained. Instead, inclusion of a blocking oligo enabled selective extension from of U87-MG template, while amplification from the purine-pyrimidine A:C template mismatch was supressed [266]; extension from this mismatch is normally permitted by DNA polymerase under conditions which lack the competitive blocking oligo. This particular base and strand orientation for the assay was carefully selected as it was predicted to produce most favourable discrimination between 'donor' U87-MG and LN18 'recipient' mtDNA [266]. As template is amplified, a dual quenched FAM probe is hydrolysed by a DNA polymerase with 5' to 3' exonuclease activity and enables real-time detection. By careful design of each oligo's position, sequence and length, reactions with an optimised annealing temperature were highly selective toward the target U87-MG mtDNA template (**Figure 4.3.2A**). At this temperature, exponential amplification of the off-target LN-18 (**Figure 4.3.2B**) mtDNA was suppressed.

For the finalised reaction conditions developed for this assay, refer to chapter 2, **Table 5.**

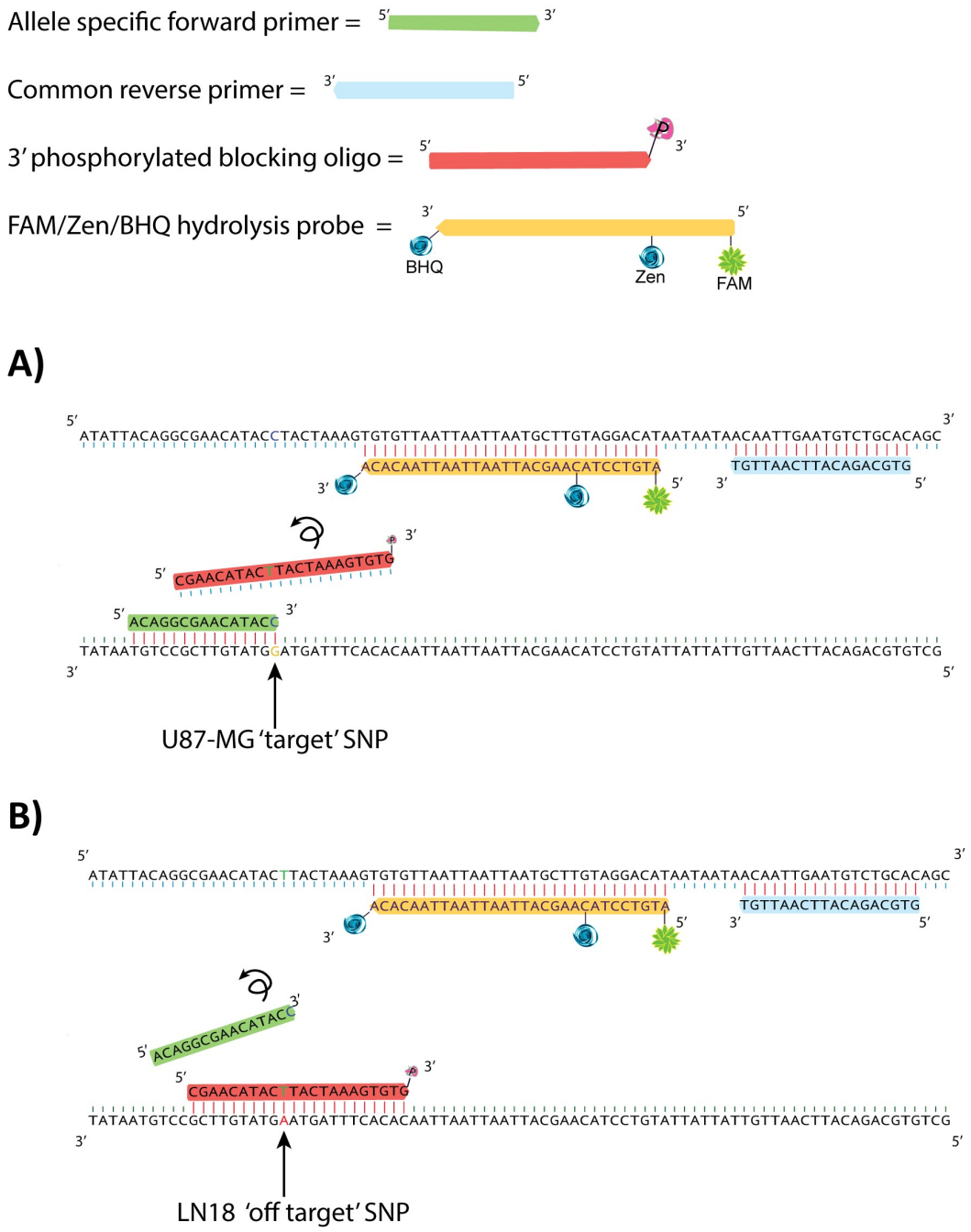

Figure 4.3.2. ASB-qPCR assay design schematic for detection of U87-MG sequence in an LN18 background

An ASB-qPCR assay was designed to selectively amplify U87-MG mtDNA sequence from a background of LN18 gDNA. **(A)** mtDNA_195G from U87-MG is targeted with an allele specific forward primer which outcompetes a mismatched blocking oligonucleotide. **(B)** If the template mtDNA originates from LN18, the allele specific forward primer is instead displaced by a 3' phosphorylated blocking oligonucleotide, which prevents extension by DNA polymerase. The reaction is monitored by qPCR, using a proprietary 6-Carboxyfluorescein (FAM) and double quenched (Zen/Black Hole Quencher (BHQ)) modified hydrolysis probe purchased from IDT.

Whether the U87-MG cell line actually engaged in mitochondrial transfer was unknown at this time. For this reason, ASB-qPCR reactions were optimised in simulated 'spike-in' mixtures of manually combined U87-MG/LN18 gDNA. Serial dilutions of U87-MG gDNA at known concentrations were each diluted into a background of 20 ng of LN18 gDNA to produce a 'spike-in' series. This series represented a simulation of diminishing mtDNA copies present within an IMT 'recipient' cell population. An assumption was put in place that each of these cell lines would carry a similar mtDNA copy number per ng of gDNA. This was unlikely to be biologically accurate, however it was a necessary assumption for the purpose of assay optimisation.

The results of ASB-qPCR targeted to U87-MG mtDNA_195 in an LN18 background are presented in **Figure 4.3.3A**. Under the optimised conditions, it was possible to resolve the presence of U87-MG mtDNA in a 10,000 fold excess of LN18 mtDNA, based on the 0.01 % dilution by gDNA mass. In the context of IMT, this indicated it would be possible to detect just 1 exogenous mtDNA per 10,000 endogenous molecules in gDNA extracted from a pure, 'recipient' LN-18 population after co-culture. It is important to reiterate the assumption made that mtDNA copy number was equivalent per ng of gDNA from each line.

These results were very promising towards quantification of biological IMT with a molecular method. As such, a second ASB-qPCR was designed and optimised to detect the presence of WI-38 mtDNA within an excess of SH-SY5Y gDNA – a co-culture condition which had shown intriguing results in chapter 3 of this thesis.

Shown in **Figure 4.3.3B,** a combination of SNVs, identified at mtDNA_16114 and 16269, were targeted in this assay design. An allele-specific reverse primer and off-target blocker were designed to discriminate between templates at mtDNA_16114. The forward primer was placed over a second SNV at mtDNA_16269 to introduce a further thermal discrimination against SH-SY5Y gDNA at mtDNA_16269.

Figure 4.3.3. Low abundance SNVs targeted by ASB-qPCR were successfully detected in simulated spike-in

To simulate IMT experiments, gDNA extracted from mitochondrial 'donor' cells was serially diluted into gDNA extracted from 'recipient' cells and amplified by ASB-qPCR. **(A)** SNV mtDNA_195G from U87-MG gDNA selectively amplified from a background of LN18 mtDNA_195A. **(B)** SNV mtDNA_16114A from WI-38 gDNA selectively amplified from a background of SH-SY5Y mtDNA_16114C. To define an assay limit of detection, gDNA from off-target cells alone was amplified alongside the spike-in dilutions. Data for both U87-MG and WI-38 selective ASB-qPCR assays are presented as the mean amplification cycle threshold (ΔCt) ± SEM relative to background only amplification from 3 biological replicates.

A)

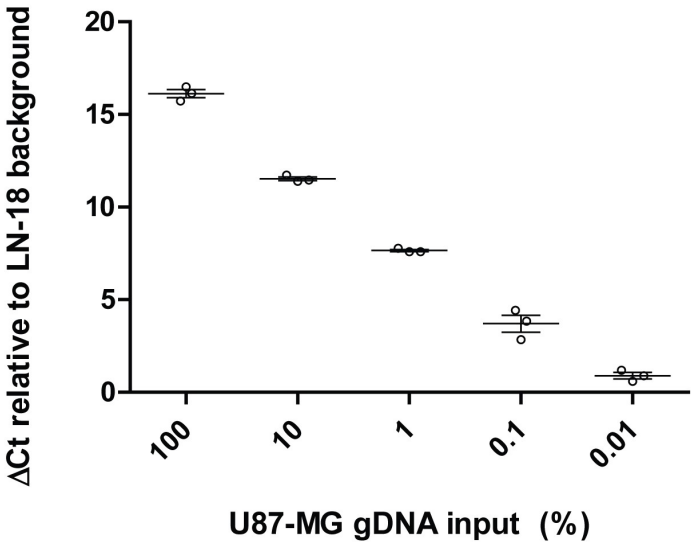
ΔCt relative to LN-18 background
20
15
10
5
0
100
10
1
0.1
0.01
U87-MG gDNA input (%)

B)

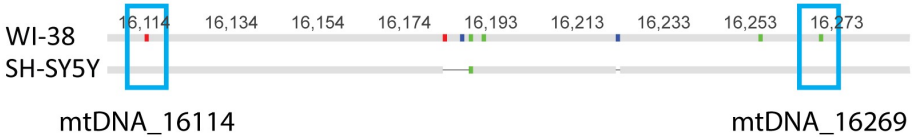
WI-38
SH-SY5Y
16,114
16,134
16,154
16,174
16,193
16,213
16,233
16,253
16,273
mtDNA_16114
mtDNA_16269

C)

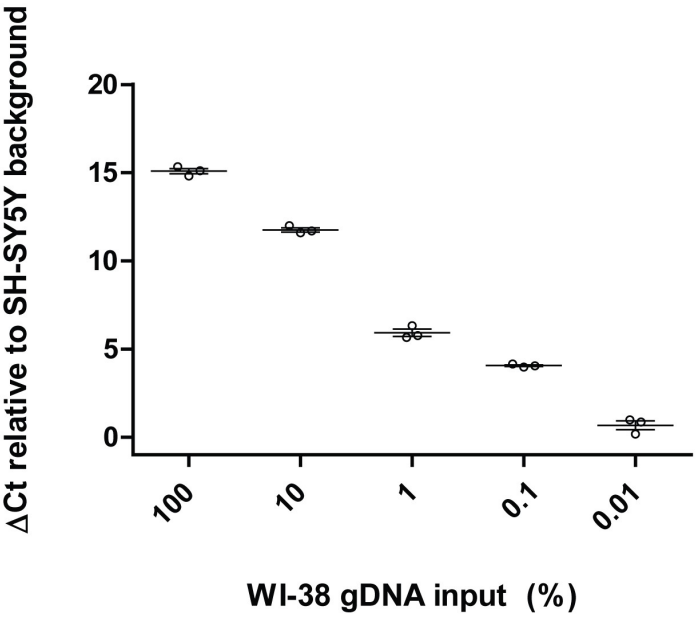
ΔCt relative to SH-SY5Y background
20
15
10
5
0
100
10
1
0.1
0.01
WI-38 gDNA input (%)

Figure 4.3.3C presents the result of a simulated 'spike-in' for an optimised ASB-qPCR assay designed to detect WI-38 mtDNA in an SH-SY5Y gDNA background. With this assay design, it was also possible to detect the target mtDNA within a 10,000 fold excess of off-target mtDNA. Again, this inference is made under an assumption of mtDNA copy number equivalency per ng gDNA. Taken together, the results of the ASB-qPCR simulated 'spike-in' for each of the optimised assays indicated it would be possible to detect target mtDNA molecules amongst an excess of endogenous mtDNA, using a gDNA sample isolated from the IMT 'recipient' cell population. Each assay demonstrated a linear relationship between 10 fold dilutions of target template. This would allow conclusions to be drawn about relative changes in 'donor' mtDNA quantity found in recipient cells, in injury models of neural cell stress.

4.3.3 Neural cell separation purity by FACS was insufficient for ASB-qPCR

To quantify IMT from *in vitro* co-culture by ASB-qPCR, mitochondrial 'donor' and 'recipient' populations first required a physical separation. The ASB-qPCR approach to quantification of IMT requires pure 'recipient' cells. Any contaminant 'donor' cell will carry with them many mtDNA molecules [270-272]. With no prior knowledge of how many mtDNA are transferred in IMT, it was critical that separation be of extremely high purity; ideally perfect. Many of the cell types of interest already expressed fluorescent proteins, which favoured cell separation by FACS. Cell sorting by FACS was performed in attempts to isolate a pure IMT 'recipient' cell population, which could be interrogated for the presence of transferred mtDNAs originating in the IMT 'donor' population.

Figure 4.3.4 depicts results of FACS separation of GFP-LN-18 cells away from U87-MG, after 24 h in a co-culture. gDNA would then be extracted from these cells for the ASB-qPCR mtDNA_195 selective assay described in **Figure 4.3.2**. In **Figure 4.3.4B**, a clearly distinguished GFP positive population was identified as GFP-LN18 cells - 47.3% of total events**.** The GFP negative events in this sample correspond to U87-MG donor cells. An enrichment sort was first performed, followed by two subsequent one-drop pure sorts to ensure maximum purity. Unfortunately as depicted in **Figure 4.3.4C**, the final sorted sample was only 90.2% GFP positive. After three rounds of FACS, up to 9.8% of events were contaminating cells. This was not conducive to ASB-qPCR for detection of IMT. Despite several replicate attempts, and extension into other IMT co-culture models, the final purity of separation did not exceed approximately 90%.

A)

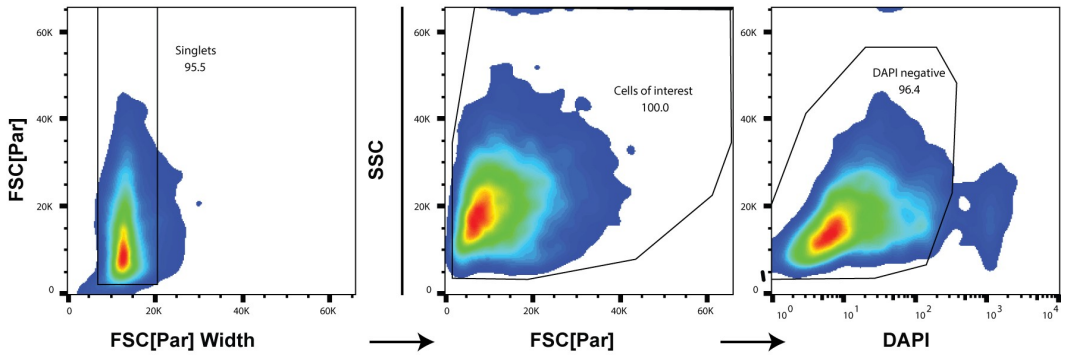

B)

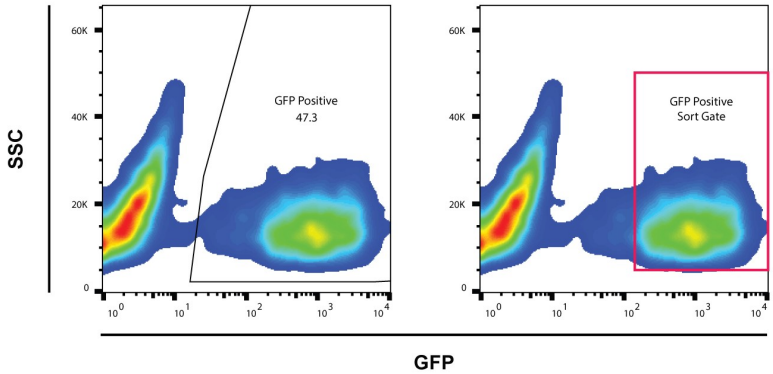

C)

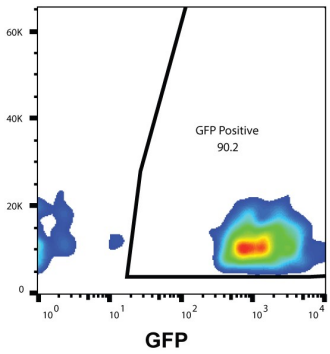

Figure 4.3.4. Separation of GFP+ cells following co-culture of GFP-LN18 with U87-MG
A co-culture of GFP-LN18 cells co-cultured with U87-MG for 24 hours before a perfect separation was attempted by FACS. This experiment is representative of sort results achieved for FACS sorting of large/neural cells. **(A)** To identify target cells, gates were first applied on FSA/FSW to isolate single cells. Cells of interest were gated on SSA/FSA to exclude small particulate/debris, before gating for live cells on the DAPI negative population. **(B)** GFP-LN18 cells were identified by gating on positive cells on a GFP/SSA axis. **(C)** The purity of the final sorted sample. FACS was performed as described in section **2.14.2**.

4.3.4 *In situ* single molecule genotyping for detection of IMT

An inability to sort cells at the required purity by FACS prevented direct analysis of gDNA from IMT models. An alternative approach was necessary; perhaps IMT in co-cultures could be detected without separation of the cells. Was it possible to detect IMT with a quantitative, molecular method *in situ*?

Detection of target sequences in both DNA and RNA *in situ* has been commonplace since the development of *in situ* hybridisation in the late 1960s [273-275]. As probe technologies have advanced, progressively smaller nucleic acid targets have become available. With specialised microscopy equipment, single molecule FISH (sm-FISH) enables direct detection of individual mRNA transcripts [276, 277]. This is achieved by hybridisation of multiple fluorophore-conjugated oligonucleotides to the target molecule. Discrimination between target molecules based on direct hybridisation to a single SNV is, however, significantly more difficult. While probe technologies are able to achieve this [278-280], a significant number of non-specific hybridisations to off-target molecules occur and are detected as false positives [278]. In the context of detection of IMT *in situ*, it was essential that false positive detections be minimised. This research was also constrained to standard microscopy equipment; therefore, signal amplification would be required.

As a possible solution, padlock probes (PDPs) were identified [281]. Padlock probes are single stranded oligonucleotides approximately 90 bases in length with 4 characteristic regions of sequence. The 5' end of the oligonucleotide consists of approximately 20 bp sequence with homology to a target nucleic acid. A flexible 'backbone' or linker region of approximately of 40 bp of non-complementary sequence follows, before a second region with sequence homology. Unlike typical linear oligonucleotides, PDPs hybridise at the 5' end and form a looped structure, with 3' homology upstream of the 5' end. A padlock probe can be circularised by a DNA ligase when hybridised in this manner; the padlock probe (PDP) catenated or 'locked' to the target molecule. A phosphorylated 5' PDP end is required for circularisation by DNA ligase; this is introduced either enzymatically or in probe synthesis.

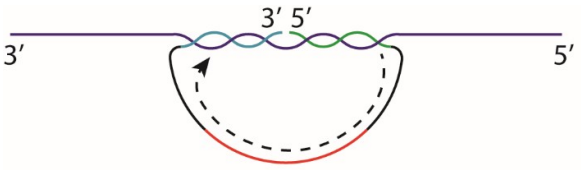

Figure 4.3.5. Padlock probe in a hybridisation
Purple = target DNA, green = padlock 5' end, blue = padlock 3' end, red = flexible linker/backbone

Early use of circularised PDPs enabled amplification reactions from both RNA and DNA targets *in situ* [282, 283]. In newer PDP reaction designs, the circularised PDP itself acts as template and the nucleic acid target is extended by a DNA polymerase; usually φ29 for its

efficient 5‘ to 3’ displacement activity. This reaction design is known as a target-primed rolling circle amplification (RCA) [284]. By extension directly from a target molecule, newly synthesised DNA is physically restricted to where the reaction was initiated. This reduces the likelihood of product loss or movement *in situ*.

The advantage of PDPs becomes clear in single molecule detection targeted to SNVs. Most DNA ligases are highly sensitive to the shape of the ligation junction [285]. Distortions in the helical conformation of dsDNA introduced through base-pair mismatches, results in a loss of contact between hydrogen bond acceptors in the minor groove of the template and the DNA ligase. This effect is enhanced on the 3’ side of the junction, when the specific mismatched nucleotides maximise distortion [285, 286]. Placement of a target SNV at the 3’ side of a ligation junction greatly enhances selectivity of PDP circularisation. Alternatively, the homologous regions of the PDP can be spaced such that a small gap exists between each end of the PDP. Short ‘gap-fill’ oligonucleotides may be designed to complement the target SNV. These oligonucleotides bridge the two homologous regions of the PDP and require two independent ligation events to circularise the probe [287, 288]. Probes of this style are known as gap-PDPs. In addition, blocker oligonucleotides with homology to the ‘off-target’ SNV may be included. A lack of a 5’ phosphorylation on the blocker oligonucleotides prevents PDP circularisation by DNA ligase and improves the selectivity of the reaction.

Target primed RCA by gap-fill ligation as described by Mignardi et al. [289] was selected as a basis for reaction designs in this research. This technique would enable mtDNAs which carried SNVs unique to the IMT ‘donor’ cell to be detected within the IMT ‘recipient’ cells after transfer. By fixing cells after a short time in co-culture, it would be possible to detect newly arrived mtDNAs, or those which had been replicated soon-after IMT.

Reactions were targeted to detection of mouse SNVs mtDNA_9461 and 9348. These targets were chosen in that the finalised assays would have greater applicability across both *in vitro* co-culture and *in vivo* transplant models.

4.3.5 Target primed RCA by gap fill ligation – assay design and development for detection of mouse SNVs mtDNA_9461 and 9348

To perform target primed RCA, target SNVs must be near the 5' end of a DNA fragment. **Figure 4.3.6** presents the reaction design first implemented in this research. In **Figure 4.3.6A,** a DraI restriction sequence TTTAAA was identified at mtDNA_9818 in mouse mtDNA. Digestion with DraI produces 9 mtDNA fragments, with target SNVs mtDNA_9461 and 9348 located in the largest, 4,544 bp fragment. Depicted in **Figure 4.3.6B,** first the target SNVs are exposed in the complementary strand by treatment of the DNA with T7 exonuclease. This reaction renders the fragment single stranded as nucleotides are removed from both 5' ends. In **Figure 4.3.6C,** a PDP with 5' homology to the complementary strand is hybridised upstream of the target SNV, while simultaneously, 3' homology directs hybridisation of the 3' end of the PDP downstream. In **Figure 4.3.6D**, the phosphorylated 5' end of the PDP is ligated to the 3' end by reaction with DNA ligase.

The initial data generated with this reaction method used T4 DNA ligase for proof of concept. In **Figure 4.3.6E,** hydrolysis of the excess complementary strand was mediated by the ssDNA 3' to 5' exonuclease activity of φ29 polymerase. This proceeds until φ29 recognises the PDP as a template for extension, as depicted **Figure 4.3.6F**. In **Figure 4.3.6G**, φ29 synthesises new DNA, templated by the PDP. When synthesis around the PDP reaches the double stranded region of the target template DNA, synthesis continues around the PDP, and the original target DNA is displaced. This is mediated by the strong 5' to 3' strand displacement activity φ29. Synthesis continues around the PDP for as long as the reaction is allowed to proceed.

For each revolution of the PDP, one ssDNA complement is produced. Interspaced between each repeat of the target SNV, the PDP backbone is also replicated. This provides a known ssDNA sequence, to which fluorescent probes are hybridised in downstream detection. The single stranded DNA concatemer is extended to many thousands of tandem repeats and collapses into what is known as a DNA 'blob' or rolling circle product (RCP) [282, 290].

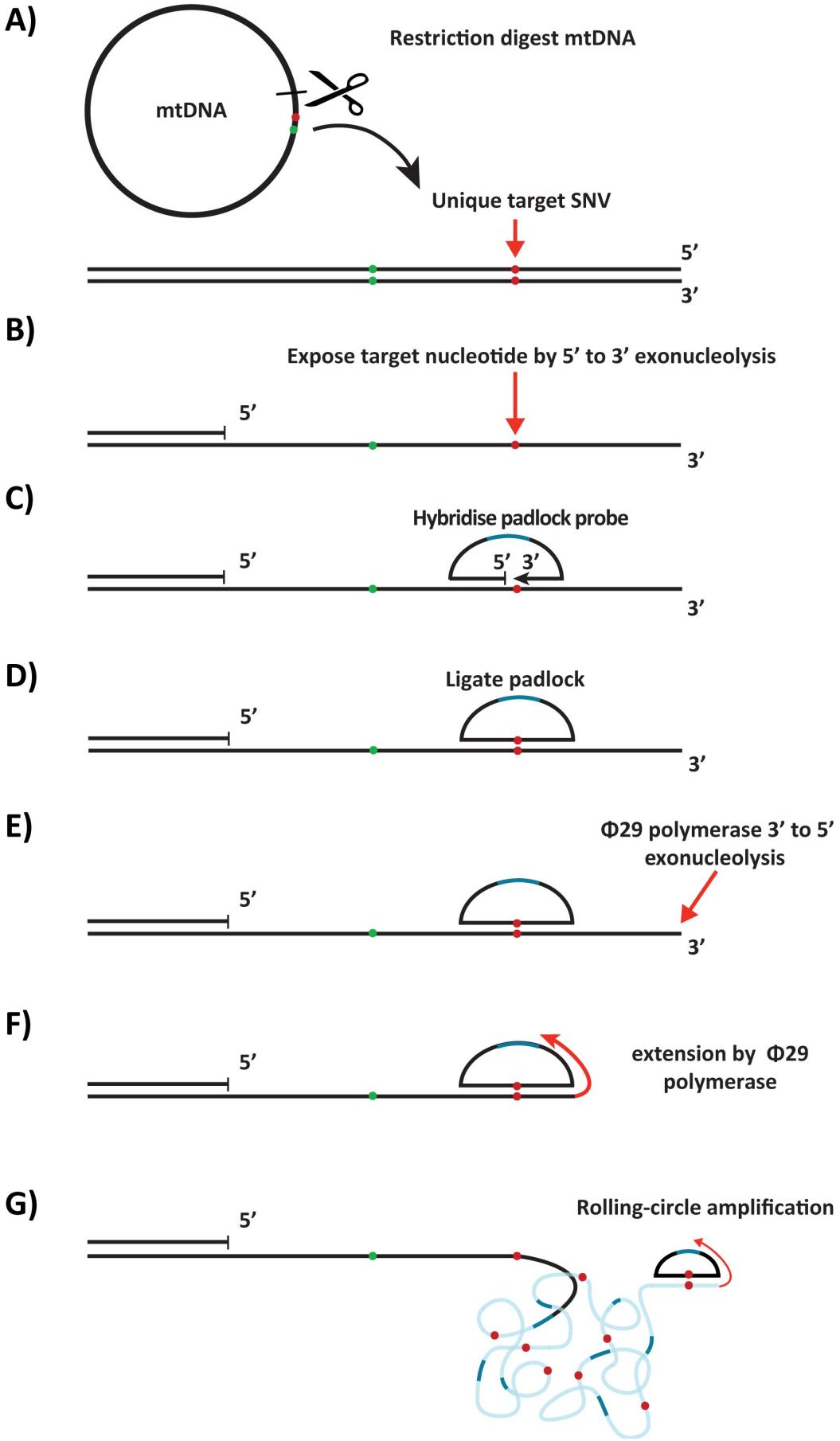
A)
Restriction digest mtDNA
mtDNA
Unique target SNV
5'
3'
B)
Expose target nucleotide by 5' to 3' exonucleolysis
5'
3'
C)
Hybridise padlock probe
5'
5' 3'
3'
D)
Ligate padlock
5'
3'
E)
Φ29 polymerase 3' to 5' exonucleolysis
5'
3'
F)
5'
extension by Φ29 polymerase
G)
5'
Rolling-circle amplification

Figure 4.3.6. Schematic of fragment preparation and target-primed RCA of mouse mtDNA_9461 or 9348

(A) Restriction digest of mtDNA releases the target fragment which contains the target SNVs (red and green circles). **(B)** 5' to 3' exonucleolysis is carried out using T7 exonuclease**. (C)** A PDP is hybridised to the exposed target SNV. **(D)** The 5' phosphorylated end of the PDP is ligated to the 3' end by DNA ligase. **(F)** Φ29 polymerase removes excess ssDNA by exonucleolysis and extends the target fragment. **(G)** A single stranded DNA concatemer is synthesised by polymerase activity. The target SNV (red circle) is replicated alongside the complement of the PDP as a repeat sequence, until reaction termination. The newly synthesised ssDNA (blue) contains multiple repeats inclusive of the target SNV. Figure adapted from Larsson et al. 2004 with permissions.

For initial RCA experiments, gap-PDPs were designed to hybridise 4 bases upstream and 3 bases downstream of each target SNV. Each gap-PDP carries a unique backbone sequence. As depicted in **Figure 4.3.7A**, the first gap-PDP (red backbone) was designed to hybridise and ligate correctly at mtDNA_9461 in BALB/CJ mtDNA, but not to the C57B/6J template. The second gap-PDP (blue backbone) was designed to hybridise at mtDNA_9348 and would ligate with mtDNA template from C57B/6J mice, but not BALB/CJ. To enhance selectivity of the ligations, 6 base-pair hexamers were designed to span the target SNVs, the gap between homologous PDP ends. At SNV mtDNA_9348 in **Figure 4.3.7B,** a phosphorylated hexamer with sequence complementary to C57B/6J was designed alongside a non-phosphorylated hexamer complementary to BALB/CJ. At Site mtDNA_9461 in **Figure 4.3.7C**, a phosphorylated hexamer with a sequence complementary to BALB/CJ was designed alongside a non-phosphorylated hexamer complementary to C57B/6J. Only perfectly matched, phosphorylated hexamers ligate successfully, which results in a selective circularisation of the correct gap-PDP at the target SNV. The finalised conditions developed for these reactions are presented in section **2.19.4** of this thesis.

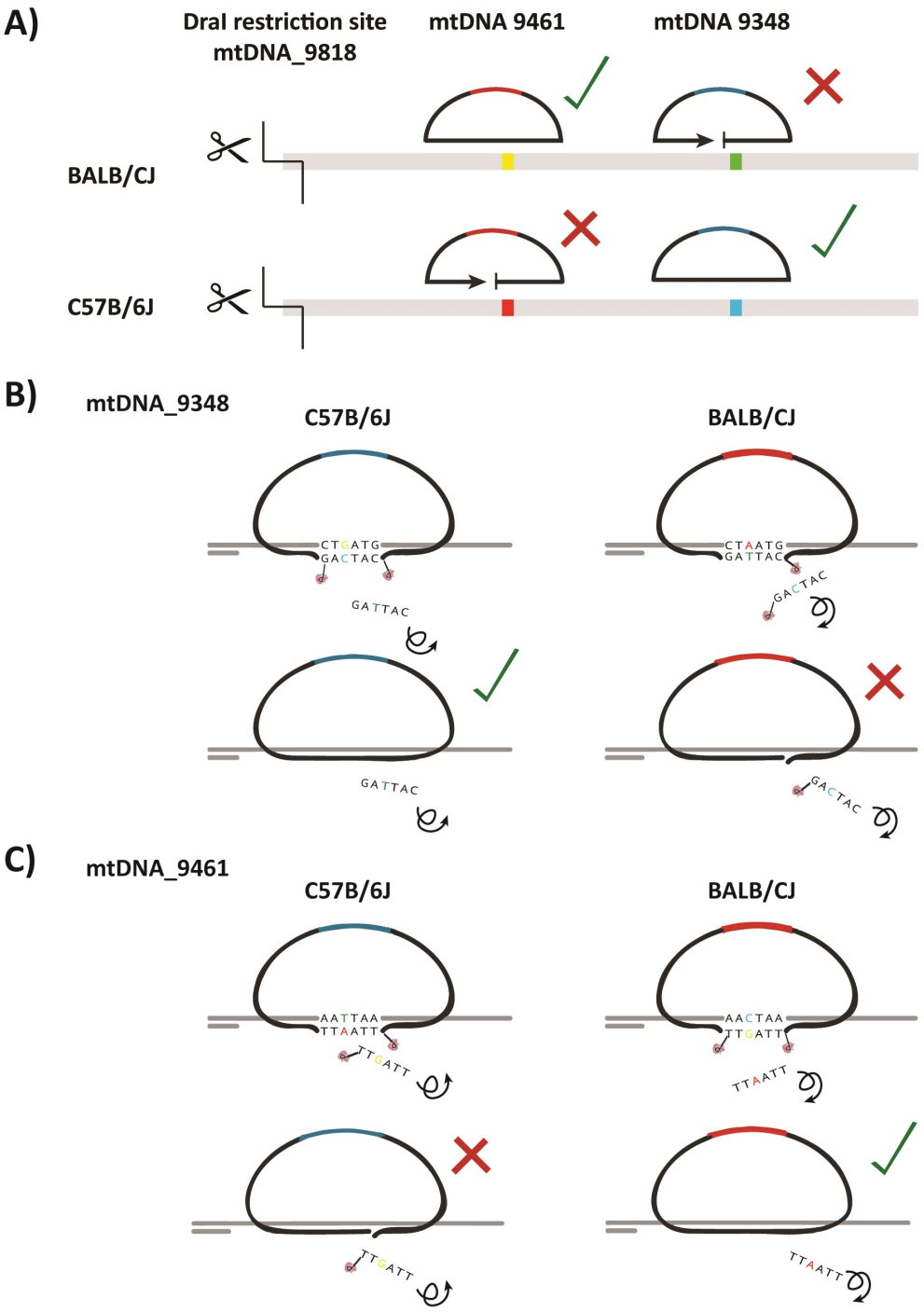

Figure 4.3.7. Molecular design schematic for target primed RCA by gap-fill ligation of mouse mtDNA_9348C and mtDNA_9461G

Unique PDPs were designed to simultaneously target two independent SNVs on a DraI digested mtDNA fragment. **(A)** The first PDP (red) was designed to ligate successfully at mtDNA_9461 on a BALB/CJ template but not C57B/6J. A second PDP (blue) was designed to ligate successfully at mtDNA_9348C on a C57B/6J template but not BALB/CJ. **(B)** For site mtDNA_9348, a phosphorylated hexamer with sequence complementary to C57B/6J was designed alongside a non-phosphorylated hexamer complementary to BALB/CJ. **(C)** For site mtDNA_9461, a phosphorylated hexamer with a sequence complementary to BALB/CJ was designed alongside a non-phosphorylated hexamer complementary to C57B/6J.

4.3.6 Target-primed RCA by gap-fill ligation at mtDNA_9461 produced RCPs at low efficiency

To evaluate the gap-fill RCA design, initial reactions targeted to mtDNA_9461 were performed on the BMSC cell line, as described by Mignardi et al. [289]. These experiments sought to visualise the mtDNA_9461 SNP *in situ*, to prove this approach would enable detection of transferred mtDNA in future co-culture experiments. Presented in **Figure 4.3.8** are representative images from these attempts. Punctate red signals approximately 1 µm are seen in close proximity to the nuclei in these fields. These correspond to ATTO647 conjugated fluorescent probes bound to single RCPs; the molecular design was capable of producing successful reactions. Unfortunately, very few products were formed, which indicated a low efficiency of detection. By acquiring images of the cells under differential interference contrast (DIC) and of the nuclear staining by DAPI, it was possible to examine the macromorphology of the samples. In **Figure 4.3.8A**, an example DIC image channel from this experiment revealed significant deterioration of the cells. While the perinuclear area appears intact on a macro-scale, the periphery of the cells appear warped and small fragments of membrane are visible on the slide. Likewise, some DAPI stained nuclei appeared unusual in shape. Together, these observations suggested that permabilisation of the fixed cells by pepsin digest of 0.01 % pepsin/0.1 M HCL for 90 s at 37 °C was too harsh and the cells have become degraded. To test this, reactions were performed with a reduced pepsin digest time and the results represented in **Figure 4.3.8B.** With a shorter digest of 25 seconds, the DIC image revealed an improvement to cell morphology and the integrity of membranes. Some folds or tears in the membranes were visible, which suggested that the cells were still highly digested. In this field, the DAPI channel revealed nuclei which have a smoother envelope than those digested for a full 90 seconds. While these digestion conditions appeared to improve macro-morphology, very few RCPs were visible. This suggested that pepsin digestion conditions likely caused loss of target molecules from the *in situ* environment for RCA; mtDNA may simply float away when protein elements are digested.

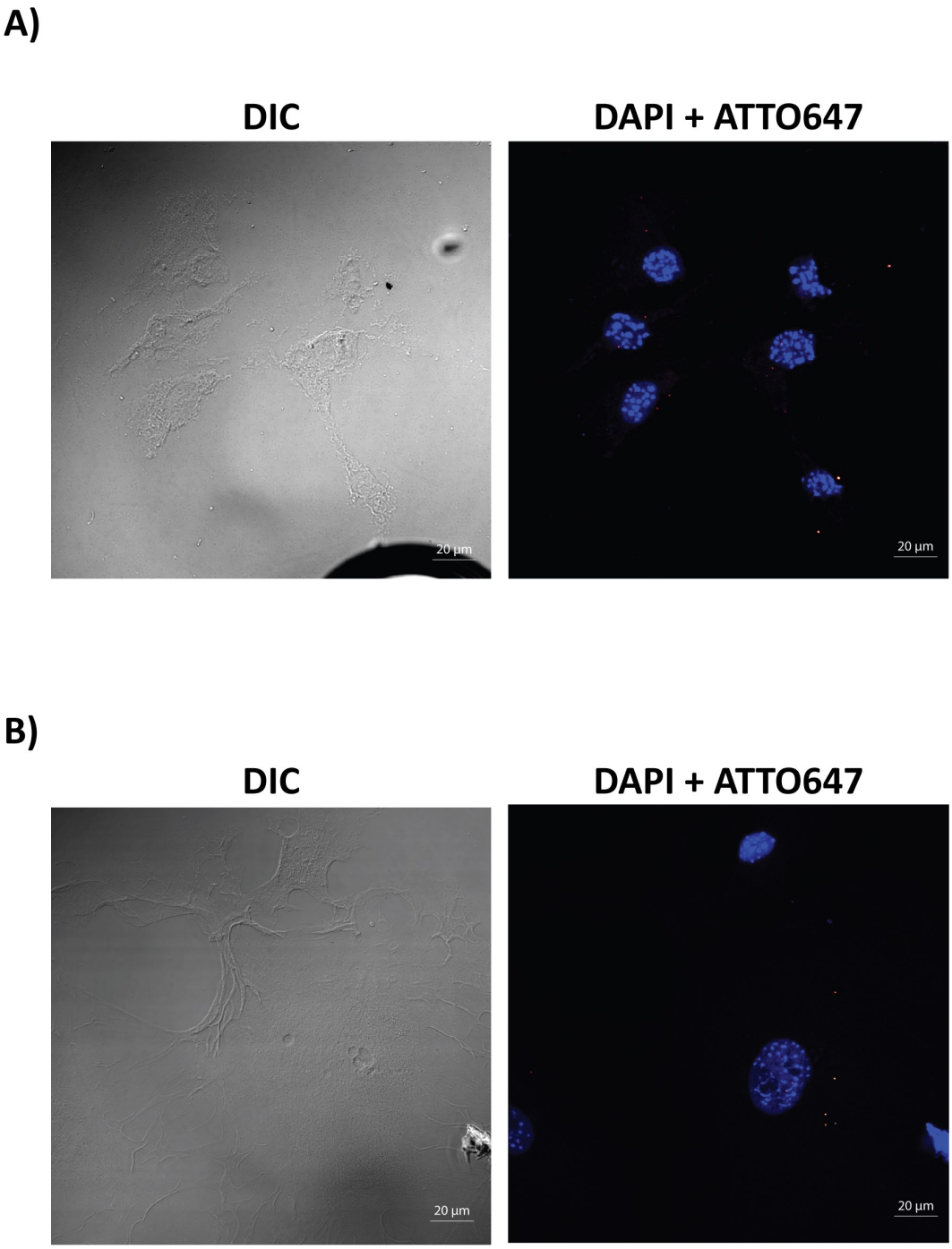

Figure 4.3.8. Early attempts at target primed *in situ* RCA by gap-fill ligation produced products for mtDNA_9461 in BMSC cells at low efficiency
Representative image fields of *In situ* target primed gap-fill ligation reactions targeted to mtDNA_9461 in mouse BMSC cells. **(A)** Over-digested cells by 90 seconds in 0.01 % pepsin-HCL treatment. **(B)** BMSC cells digested in 0.01 % pepsin-HCL for 25 seconds. Images were collected by LSCM at 600 x magnification. DAPI = blue, ATTO647 RCP at mtDNA_9461 = red, DIC = grey.

Experiments were performed to better understand how pepsin digest affected cell morphology, with reduced pepsin concentration and slightly shorter digest time of 45 s. The eGFP-astrocytes were selected to perform a titration of pepsin concentrations, for their more consistent morphology than BSMC cells. Representative phase contract image fields of these results are presented in **Figure 4.3.9**. With no digest, the eGFP-astrocytes display a fibroblast-like morphology, with many cellular projections. At concentrations of 0.0125, 0.025, 0.05 and 0.1 μg/mL pepsin, no obvious visual change in morphology occurred when compared to undigested control. At 0.25 μg/mL, small cell residues appear to have detached from the glass surface. These are seen as small dark/black particulate matter. At 0.5 μg/mL, the smallest cells appeared to lose edge definition. At 1 μg/mL; the concentration suggested in the related literature; a large change is obvious in the morphology of the cells. The smallest cells are detached and have likely floated away from the glass surface, while the larger cells show significant degradation of the cell membrane. At 5 μg/mL, the vast majority of cells have detached; only the remnants of nuclei appear to remain.

From these results, 0.1 μg/mL pepsin with a 45 s digest time at 37 °C was selected for all further experiments. It was presumed that in these conditions, enzymatic access to mtDNA would be improved without major loss of cell morphology or target molecules [284].

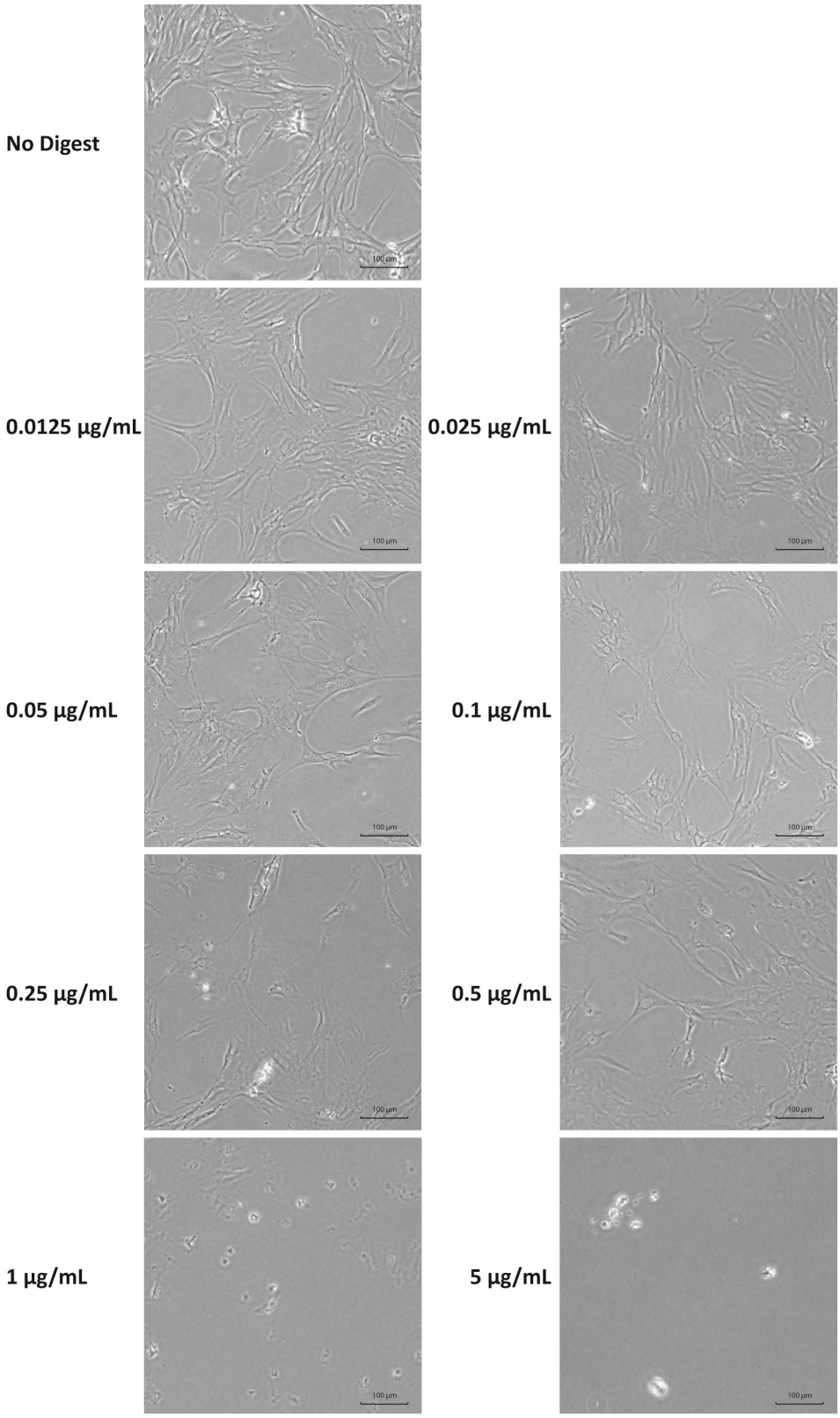

Figure 4.3.9. Optimisation of pepsin digest conditions in RCA sample preparation
Representative image fields taken of eGFP-astrocytes digested in varied concentrations of pepsin/0.1M HCL for 45 seconds. Phase contrast Images were collected by light microscope at 100 x magnification with a constant 15.4 ms exposure for all images.

Inclusion of a cytoplasmic marker would be valuable to allow identification of 'donor' or 'recipient' cells in co-cultures, independent of their mitochondrial genotype. Cytosolic and mitochondrial fluorescent proteins were rendered completely non-fluorescent upon denaturation by ethanol fixation. A suitable marker would need to persist through multiple days in co-culture and remain fluorescent with ethanol fixation. As described for mitochondrial dyes in chapter 3, it was essential that any marker would also remain confined to a directly labelled cell population. A leaky or transferrable label would cause confusion around cell identity in an IMT co-culture model and render experimental results uninterpretable.

The amine reactive carboxyfluorescein succinimidyl ester (CFSE) was identified as a candidate dye that would meet these requirements. CFSE becomes covalently bound to protein upon contact and would be well retained in the extended co-cultures required for IMT models. CFSE is stable in ethanol, so would remain fluorescent and bound to protein in target cells with ethanol fixation. Spectral variants of CFSE are available as the proprietary CellTrace™ series, which would enable flexibility in colour combinations for RCA experiments.

To test the retention properties of CFSE, WI-38 cells were stained and placed into culture. After 24 hours, medium conditioned by these cells was harvested, passed through a 1.2 µm syringe to remove cell debris and delivered to an unstained WI-38 culture. The cells were cultured for a further 24 hours before fluorescence was examined.

As depicted in **Figure 4.3.10A** after 48 h, directly stained cells demonstrate bright, green fluorescence. As expected for **Figure 4.3.10B**, unstained control cells lack appreciable auto-fluorescence. In **Figure 4.3.10C,** the WI-38 cells cultured in medium conditioned for 24 h by directly stained cells did not demonstrate appreciable green fluorescence. These cells appear similarly to the unstained control. These results provided confidence that CFSE and derivative dyes would not transfer between cell populations directly in IMT co-culture models.

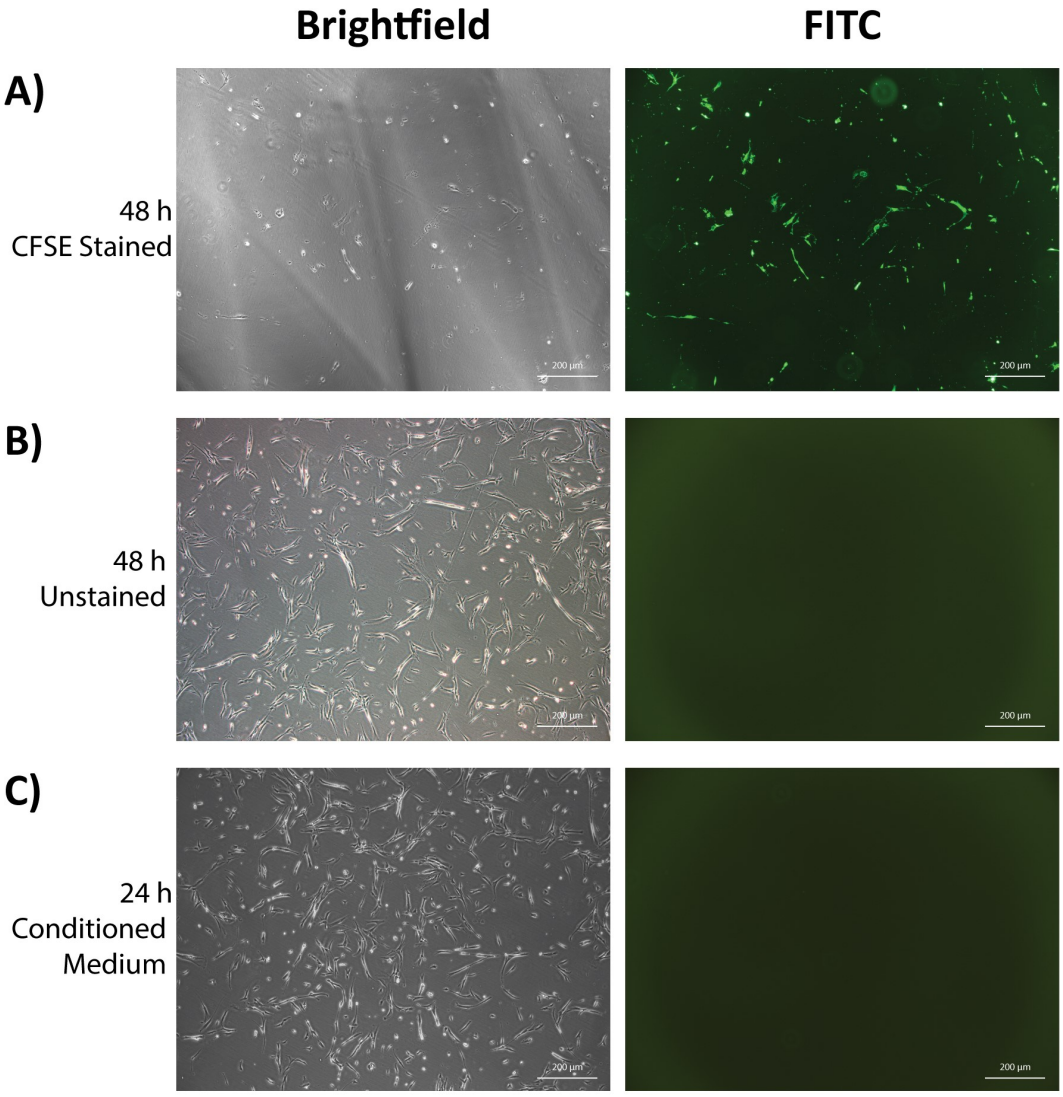

Figure 4.3.10. Medium conditioned by CFSE stained cells does not contain sufficient free dye to fluorescently label unstained cells after 24 h
Representative image fields of WI-38 cells stained with CFSE. **(A)** Conditioned medium was collected from directly stained cells after 24 h. After a further 24 h, the background fluorescence of unstained cells **(B)** and cells cultured in the conditioned medium collected from stained WI-38 **(C)** were assessed by fluorescence microscopy. Images were collected at 50 x magnification, with a constant FITC channel exposure of 125 ms for all images. CFSE = green.

In combination with an optimised pepsin digest time, a minor change was made to the enzymatic preparation of target mtDNA fragments. Target primed RCA relies on the 3' to 5' exonuclease activity of φ29 polymerase [291] to remove all ssDNA from the initial restriction fragment site, to the point of PDP hybridisation. This is typically a corrective function of φ29 in DNA synthesis. By producing an mtDNA fragment with a shorter 3' ssDNA region, it was hypothesised that RCA reaction efficiency could be improved [284].

In **Figure 4.3.11A**, a NdeI restriction sequence was identified in the target mtDNA region. Digestion at this site would reduce the 3' ssDNA region created by 5' exonucleolysis by 253 nucleotides. In **Figure 4.3.11B**, RCA reactions were performed on overnight cultures of BMSC cells after fragment preparation with NdeI. In these experiments, the combination of optimised pepsin digest and the reduced 5' exonuclease activity required of φ29 polymerase resulted in many more RCPs, when compared to experiments in **Figure 4.3.8.**

With these improvements in place, attempts were made to generate RCPs from the mtDNA_9341 locus in C57-eGFP-astrocytes. Depicted in **Figure 4.3.11C**, multiple attempts to produce RCPs at this locus were not successful with this reaction design. Signal can be seen in what appear to be the mitochondria, however it is not characteristic of RCPs in shape or intensity. This is likely background signal from naturally fluorescent biomolecules such as NADH or NADPH [292].

In experiments which examined the effect of fragment length on RCA efficiency, Larsson et al. [284] determined that reactions were approximately half as efficient with a 130 base 3 prime ssDNA region when the PDP was hybridised immediately adjacent to the restriction site. In mouse mtDNA fragmentation by NdeI, removal of 246 bases by T7 exonuclease is required to reach the downstream end of the mtDNA_9348 PDP hybridisation site. Similarly, the NdeI digest site is 200 bases upstream of the PDP hybridisation site. This combination was a likely cause for failure of reactions targeted to mtDNA_9348 with this molecular design.

Figure 4.3.11. Alternative digest of mtDNA by NdeI improves RCA reaction efficiency for mtDNA_9461 but not mtDNA_9348
Representative image fields from *in situ* RCA reactions performed with a NdeI restriction digest in mouse BMSC cells or C57-eGFP-astrocytes. **(A)** NdeI digest of mouse mtDNA produces a fragment 253 base pairs closer to the mtDNA_9461 and 9348 target sites. **(B)** *In situ* RCA targeted to mtDNA_9461 in BMSC cells after NdeI digest. **(C)** *In situ* RCA targeted toward mtDNA_9348 in CFSE stained C57-eGFP-astrocytes. Images were collected by LSCM at 600 x magnification. ATTO647 RCP at mtDNA_9461 = red, CFSE = green, AF405 RCP at mtDNA_9348 = blue, DIC = grey.

A)

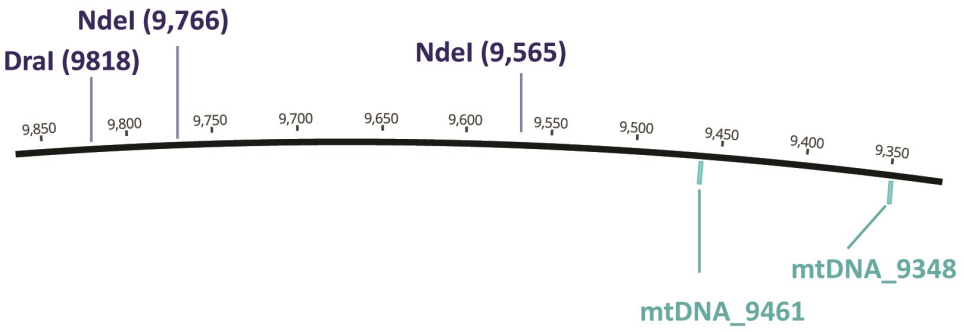
NdeI (9,766)
DraI (9818)
NdeI (9,565)
9,850
9,800
9,750
9,700
9,650
9,600
9,550
9,500
9,450
9,400
9,350
mtDNA_9348
mtDNA_9461

B)

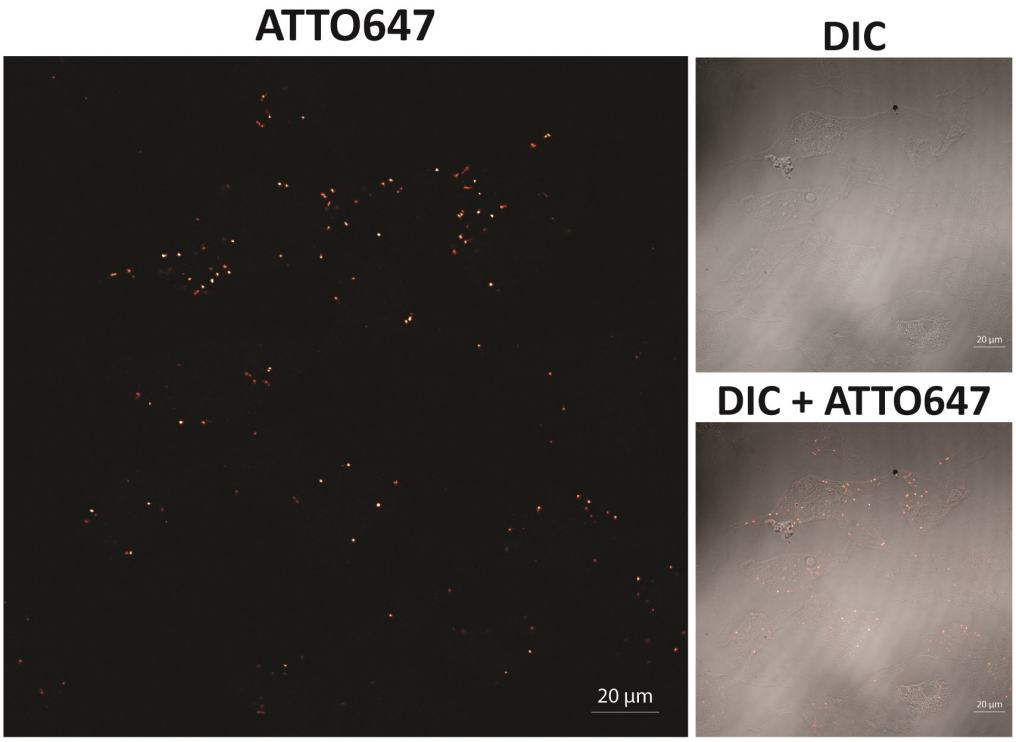
ATTO647
DIC
DIC + ATTO647
20 µm

C)

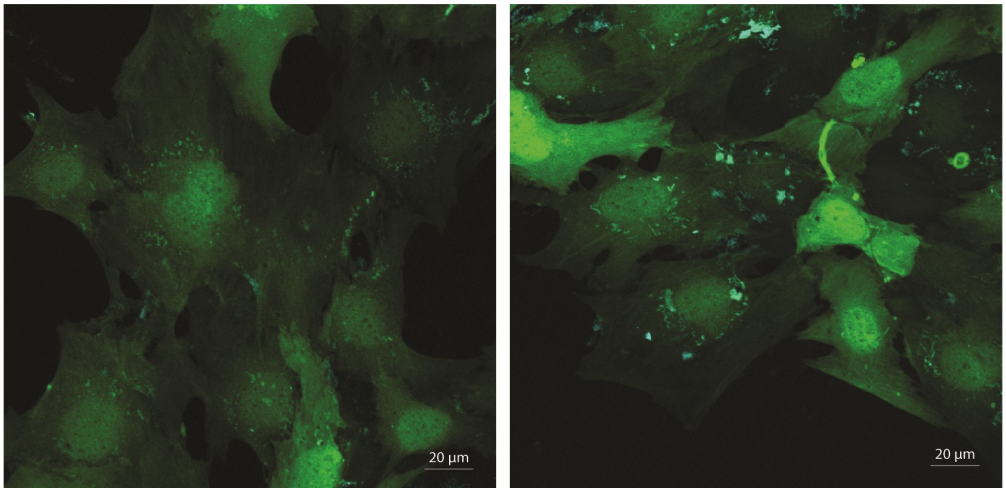
20 µm
20 µm

NdeI digest improved reaction efficiency targeted to mtDNA_9461 relative to DraI digest. This represented an important development in the strategy, however I was not convinced this reaction design would see success when applied to IMT experiments. In addition, the 16299 base pair mtDNA molecule is digested into 9 or 5 restriction fragments by DraI or NdeI respectively. Smaller fragments are more likely to be displaced from the intracellular environment and lost to detection in *in situ* RCA. The initial reaction design provided insight into a number of considerations for an improved, secondary reaction design.

4.3.7 Target primed RCA with high fidelity ligases – assay design and development for detection of mouse SNVs mtDNA_9461 and 9348

To successfully use a molecular method to investigate IMT, reaction selectivity was considered of principle importance. Results with the initial RCA reaction design as those described in **Figure 4.3.8** and **Figure 4.3.11** demonstrated that reaction efficiency was a higher priority than first considered. Mignardi et al. describe highly selective target primed RCA by gap-fill ligation [289], however, the authors determined that gap-PDPs reduced reaction efficiency by approximately 20 % compared to traditional PDPs. I decided that traditional PDPs in combination with a redesigned fragmentation strategy would improve detection of the target mtDNA SNVs.

A BsaBI restriction sequence identified (**Figure 4.3.12A**) at mtDNA_9383 would introduce a blunt ended 5' fragment in mouse mtDNA. This site is located in between the target SNVs. In addition, this enzyme has no other recognition sequences in mouse mtDNA, so the molecule is simply linearised into a single fragment upon digestion. This was hypothesised to be advantageous in the new reaction design; the full length 16,299 bp mtDNA will be less susceptible to displacement and loss from detection by RCA. In addition, the restriction site is positioned just 36 bp upstream of mtDNA_9348 and 78 bp downstream of 9461. T7 exonuclease treatment exposes the target SNVs in each 3' strand more efficiently than compared to the initial reaction design. Padlock probes are hybridised simultaneously to each end of the fragment (**Figure 4.3.12B**), targeted to the exposed SNV in opposite strands of the mtDNA. In this configuration, the number of base pairs which require removal by exonucleolysis to reach the double stranded region of PDP hybridisation is reduced to just 55 bp and 15 bp for mtDNA_9461 and 9348 respectively. This reduces the requirement of 3' ssDNA exonucleolysis by φ29 polymerase significantly compared to the initial reaction design.

The secondary reaction design also relied on a single ligation junction, rather than two as used with gap-PDPs. For this reason, the strand orientation to be targeted by the PDPs was also a significant consideration. Lohman et al. [286] produced an extensive profile for

different DNA ligase species across every possible combination of template/substrate ligation junction. The results for two of these ligases; Ampligase™ and Taq HIFI ligase™, are reproduced in **Figure 4.3.12C**. Ampligase™ is the enzyme of choice for high fidelity ligations in PDP literature. Taq HIFI ligase™ was released commercially at the time these molecular designs were produced. Based on the results of Lohman et al. with Ampligase™, a <10 % ligation activity was detected for one of the 'off-target' ligation junctions equivalent to those created at mtDNA_9461 and 9348 in either strand orientation. While low, this would result in false positive ligations that if possible, should be avoided to improve analysis of IMT experiments. Taq HIFI ligase™ did not produce detectable ligation activity for these ligation junctions. This suggested I would achieve a higher reaction selectivity with Taq HIFI ligase™, however as a new product, no literature had been published prior which demonstrated its use with PDPs for *in situ* RCA. As such, I would need to benchmark Taq HIFI ligase™ against Ampligase™ for this application. This was required to ensure comparability between these enzymes.

The secondary reaction design made use of an additional oligonucleotide known as a compaction oligo, as described by Clausson et al. [293]. This oligonucleotide was designed to complement the newly synthesised RCA concatemer at interspaced repeats of PDP backbone complement. The purpose of this oligo is to hybridise across the tandem repeats produced in the RCA. By hybridisation of this oligo across repeats, the physical size of the RCP is compacted and thus a higher signal to noise ratio is produced at each product. The compaction oligo was designed with 3 additional 2'-O-methyl-adenosine nucleotides at the 3' end to protect the oligo from the 3' exonuclease activity of φ29 polymerase. Sequence elements of the flexible PDP backbone shared between mtDNA_9461 and 9348 PDPs were targeted, and the oligo equally able to compact RCPs generated at either locus.

The finalised conditions developed for these reactions are presented in section **2.19.5** of this thesis.

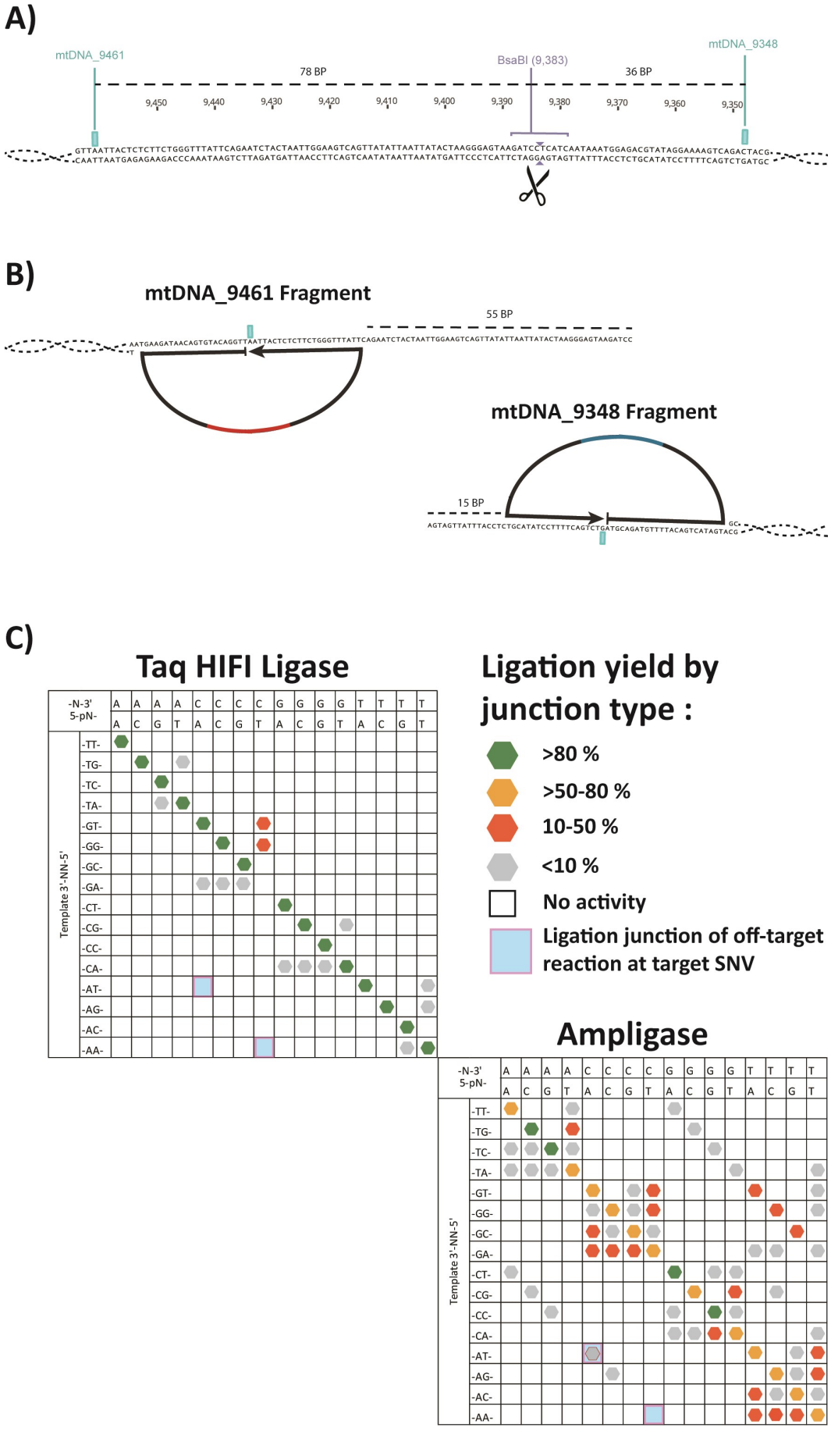
A)
mtDNA_9461
mtDNA_9348
BsaBI (9,383)
78 BP
36 BP
9,450
9,440
9,430
9,420
9,410
9,400
9,390
9,380
9,370
9,360
9,350
B)
mtDNA_9461 Fragment
55 BP
mtDNA_9348 Fragment
15 BP
C)
Taq HIFI Ligase
Ligation yield by junction type :
>80 %
>50-80 %
10-50 %
<10 %
No activity
Ligation junction of off-target reaction at target SNV
Ampligase
-N-3'
5-pN-
Template 3'-NN-5'

Figure 4.3.12. Schematic of a secondary reaction design for target primed RCA of mouse mtDNA_9348G and mtDNA_9461G

(A) A BsaBI restriction site was identified in mouse mtDNA between target SNVs mtDNA_9461 and 9348**. (B)** Both mtDNA SNVs are positioned near the fragment ends after digest, which enables hybridisation of two PDPs simultaneously, targeted to opposite strands of the mtDNA. **(C)** The ligation fidelity of ligases Taq HIFI ligase and Ampligase™ as profiled extensively by Lohman et al. [286] adapted, with permissions.

4.3.8 *In situ* single molecule genotyping with secondary target-primed RCA strategy is improved over original design

To test functionality of the secondary reaction design, 24 hour monocultures of BMSC cells were prepared on glass slides and target primed RCA reactions of mtDNA_9461G performed as described in section **2.19.5**. These experiments were performed to confirm the secondary reaction design would enable *in situ* detection of transferred mtDNA at high efficiency in future IMT co-culture experiments. In **Figure 4.3.13A**, T4 DNA ligase was used to circularise the newly designed PDP as a positive control for ligation, due to the unknown properties of Taq HIFI ligase™ in this assay. When placed under LSCM, an abundance of bright, punctate ATTO647 signals were readily apparent, characteristic of RCPs. This indicated that the reaction design targeted to mtDNA_9461G was functional. In **Figure 4.3.13B**, Taq HIFI Ligase™ based reaction also produced RCPs in abundance. Although not quantified in these experiments, the increased efficiency of these reactions design was immediately obvious when compared to the initial reaction designs (**Figure 4.3.8** and **Figure 4.3.11**). The number of RCP signals observed with both T4 and Taq HIFI ligases were estimated to be similar in number, which suggested that the performance of Taq HIFI ligase was not inhibited when used *in situ*. The density of RCPs detected in the perinuclear area was higher than in the periphery, consistent the location of mitochondrial organelles in cells [294]. In **Figure 4.3.13C**, negative control reactions were performed with the mtDNA_9461G PDP omitted. In this condition, RCP signals were not observed in across multiple image fields. Likewise, reactions carried out with no ligase present did not produce signals. Together, these results indicated the newly designed strategy could initiate an RCA reaction in cells with the target mtDNA genotype, at a higher efficiency than the original design. These reactions were both PDP and ligase dependent, indicative that the targeted loci was likely to be the correct site of RCP initiation.

Figure 4.3.13. Secondary reaction design detects mouse mtDNA_9461G from BMSC *in situ*

Representative image fields of *in situ* RCA in BMSC cells from mtDNA_9461G reactions carried out with T4 DNA ligase **(A)** or Taq HIFI ligase **(B)**. **(C)** Representative fields collected from negative control reactions with omission of either the mtDNA_9461G PDP, or Taq HIFI ligase, do not produce RCPs. Images were collected by LSCM at 600 x magnification. DAPI = blue, ATTO647 RCP at mtDNA_9461G = yellow, DIC = grey.

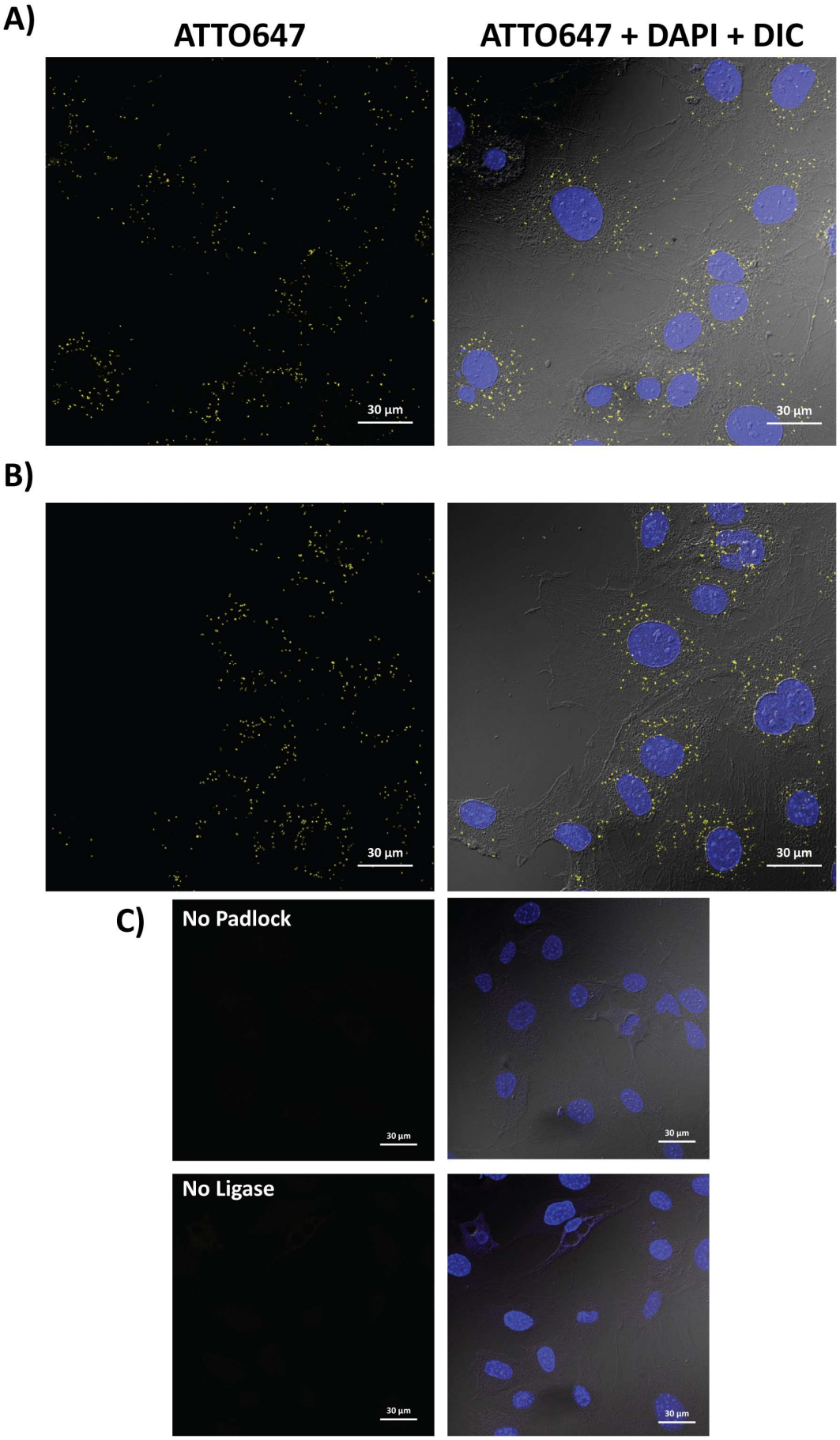
A)
ATTO647
ATTO647 + DAPI + DIC
30 µm
30 µm
B)
30 µm
30 µm
C)
No Padlock
30 µm
30 µm
No Ligase
30 µm
30 µm

With positive reactions at mtDNA_9461G in BMSC cells, the 9348G SNV was next targeted. eGFP-astrocytes were prepared on glass slides as an overnight culture and target primed RCA at mtDNA_9348G carried out as described in section **2.19.5**. With new knowledge that Taq HIFI Ligase™ was compatible with PDPs *in situ*, positive control mtDNA_9641G reactions were performed in BMSC cells in parallel. In **Figure 4.3.14A**, representative image fields from these experiments demonstrated success of this new reaction design for detection of mtDNA_9348G. eGFP-astrocyte cells produced an abundance of bright, punctate AF405 signals; dissimilar to the initial reaction design. With an unknown difference in the mtDNA copy number of BMSC or eGFP-astrocytes acknowledged, it appeared that RCPs were similar in number to those produced in **Figure 4.3.13B**. In **Figure 4.3.14B**, omission of the genotype specific PDP, or Taq HIFI Ligase™ also prevented the formation of RCPs in eGFP-astrocyte cells.

Together, the results presented in **Figure 4.3.13** and **Figure 4.3.14** represent a functional molecular approach for detection of mtDNA_9461G or 9348G in cell-types which harbour each of these variants.

Figure 4.3.14. Secondary reaction design detects mouse mtDNA_9348G in eGFP-astrocyte cells

(A) Two representative image fields of *in situ* RCA in eGFP-astrocyte cells targeted toward mtDNA_9348G and carried out with Taq HIFI ligase. **(C)** A representative field of negative control reactions with omission of either the mtDNA_9348G PDP, or Taq HIFI ligase. Images were collected by LSCM at 600 x magnification. PI = red, Alexafluor 405 RCP at mtDNA_9348G = cyan, DIC = grey.

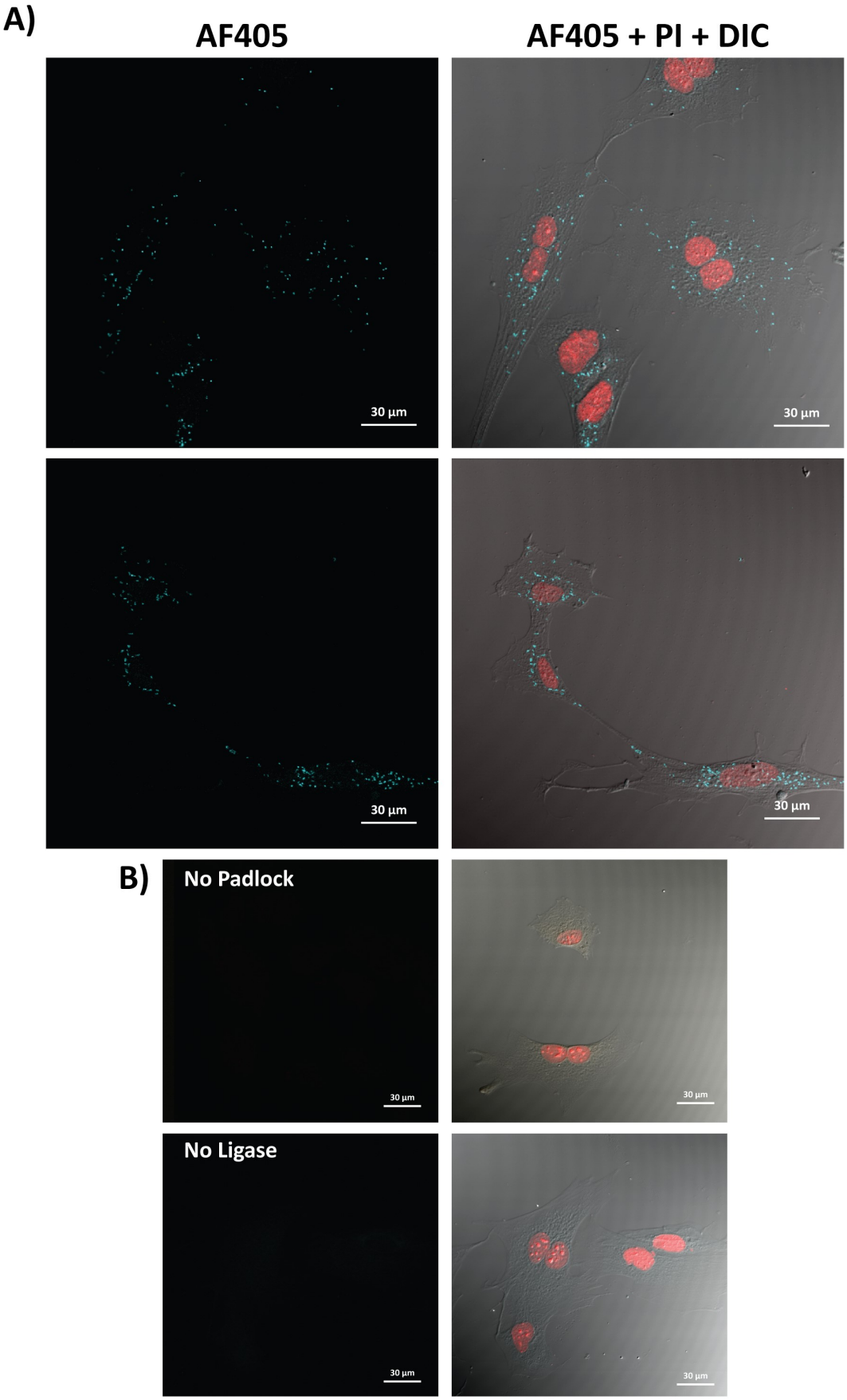
A)
AF405
AF405 + PI + DIC
30 µm
30 µm
30 µm
30 µm
B)
No Padlock
30 µm
30 µm
No Ligase
30 µm
30 µm

To detect IMT by single molecule genotyping *in situ*, the rate of false positive RCP generation needs to be calculable. In addition, the false positive rate must be lower than the biological frequency of mtDNA in IMT. A series of control reactions were performed with a single mtDNA PDP on monocultures of cells which did not contain the target SNV to evaluate the selectivity of these reactions. Positive control reactions were performed in parallel, to ensure all stages of the RCA protocol were successful. In addition, it was important to address whether RCP signals were intracellular, as opposed to surface associated.

In **Figure 4.3.15A**, randomly selected fields of BMSC cells targeted for RCA with the mtDNA_9348G PDP are presented. Without the target loci present in these cells, very few RCPs are produced. Likewise, eGFP-astrocytes presented as randomly selected fields in **Figure 4.3.15B** also produced very few RCPs when targeted with mtDNA_9461G PDP. Typically, each nucleus of either cell type presented with 1 or fewer RCP signals associated with the cytoplasm seen by DIC. For both PDPs, these signals likely correspond to imperfect ligation events or natural mtDNA mutations. For the purposes of this research, both are to be considered false positive detections.

In **Figure 4.3.15C**, an X-Y and Z-Y planar projection is presented of positive RCP detections at mtDNA_9461G in BMSC cells. The signal from the RCPs is both bright and discrete. By acquisition of stacked images through the Z plane, the intracellular nature of the RCPs is clearly demonstrated by localisation within the cytoplasm. The numerous washes/buffer exchanges required to produce these RCPs *in situ* is likely to remove any cell surface associated vesicles. For this reason, any free mtDNAs or those associated with a vesicle are likely to be excluded from detection. These results indicate that for the purpose of quantitative imaging, it was appropriate to assume that RCP signals detected in single plane images would correspond to intracellular mtDNAs.

Figure 4.3.15. Secondary design *in situ* RCA reactions targeted to mtDNA_9461G and mtDNA_9348G are selective and produce intracellular signals
The selectivity of *in situ* RCA reactions was assessed qualitatively by performing reactions on cells which did not carry the target genotype, alongside the reactions performed in **Figure 4.3.16**. **(A)** Six representative fields of *in situ* RCA performed on a BMSC monoculture with the C57-eGFP-astrocyte genotype-selective PDP for mtDNA_9348G. **(B)** Six representative fields of *in situ* RCA performed on a C57-eGFP-astrocyte monoculture with the BMSC genotype-selective PDP for mtDNA_9461G. White circles have been superimposed around any non-specific RCPs present. **(C)** A Z-stack image with 150 µm step-size of CFSE stained BMSC cells targeted with mtDNA_9461G. The image is presented in both X-Y and Z-Y views to demonstrate intracellular RCPs. Images were collected by LSCM at 600 x magnification. PI = red, CFSE = magenta, DAPI = blue, RCPs = yellow, DIC = grey.

A)

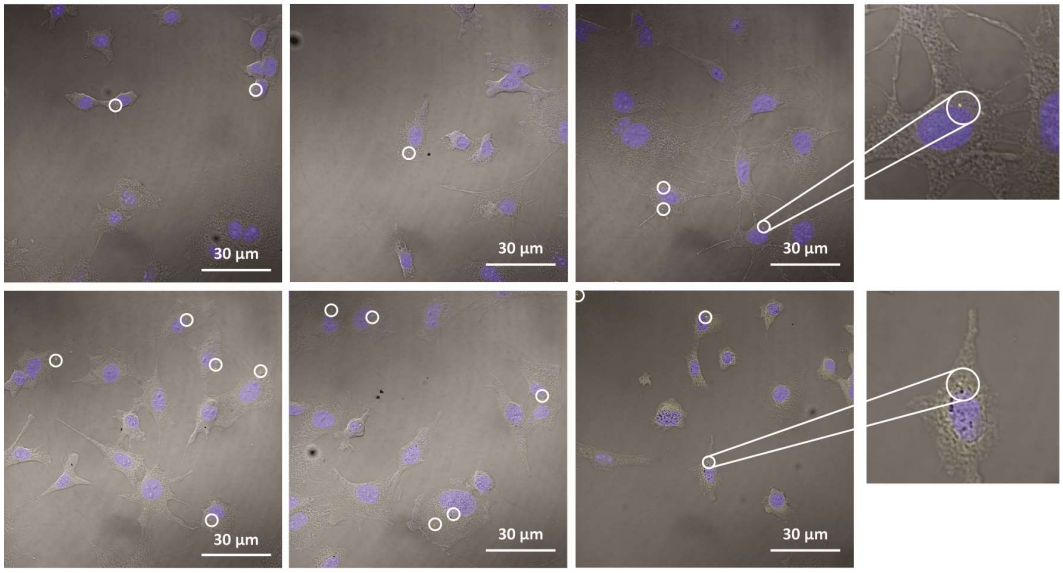
30 µm
30 µm
30 µm
30 µm
30 µm
30 µm

B)

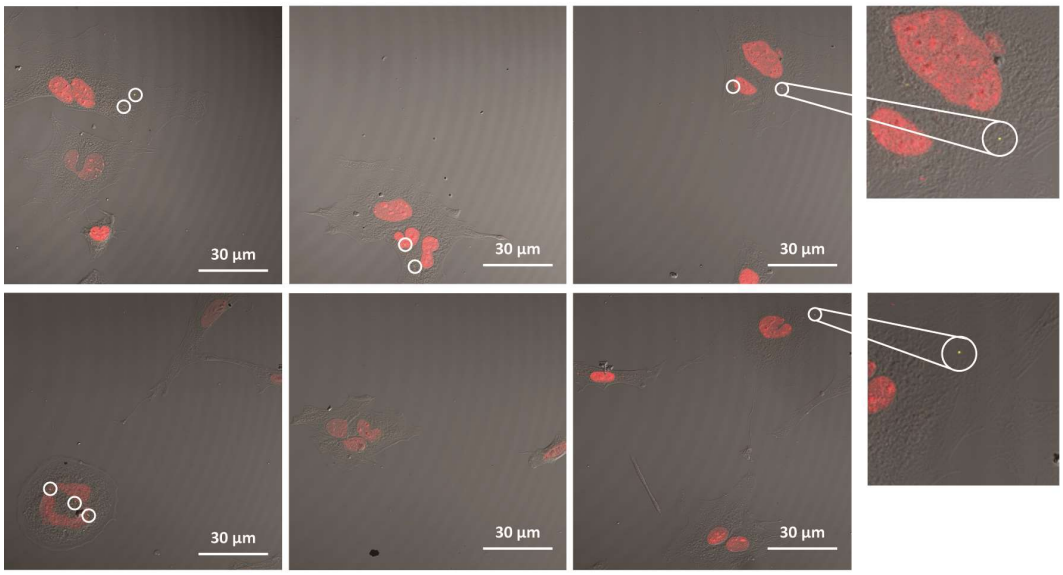
30 µm
30 µm
30 µm
30 µm
30 µm
30 µm

C)

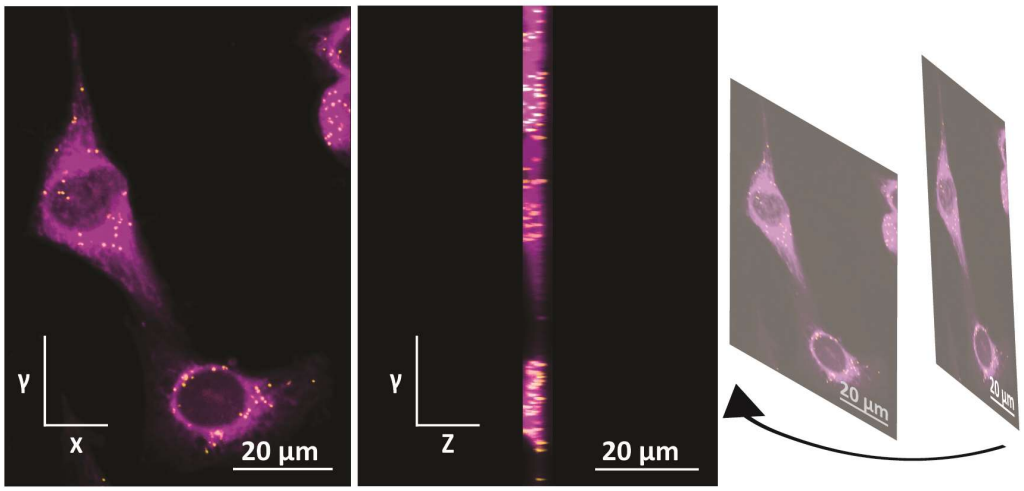
Y
X
20 µm
Y
Z
20 µm
20 µm
20 µm

4.3.9 Single-molecule genotyping of mtDNA in co-culture models

With a newfound means to identify mtDNA genotypes of cells *in situ*, a logical progression was to address if it were possible to identify cell types in co-culture by *in situ* RCA, inferred from the known mitochondrial genotypes. To address this, RCA reactions with mtDNA_9461G and/or 9348G PDPs were performed on overnight co-cultures of BMSC and eGFP-astrocytes. Represented by cells in **Figure 4.3.16A**, CFSE labelled eGFP-astrocytes were cultured overnight with BMSC cells which were then targeted with the mtDNA_9461G PDP alone. In this representative field, two BMSC cells and three CFSE-labelled eGFP-astrocyte cells are clearly distinguishable. The bright, green CFSE stain clearly isolates the eGFP-astrocyte cell boundaries from the unlabelled membrane of the BMSC cells. Scattered across the unlabelled membrane areas (visible in the DIC) are bright, punctate ATTO647 RCPs produced in the BMSC cells. With the DIC channel removed, it was clear that there were no ATTO647 signals associated with the CFSE stained area in this particular image. This was further clarified with display of the ATTO647 channel only.

Figure 4.3.16. Secondary RCA reaction design enables multiplex reactions at mtDNA_9461G and mtDNA_9348G
Representative images of *in situ* RCA performed on twenty four hour co-cultures of BMSC cells and eGFP-astrocytes. **(A)** CFSE stained eGFP-astrocytes were cultured with BMSC cells and *in situ* RCA performed as a single-plex reaction targeted towards mtDNA_9461G. **(B)** *In situ* RCA with probes targeted to both mtDNA_9461G and mtDNA_9348G performed simultaneously in a BMSC/eGFP-astrocyte co-culture. **(C)** A subsection of the total reaction surface area generated by *in situ* RCA, composed of tiled image fields. Images were collected by LSCM at 600 x magnification. PI = red, CFSE = green, DAPI = blue, Alexafluor 405 RCP at mtDNA_9348G = cyan, ATTO647 RCP at mtDNA_9461G = yellow, DIC = grey.

A)

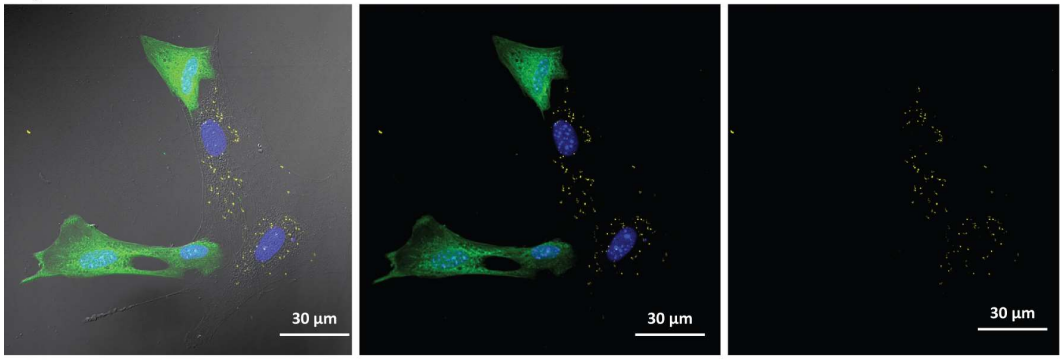

B)

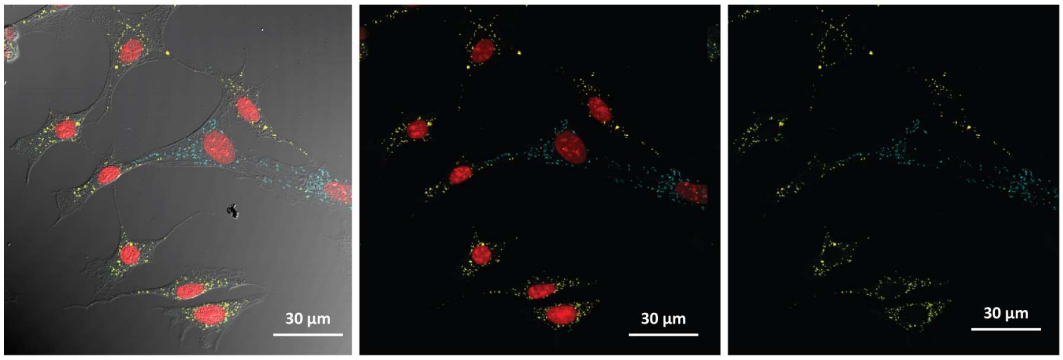

C)

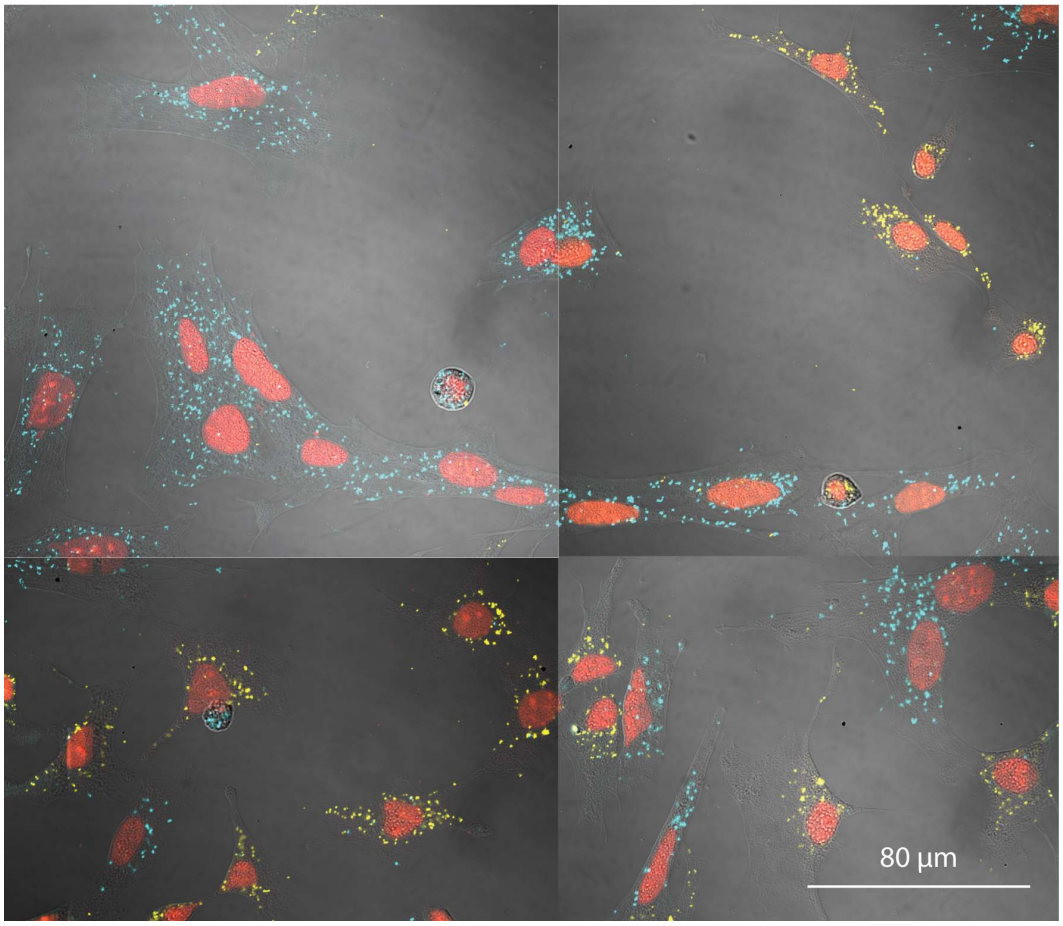

RCA reactions on co-cultures of these cell types were performed with both genotype selective PDPs, to determine whether this reaction could be performed in multiplex. In the absence of IMT, eGFP-astrocytes were expected to generate AF405 RCPs from mtDNA_9348G, while BMSCs would generate ATTO647 signals.

In **Figure 4.3.16B**, a representative field from these experiments is presented. The majority of the cell bodies of 7 BMSC cells and 2 eGFP-astrocytes are clearly identified based on the predominant mtDNA genotype alone. A low count of RCP signals which do not match the majority genotype are present in some, but not all cells. These could be false positive detections as defined in **Figure 4.3.15,** or genuine mtDNA transfer events. These experiments showed conclusively that this molecular design permitted use of PDPs targeted to both mtDNA loci simultaneously. By detection of both loci simultaneously in cells of varied mtDNA genotypes, confidence was established that these reactions are templated from the target mtDNA SNVs, rather than other non-specific nucleic acids.

In **Figure 4.3.16C**, multiple image fields tiled together represent how data acquisition for quantitative assessment is possible. The whole reaction area is imaged so mtDNA genotypes may be interrogated across large swathes of the co-culture. This image acquisition approach is valuable in collection of data from a sufficient number of cells.

4.3.10 High throughput single molecule genotyping of mtDNA by RCA – Image acquisition and processing

Microscopy data in published reports of IMT typically consists of a few image fields from dye or FP based IMT experiments. The total number of fields/cells examined is not likely to be reported along with these anecdotal images. From our own experience with these methods, a large number of cells need to be viewed before any signs of IMT are observed. The single molecule genotyping approach presented in this chapter enables us to progress beyond this 'hunt then present' approach and generate quantitative data on IMT. A strategy to image the target mtDNA SNVs *in situ* by high throughput confocal microscopy (HTCM) was developed, alongside an image processing pipeline. Together, these allowed mass image acquisition and analysis from *in situ* RCA experiments in this thesis.

Automated imaging HTCM comes at a cost in acquisition accuracy and overall image quality. A major challenge for instruments like the GE InCell 6500 used in this research, is autofocus and selection of the correct optical plane at high speed. To minimise this issue, adaptations to sample preparation for HTCM were required. The following adaptations were made to improve automated imaging. Represented in **Figure 4.3.17A**, the Superfrost glass slides used in cell culture were exchanged for number 1.5H, 60 x 22 mm glass coverslips. This is the optimal thickness for use with high numerical aperture objective lenses in microscopy. By moving the cells from the slide surface, to the coverslip surface, improvement was seen in image contrast and intensity. In addition this minimises artefacts such as spherical aberration. This significantly improves the HTCMs ability to autofocus correctly. Though a seemingly small change, this was critical for high throughput acquisition of quality images from *in situ* RCA. Coverslips were placed cell-side up against a glass slide, after removal from the tissue culture vessel. This was to provide reinforcement in the numerous manipulations required for the RCA protocol.

In **Figure 4.3.17B**, Secure-Seal™ chambers used to perform the RCA were exchanged for CultureWell™ silicone gaskets. This was because the adhesives on Secure-Seal™ chambers prevented removal without destruction of the delicate 170 µM glass coverslip. The CultureWell™ gaskets are flexible and do not use adhesives to seal, so could be peeled away without damage to the coverslip. Secure-Seal™ chambers used reaction ports which could be sealed for extended incubations or for those at higher temperatures. CultureWell™ gaskets simply form an open well on the glass surface. Demonstrated in **Figure 4.3.17C,** to seal these wells for various RCA reaction steps, a HybriSlip™ was used. This flexible material could be placed on or peeled away from the gasket surface as in **Figure 4.3.17D**, without detachment of the gasket from the coverslip surface.

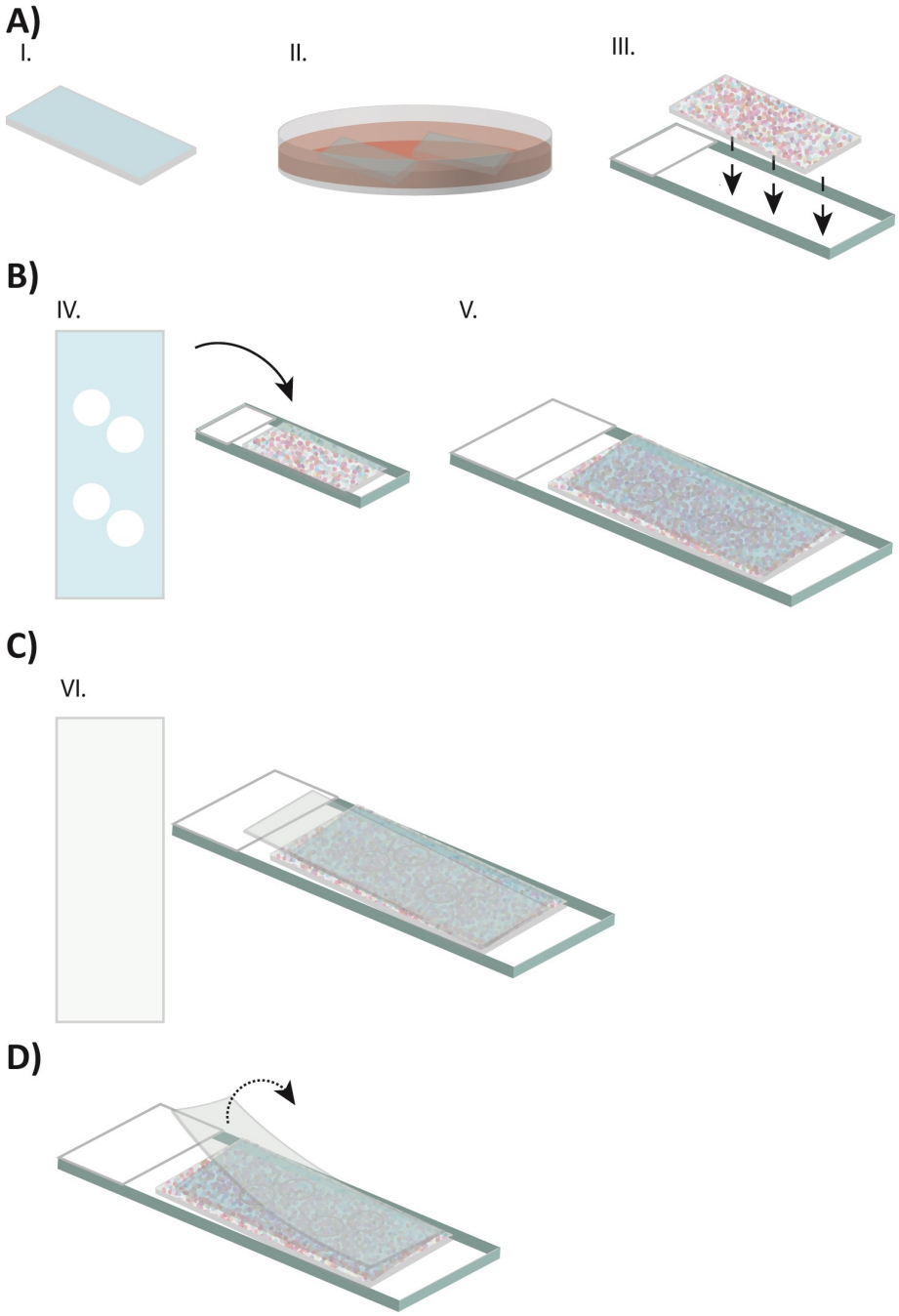

Figure 4.3.17. Schematic for adaptation of *in situ* RCA reactions to HTCM
Number 1.5 60 x 22 mm glass coverslips **(A, I.)** are placed into 10 cm dishes and seeded with cells of interest **(A, II.)** and placed into culture. **(A, III.)** Cell-covered coverslips are carefully removed from culture and immediately placed on to a glass microscope slide for reinforcement. After fixation and permeabilisation, a CultureWell™ silicone gasket **(B, IV.)** is fitted to the cell-covered surface of the coverslip **(B, V.)**. **(C, VI.)** Reactions are performed directly in the open wells, however steps which require elevated temperature or extended duration, the assembly is fitted with a flexible HybriSlip™ to seal the chambers. **(D)** The HybriSlip™ is removed for reagent exchange by peeling the flexible material away, such that the gasket/glass assembly below is not disrupted.

For any given RCA reaction imaged by HTCM in this thesis, approximately 360 fields were collected, each with 3 or 4 fluorescence channels. To extract relevant information from these, an automated image analysis pipeline was developed in the open source image processing platform, CellProfiler [295-297]. The CellProfiler master branch source code was compiled from https://github.com/CellProfiler/CellProfiler and executed in Python 2.7.

Figure 4.3.18, **Figure 4.3.19** and **Figure 4.3.20** each describe the steps taken to process the nuclear, cytoplasmic and RCP channels respectively from high throughput RCA experiments. An emphasis was placed on conservative extraction of data from the RCP and cytoplasmic channels. This was to minimise the detection of non-specific signals as objects. With this approach, a degree of true signals are likely to be lost from quantification, albeit at a lower rate than non-specific signals. It was expected that real biological effects would still be evident in data processed this way, though the effect size may be reduced. This was an acceptable limitation for unbiased analysis of the many thousands of images acquired over the course of these studies.

'Cytoplasmic segments' were identified in place of individual cells. This was due to the highly variable morphology of neural cell types, along with frequently captured images of multinucleated cells. A cytoplasmic segment typically (but not always) represents one cell.

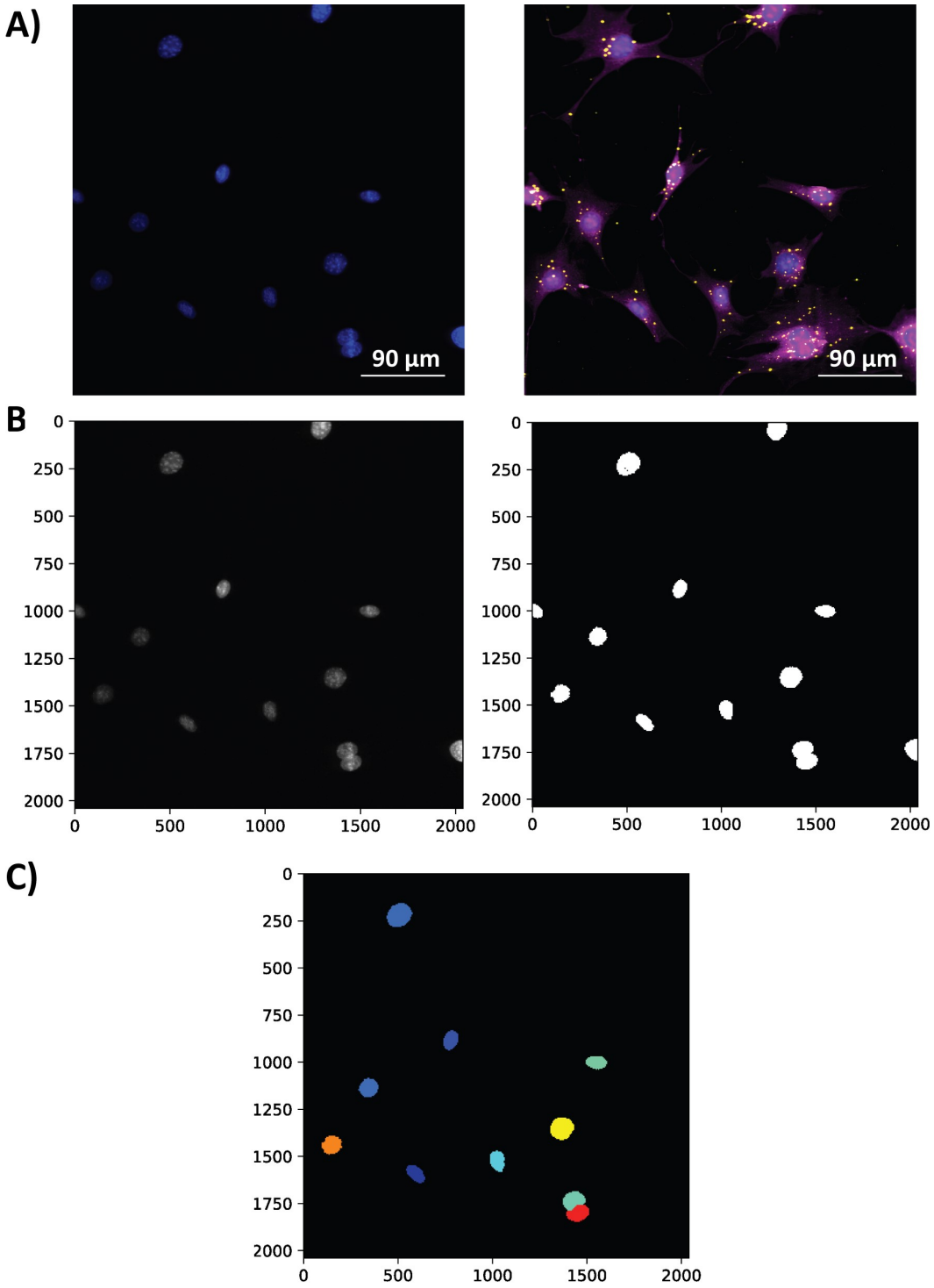

Figure 4.3.18. Image analysis strategy for the nuclear channel in HTCM
(A) A representative image field of *in situ* RCA targeted to mtDNA_9461G in BMSC cells is used to demonstrate the image analysis strategy for the nuclear channel **(left)** of multichannel high throughput RCA images **(right)** using CellProfiler. DAPI = blue, CellTrace™ Yellow = magenta, ATTO647 RCP at mtDNA_9461G = yellow. **(B)** The nuclear channel is extracted from the image set and thresholded by the Otsu method [298]**. (C)** Object identification is performed (shown as pseudo-colour representations) with nuclei detected on the edge omitted in final counts**.** Images were collected at 400 x magnification by HTCM.

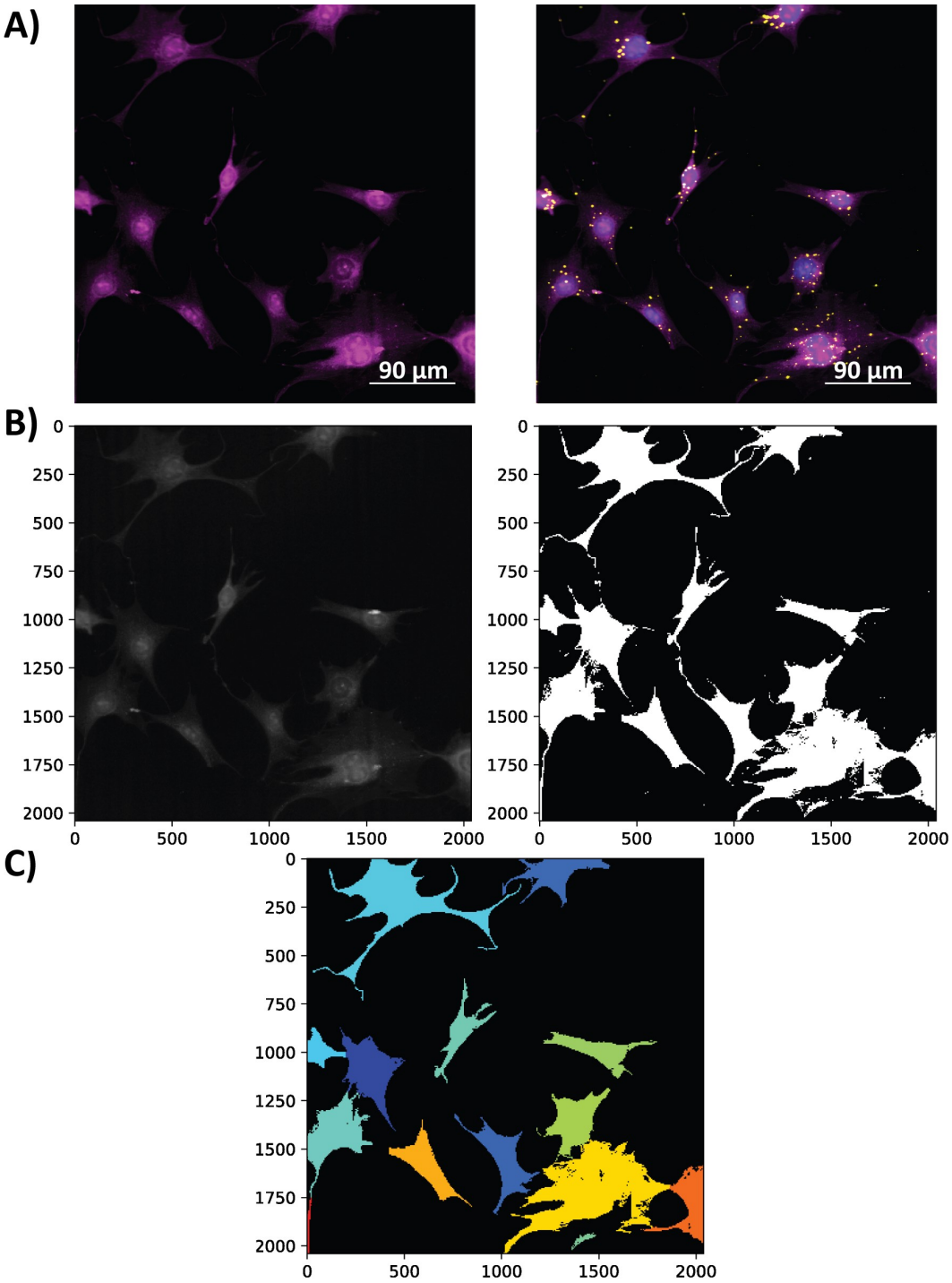

Figure 4.3.19. Image analysis strategy for the cytoplasmic channel in HTCM
(A) A representative image field of *in situ* RCA targeted to mtDNA_9461G in BMSC cells is used to demonstrate the image analysis strategy for the cytoplasmic channel **(left)** of multichannel high throughput RCA images **(right)** using CellProfiler. DAPI = blue, CellTrace™ Yellow = magenta, ATTO647 RCP at mtDNA_9461G = yellow. **(B)** The cytoplasmic channel is extracted from the image set and thresholded by the Otsu method [298]**. (C)** Object identification and segmentation is performed, optimised for detection of major cytoplasmic segments (shown as pseudo-colour representations)**.** Images are collected at 400 x magnification by HTCM.

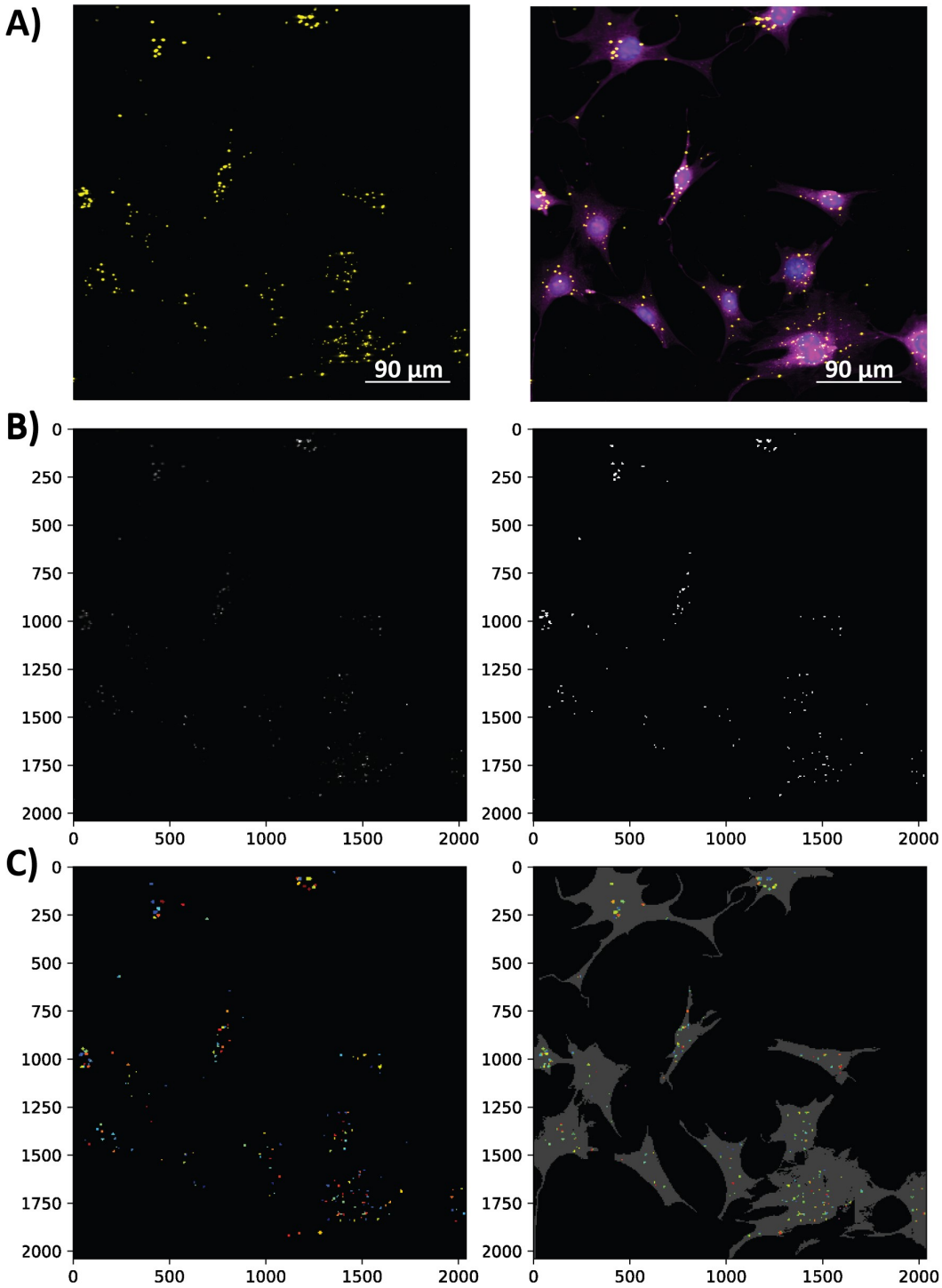

Figure 4.3.20. Image analysis strategy for RCP channel in HTCM
(A) A representative image field of *in situ* RCA targeted to mtDNA_9461G in BMSC cells is used to demonstrate the image analysis strategy for the RCP channel of multichannel high throughput RCA images using CellProfiler. DAPI = blue, CellTrace™ Yellow = magenta, ATTO647 RCP at mtDNA_9461G = yellow. **(B)** The RCP channel is extracted from the image set and thresholded by the Otsu method [298]**. (C)** Object identification and segmentation is performed, optimised for detection of RCPs of a uniform radius (shown as pseudo-colour representations)**.** A binary mask generated from the cytoplasmic channel in **Figure 4.3.19** is applied to the RCP channel to exclude enumeration of RCP signals not associated with a cell body. Images are collected at 400 x magnification by HTCM.

Many images acquired by HTCM are imperfect. Abnormalities in image quality can impact as many as 5 % of the acquired fields, for even the most sophisticated or experienced microscopy labs [299]. Manual inspection of each image field is simply not feasible for high throughput screens. A robust, automated quality control (QC) strategy is essential and must be employed in parallel with image analysis.

For QC of HTCM images in this research, **Figure 4.3.21A** describes the steps taken to identify and exclude problematic images from the dataset. A total of 256 individual metrics were calculated for every image analysed by the CellProfiler pipeline. The majority of these metrics were calculated solely to inform image quality. The open source analysis platform CellProfiler Analyst [300] and the methods described by Bray and Carpenter [299] were used to interpret manually classified images and their associated CellProfiler output metrics. CellProfiler Analyst was compiled from the master branch of the source code at https://github.com/CellProfiler/CellProfiler-Analyst and executed in Python 2.7.

Approximately 100 images from each *in situ* RCA experiment were manually classified into positive or negative bins. High quality images most suitable for analysis were classified as positive. Images which contained artefacts, or those of low quality were classified as negative. It is important to clarify that classifications were made solely by the quality of an image, not on any specific biology within an image, related to the experiment.

Supervised machine learning was carried out in CellProfiler Analyst by the FastGentleBoosting algorithm. Through this, the metrics which discriminate between image classifications were discovered. In **Figure 4.3.21B**, two metrics selected at random are presented as a hexplot, as an example of how images fall into clusters by quality metrics. A total of 32,640 X-Y metric comparisons could be made to manually find which metrics best clustered images by quality, but this was not useful in practice. The machine learning approach used in this study was far more practical for this purpose. The machine learning algorithm was trained such that images of ambiguous quality were likely classified as negative, to reduce occurrences of image analysis performed on low quality images.

In **Figure 4.3.22**, representative images flagged by this QC strategy are presented. These fields each depict a particular type of aberration or artefact. These image quality issues are extremely detrimental to the accuracy of automated analysis. Fortunately, the analysis pipeline and QC process allowed the vast majority of poor quality images to be excluded. In each experiment, the final data was manually inspected for any unusual values. When present, the original image was manually cross referenced for quality and a decision made to keep or exclude the image from the dataset.

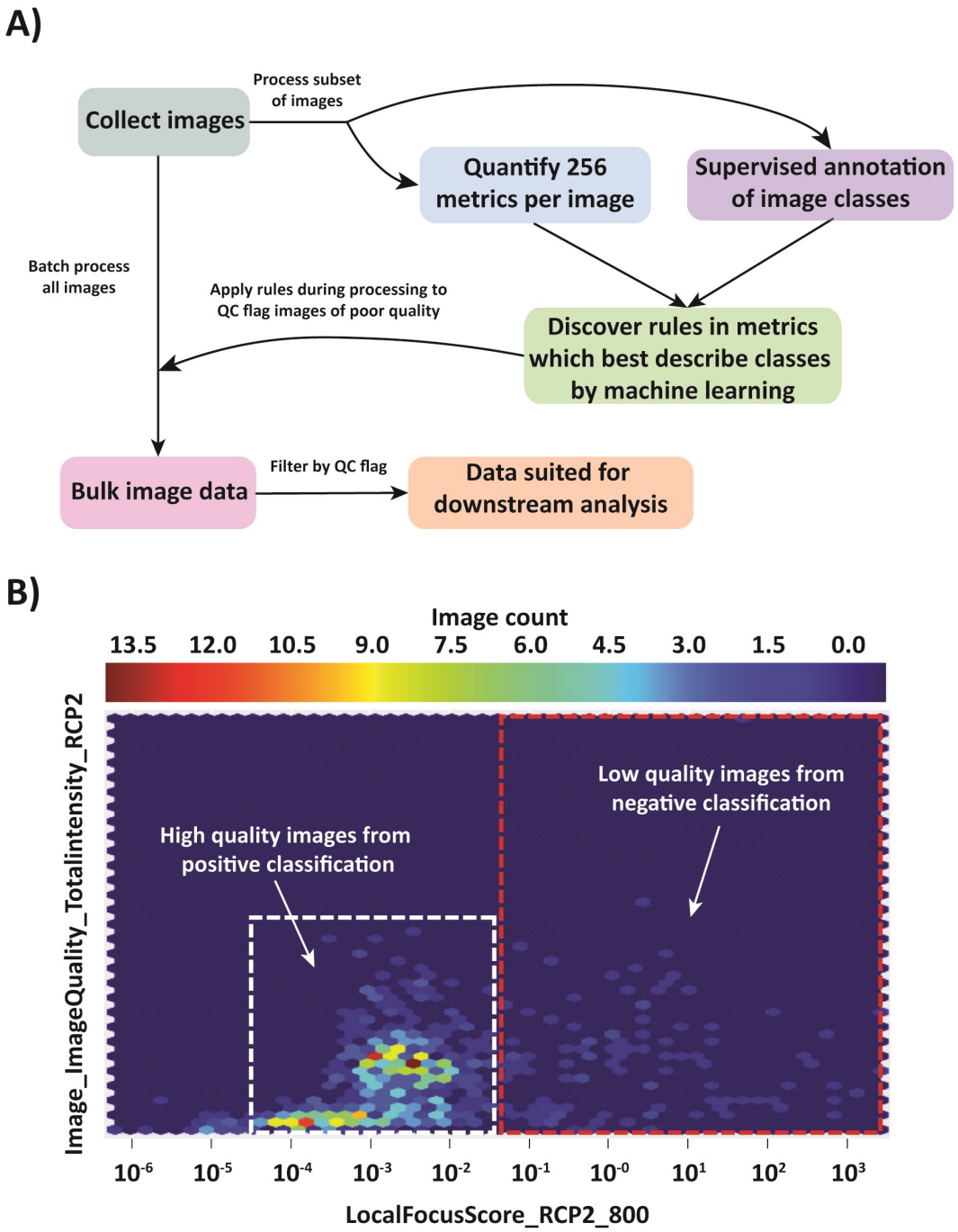

Figure 4.3.21. HTCM data includes low quality images which require QC
(A) A flow chart of image analysis strategy applied in this research describes the strategy employed to remove low quality, out of focus, or artefact image data. **(B)** A hexplot of two individual metrics chosen at random from 256 calculated per image. Two gates have been placed to indicate how high (white) and low (red) quality images cluster by the value of these two metrics. The data presented in this figure was generated from a 425 image dataset of BMSC cells with RCA targeted to mtDNA_9461G.

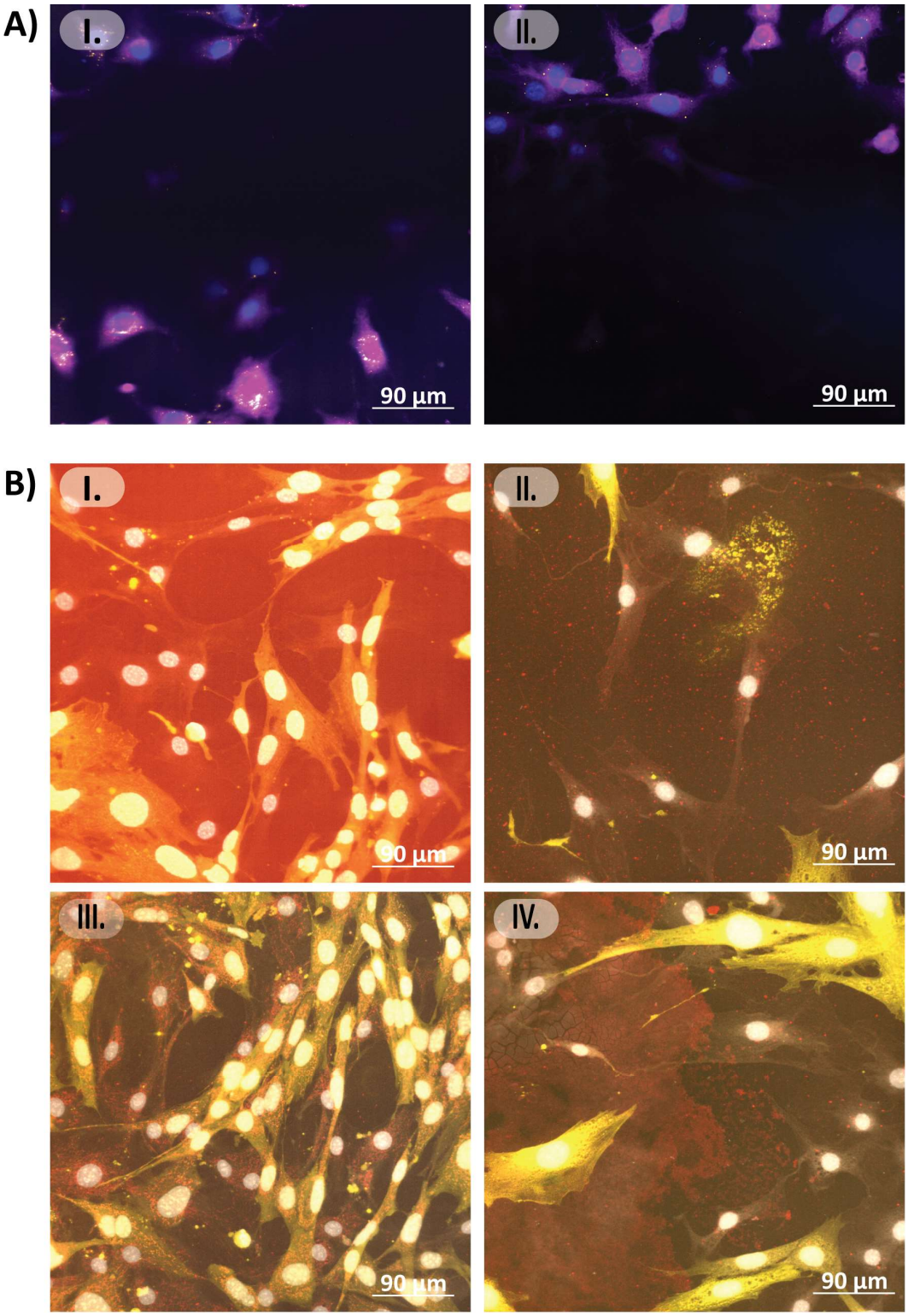

Figure 4.3.22. Low quality images were removed from the *in situ* RCA datasets by image QC

Each representative a unique issue causative of a poor quality flag. **(A, I.)** Localised blur or global focal plane issues **(A, II.)**. For panel **(A)**, DAPI = blue, ATTO647 RCP at mtDNA_9461G = yellow. **(B, I.)** Over exposure. **(B, II.)** Auto fluorescent artefacts. **(B, III.)** Auto-fluorescence from organelles. **(B, IV.)** Salt or other residues. For panel **(B)**, DAPI = white, CellTrace™ Yellow = green, ATTO647 RCP at mtDNA_9461G = red. Images in panel **(B)** are heavily contrast adjusted to assist with visualisation. All images were collected at 400 x magnification by HTCM.

4.3.11 Quantitative assessment of *in situ* RCA targeted to mtDNA_9461G – Reaction efficiency and selectivity

With methods in place for HTCM and quantification of single molecule genotyping by *in situ* RCA, I evaluated the efficiency of *in situ* RCA reactions targeted to mtDNA_9461G.

At a low concentration, the nucleic acid intercalating dye SYBR Green I directly stains mtDNA alongside nuclear DNA [43]. This makes SYBR Green I useful in direct visualisation of mtDNA nucleoids. To approximate the mtDNA copy number of the BMSC cell line, SYBR Green I was used to stain live cells for HTCM, from two biological preparations. The results of these experiments would function as a reference point to understand roughly how many available target molecules successfully generate an mtDNA_9461G RCP by *in situ* RCA.

In **Figure 4.3.23,** a single representative image field demonstrates mtDNA nucleoids as they appeared in these experiments. Presented is the analysis strategy used to approximate mtDNA copy number per cell. SYBR Green I staining produced intense nuclear staining alongside punctate mtDNA nucleoid signals, seen most clearly in **Figure 4.3.23B.** Hoechst 33342 was used as a counterstain, to enable exclusion of the nuclear SYBR Green I signal. In addition, the highly stained nuclear region prevented accurate thresholding of the immediately adjacent, weaker signals of mtDNA nucleoids. For this analysis, Hoechst 33342 nuclear signals were dilated by 30 pixels **(C, III.)** and converted to a binary mask **(C, IV.).** The area within this mask was then excluded from nucleoid quantification. While this method provided a useful reference value for mtDNA copy number of BMSC cells, exclusion of the perinuclear area results in an underrepresentation of mtDNA nucleoids in these cells. With this limitation in mind, the data presented in **Figure 4.3.23** and **Figure 4.3.24** are referred to as an approximation, rather than an absolute determination of mtDNA copy number in the cells.

Table 10. Summary counts for Image analysis of SYBR Green I stained BMSC cells

Image set	Count nuclei detected	Count mtDNA signals detected	Mean mtDNA signals per nucleus ± SEM
SYBR Green 1 BMSC set 1	917	31160	34.0 ± 1.6
SYBR Green 1 BMSC set 2	621	17376	28.0 ± 1.4

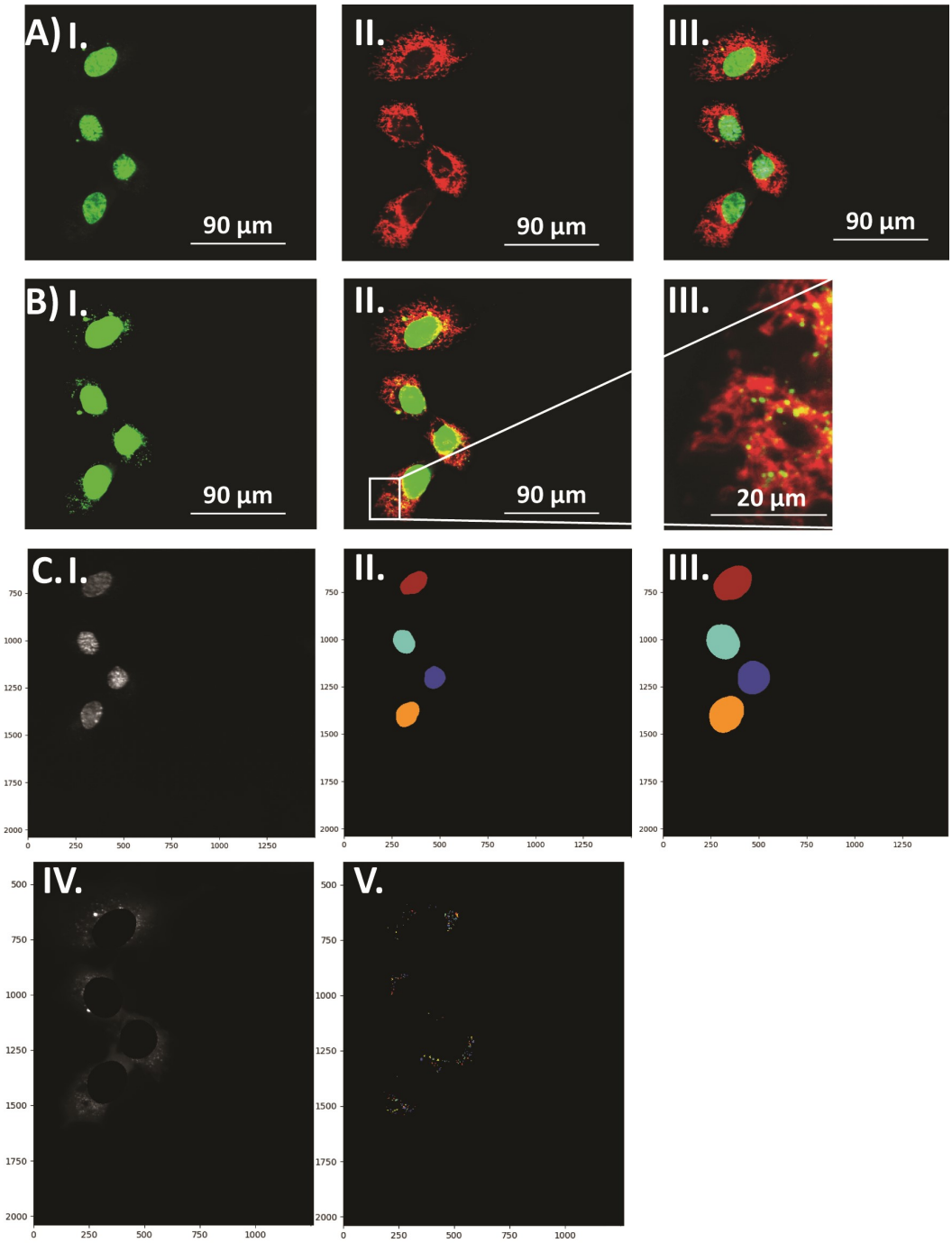

Figure 4.3.23. SYBR Green I stains mtDNA in BMSC cells and enables automated image analysis for approximation of mtDNA count

(A) A representative HTCM image of BMSC cells stained to approximate mtDNA nucleoid count. **(A,I.)** SYBR Green I nuclear staining. **(A, II.)** MitoTracker Red™ CMXRos. **(A, III.)** Combined SYBR Green I, CMXRos and Hoechst 33342 staining. **(B, I.)** Image contrasted SYBR Green I stain reveals punctate cytoplasmic staining. **(B, II.)** Overlaid SYBR Green I (adjusted) and CMXRos stain alongside an enlarged subsection **(B, III.)**. **(C, I.)** Hoechst 33342 signal is extracted and the nuclei identified **(C, II.)**. **(C, III.)** Nuclear object dilation. **(C, IV.)** Nuclear mask as applied to SYBR Green I channel. **(C, V.)** Quantification of SYBR Green I signals**.** Images were collected at 400 x magnification by HTCM from two independent biological replicates.

In **Figure 4.3.24**, the mean number ± SEM for mtDNA nucleoids per nucleus per image in BMSC cells was approximated to be 34.0 ± 1.6 and 28.0 ± 1.4 for image sets 1 and 2 respectively. A probability distribution (**Figure 4.3.24B**) was modelled by kernel density estimate (KDE) from the mtDNA copy number per nucleus approximated from the image dataset. In a KDE, the area under curve between any two X-axis values represents the frequency; the probability that a BMSC nuclei has an mtDNA copy number within this range. Modelled probability distributions were useful to compare these data sets given the large inter-cell variability.

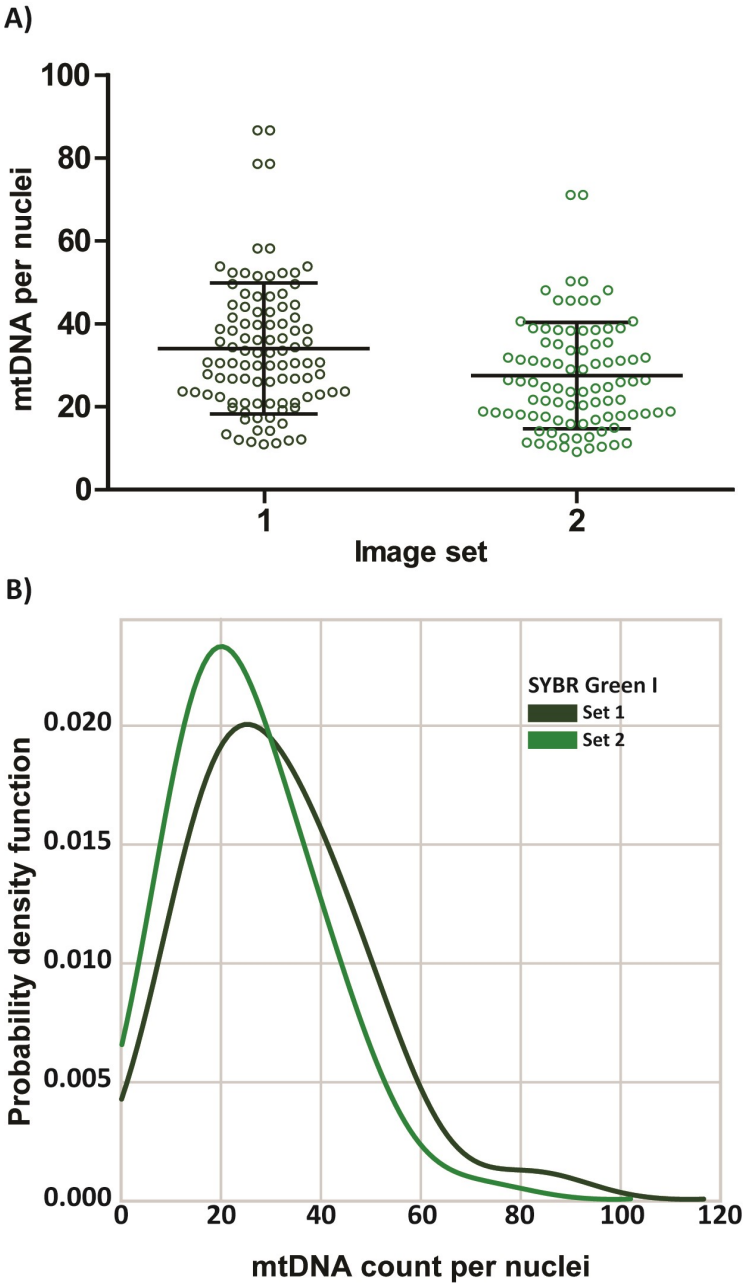

Figure 4.3.24. Approximation of mtDNA molecule count in BMSC cells by SYBR Green I stain

(A) Scatter plot of the mean number of mtDNA signals detected per nucleus ± SD, from each collected image. **(B)** The distribution of the mean mtDNA signals per nucleus in BMSC cells is modelled from each image data set by KDE.

In **Table 11** and **Figure 4.3.25**, RCA reactions were performed with either Ampligase™ or Taq HIFI ligase™ to evaluate the reaction efficiency of RCP generation by each ligase at mtDNA_9461G. This comparison was made to ensure that the performance of Taq HIFI Ligase™ was equivalent to, or better than Ampligase™. *In situ* RCA for HTCM was performed with each ligase in parallel, on three independent preparations of CellTrace Yellow™ stained BMSC cells. Images from each HTCM dataset were processed independently, as described in **Figures 1.3.18-20.** These experiments were performed to ensure Taq HIFI™ ligase would perform similarly to Ampligase™, the ligase commonly used for *in situ* RCA.

Table 11. Summary counts for Image analysis of mtDNA_9461G reaction efficiency in BMSC cells

Image set	Count cytoplasmic segments detected	Count RCP signals detected	Mean RCPs per cytoplasmic segment ± SEM
Ampligase BMSC set 1	1197	15746	13.2 ± 0.3
Ampligase BMSC set 2	1629	22657	13.9 ± 0.3
Ampligase BMSC set 3	9780	80387	8.2 ± 0.1
Taq HIFI BMSC set 1	535	3546	6.6 ± 0.4
Taq HIFI BMSC set 2	1705	30972	18.2 ± 0.4
Taq HIFI BMSC set 3	556	20357	36.7 ± 2.2

The results from this experiment are represented in **Figure 4.3.25A** where mtDNA signals per cell are presented as a box and whisker plot with the range (whiskers), quartiles (box) and median indicated on each bar. Alongside the RCA results, the mtDNA copy number approximated in **Figure 4.3.24A** is displayed for comparison. As the RCP counts and mtDNA copy number approximation are derived differently, this data is not directly comparable. It does however, provide some insight into approximately how many available target molecules successfully produced a detectable RCP in these reactions.

For all individual RCA image sets, the number of mtDNA signals per nucleus was highly variable. This was consistent with prior observation of variability in mtDNA nucleoids per cell in **Figure 4.3.24**. By comparison of the probability distributions modelled by KDE in **Figure 4.3.25B,** reactions performed with Ampligase™ produced a consistent detection of RCPs in the population. This is illustrated by similarity in the three distributions. The distributions produced by Taq HIFI Ligase™ reactions were less similar to each other, compared with those produced using Ampligase™. This appears to be caused by two datasets with a higher detection efficiency than the third. For Taq HIFI ligase, two of the three datasets share a distribution more similar to the approximation made by direct SYBR Green I stain. Together, these results indicated that reactions performed with Taq HIFI Ligase™ trend towards a higher reaction efficiency than Ampligase™. The Taq HIFI mtDNA_9461G BMSC set 3 data set had a greater range in the count of RCPs detected. A potential cause of this may have been segmentation in the image processing. Clumped cells identified as a singular cytoplasmic segments could potentially drive up the mean range in this dataset.

A)

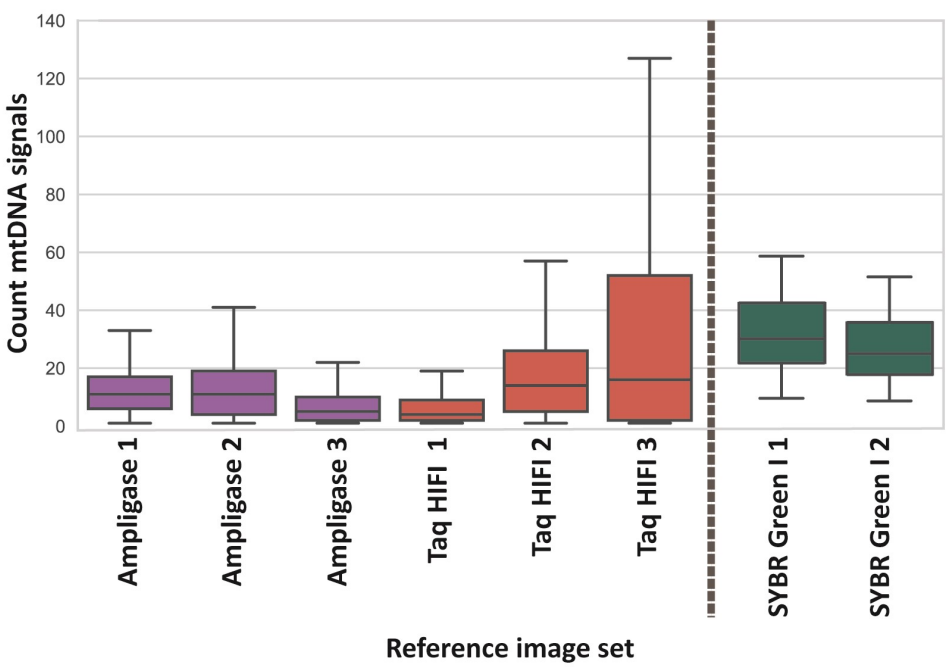
Count mtDNA signals
140
120
100
80
60
40
20
0
Ampligase 1
Ampligase 2
Ampligase 3
Taq HIFI 1
Taq HIFI 2
Taq HIFI 3
SYBR Green I 1
SYBR Green I 2
Reference image set

B)

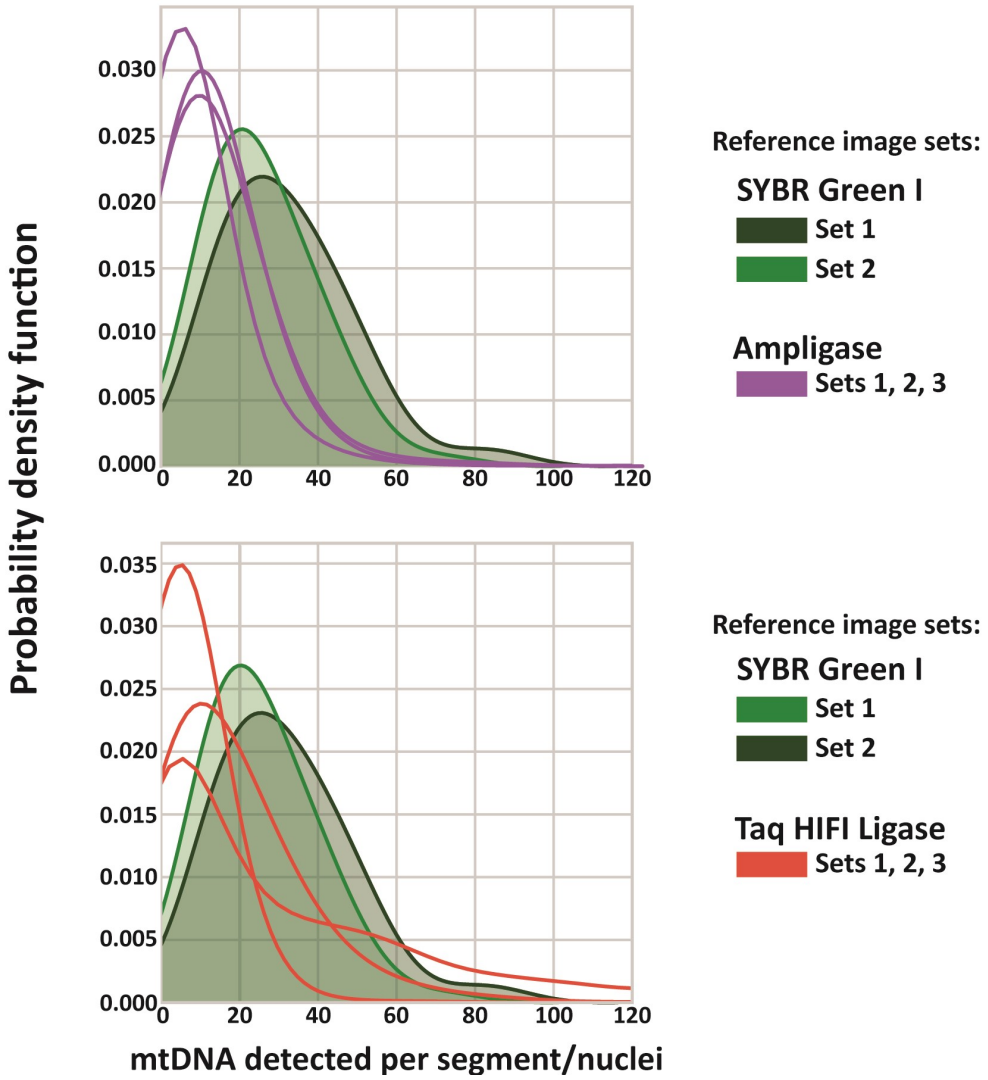
Probability density function
0.030
0.025
0.020
0.015
0.010
0.005
0.000
0
20
40
60
80
100
120
Reference image sets:
SYBR Green I
Set 1
Set 2
Ampligase
Sets 1, 2, 3
0.035
0.030
0.025
0.020
0.015
0.010
0.005
0.000
0
20
40
60
80
100
120
Reference image sets:
SYBR Green I
Set 1
Set 2
Taq HIFI Ligase
Sets 1, 2, 3
mtDNA detected per segment/nuclei

Figure 4.3.25. Reaction efficiency of mtDNA_9461G targeted RCA in BMSC cells
RCA Reactions were performed with either Ampligase or Taq HIFI ligase to evaluate the relative reaction efficiency of RCP generation at mtDNA_9461G. **(A)** Box and whisker plot of the count of RCPs detected per cytoplasmic segment. The approximated mtDNA copy number per BMSC nuclei from **Figure 4.3.24** is displayed alongside these results. The dotted partition represents segregation of these two datasets by measurement technique. **(B)** Probability distribution modelled by KDE from each replicate, for each ligase. The KDE for approximated mtDNA copy number per BMSC nuclei from **Figure 4.3.24B** is also displayed for comparison.

From all image sets generated with each of the ligases, it was apparent that the mean mtDNA copy number approximated by SYBR Green I was greater than the mean RCP count per cytoplasmic segment. This was an expected result, given target-primed RCA *in situ* is not 100 % efficient. For detection of IMT by *in situ* RCA, this inefficiency may be negated simply by collection of data from more cells. What is critical for the success of this method to study IMT is reaction selectivity.

To assess the selectivity of the PDP targeted to mtDNA_9461G, *in situ* RCA for HTCM was performed on three independent preparations of CellTrace Yellow™ stained eGFP-astrocytes. These cells do not contain the target SNV, therefore any detected RCPs are false positive. Reactions were performed with both Taq HIFI Ligase™ and Ampligase™ in parallel. This was to determine whether the selectivity of Taq HIFI Ligase™ was at least equivalent to, or better than Ampligase™ in this novel application. Positive control reactions were performed on BMSC cells in parallel to ensure all stages of the RCA protocol were successful. Images from each HTCM dataset were processed independently, as described in **Figures 1.3.18-20**.

The results of these experiments are presented in **Figure 4.3.26.** As the mtDNA copy number of C57-eGFP-astrocyte cells is unknown, the most useful way to evaluate the selectivity of each ligase was to compare discrete counts of false positive RCP(s) detected per cytoplasmic segment. In **Figure 4.3.26A,** the result of these experiments indicated no significant difference between each ligase, as tested by two-way ANOVA. With 80.8 ± 3.9 % ± SD for Taq HIFI Ligase™, the vast majority of cytoplasmic segments contained zero false positive RCPs. This was highly consistent with the low rate of false positive RCPs observed by LSCM in **Figure 4.3.15**. The percentage of segments with one or more false positive RCPs, reported in **Table 12**, rapidly decreased with each increase in RCP count. This decrease is modelled from the image data by KDE in **Figure 4.3.26B.** Here**,** the distribution of false positive RCPs are modelled for each individual dataset, with both Ampligase™ and Taq HIFI Ligase™. The tight KDE profile of all six distributions indicates that the decay in false positive RCP generation occurs independently of any particular cell, but instead is a constant. This is consistent with the biochemical properties of the ligase itself. The enzyme governs the rate of false positive ligation.

Table 12. Summary data for false positive RCPs at mtDNA_9461

	Percent of cytoplasmic segments (% ± SD)	
Number of RCPs detected	**Ampligase™**	**Taq HIFI Ligase™**
0	77.0 ± 1.9	80.8 ± 3.9
1	12.6 ± 3.2	10.5 ± 3.6
2	5.0 ± 0.7	3.3 ± 0.8
3	1.8 ± 0.2	1.8 ± 0.3
4	1.2 ± 0.8	1.5 ± 0.9
5	1.0 ± 0.7	1.0 ± 0.4
6	0.8 ± 0.4	0.5 ± 0.2
7	0.6 ± 0.4	0.6 ± 0.3

Table 13. Summary counts for Image analysis of mtDNA_9461G RCA selectivity in eGFP-astrocyte cells

Image set	Count cytoplasmic segments detected	Count RCP signals detected
Ampligase mtDNA_9461G BMSC set 1	997	363
Ampligase mtDNA_9461G BMSC set 2	827	419
Ampligase mtDNA_9461G BMSC set 3	977	506
Taq HIFI mtDNA_9461G BMSC set 1	393	197
Taq HIFI mtDNA_9461G BMSC set 2	810	297
Taq HIFI mtDNA_9461G BMSC set 3	1111	575

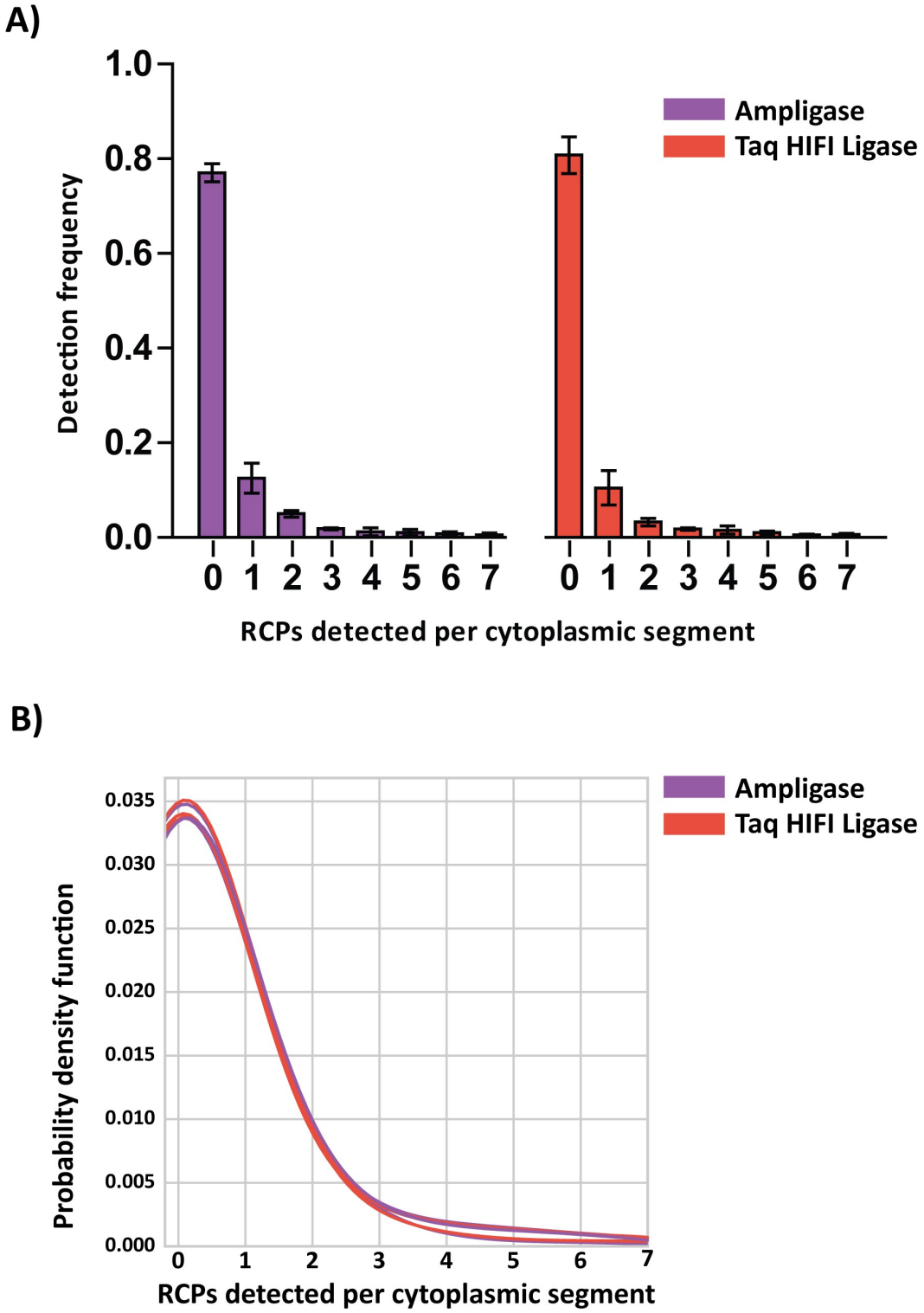

Figure 4.3.26. Reaction selectivity of mtDNA_9461G targeted RCA in eGFP-astrocytes
In situ RCA Reactions targeted to mtDNA_9461G in C57-eGFP-astrocytes with Ampligase or Taq HIFI ligase, to evaluate reaction selectivity. Reactions were performed and images collected from CellTrace™ CFSE stained C57-eGFP-astrocytes from 3 independent preparations, analysed as described in **Figure 4.3.18-20**. No significant difference was determined between ligases at any RCP count, tested by two way ANOVA. **(A)** Bar graph of the mean frequency ± SD of cytoplasmic segments with the count of false positive RCPs. **(B)** The distribution of RCPs detected per cytoplasmic segment is modelled as a kernel density estimate for 3 independent replicates, for each ligase.

4.4 Summary

The aim of this chapter was to develop a novel approach for detection of IMT. I hypothesised that mitochondria transferred between two cells also carry a number of mtDNA molecules. How to leverage these mtDNAs, to trace the movement of mitochondria between cells became a major focus of my research. I recognised unique SNVs were a valuable means to infer the cellular origin of mtDNA; whether an individual mtDNA was an endogenous or exogenous molecule. gDNA isolated from 'recipient' cells from IMT experiments could be interrogated for the presence of 'donor' mtDNA.

In the context of IMT, no prior knowledge describes the count of mtDNA molecules which move between cells. Ideally, recipient cells would be subjected to ultra-deep amplicon sequencing to detect transferred mtDNA. This approach was simply not feasible given the associated cost, particularly as the contexts where IMT occurs are so poorly understood.

In this chapter, I have developed two distinct molecular strategies. Each exploit SNVs to discriminate between target mtDNAs. By amplification in ASB-qPCR, or by single molecule genotyping *in situ*, each approach demonstrates capable detection of the target mtDNA. In the context of application to IMT research, either strategy would enable quantification of mtDNA transferred into 'recipient' cells.

Unfortunately, a critical limitation to the ASB-qPCR approach revealed itself in the form of FACS impurity. Genomic DNA extracted from neural cell types would simply contain too many contaminant mtDNA molecules which originated from mis-sorted 'donor' cells. It was possible that biologically transferred mtDNA molecules in IMT experiments would not exceed this level of 'background' signal caused by contaminants in the 'recipeint population due to FACS impurities. Even a single contaminant cell could introduce up to thousands of contaminant mtDNAs. Unless perfect separation of the two populations had been achieved and validated, gDNA extracted from sorted 'recipient' cells would not be suitable for direct molecular analysis. This is true not only for ASB-qPCR, but for any alternative molecular strategy in 'recipient only' samples.

Across the McConnell laboratory, FACS separation of co-culture models yielded similar results when the cells involved were large, as in the case of neural cell types. It is likely that the large sort nozzle and low fluidics pressure required for FACS of large cells prevented separation at the purity required. Fortunately, smaller, more regular cell types have since been sorted to exceptional purity by others in the McConnell laboratory. ASB-qPCR methods, including the mtDNA_195 selective assay, have been successfully pursued by other in studies of IMT.

Because cell separation would continue to be an issue with large and irregular neural cells in co-culture, I developed an approach to circumvent it entirely. The *in situ* single molecule genotyping for mouse mtDNA presented in this chapter was successful in detection of the target mtDNA SNVs. The molecular design presented here has highly flexible application to mouse IMT models, both *in vitro* and *in vivo*. By designing IMT models with mtDNA_9461G in the mitochondrial donor, and mtDNA_9348G in the recipient or vice-versa, IMT can be studied between numerous combinations of cell line, or any mouse tissues from specific mouse strains.

mtDNA_9461G targeted PDPs were highly selective towards the target genotype. For this PDP, the frequency of false positive RCP reactions was accurately determined, in eGFP-astrocytes. mtDNA_9461G targeted RCA detected sufficient target molecules per cell to apply the technique to quantitative IMT studies. It was now theoretically possible to detect mtDNA_9461G transferred between cells, or replicated shortly after transfer, above a known, stable frequency of false positive RCP generation. As we do not yet understand how transferred mtDNA are replicated, an assumption that mtDNA detected in 'recipient' cells would be predominantly the result of transfer, though it is possible that replication of newly arrived mtDNA could contribute to detected mtDNAs. By collection of image data from enough 'recipient' cells, sufficient mtDNAs are sampled to overcome the imperfect reaction efficiency of RCA. In these studies, Taq HIFI™ ligase was also determined to be equally appropriate in this novel application as Ampligase™; the ligase commonly used in literature.

Regretfully and for reasons undetermined, quantification of mtDNA_9348G targeted PDPs was unsuccessful by HTCM. By LSCM, eGFP-astrocytes clearly demonstrate AF405 positive RCA reactions when targeted to this locus. Images of the RCPs were collected by HTCM, however image quality was not sufficient for automated image analysis. For this reason, the efficiency and selectivity of mtDNA_9348G targeted RCA reactions was not determined in this thesis. Despite various modifications to the reactions, this issue remains unresolved. I hypothesise that mtDNA_9348G RCPs hybridised with ATTO647 labelled oligonucleotides, like those used for the mtDNA_9461G RCPs, would enable quantitative HTCM at this locus. I suspect a combination of fluorophore properties and the optical capabilities of the In Cell 6500 instrument are the cause of this issue. All further quantitative studies of IMT in thesis use mtDNA_9461G mitochondrial 'donors' alone for this reason.

Fortunately, biological instances of IMT were not required to design or validate the technical function of these strategies. This was of importance, given how little we know of what drives or regulates IMT, or of the replication of mtDNA following transfer. We also

lack knowledge of which cell types are capable of IMT, or why this process even occurs. Instead, I intended to use single molecule genotyping of mouse mtDNA as developed in this chapter to screen for or quantify IMT in novel biological contexts.

5 Discovery of novel mitochondrial donor cells

5.1 Introduction

With a novel molecular approach for detection of IMT now developed, this chapter explored the application of this method to potential *in vitro* models of IMT. From these, a model will be selected in which to carry out studies to assess how cellular injury alters the rate of IMT.

IMT is a biological phenomenon only identified in relatively recent scientific reports. As such, the types of cells capable of engaging in this process are not yet thoroughly characterised. Without a proper understanding of what drives the phenomenon, we have little basis on which to predict which cell types may be capable of IMT. Is it an activity restricted to certain cell types? Or rather, a specific cellular state that causes a cell to act as a mitochondrial 'donor' or 'recipient'. Perhaps the process is regulated by some other factor altogether. In order to investigate whether cellular injury would alter the rate of IMT, I first required a reliable model in which genuine IMT actually occurred.

In existing literature, the cell type most regularly reported as mitochondrial 'donors' are without a doubt mesenchymal stem cells (MSCs) [175, 176, 186, 188, 195, 196, 199-203, 205, 207, 208, 212, 213]. It is unclear whether the prevalence of this cell type in published material is due to these cells being the 'best' mitochondrial donor cell type. Perhaps reports of the phenomenon are simply prevalent based on a large number of labs looking at mesenchymal stem cells, in the context of regenerative medicine. Reports of IMT from MSCs appears in many ways, to be an offshoot research topic for laboratories primarily focused on stem cells.

Mesenchymal stem cells were an attractive candidate for use in my intended injury study; however, a lack of a known MSC niche within the brain microenvironment was problematic. Unpublished work in the Berridge laboratory using ρ^0-GL261 cells implanted intracranially formed tumors after a long lag period, relative to wild-type GL261. Cells from these tumors carry mtDNA sequence from the host animal. This suggested that cell types within the brain microenvironment are capable of donating and receiving mitochondria *in vivo*. From this, a question was formed; Are MSCs likely to be involved in physiological IMT in the brain? While not impossible, a rational approach for my investigations was to first pursue potential 'donor' cell types that are prevalent in the brain microenvironment naturally. Identification of an IMT 'donor' cell type naturally found in the brain microenvironment would be valuable for my intended *in vitro* injury studies.

To these ends, this chapter explores numerous murine cell lines to identify those capable of engaging in IMT. Among these were a number of lines derived from neural tissues. These included astrocytes, glioma and neural progenitor cells; ideally, one or more of these would be a capable 'recipient' of mitochondria. To increase the likelihood of detecting IMT in these cells, a ρ^0-eGFP-astrocyte cell line was also included in the panel as a potential IMT 'recipient'. Because these cells lack mtDNA, recovery of mitochondrial function and the mtDNA is easily monitored. From the outset of the research presented in this chapter, I hypothesised that one or more of the cell types in this panel would be a capable recipient of exogenous mitochondria. All that was required was to identify a 'donor' cell type, which would readily interact with them through IMT.

5.2 Aims

The aim of this chapter is to identify an *in-vitro* IMT co-culture model, with cell types native to the brain. Using the molecular methods developed in chapter 4, I aimed to detect IMT in new co-culture contexts. The model found to be most suitable would be used to study the effect of cellular injury on the rate of IMT in further research.

5.3 Results

5.3.1 ρ^0-eGFP-astrocytes were confirmed to be mtDNA null

Before ρ^0-eGFP-astrocytes were used as potential mitochondrial 'recipients', a confirmation of ρ^0 status was necessary. It was essential to confirm true ρ^0 status in these cells, so both mtDNA transfer and recovery of respiratory capacity in these cells could only result from IMT. Demonstrated in **Figure 5.3.1**, the absence of mtDNA in these cells was confirmed by PCR and gel electrophoresis. The PCR reaction was carried out with 30 amplification cycles to ensure any mtDNA present would be amplified to a detectable level. In lane 1, a singular product corresponding to a 148 bp target sequence of mtDNA was amplified from eGFP-astrocyte gDNA. This is the parental cell line from which ρ^0-eGFP-astrocytes were derived by extended treatment with low concentration EtBr, by RTS in the McConnell laboratory. gDNA extracted from the ρ^0-eGFP-astrocyte line did not produce the mtDNA target fragment when amplified by PCR (lane 2). To ensure the quality of gDNA extracted from both cell lines was sufficient for PCR amplification, a fragment of the apolipoprotein B gene, encoded in the nuclear genome, was amplified alongside the mtDNA fragment. In lanes 4 and 5, a singular apolipoprotein B PCR product was successfully amplified for each cell line. This control indicated that gDNA quality did not likely impact successful amplification of the target mtDNA from the ρ^0 cells. The no template control reactions for both the mtDNA fragment (lane 3) and apolipoprotein B (lane 6) did not produce PCR fragments, as expected. Taken together, these results confirmed the absence of mtDNA in the eGFP-astrocyte cell line. The ρ^0-eGFP-astrocyte cell line was suitable for use in co-culture experiments as a potential mitochondrial 'recipient'.

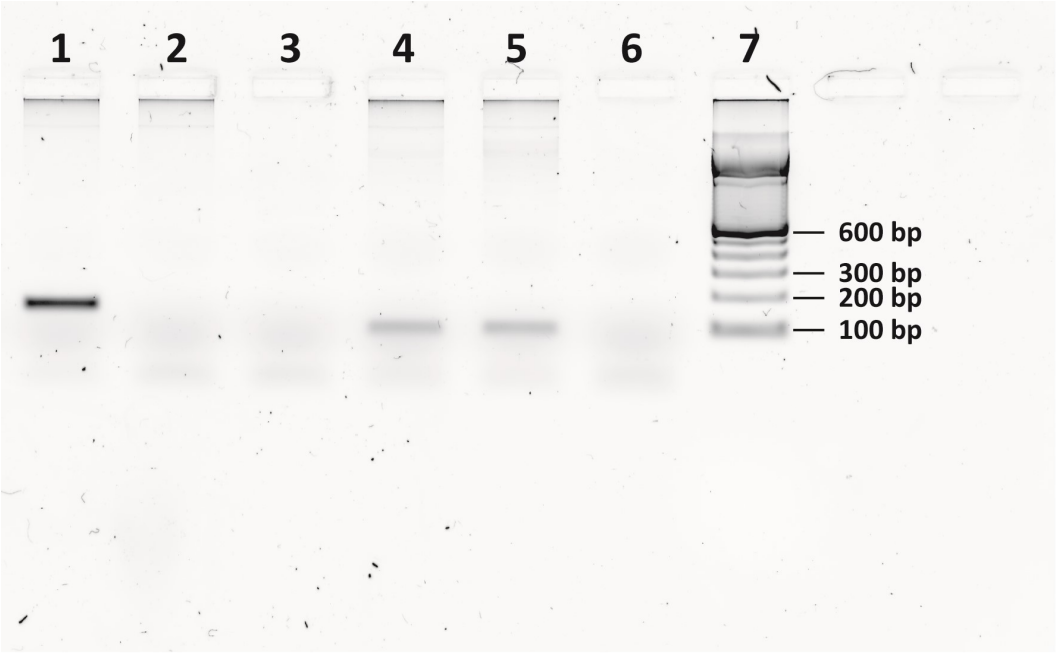

Figure 5.3.1. ρ^0-eGFP-astrocytes were confirmed negative for mtDNA by PCR
gDNA extracted from ρ^0-eGFP-astrocyte and the parental eGFP-astrocyte lines was PCR amplified to confirm absence of mtDNA in the ρ^0 cell line. A 148 bp fragment of mtDNA was amplified alongside a 114 bp fragment of the mouse apolipoprotein B gene as a positive nuclear control for gDNA quality. **Lanes 1, 2 and 3** = parental eGFP-astrocyte gDNA, ρ^0-eGFP-astrocyte gDNA and a no template control respectively, amplified with the mtDNA targeted primers. **Lanes 4, 5 and 6** parental eGFP-astrocyte gDNA, ρ^0-eGFP-astrocyte gDNA and a no template control respectively, amplified with the apolipoprotein B targeted primers. **Lane 7** = 100 bp TrackIt™ dsDNA ladder.

5.3.2 *In situ* single molecule genotyping to screen for IMT interactions

A powerful aspect of the single molecule genotyping for detection of IMT developed in chapter 4, is the applicability to uncharacterised IMT models. This enabled an unbiased approach to identification of IMT in new cell line combinations. The following experiments were performed to identify combinations of cells lines which appeared to interact via IMT. **Figure 5.3.2A** describes a matrix of 7 murine cell lines in which every possible IMT directionality was examined. Twenty-eight unidirectional, IMT conditions between cells with normal, endogenous mtDNA were explored. An additional 6 ρ^0-eGFP-astrocyte 'recipient' conditions were also explored. The purpose of these experiments was to identify candidate cell types most capable of, or likely to engage in IMT, from the lines available.

To further expedite identification of these candidates, I developed the first-pass 'multi-culture' screening strategy described in **Figure 5.3.2B**. Multiple 'recipient' cell types, each labelled with a unique CellTrace™ colour, were co-cultured for 24 h with a singular 'donor' cell type to be interrogated in the experiment. An assumption was made that the presence of multiple or specific cell-types does not interfere with IMT. With this limitation accepted, I was able to rapidly identify multiple novel IMT interactions, with significantly less resource expenditure than required by traditional methods.

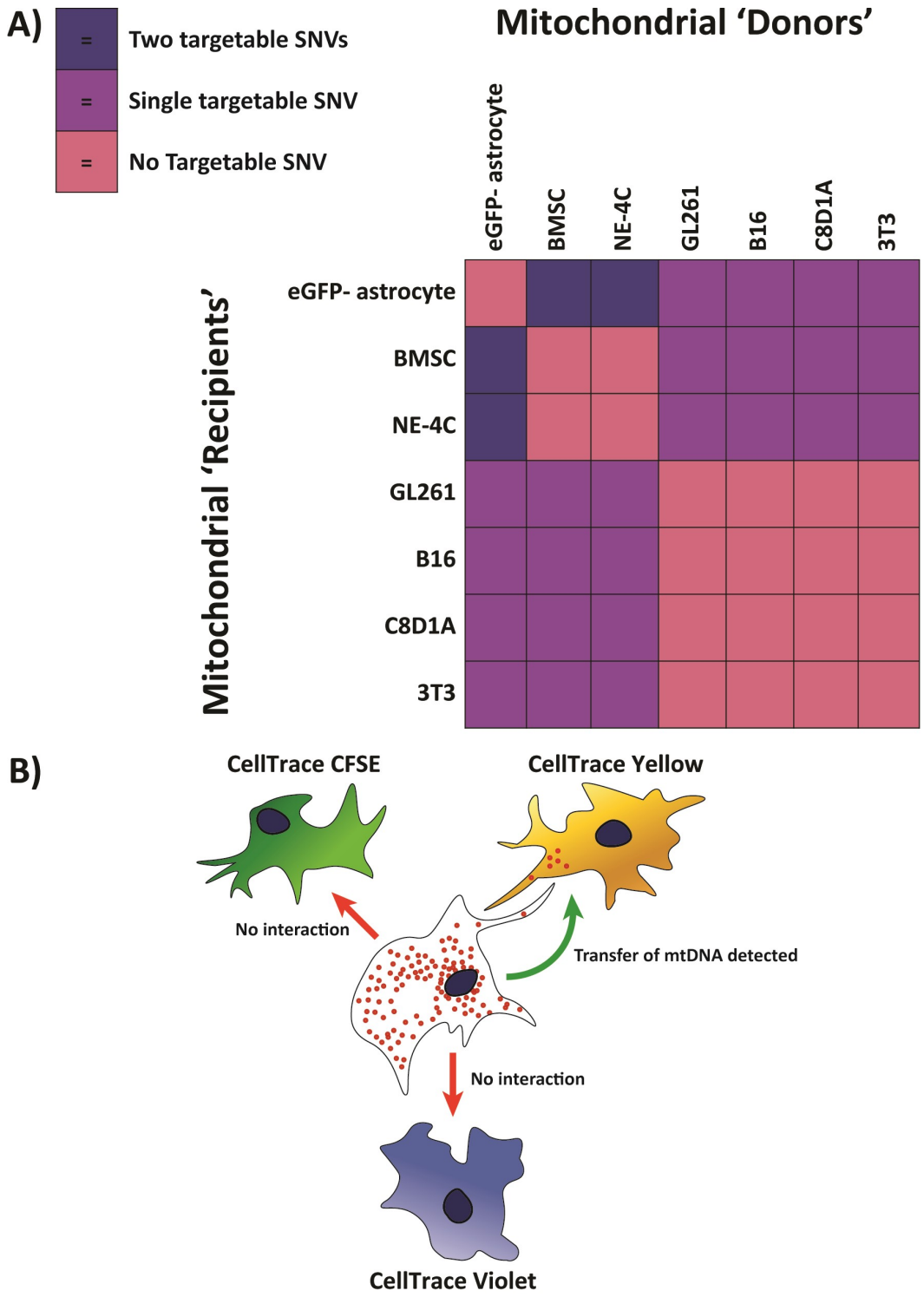

Figure 5.3.2. Rapid screening strategy to identify potential IMT models by *in situ* RCA

(A) Seven cell lines of mouse origin available in the McConnell laboratory as a matrix of 28 individual co-culture pairs with compatible mtDNA genotypes to detect IMT by *in situ* RCA. **(B)** Schematic for a 'multi-culture' approach for rapid identification of IMT in new contexts.

The eGFP-astrocyte cells (both the parental and ρ^0 derivative) were found to be a capable recipient of mtDNA from multiple cell types. In 'multi-culture', mtDNA_9461G RCPs were detected in 'recipient' eGFP/ρ^0-eGFP-astrocytes. **Figure 5.3.3**, representative cells are presented from co-culture conditions where transfer of mtDNA was readily detected in the 'multi-culture' rapid screening approach. To verify these interactions, 24 h co-cultures with just two individual cell lines (as opposed to 'multi-culture') were established with eGFP-astrocytes and one of 3T3 mouse fibroblasts **(A)**, B16 melanoma **(B)** or C8D1A astrocytes **(C)**. The ρ^0-eGFP astrocytes were found to receive mtDNA from the C8D1A line through mtDNA transfer **(D)**. This indicated mtDNA had transferred into these cells from the 'donor' cell population. In cells where mtDNA transfer was detected, typically five or more RCPs were observed. Notably, not all cells within the population demonstrated uptake of mtDNA.

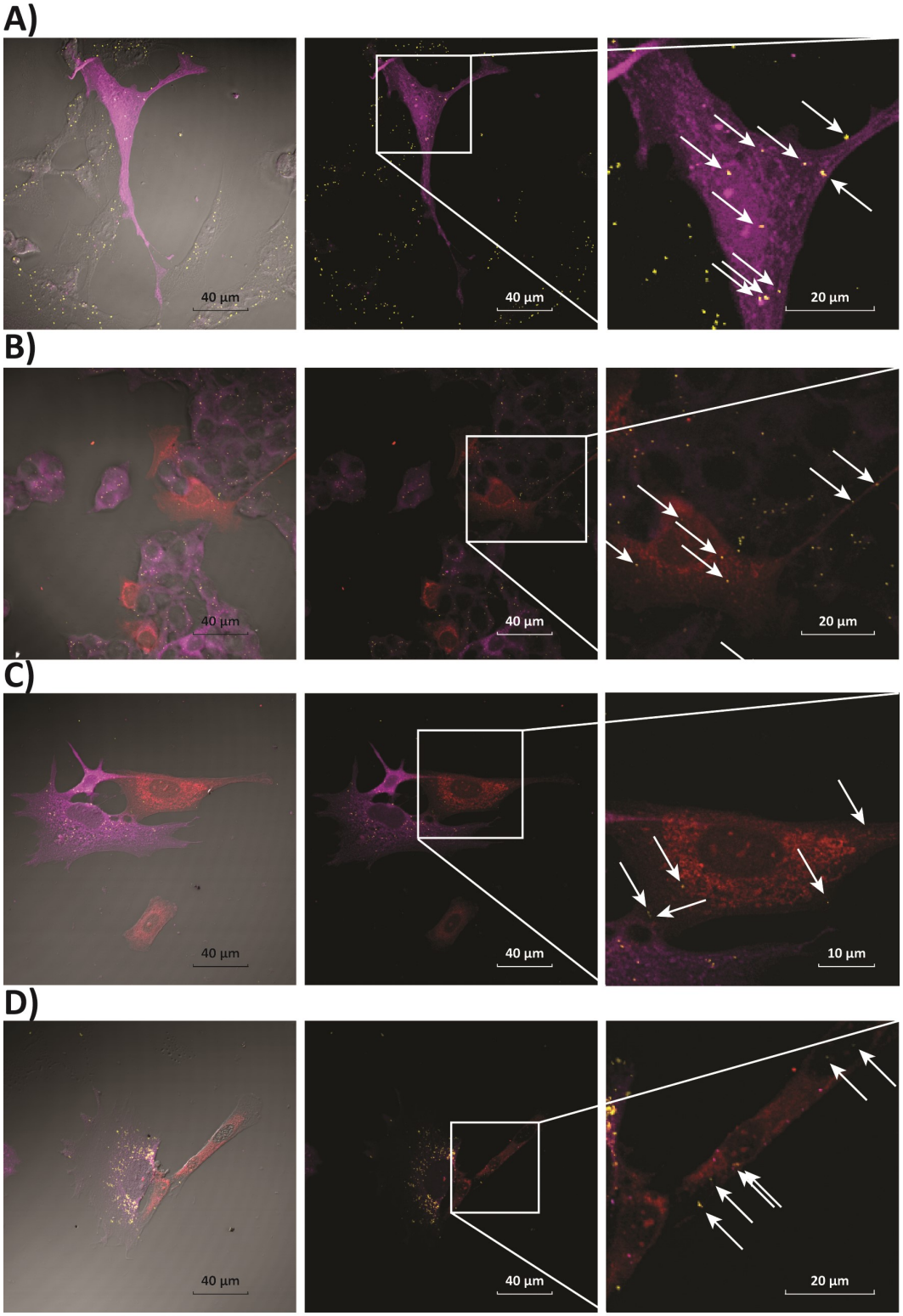
A)
40 µm
40 µm
20 µm
B)
40 µm
40 µm
20 µm
C)
40 µm
40 µm
10 µm
D)
40 µm
40 µm
20 µm

Figure 5.3.3. Discrete mtDNA transfer into eGFP-astrocytes detected by mtDNA_9461G RCA

eGFP-astrocytes are capable 'recipients' of mtDNA from multiple donor cell types, in 24 h co-cultures. Each panel set depicts a representative eGFP-astrocyte which has taken up exogenous mitochondrial DNA. **(A)** eGFP-astrocytes (magenta) co-cultured with 3T3 breast cancer cells (unlabelled). **(B)** eGFP-astrocytes (red) co-cultured with B16 melanoma cells (magenta). **(C)** eGFP-astrocytes (red) co-cultured with C8D1A astrocytes (magenta). **(D)** ρ^0-eGFP-astrocytes co-cultured with C8D1A astrocytes (magenta). Images were collected by LSCM at 600 x magnification. The area within the white square are enlarged (right) for each panel set. CFSE = magenta, CellTrace Yellow™ = red.

5.3.3 eGFP-astrocytes co-cultured with C8D1A reveal IMT by an unexpected mechanism

In situ single molecule genotyping of eGFP-astrocytes or ρ^0-eGFP astrocyte co-cultured with C8D1A revealed mtDNA uptake by an additional, unexpected mechanism. In **Figure 5.3.4**, examples of cell to cell fusion are presented. Cells could be found that were highly positive for both CellTrace Yellow™ and CellTrace CFSE™, which indicated extensive co-localisation of proteins from each of the two original cell types. As fusion occurred for both eGFP-astrocytes and ρ^0-eGFP astrocytes in these co-cultures, cell fusion was not caused by the lack of mitochondrial function associated with the ρ^0 phenotype.

Cells engaged in fusion were observed in varied states of completion. In **Figure 5.3.4A** the eGFP-astrocyte (pictured in red) appeared to have spread protein components throughout the entire cell body of the magenta C8D1A. Intriguingly, the opposite was not true. The magenta coloured C8D1A cell body does not extend fully into the eGFP-astrocyte area. In the fused cell, it was possible to determine which of the two nuclei belonged to each original cell, on the basis of stain intensity. mtDNA_9461G RCPs were localised within the C8D1A area as expected, however did not extend into the area of the eGFP-astrocyte. Together, these observations suggest the C8D1A cell has either absorbed the eGFP-astrocyte, or the eGFP-astrocyte has infiltrated the C8D1A. It is not possible to determine which is true from these data. This cell appears to have been fixed before cell fusion had proceeded to completion.

Similarly, in **Figure 5.3.4B** the depicted ρ^0-eGFP-astrocyte was captured in a state of partial fusion with C8D1A. In this instance, protein components of the ρ^0-eGFP-astrocyte are localised throughout the C8D1A cell body, but the opposite has not occurred. Intriguingly, mtDNA_9461G RCPs are detected within the ρ^0-eGFP-astrocyte area, unlike **Figure 5.3.4A**. In combination with the data presented in **Figure 5.3.3**, these results indicated that multiple mechanisms for IMT were likely to be occurring in this particular co-culture model.

Figure 5.3.4. C8D1A astrocytes and eGFP-astrocytes undergo cell fusion as detected by mtDNA_9461G RCA
After 24 h co-culture, C8D1A astrocytes appear to fuse with either eGFP-astrocytes, or ρ^0-eGFP astrocytes. Each panel set depicts a representative cell fusion event as seen in these co-cultures. **(A)** mtDNA normal eGFP-astrocyte (red) with C8D1A (magenta). **(B)** mtDNA deficient ρ^0-eGFP-astrocyte (red) with C8D1A (magenta). For both panels, **I.** = combined DIC, RCP and dual cytoplasmic channels. **II.** = dual cytoplasmic channels and RCPs. **III.** = eGFP-astrocyte/ρ^0-eGFP-astrocyte cytoplasmic channel and RCPs. **IV.** C8D1A cytoplasmic channel and RCPs. Images were collected by LSCM at 600 x magnification. Red = CellTrace CFSE™, magenta = CellTrace Violet™, yellow = ATTO647 mtDNA_9461G RCPs.

A)

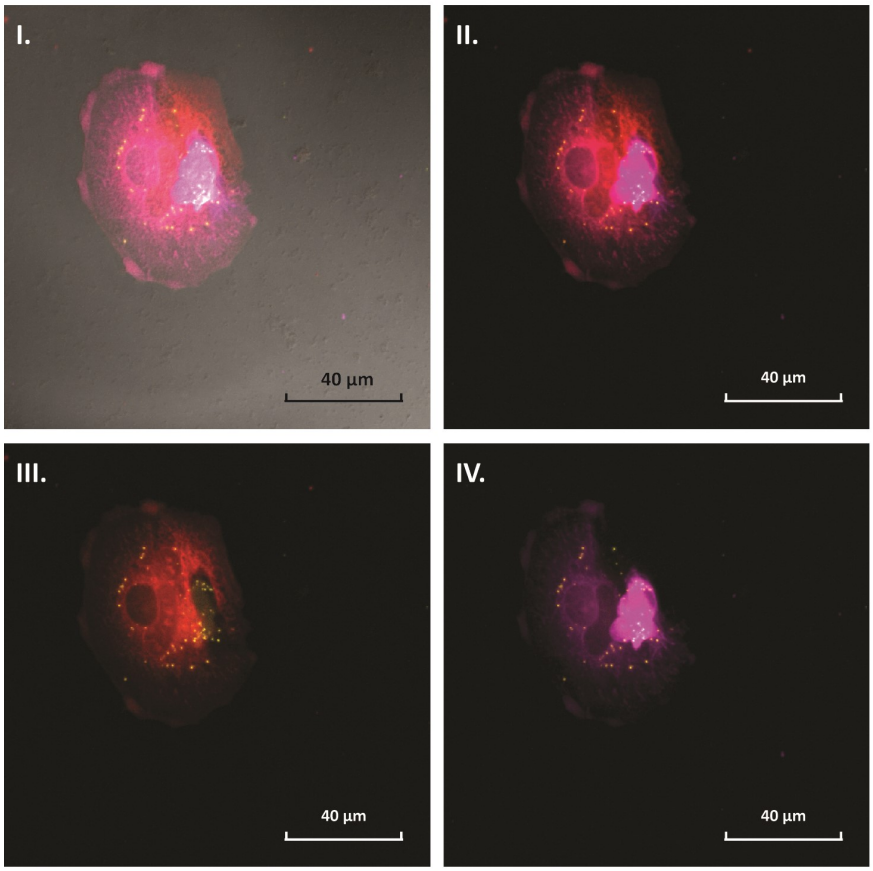

B)

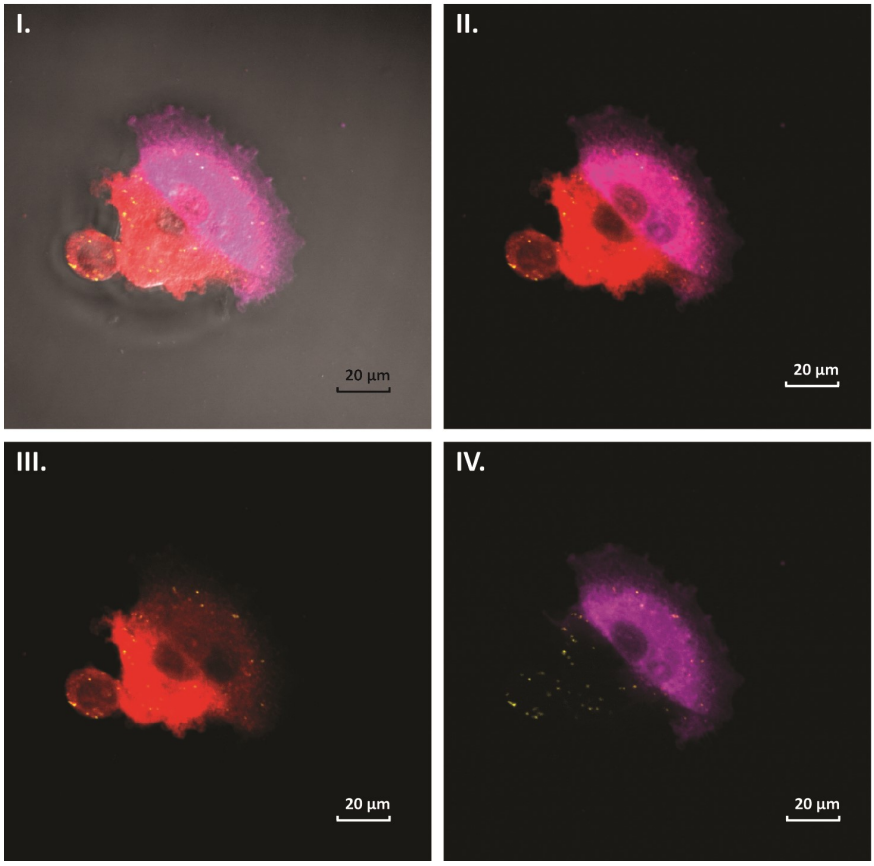

To ensure these observations were not an artefact of the CellTrace™ staining strategy for *in situ* RCA, fusion in ρ^0-eGFP/eGFP-astrocyte and C8D1A co-cultures were replicated in live-cells. Here, the eGFP expression in eGFP-astrocytes was imaged directly, as opposed to CellTrace CFSE™ as required for *in situ* RCA.

Depicted in **Figure 5.3.5**, live-cell imaging confirmed the cell fusion phenomenon in 24 h, 1:1 co-cultures. Cell fusion events were readily identified in cultures of both ρ^0-eGFP and eGFP-astrocytes. Because cell fusion events increased the total cytoplasmic area/volume of the final cell, the intensity of fluorescent signals corresponding to either original cell type appeared much dimmer in fused cells. The vast majority of fused cells appeared to be multinucleated. In many cases, the original nucleus of each cell type can be identified. From the images presented, this was most obvious in **Figure 5.3.5D**.

Because ρ^0-eGFP-astrocytes are auxotrophic for pyruvate and uridine, conditions with medium either supplemented with, or deprived of pyruvate and uridine were included in this experiment. This was to determine whether essential nutrient availability altered the fusion phenotype markedly. Cultures in all medium conditions produced fused cells, however there was no obvious difference between conditions.

While cell fusion was not an anticipated expected mechanism of IMT to be explored in this thesis, the phenomenon represents a means for mitochondria, presumably alongside all other cellular components, to transfer between cells. In the case of ρ^0 cells, it was possible that cell fusion could restore mitochondrial function. For this reason, further investigation of this phenomenon was carried out.

Figure 5.3.5. Live cell confocal microscopy confirms cell fusion events between eGFP-astrocytes and C8D1A astrocytes in plus or minus pyruvate/uridine medium
Live-cell LSCM of 24 h co-cultures of eGFP-astrocytes or ρ^0-eGFP-astrocytes with CellTrace Violet™ stained C8D1A cells. Co-cultures were seeded at a 1:1 ratio of each cell line. Each field presented here is representative of cell-cell fusion events across the population. Green = eGFP, Magenta = Celltrace Violet™. White arrows indicate cells within the field which appear to have fused. **(A)** eGFP-astrocytes in pyruvate/uridine positive medium. **(B)** eGFP-astrocytes in minus pyruvate/uridine medium **(C)** ρ^0-eGFP-astrocytes in pyruvate/uridine positive medium. **(D)** ρ^0-eGFP-astrocytes in minus pyruvate/uridine medium. For all panels, both cytoplasmic channels are displayed combined (left), alongside the eGFP/ρ^0-eGFP astrocyte channel alone (center) and C8D1A channel alone (right). Images were collected by LSCM at 600 x magnification.

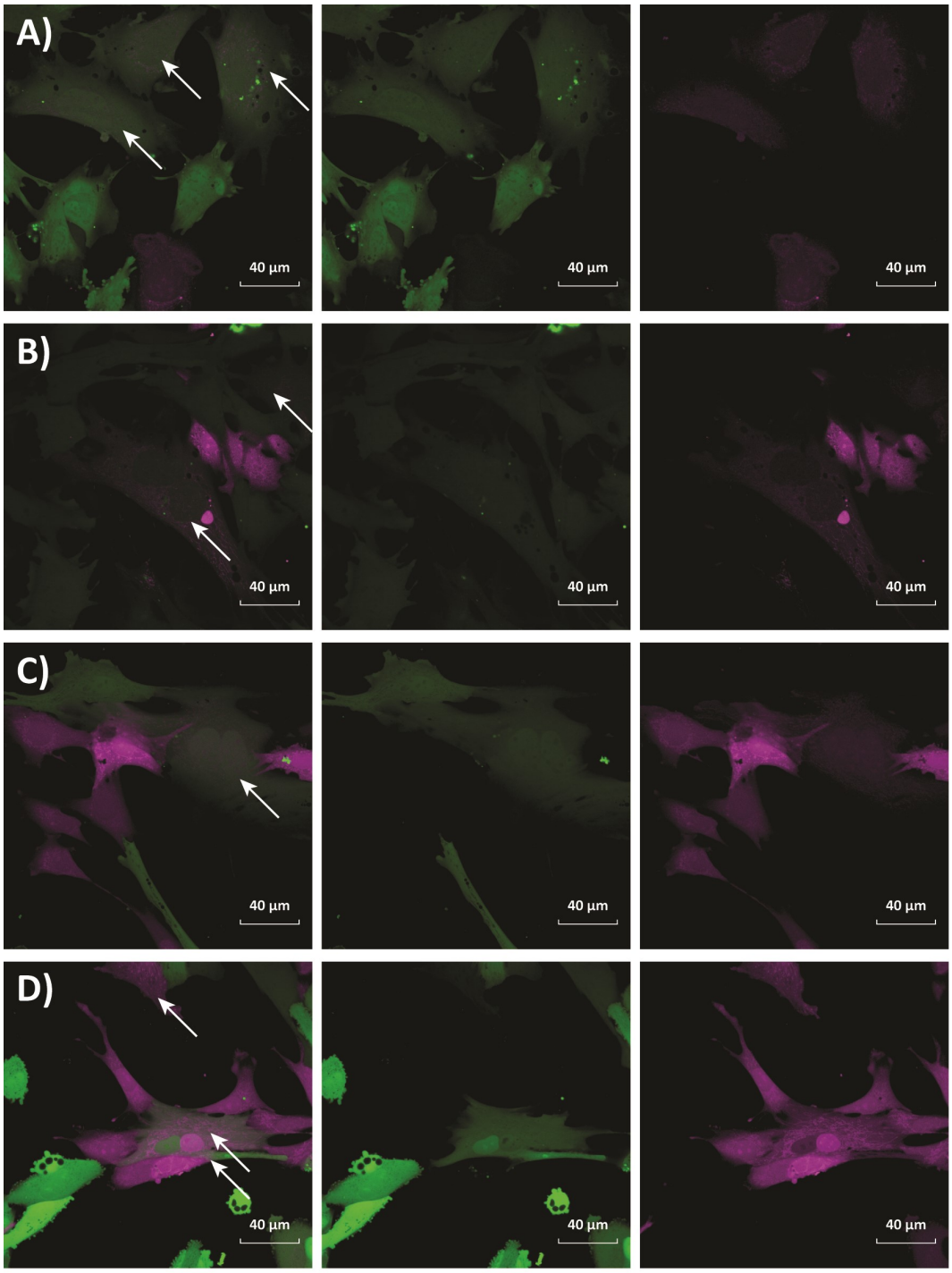
A)
40 µm
40 µm
40 µm
B)
40 µm
40 µm
40 µm
C)
40 µm
40 µm
40 µm
D)
40 µm
40 µm
40 µm

Cell fusion between ρ^0-eGFP/eGFP-astrocytes with C8D1A was abundant when viewed by LSCM. However qualitative microscopy was not sufficient for accurate quantification of this phenomenon.

To gain insight into how regularly this process occurred, cell fusion in eGFP-astrocytes/C8D1A co-cultures was quantified by flow cytometry. Conveniently, the existing labelling strategy enabled cytometric identification of each original population of cells, along with the dual-labelled, fused cells.

In **Figure 5.3.6A**, a simple gating strategy is represented, and was used to identify each cell population. Intact cells were first separated from debris on the basis of size by applying a gate on FSA/FSH. For mono-cultures of each cell line, a singular, bright population resulted from events within this gate in the corresponding fluorescence channel.

When applied to a co-culture, three discrete populations were immediately identifiable, as demonstrated in **Figure 5.3.6B**. Each individual cell line appears as a discrete population separated by the fluorescence axis which corresponds to a CellTrace™ colour, in quadrants Q1 and Q3. A third, defined population of events fall into quadrant Q2. These correspond to dual labelled, fused cells. The cells with the lowest stain intensity were gated into Q4, as any fused cells made up from these would not be adequately separated from Q1 or Q3. Events within Q4 were removed from the analysis. This allowed for fusion in independent co-culture experiments to be compared accurately.

This simple gating strategy does not include a typical doublet exclusion by FSA/FSW, SSA/SSW, FSA, SSW or SSA, FSW plots [301]. This was avoided, as the unusual morphology of fused cells distorted the typical position of some, but not all, fusion events. To control for doublets, monocultures of each line were harvested in parallel to the co-cultures. Each was mixed at a 1:1 ratio and immediately processed alongside the co-culture samples, to determine the level of doublet formation resulting from cell-cell interactions post-harvest. Typically, doublets formed in this way were never observed above 1% of the total events. This control enabled conservative quantification of genuine fused cells from co-cultures.

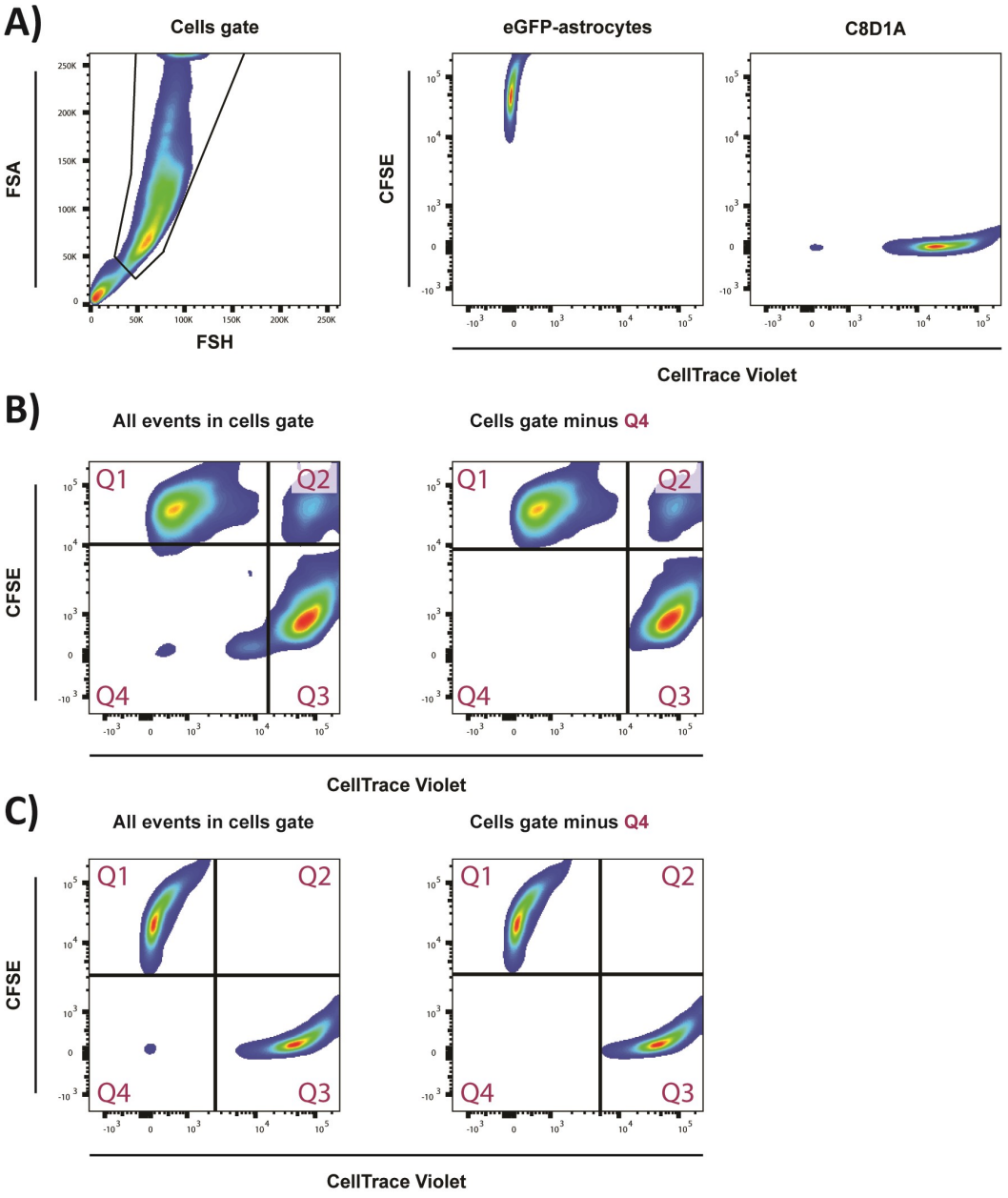

Figure 5.3.6. Cell fusion between eGFP-astrocytes and C8D1A astrocytes is quantifiable by flow cytometry

To quantify cell fusion between eGFP-astrocytes and eGFP astrocytes by flow cytometry, the gating strategy adopted was as follows. **(A)** Events were gated first by FSA/FSH to exclude debris. Events within this gate are then separated by fluorescence channels for CFSE and CellTrace Violet™. To demonstrate, a monoculture of eGFP-astrocytes (middle) or C8D1A (right) are displayed. **(B)** A 24 h co-culture of stained eGFP-astrocytes (CFSE) and C8D1A (CellTrace Violet™) astrocytes, separated by fluorescence. Q4 is excluded (right) to remove events below a minimum intensity threshold. A new quadrant gate is applied and Q1, 2 and 3 quantified. Fused cells appear as events in Q2. **(C)** 'Doubleting control' for fusion experiments. Monocultures of stained eGFP-astrocytes or C8D1A were mixed immediately prior to co-culture harvest, to determine the extent of natural doublet formation in cytometry samples. A typical doublet exclusion by SSA/SSW gates was not made for these analysis due to the atypical morphology of fused cells.

In **Figure 5.3.7**, the frequency of cell fusion in eGFP-astrocyte/C8D1A co-cultures was determined, as a function of seed ratio. Cell fusion requires at least two individual cells; one or more from either individual population. For this reason, the availability of each line to engage in fusion with the other, was hypothesised to influence the frequency of fusion events in the population. A series of co-culture experiments were performed whereby 100,000 eGFP-astrocytes were seeded with varied ratios of C8D1A, and vice versa. Through these experiments I sought to determine which cell line drove the fusion phenotype.

In **Figure 5.3.7A**, 100,000 eGFP astrocytes were seeded with varied ratios of C8D1A. The number of eGFP-astrocytes involved in fusion events increased in a near-linear fashion when additional C8D1A were seeded into co-culture. The number of C8D1A involved in cell fusion trended towards a decrease as additional C8D1A were seeded into co-culture. When the roles of each cell line was reversed, as in **Figure 5.3.7B**, the opposite relationship was observed. This indicated that the number cells involved in fusion events was dependent on a cells ability to contact a cell of the other type in the culture.

Interestingly, the trend lines from this data cross at an approximate 1:1 seed ratio, for each dataset in **Figure 5.3.7A** and **(B)**. This suggests that neither the eGFP-astrocytes nor C8D1A cells were dominant in the fusion interaction. From these results, it appeared that fusion interactions between these two cell lines was likely driven by some other, unknown variable.

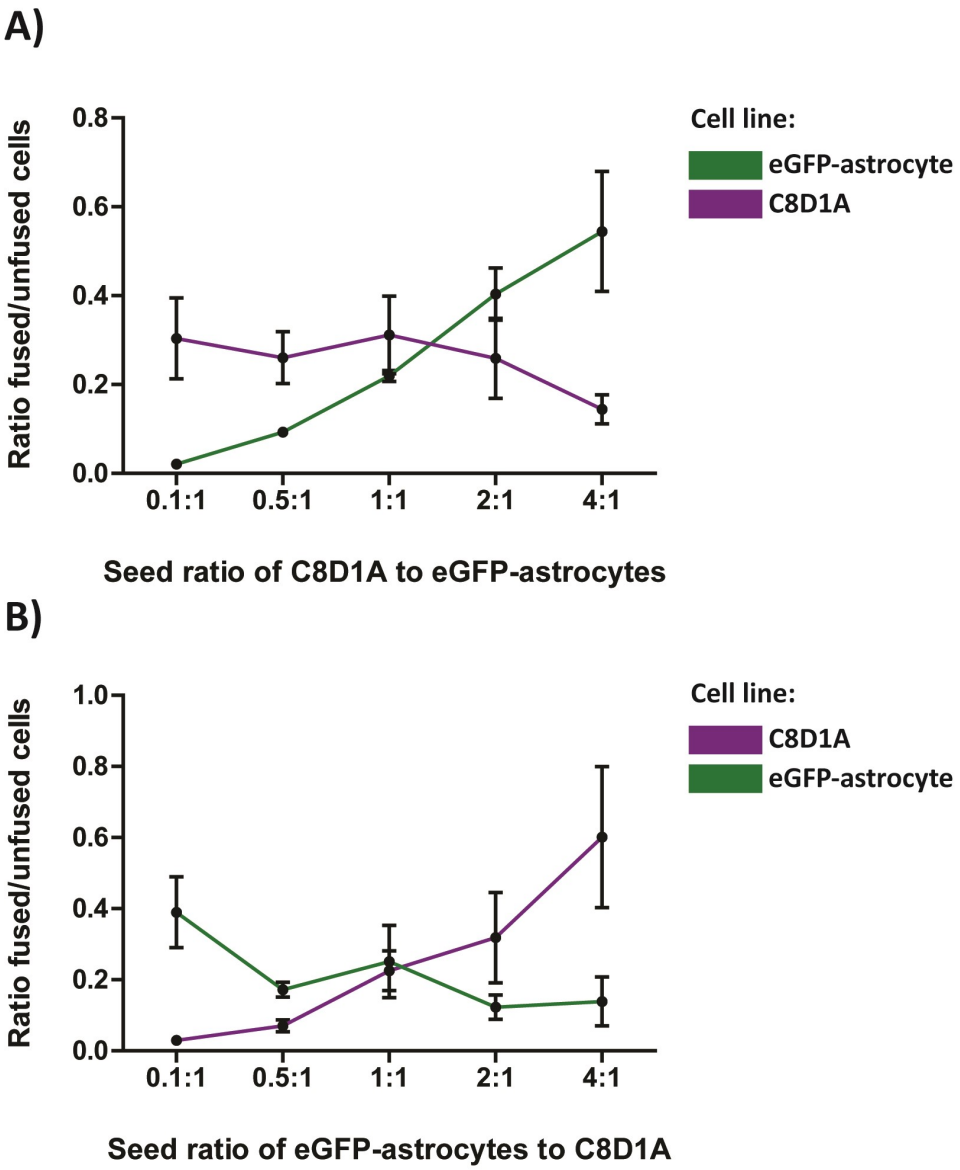

Figure 5.3.7. The frequency of cell fusion between C8D1A and eGFP-astrocytes is altered by 'fusion partner' availability

Twenty-four h co-cultures of CFSE stained eGFP-astrocytes and CellTrace Violet™ stained C8D1A were assessed for fusion by flow cytometry, as described in **Figure 5.3.6**. One hundred thousand eGFP-astrocytes **(A)** or C8D1A **(B)** were seeded per well of a 6-well plate and co-cultured with varied ratios of the C8D1A **(A)** or eGFP-astrocytes **(B)**. Results are reported as the mean ratio of fused cells ± SD from 3 and 4 independent biological replicates for **(A)** and **(B)** respectively. The ratio of fused cells is defined as the proportion of double positive events from the total single positive events of the cell line in limited abundance, within the co-culture.

I was interested in how (or if) these astrocyte lines resolved the state of multi nucleation caused by cell fusion. If these cells were stable entities, presumably one cell nucleus would assert transcriptional control while the other underwent nuclear fragmentation. If the cell fusion observed here was a component of a survival mechanism, I hypothesised the fused cell would resolve the multinucleated state and persist in culture.

In **Figure 5.3.8**, the results of a DNA content analysis on 1:1 co-cultures of eGFP-astrocytes and C8D1A are presented. In this experiment, a co-culture was harvested and fixed from each of 12, 24, 48 and 72 h time-points after initial seeding. If the multinucleated state was resolved over time, I expected to see growth in the relative area under curve corresponding to the G1 peak (2N).

While only a single replicate of this experiment, the results presented indicate that multinucleated cells persisted in culture over time. This was either because resolution requires more than 72 h, or new fusion events constantly renew the multinucleated population. Within the fused cell population, DNA content for a large proportion of the fused cells remained well above the typical G2 (4N) peak. Peaks which correspond to 6N, 8N and even up to 10N DNA content were detected in this cytometry. Interestingly, minor peaks which correspond to half a nuclear complement are also visible in these results. This could be due to partial degradation of individual nuclei, or replication of some, but not all nuclear material. The higher order DNA content peaks are likely caused by multiple cells becoming fused with a single heterokaryon, or an endoreduplication process after the initial fusion event.

Based on these results, it is tempting to speculate that cells with higher nuclear DNA content (4N+) accumulate over time, but as a single experiment, this remains undetermined.

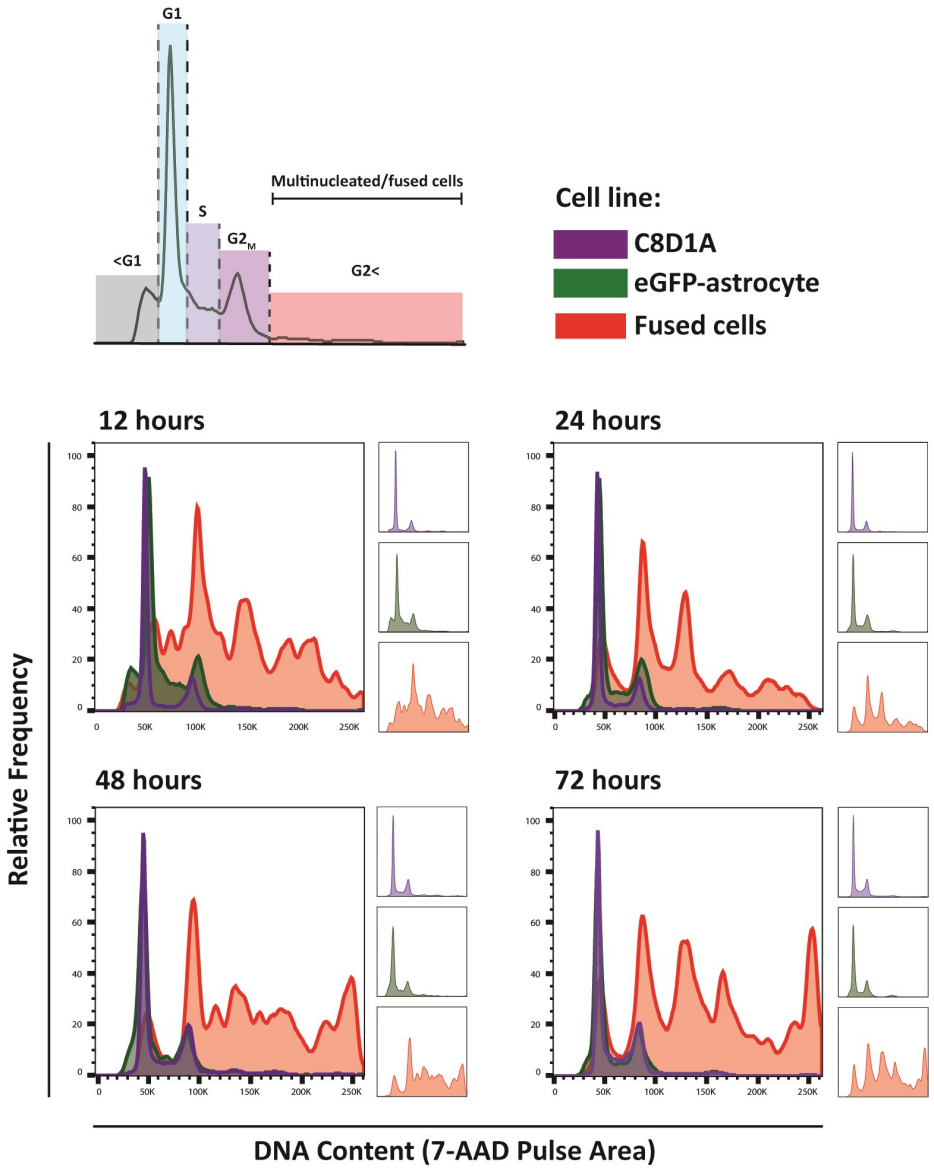

Figure 5.3.8. DNA content by flow cytometry reveals chaotic nuclear content in eGFP-astrocyte/C8D1A fused cells from varied durations of co-culture
Cells from 1:1 co-cultures of CFSE stained eGFP-astrocytes and CellTrace Violet™ stained C8D1A were harvested at 12, 24, 48 and 72 h for DNA content analysis. Cells were fixed with 70% ethanol and stained with 7-AAD before cytometric analysis. 7-AAD pulse area vs width was used to identify events which corresponded to single cells. Results are presented as a normalised histogram from a single preparation of co-cultures.

5.3.4 Primary murine brain pericytes as candidate IMT 'donor' cells.

In parallel to the discovery of mitochondrial 'donor' cells via the strategy presented in **Figure 5.3.2**, primary brain pericytes were investigated as candidate IMT donor cells. These cells were generated from adult brain microvessel fragments cultured in a defined medium, where the vast majority of adult neural cells do not survive *in vitro*. This was exploited to generate uniform cultures, in medium which favoured growth of pericytes.

In **Figure 5.3.9**, development of a brain microvessel culture is presented as representative images over time. Here, isolated microvessels fragments from whole brain initially associated with the collagen-coated surface of a standard tissue culture flask. On the first day *in vitro* **(DIV1)**, gentle washes removed the majority of neural cell types and residual blood cells, which did not adhere. Depicted in **DIV1 P0** (passage 0) are microvessels as observed after these initial washes. Multiple individual microvessel fragments were visible, marked by yellow stars. The macro-structure of these fragments remained intact in the initial stages of culture development. Cells were seen to out-migrate from under the fragments. Very few cells were adhered to the flask surface, other than those directly adjacent to the fragments.

Figure 5.3.9. Primary microvessel cultures derived from murine brain
Representative phase contrast images of a primary pericyte culture over time. Yellow stars demarcate microvessel fragments from which cells out-migrate over time. DIV(n) = days *in vitro*, P(n) = Passage. Images were collected at 50 x magnification by light microscope.
To further characterise the cells derived from primary brain microvessel cultures, a six colour antibody panel was designed for use in flow cytometry. Immunophenotyping was performed after the third passage of DIV8 P2 microvessel cultures, to gain insight into the identity of these cells.

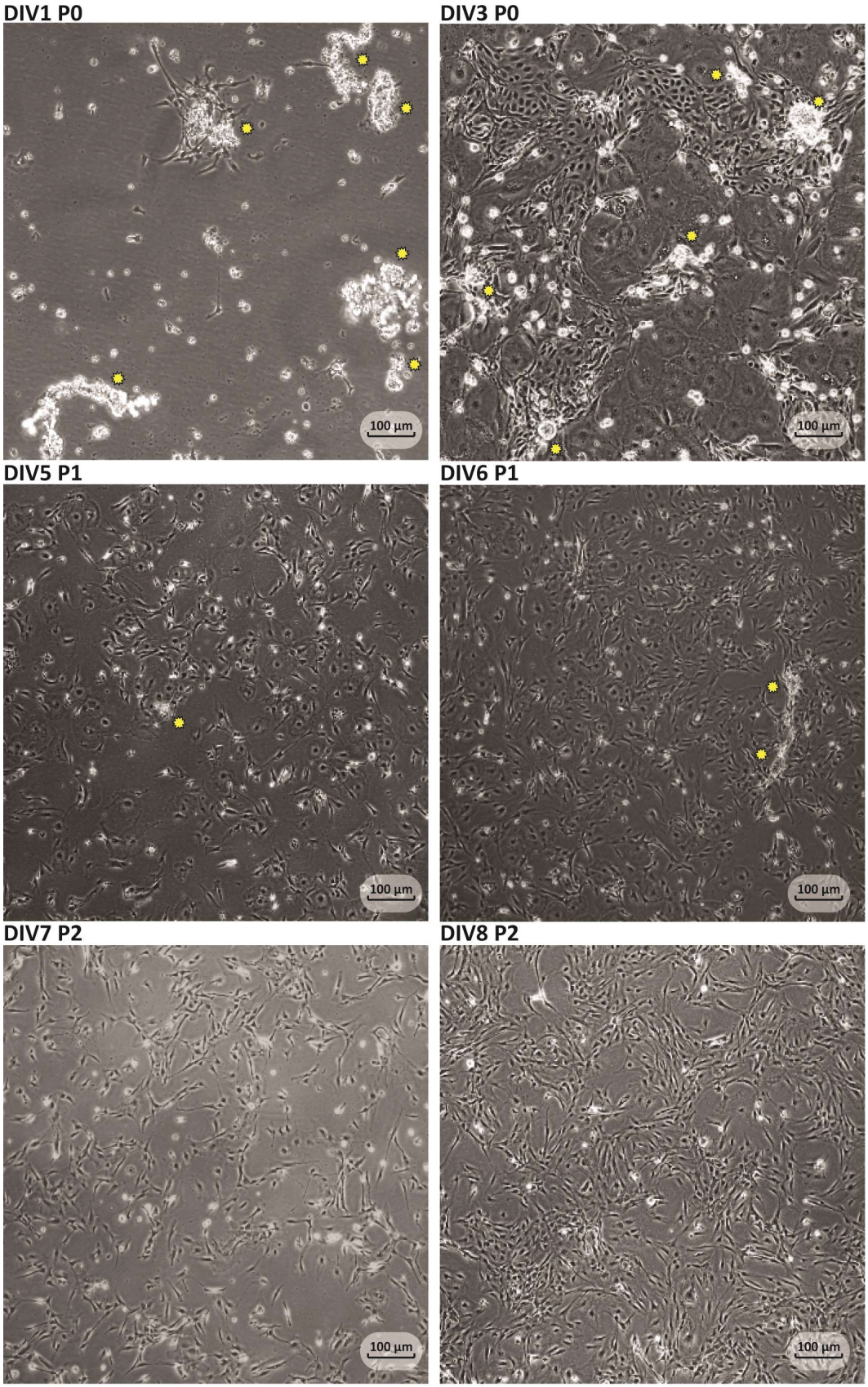
DIV1 P0
100 µm
DIV3 P0
100 µm
DIV5 P1
100 µm
DIV6 P1
100 µm
DIV7 P2
100 µm
DIV8 P2
100 µm

By **DIV3 P0** *in vitro*, the cultures reached a high density. Vessel fragments were still present, but were less prevalent. This was because almost all cells have out-migrated from the fragments. At this stage, two clearly identifiable cell populations were present. Large circular cells approximately 50 µm in diameter were seen in clusters, with smaller, darker cells arranged into streaky regions. These corresponded to endothelial cells and pericytes respectively [302-305]. The pattern formed was highly ordered, as the pericyte/endothelial cell relationship continued to drive self-arrangement on the 2D plastic surface.

At **DIV3**, the cells were redistributed into new uncoated flasks at 50% density. At **DIV5 P1**, endothelial cells were reduced in relative abundance. By redistributing the cells at passage 1, the cultures lost self-arrangement characteristics and remained more evenly spread over the surface. By the following day at **DIV6 P1,** the proliferative capacity of the pericytes, compared to endothelial cells, became apparent. The endothelial cells lose their 'pillow-like' appearance, possibly in connection to the known inability of these cells to thrive under these conditions *in vitro* [302, 305].

After a further passage, **DIV7 P2** cultures were made up of uniform, spindly or trapezoid shaped cells. Very few circular endothelial cells survive or have proliferated this point. By **DIV8 P2**, a high cell density for the cultures was reached once more. All experiments with primary cells from brain microvessel cultures were seeded with cells harvested in this state.

In **Figure 5.3.10A**, the gating strategy for phenotyping, and antigen positivity for each surface marker is presented. A gate was first placed on the FSA/FSH axis to separate debris away from the cell populations on the basis of size. FSA/FSW was then used to exclude doublets from the population. Representative histograms are presented for each surface marker, from a single preparation of a microvessel culture.

Presented in **Figure 5.3.10B** and summarised numerically in **Table 14**, are the immunophenotyping of results from three independent BALB/cByJ brain microvessel cultures.

Table 14. Quantification of pericyte surface antigens

Surface antigen	Percent of cells (% ± SD)
CD90.2	78.70 ± 9.17
CD73	97.60 ± 2.01
CD140b	99.90 ± 0.10
CD105	80.43 ± 26.63
AN2	83.23 ± 6.67
CD146	88.83 ± 10.17

The antigens used to characterise murine pericytes here were selected from literature [302, 306-314]. Almost every cell within DIV8 P2 microvessel cultures was found to be positive for CD140b (also known as PDGFRβ). At 99.90 ± 0.10% positivity in the population, the presence of this principle marker was a strong indication that these cultures were in fact pericytes. This marker is not expressed at levels detectable by immunofluorescence, by other cells in brain tissue. The mesenchymal marker CD73 was found to co-stain at an equivalent frequency to PDGFRβ. Two other characteristic mesenchymal stem cell markers, CD90.2 and CD105 were also detected on majority of cells in the culture. Two of the three cultures had almost complete positivity for CD105, while the third had approximately 50% fewer cells positive for this marker. CD90.2 was more consistently expressed in the population, at 78.70 ± 9.17%. The loss of CD105 expression from a large number of cells in a single replicate was an intriguing result, and may indicate that this particular culture had begun to differentiate. This culture appeared to be a major source of

variation within the datasets. Alternatively this could have been a technical issue with staining, or similar.

Two additional characteristic murine brain pericytes markers, CD146 and AN2 were detected on approximately 80-90% of the population. Interestingly, CD90.2, CD146 and AN2 were not lost from the same individual cells in the culture. This suggests that under these conditions *in vitro,* partial differentiation or subtypes of pericytes were developed. This is consistent with the heterogeneous descriptions of these cells *in vitro*, in the literature [310, 315-319], where pericytes remain poorly defined in terms of identity.

Taken together, the morphological features observed in **Figure 5.3.9** and the results of immunophenotyping in **Figure 5.3.10** provided confidence that high purity pericytes were successfully cultured *in vitro,* and were suitable for use in IMT experiments.

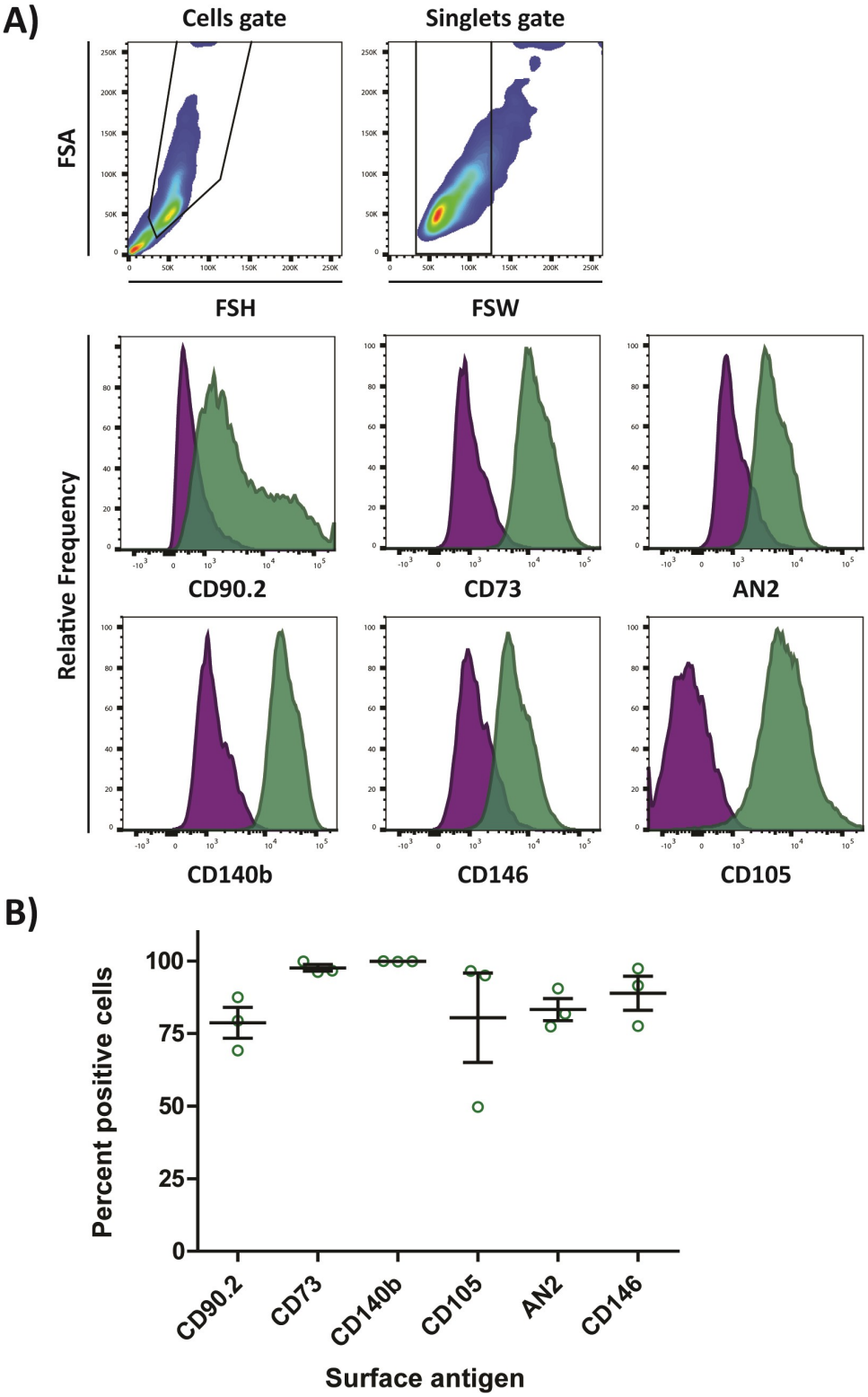

Figure 5.3.10. Cells derived from brain microvessels are positive for pericyte markers

(A) Immunophenotyping of murine microvessel cultures by flow cytometry. A cells gate was first set to remove debris from analysis, before a FSA/FSW doublet exclusion was applied. A six colour antibody panel was used to detect surface antigens characteristic of brain pericytes. Representative histograms are presented for each surface antigen as stained vs unstained controls. **(B)** Summary scatter plot of surface antigen positivity from three independent biological preparations of DIV8 P2 BALBC/cByJ brain microvessel culture. Results are presented as the mean ± SD.

To establish if primary murine pericytes were capable of mitochondrial donation, 24 h 1:1 co-cultures with eGFP-astrocytes were established. These cultures were prepared with pericytes generated from C57BL/6 x mito-DsRed tissue. In **Figure 5.3.11**, representative images are presented of eGFP-astrocytes which have engaged in IMT with primary pericytes. In **Figure 5.3.11A**, *in situ* RCA was performed on these co-cultures, with PDPs targeted to both mtDNA_9461G and 9348G. Many mtDNA_9348G RCPs were detected within CFSE stained eGFP astrocytes, which corresponded to the endogenous mtDNA of these cells. Unlabelled pericytes are present in the first image **(top)**, filled with mtDNA_9461G RCPs, which correspond to pericyte mtDNA.

Within various individual eGFP-astrocytes, multiple mtDNA_9461G RCPs (yellow) were detected. Each of the enlarged panels **(AI, AII, AIII and AIV)** depict the majority of the cytoplasmic area from one or two individual cells. These cells each display several mtDNA_9461G RCPs indicated by the white arrows; far more than would be expected as false positive ligation events. In contrast, other cells in these two representative fields display either no, or a single, non-specific mtDNA_9461G RCP. Cells like those shown were readily located within the co-culture. This was expected based on the reaction selectivity data determined in chapter 4. Together, these observations indicated that mtDNA transfer had occurred from pericytes into some, but not all eGFP-astrocytes. Interestingly, transfer of eGFP-astrocyte mtDNA into pericytes was not obvious, as mtDNA_9348G RCPs were not readily identified in unlabelled cells.

With these promising results, I replicated the observation of IMT with these pericytes as 'donor' cells using live-cell microscopy. The mito-DsRed mouse strain expresses a mitochondrial import sequence in frame with the fluorescent protein DsRed2; hence mitochondria in this mouse are brightly labelled. In **Figure 5.3.11B**, two representative image fields from an eGFP-astrocyte/pericytes culture are presented. In each of the two images, two eGFP-astrocyte cells (magenta) have been identified within the magnified regions **(BI, BII)**. Each of these cells displays numerous point sources, or elongated objects in the DsRed2 optical channel (yellow). These objects are consistent with the appearance of singular mitochondrion labelled with fluorescent protein. This indicated that whole mitochondria from pericytes were transferred into eGFP-astrocytes. While many cells were present in which this could be observed, the transfer events were more difficult to locate than those detections made by RCA in **Figure 5.3.11A**.

Taken together, these results indicated that primary brain pericytes were a capable mitochondrial donor for use in co-culture with eGFP-astrocytes.

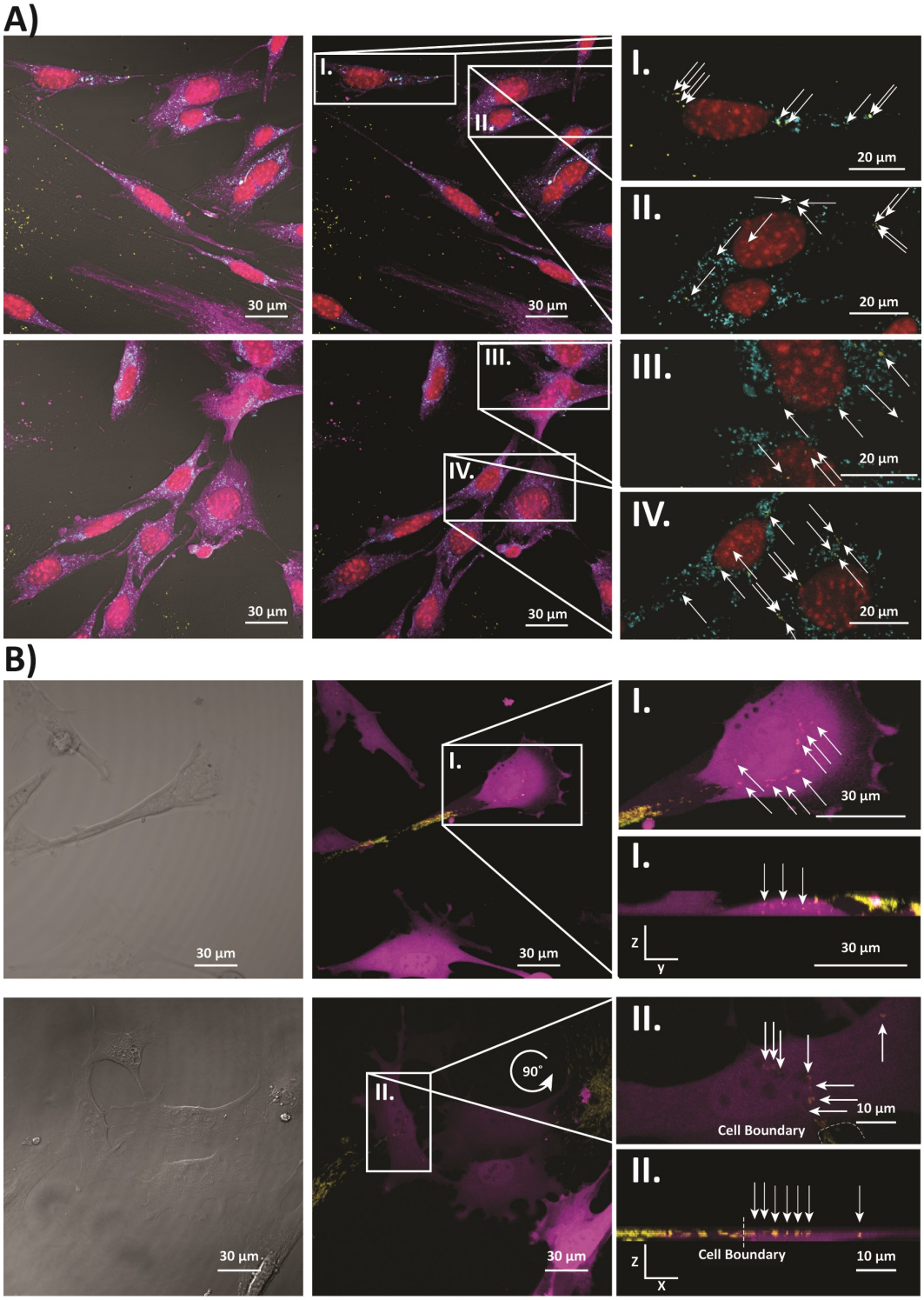

Figure 5.3.11. Murine brain pericytes are capable mitochondrial donors to eGFP-astrocytes

Primary cultures of C57BL/6 x mito-DsRed pericytes co-cultured with eGFP-astrocytes for 24 h. **(A)** Two representative fields of CellTrace CFSE™ stained eGFP-astrocytes (magenta) with unlabelled pericytes in RCA reactions targeted to mtDNA_9461G (yellow) and 9348G (cyan). Each image sub-field in white squares I, II, III and IV **(right)**, demonstrate mtDNA_9461G RCPs in eGFP-astrocytes, indicated by the white arrows. The cell nuclei are labelled with PI (red). **(B)** Two representative image fields from live-cell LSCM of eGFP astrocytes (magenta) with mito-dsRed (yellow) pericytes. A sub-field from each image **(I, II.)** is presented in X-Y and an orthogonal axis. Images were collected by LSCM at 600 x magnification.

5.4 Discussion

The 'multi-culture' screening approach enabled by *in situ* RCA for 'donor' mtDNA made identification of these combinations of cells a highly efficient process. I was able to rapidly identify novel IMT interactions, with significantly less resources than required by traditional methods. To look for IMT in this number of live-cell, two cell type co-cultures, would have required hundreds of hours, in both preparation and observation of the cultures by LSCM. It was possible that IMT could be in some way restricted by the presence of multiple cell types in the 'multi-cultures', but the gain in efficiency for identifying these interactions made this an acceptable limitation.

Among those interactions observed, the eGFP-astrocyte cell line and its ρ^0 derivative were determined to be capable IMT 'recipient' cells. These cells were immortalised from PO mouse astrocytes [262], so also fit well with my intention to study IMT in a neural cell type.

The way the eGFP-astrocytes and its ρ^0 derivative interacted with C8D1A was highly unexpected. Cell fusion certainly fits the definition of IMT, albeit less elegantly than vesicle mediated or TNT mediated transfer of organelles. Whether or not the fusion process is linked to cell survival in some way is less clear. Cell fusion is a reasonable hypothesis by which to explain the recovery of mtDNA in intracranial ρ^0-GL261, as had been observed in the Berridge laboratory. For this reason, cell fusion in the eGFP-astrocyte/C8D1A co-culture model was explored further in this thesis.

Interestingly, co-cultured cells were examined by flow cytometry, the fluorescence of each line in the channel it was not directly stained for, increases. This is seen via the shape of each initial population in **Figure 5.3.7**; a warped circular cloud of events as opposed to a narrow, straight line for mono-cultured cells. This is likely caused by cellular sharing of membrane fragments, extracellular vesicles or secreted proteins when placed in co-culture, as was often seen in microscopy.

While ρ^0 cell types are incredibly useful tools to study IMT, a powerful aspect of *in situ* RCA to study IMT is the ability to study these processes in mtDNA replete cells. Demonstrating mtDNA transfer into mtDNA replete cells *in vitro,* as presented in this chapter, is a highly original result.

With confidence in the ability of *in situ* RCA to detect IMT, I sought to identify a cell type in the brain microenvironment capable of acting as an IMT 'donor' *in vitro*. A question was posed: What types of cell are actually found in the brain? A broad and overly simplified answer to this is the neuron, astrocyte/astroglia, oligoglia/oligodendrocyte, microglia and

neural progenitor or stem cells. Neural progenitor cells stood out as a candidate of interest, as perhaps something about 'stemness' could mean these cells would act like MSCs. This was a major driver behind the inclusion of the NE-4C neural progenitor cell line in my *in vitro* experiments. Disappointingly, NE-4C did not demonstrate obvious IMT interactions in the 'multi-culture' screens, so was not investigated further.

Still interested in the idea of 'stemness' and how it may relate to IMT, I looked for possible 'donor' cells which appeared most similar to MSC, within the brain microenvironment. While the brain consists largely of those cell types listed previously, additional candidate cell types were hidden in plain sight; the brain itself is highly vascularised, as well as covered in meningeal layers. With these additional structures, fibroblast, endothelial, smooth muscle, and most intriguingly, pericytes are also cell types abundant in the brain microenvironment.

Pericytes of the CNS are derived from both the neuroectodermal and mesenchymal cell lineages [320]. They share canonical surface antigens with MSCs (CD90.2, CD73 and CD105) [302, 306-314, 321] and exhibit multipotential stem cell activity *in vitro* [322], though there is evidence to suggest this does not occur *in vivo* [323]. Additionally, pericytes are reported to have various reactive activities under inflammation or injury that may be involved with regeneration [324-330] and have been shown to transfer α-synuclein [331] between cells via tunneling nanotubules. It is possible that α-synuclein aggregates associate with mitochondria, as proteins prone to aggregation are known to accumulate in the mitochondria [332, 333]. Regardless, these shared characteristics, and their presence within the brain microenvironment, led to the hypothesis that primary pericytes might act as good 'donor' cells for IMT.

After primary pericytes cultures were established and characterised, the ability of these cells to transfer mtDNA into eGFP-astrocytes was assessed by RCA. Fortunately, IMT was readily identified in these co-cultures, and successfully confirmed by live-cell microscopy. This was an exciting result, given no similar report appears in the literature. Given the prevalence of the interactions, primary pericytes were selected to act as 'donor' cells for IMT with eGFP-astrocyte 'recipient' cells for my intended injury studies. The interactions were readily detected by RCA, but were more difficult to find using mitochondrial targeted fluorescent proteins. While anecdotal, this observation supports the use of *in situ* RCA to detect genuine IMT via transfer of mtDNA.

The results presented here demonstrate that eGFP-astrocytes and pericytes *in vitro*, but in no way implicates a pericytes/astrocyte IMT interaction *in vivo*. While it is tempting to speculate that pericytes could interact with neural cells like this *in vivo*, experimental

validation is required and is beyond the scope of this thesis. With brain pericytes identified as a novel 'donor' for IMT, and eGFP astrocytes a good 'recipient', results presented in this chapter established a suitable model in which to investigate the effect cellular injury has on the rate of IMT.

6 Cellular injury and IMT

6.1 Introduction

In chapter 5, primary pericytes were identified as an IMT 'donor' cell type suitable for quantitative studies of IMT, when co-cultured with eGFP-astrocytes. It was now possible to apply the novel molecular strategy developed in chapter 4 to this *in vitro* model, to quantify IMT between cells derived from the brain microenvironment. Intercellular mitochondrial transfer was found to occur readily between the pericyte 'donor' cell and the eGFP-astrocyte recipient under basal conditions. With this established, the rate of IMT in basal conditions could now be compared to co-cultures where the eGFP-astrocytes were subject to injury. If the rate of IMT increased in response to injury, this would suggest IMT may act as a component of the cellular response to injury. This is of particular interest in cancer therapy, whereby cells may use IMT to resist the direct effects of therapy. Alternatively, disease recurrence after therapy may also be influenced by recovery of mitochondrial function in residual cancer cells.

With this knowledge, three means to induce stress in eGFP-astrocytes were selected, to investigate how each would impact on the rate of IMT in the eGFP-astrocyte/pericyte co-culture model.

6.1.1 Chloramphenicol

Chloramphenicol (CMP) is a small molecule antibiotic originally isolated from *Streptomyces venezuelae* in 1947 [334]. With several valuable pharmacological properties, chemical syntheses were rapidly developed [335, 336] and the compound deployed for clinical trial. Reversible binding of CMP to the 50s and 70s ribosomal proteins of prokaryotic organisms mediates toxicity by inhibition of peptidyl transferase activity [337]. Unfortunately, the mammalian mitochondrial ribosome (mtR) retains enough homology with the prokaryotic forms at several binding sites, so are susceptible to this antibiotic [338]. Use of CMP in humans rapidly declined, given several clinical complications associated with treatment emerged soon after the compound became available [339-344].

Because CMP inhibits peptide elongation within the mitochondria, each of the 13 proteins and other peptides translated in the mitochondria are impacted in treated cells. This has been shown to impair mitochondrial bioenergetics, cause profound changes in mitochondrial morphology, increase cellular production of lactate and decrease the growth rate of treated cells [345-351]. Chloramphenicol has been implicated in resistance to apoptosis in HepG2 and H1299 cells treated with mitomycin, through a p21 dependent

pathway by Li et al. [352]. Morphological changes and activation of the senescence biomarker SA-βGal were also described in this study [352]. In follow up studies, Li et al. describe reduced ATP biosynthesis, increased MMP-13 expression, enhanced invasion and senescence-like phenotype in H1299 cells treated with CMP [353]. Together, these cellular effects describe mitochondrial dysfunction induced by direct inhibition of mitochondrial protein synthesis. This made CMP a compound of interest for injury of IMT 'recipient' cells, as all aspects of the induced mitochondrial dysfunction could potentially be alleviated by IMT. I hypothesised that the rate of IMT would be enhanced by CMP treatment, to aid cell survival.

6.1.2 Cisplatin

Cisplatin (CSP), or cis-diamminedichloroplatinum^{2+} is a square planar co-ordination complex originally identified as bioactive among a series of platinum salts found to induce filamentous growth in *E. coli* [354, 355]. This discovery was made serendipitously while investigating the effect of electric fields on *E. coli* growth. Soluble Pt^{2+} complexes were produced at platinum electrodes by electrolysis, when an electric field was applied to cultures of *E. coli* [356]. The potent anti-tumour properties of these platinum compounds were quickly recognised [357], and CSP approved for use in cancer therapy by the U.S. FDA in 1978 [358]. The compound has found widespread therapeutic use in the treatment of ovarian, testicular, head and neck, colorectal, prostate, lung and breast cancer [358, 359] and is considered an effective chemotherapeutic.

Cisplatin exerts potent cytotoxic effects through multiple mechanisms, though best understood is the interaction with DNA [360, 361]. Within the cytosol, chloride atoms are displaced from the complex by H_2O. In this form, the diamminated cisplatin complex acts as a potent electrophile; sulfhydryl groups on proteins or nitrogen electron donors, particularly those within purine residues of DNA, become susceptible to drug binding [359]. The compound forms both inter- and intra-strand cross links between purine residues, though the latter occurs at a higher rate [360, 361]. The presence of these adducts disrupts DNA repair mechanisms, replication, transcription and leads to an induction of apoptotic cell death [359].

The toxicity of cisplatin however, is not entirely explained by damage to the nuclear genome. Treatment with the compound produces an oxidative stress phenotype in cells [362-364]. Production of ROS after CSP treatment was demonstrated to be dependent on mitochondrial redox status by Marullo et al. [365]. This implicated the mitochondria as a second major site where the cytotoxic effects of CSP are mediated. Indeed, cisplatin is found to accumulate in mitochondria and mtDNA, potentially driven by the

electrochemical gradient associated with mitochondrial membrane potential [366, 367]. In mtDNA, intra-strand crosslinks caused by CSP are found at frequencies that exceed multiple orders of magnitude, compared with nDNA; this is thought to be due to both enhanced accumulation of adducts [366, 367], and a lack of a base excision repair mechanism capable of acting on intra-strand crosslinks within the mitochondria [368].

The mitochondrial specific component of CSP induced damage made this a valuable injury to explore in the context of IMT. Damage to the mitochondrial proteins and to mtDNA, the resultant generation of ROS, and eventual loss of mitochondrial function likely caused by cisplatin, all fit the profile of agents shown to influence IMT. A single report by Boukelmoune et al. during the course of this thesis describes IMT mediated neuroprotection of neural stem cells from cisplatin toxicity [205].

6.1.3 The ρ^0 cell as a model of chronic metabolic injury

A lack of functional respiratory complexes in ρ^0 cells means these cells are incapable of mitochondrial respiration [113]. In order to survive, ρ^0 cells must be supplemented with exogenous pyruvate and uridine through the growth medium. When glucose is provided, ρ^0 cells utilise glycolysis to generate ATP, however to sustain this process, conversion of pyruvate to lactate is required to re-oxidise NADH to NAD^+ [369]. The pool of available pyruvate is depleted to maintain the cellular redox balance through generation of lactate and NAD^+. This comes at the expense of acetyl-CoA production, which would typically fuel the TCA cycle to produce numerous biosynthetic intermediates as well as more NADH and $FADH_2$, in respiratory competent cells. NADH and $FADH_2$ would then be re-oxidised during mitochondrial electron transport as part of aerobic respiration, to fuel continued glycolytic and TCA cycle activities. In the ρ^0 cell deprived of supplementary pyruvate, glycolysis stalls as pyruvate is less available for conversion to lactate, to maintain re-oxidation of NADH to NAD^+ [370]. The cell ceases to produce acetyl-CoA as any pyruvate is consumed to maintain glycolytic production of ATP. This prevents synthesis of many biosynthetic intermediates via TCA, halting cellular growth and repair.

In addition to the requirement of exogenous pyruvate, a lack of functional complex III in ρ^0 cells prevents conversion of dihydroorotate to orotate in the mitochondria [371]. This process is essential for the *de-novo* synthesis of pyrimidine nucleotides. Supplementing ρ^0 cells with exogenous uridine by-passes this critical role of mitochondrial respiratory function and allows the cells to generate the nucleotides necessary for replication and repair of DNA, and thus tumour growth.

When ρ^0 cells are deprived of pyruvate and uridine, an inevitable metabolic crisis unfolds. This makes ρ^0 cells useful as a model of chronic metabolic injury, particularly for use in the

context of IMT. All elements of metabolic crisis in the deprived ρ^0 phenotype could potentially be alleviated by receipt of functional mitochondria via IMT. For this reason, the ρ^0 injury phenotype was selected to examine whether removal of pyruvate and uridine would influence IMT activity in these cells. A ρ^0-eGFP-astrocyte line, derived from the parental eGFP-astrocyte line was available [262].

6.2 Aims

The aim of this chapter was to determine if acute cellular injuries altered the rate of IMT in co-cultures of eGFP-astrocytes and primary pericytes. The effects of chloramphenicol (CMP) and cisplatin (CSP), were characterised in eGFP-astrocytes, to establish that these compounds caused appropriate cellular injuries, before they were placed into IMT co-cultures. In addition, a ρ^0-eGFP-astrocyte and pericyte co-culture model was used to determine if a chronic metabolic injury caused by mitochondrial dysfunction altered the rate of IMT.

6.3 Results: Acute cellular injury and IMT

6.3.1 Chloramphenicol as an acute cellular injury

Before CMP could be used to injure an IMT 'recipient' cell population of eGFP-astrocytes, it was essential that the injury be characterised in these cells. A sufficient concentration of the compound, with a suitable exposure time, aimed to push cells into a state of stress, rather than kill them outright. I hypothesised that in this state, any possible effect of injury on IMT processes would be most pronounced.

As an initial test, a titration of CMP was performed on eGFP-astrocytes. The cells were treated with CMP, or an equivalent volume of EtOH, the vehicle for CMP. Each day, the cells were inspected by light microscopy, to monitor drug effect. Depicted in **Figure 6.3.1**, an obvious effect on culture density was visible at 48 h. With each increase in concentration of the compound, the surface area covered by cells decreased. The difference between vehicle only untreated, 100 µg/mL and 200 µg/mL CMP was less pronounced than for concentrations of 400 µg/mL CMP and above. At this concentration, rounded cells were estimated to be more prevalent in the culture. At 800 µg/mL and 1200 µg/mL CMP, a severe effect on culture density was visible. At these higher concentrations, cells were either dying, or the growth inhibition was so severe that this level of injury could be considered as more than a transient stressor. Concentrations of 200 µg/mL and 400 µg/mL were therefore selected to progress into a quantitative co-culture assay of growth inhibition.

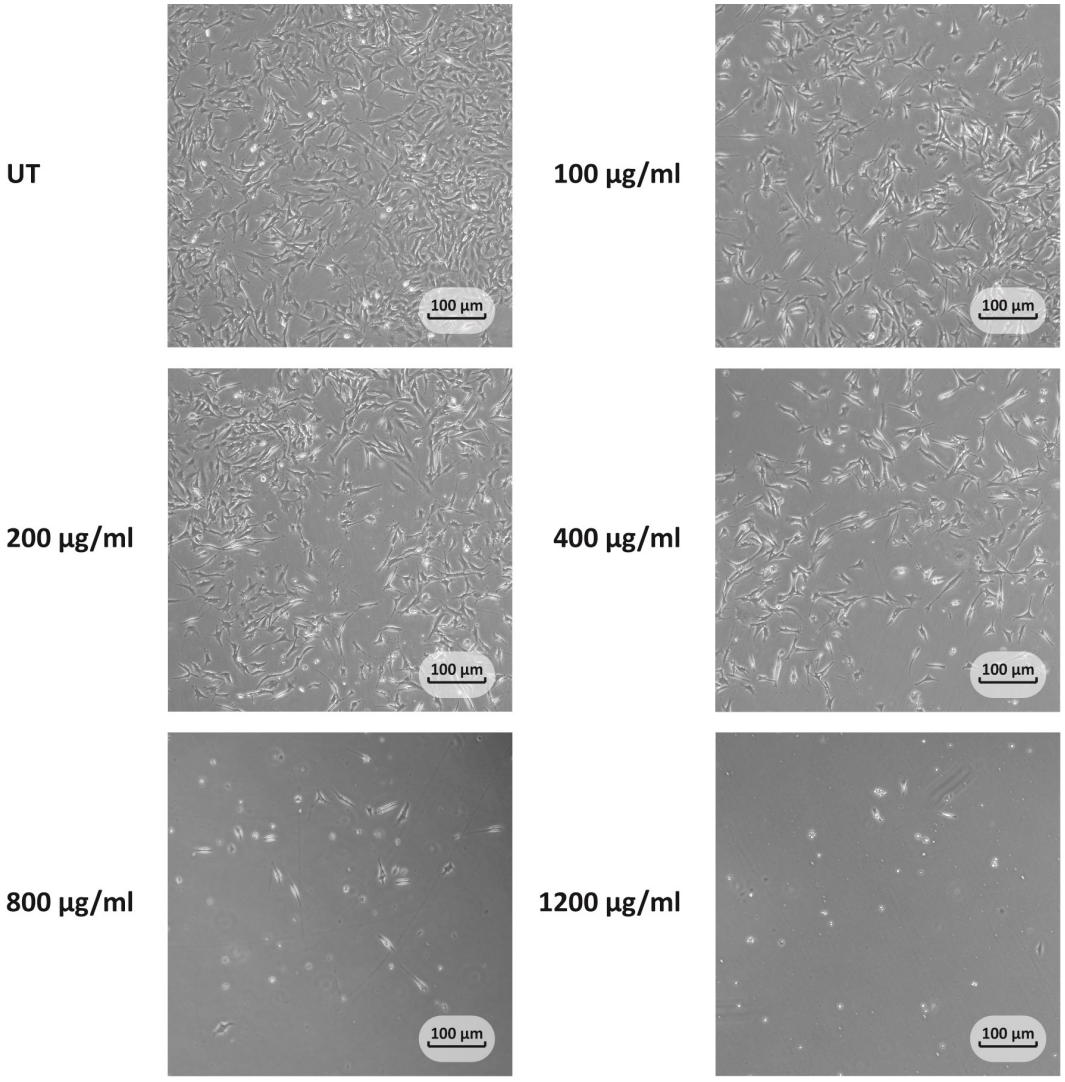

Figure 6.3.1. eGFP-astrocyte culture density is effected by acute exposure to chloramphenicol
Three hundred thousand eGFP-astrocytes were seeded into T75 culture flasks in medium which contained different concentrations of CMP, or left untreated as a vehicle only control (UT). The cultures were incubated for 48 h before imaging. Each phase contrast image presented is representative of cells exposed to a different treatment condition. Images were collected at 40 x magnification by light microscope. Data are representative of cells from a single experiment.

To assess growth inhibition by CMP in eGFP-astrocytes, culture density monitoring was performed using an Incucyte S3™ live-cell imaging incubator. eGFP-astrocytes treated with 200 μg/mL, 400 μg/mL CMP or vehicle only untreated controls were monitored for 70 h. The growth curve data generated in these experiments are presented in **Figure 6.3.2**. After 70 h of growth time, there was no appreciable difference in the growth curve between samples treated with 200 μg/mL and the vehicle only, untreated control. These two conditions reached approximately 100% coverage in 70 h of growth. Samples treated with 400 μg/mL however, reached approximately 60-70% coverage in this same period. It was unclear whether CMP inhibited growth of the eGFP-astrocytes by slowing the rate of proliferation, or if cells were dying.

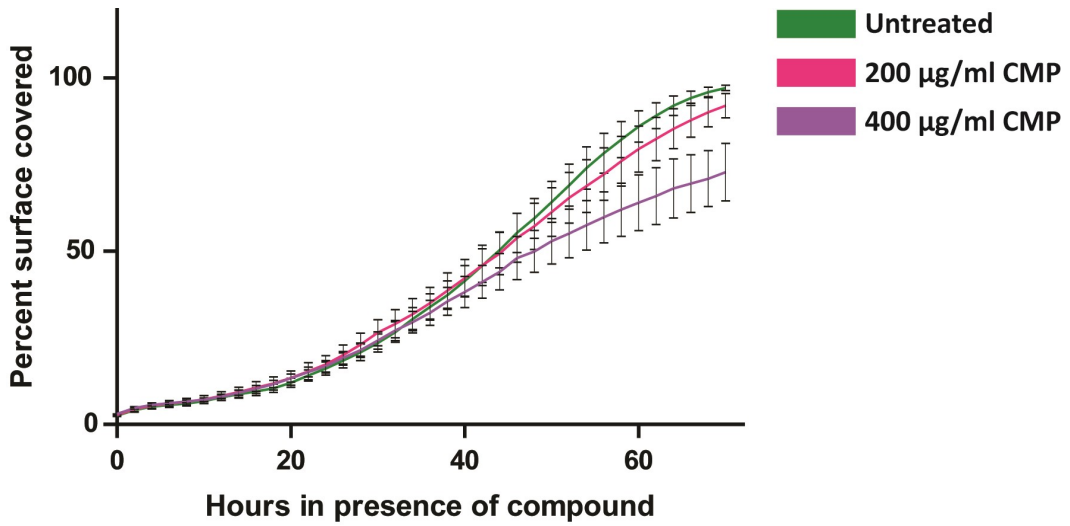

Figure 6.3.2. The growth rate of eGFP-astrocytes is inhibited by exposure to chloramphenicol

Fifty thousand eGFP-astrocytes were seeded into each well of a six-well plate, in medium which contained either 200 or 400 µg/mL CMP, or in vehicle only untreated control medium. The cells were monitored by collection of 32 images from each well every 2 h, in an Incucyte S3™ imaging incubator. The percent of the vessel surface area covered by cells was determined for each image. Data are presented for 70 h incubation, whereby vehicle only untreated control samples reach complete coverage of the available growth area. Data are presented as the mean percent coverage by area ± SEM from 4 independent biological replicates.

To address this question, apoptotic cell death was quantified by flow cytometry. eGFP-astrocytes were treated with 400 µg/mL CMP for 48 h, alongside untreated vehicle only controls. The cells were harvested and stained with annexin V and the live/dead detection dye Zombie NIR™, before cytometry. The results of these experiments, alongside the gating strategy used in analysis, are presented for treated and untreated vehicle only controls in **Figure 6.3.3**.

In **Figure 6.3.3A**, cells were first gated by FSA/FSH to exclude subcellular debris. Only intact cells were included in the downstream analysis. A gate for annexin V positive events **(B)**, and for zombie high **(C)** stained events was set based on unstained controls. A gate for double positive events **(D)** was set by placement of quadrants on both fluorescence axes. In **Figure 6.3.3E**, a scatter plot is presented to summarise data collected from these experiments. When eGFP-astrocytes were treated with 400 µM/mL CMP for 48 h, the proportion of cells positive for annexin V was found to increase significantly from a mean of approximately 24% to 41%. This indicated that cells making up approximately 17% of the population had externalised phosphatidyl serine in response to this treatment. Likewise, Zombie NIR™ highly stained cells were detected at approximately 11% above basal levels. By comparing events highly stained with both annexin V and Zombie NIR™, it is clear that vast majority of Zombie NIR™ positive cells are also positive for annexin V, indicative of late stage apoptosis. Single positive annexin V events detected in CMP treated samples were present approximately 8% over those double positive for annexin V and Zombie NIR™. This indicates a population of early-apoptotic eGFP-astrocytes were present at this point in time after CMP treatment. It is likely that these cells would proceed into late stage apoptosis and eventual cell death, if the cultures were examined at a later time point. Taken together, these results indicate that CMP induced cell death via apoptosis in eGFP-astrocytes. At the selected concentration and time, the overall level of cell death was not considered severe. Chloramphenicol treatment at 400 µg/mL for 48 h would be an appropriate level of injury for IMT experiments.

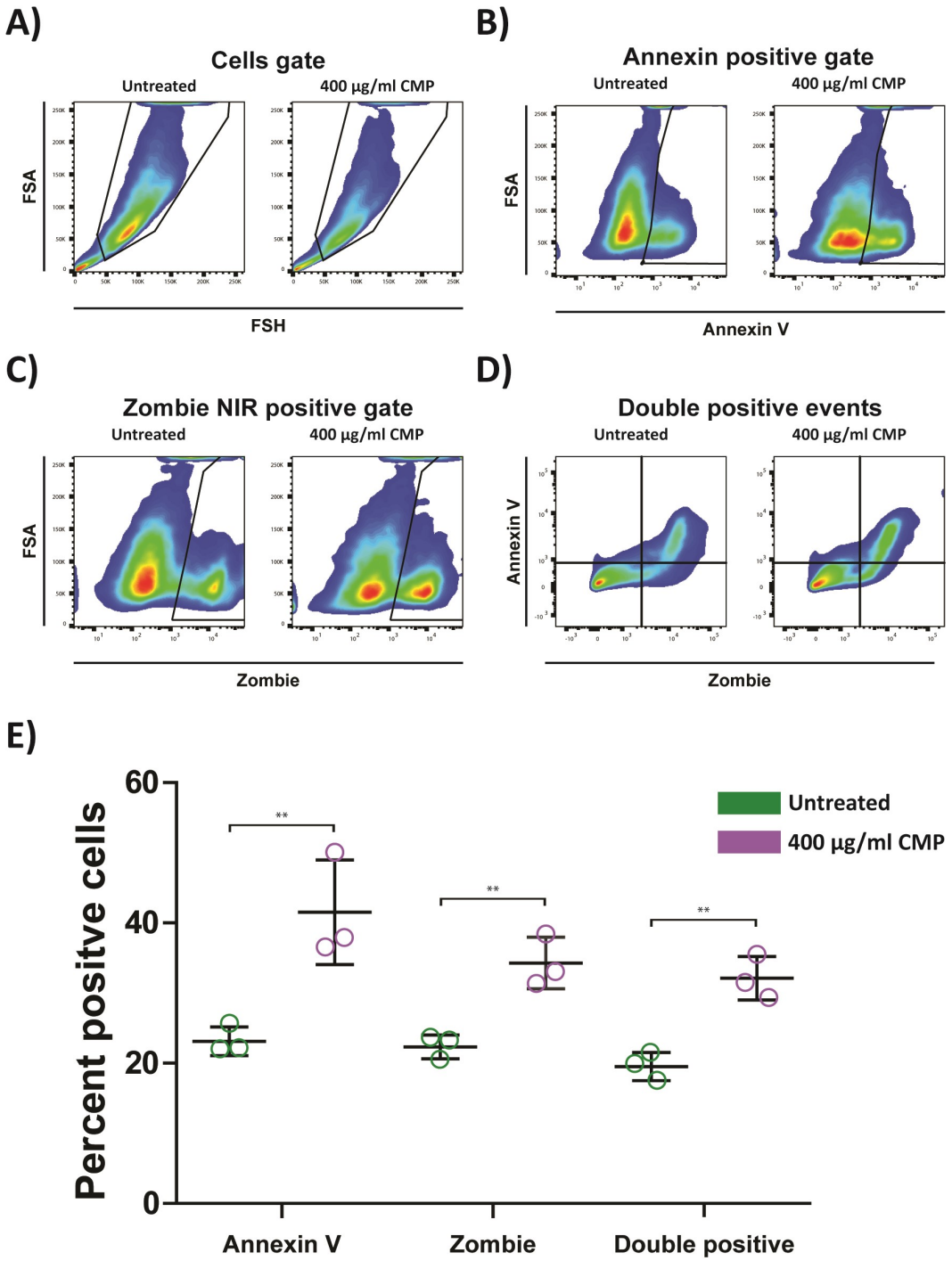

Figure 6.3.3. Acute exposure to chloramphenicol induces apoptotic cell death in eGFP-astrocytes

Three hundred thousand eGFP-astrocytes in a T75 flask were treated with CMP at 400 µg/mL, or vehicle only untreated control for 48 h. Annexin V positive cells and dead cells were quantified by flow cytometry. **(A)** Samples were first gated by FSA/FSH to separate cells away from debris. **(B)** An annexin V positive gate was set, based on unstained controls. **(C)** A Zombie positive gate was defined based on Zombie NIR™ highly and lowly stained cells. **(D)** Double positive cells were identified by quadrant gates placed on the Zombie/Annexin V axis. **(E)** Scatter plot of cells detected positive for each stain in treated or vehicle only untreated control samples. An unpaired students t-test was used to compare treated vs vehicle only untreated control samples, **: $p < 0.01$. Results are presented as the mean ±SEM from three independent experiments.

Because CMP interferes with mitochondrial protein synthesis by inhibition of the mtR, I expected that eGFP-astrocytes exposed to CMP would lack mitochondrial protein components and have a more glycolytic phenotype as a consequence of injury. To test this, eGFP-astrocytes treated with 400 µg/mL CMP for 48 h, or untreated vehicle only controls were subject to a glycolytic rate assay performed with a Seahorse XFe96 extracellular flux analyser.

The Seahorse glycolytic rate assay involves measurement of extracellular O_2 and H^+ flux in basal conditions over fixed period, after which oxidative phosphorylation is inhibited. This is achieved by injection of both rotenone and antimycin A (rot/AA); these compounds are potent inhibitors of respiratory complex I and complex III respectively. With this challenge, cells are forced into a glycolytic metabolic program. The change in ECAR under these conditions describes the ATP demand-limited rate of glycolytic activity [112]. 2-deoxyglucose (2-DG) is then injected to inhibit glycolysis at the level of glucose hexokinase (the first step of the glycolytic pathway). This allows background rates of O_2 and H^+ flux to be recorded in the absence of both glycolytic and mitochondrial respiratory function.

In **Figure 6.3.4A**, the ECARs for treated and untreated eGFP-astrocytes are presented in a line plot, as a function of time. Here, the basal ECAR of untreated control cells was demonstrably higher than that of CMP treated cells. As expected, after rot/AA challenge the ECAR of untreated cells was found to increase, as rot inhibits respiratory complex I and AA inhibits respiratory complex III; while ECAR in CMP treated cells remained constant. When further challenged with 2-DG, the ECAR of both treated and untreated cells decreased, consistent with the expected inhibition of glycolysis by this glucose analogue.

In **Figure 6.3.4B**, the OCRs for treated and untreated eGFP-astrocytes are presented in a line plot, as a function of time. It is immediately apparent that the basal OCR of untreated cells was larger than the basal OCR of CMP treated cells, indicative of a greater cellular requirement for ATP derived from oxidative phosphorylation. Inhibition of complexes I and III by Rot/AA decreased the OCR for both treated cells and untreated cells, although the magnitude of this change was greater in the untreated cells. Further challenge with 2-DG did not alter the OCR of either treatment condition.

Taken together, these results provide multiple insights into the metabolic state of CMP treated vs untreated cells. Most strikingly, the lack of change in ECAR for treated cells after rot/AA challenge is indicative of cells which lack reserve glycolytic capacity. These cells were unable to increase glycolytic rates to compensate for loss of oxidative phosphorylation after rot/AA challenge. The change in OCR after rot/AA challenge for CMP treated cells

indicates that respiration was not completely inhibited by treatment. The much smaller decrease in OCR with CMP treatment compared to untreated cells suggests a reduction in mitochondrial respiration and an altered metabolic balance. The overall rates of both ECAR and OCR in CMP treated cells were lower than in untreated cells. This suggests the cells have been pushed towards a state of reduced metabolic activity, and are more reliant on glycolytic metabolism. These results clearly show that treatment of eGFP-astrocytes with 400 µg/mL CMP for 48 h was sufficient to induce a metabolic injury in eGFP-astrocytes, which affected their glycolytic/respiration balance.

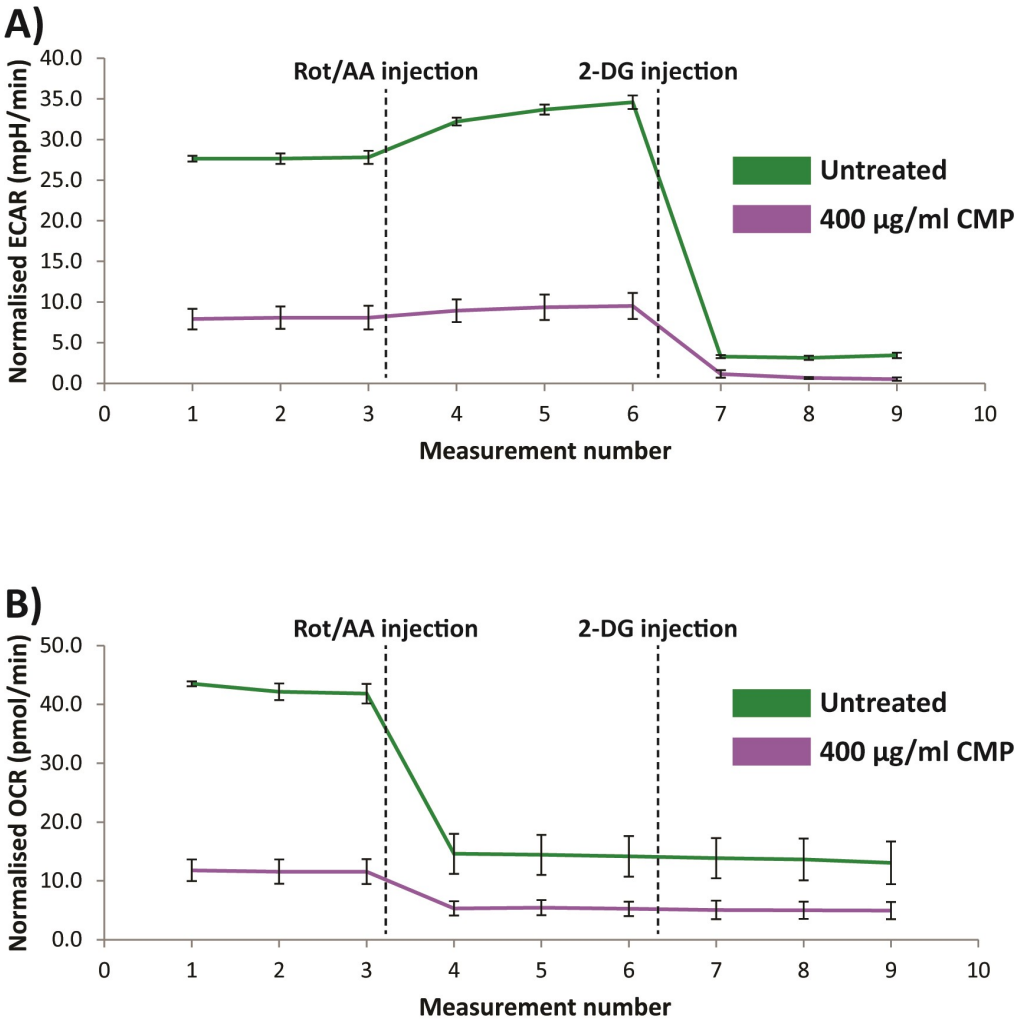

Figure 6.3.4. Chloramphenicol exposure induces mitochondrial respiratory deficiency in eGFP-astrocytes

The extracellular acidification rate and oxygen consumption rate of eGFP-astrocytes treated with 400 µg/mL CMP for 48 h, or vehicle only untreated control, were measured by Seahorse XFe96 Glycolytic Rate Assay. Rotenone/antimycin A or 2-deoxyglucose were injected into the medium at specific time points, to inhibit oxidative phosphorylation and glycolysis respectively. **(A)** Extracellular acidification rate recorded every 6.5 min over approximately 1 h. **(B)** Oxygen consumption rate recorded every 6.5 min over approximately 1 h. Data are normalised as described in the methods. Results are presented as the mean ± SEM from three independent biological replicates, with six replicate wells per biological condition per assay.

A curious finding in **Figure 5.3.4** and **Figure 5.3.5** was the ability of eGFP-astrocytes to engage in cell fusion with the astrocytic cell line C8D1A. Given this phenomenon in IMT, I was interested in whether or not eGFP-astrocytes which had engaged in fusion demonstrated enhanced survival, compared to those which remained singular. If cell fusion was involved as a survival mechanism or means to overcome the effect of CMP, I hypothesised that fused cells would demonstrate a reduction in the proportion of cells stained double positive for annexin V and Zombie NIR™ compared to untreated vehicle only controls. eGFP-astrocytes were treated with 400 μg/mL CMP for 48 h before staining with CFSE, and co-culture with untreated CellTrace Violet™ stained C8D1A. After a further 24 h, the cells were harvested and prepared for flow cytometry.

In **Figure 6.3.5**, the results of these experiments are presented alongside the gating strategy used for analysis. In **Figure 6.3.5A**, total events were first separated by a size exclusion performed on a FSA/CellTrace Violet™ axis. While unusual, this allowed an appreciation of the proportions of cellular debris likely to have originated from either eGFP-astrocytes or C8D1A cells. A set of quadrants were placed on the remaining events based on fluorescence of CellTrace Violet or CFSE; single stains used to independently label each cell line. Unlike cytometry performed on fused cells in chapter 5, here it was important to shape these gates to appropriately account for the altered shape and size, and thus fluorescence intensity, associated with dying cells. Events in quadrants A1 and A3 correspond to eGFP-astrocytes and C8D1A respectively. The double stained population of events present in quadrant A2 corresponds to fused cells.

Figure 6.3.5. Recovery of eGFP-astrocytes after chloramphenicol exposure is not enhanced by fusion with untreated C8D1A cells

Three hundred thousand eGFP-astrocytes were pre-treated with 400 μg/mL CMP for 48 h in a T75 flask, before placement into a 1:1 24 h co-culture with untreated C8D1A. Annexin V positive cells and Zombie NIR™ highly-stained dead cells were quantified by flow cytometry. **(A)** All events collected from co-cultures of CellTrace CFSE™ stained eGFP astrocytes and CellTrace Violet™ stained C8D1A were first gated by FSA against CellTrace Violet™ to exclude sub-cellular debris. When plotted against CellTrace Violet™ and CFSE™, a number of populations are revealed. Events in **A1**, **A2** and **A3** correspond to eGFP-astrocytes, fused cells and C8D1A respectively. **(B)** Annexin V positive events, Zombie positive events and double positive events are quantified by gates, based on unstained controls. **(C)** Scatter plots of annexin V positive, zombie positive and double positive events, for singular eGFP-astrocytes or fused cells. Results are presented as mean percent positive events from the total of each class of cell ± SEM, from three independent experiments. An unpaired students t-test used to compare eGFP-astrocytes to fused cells indicated no significant difference between groups at $p \leq 0.05$.

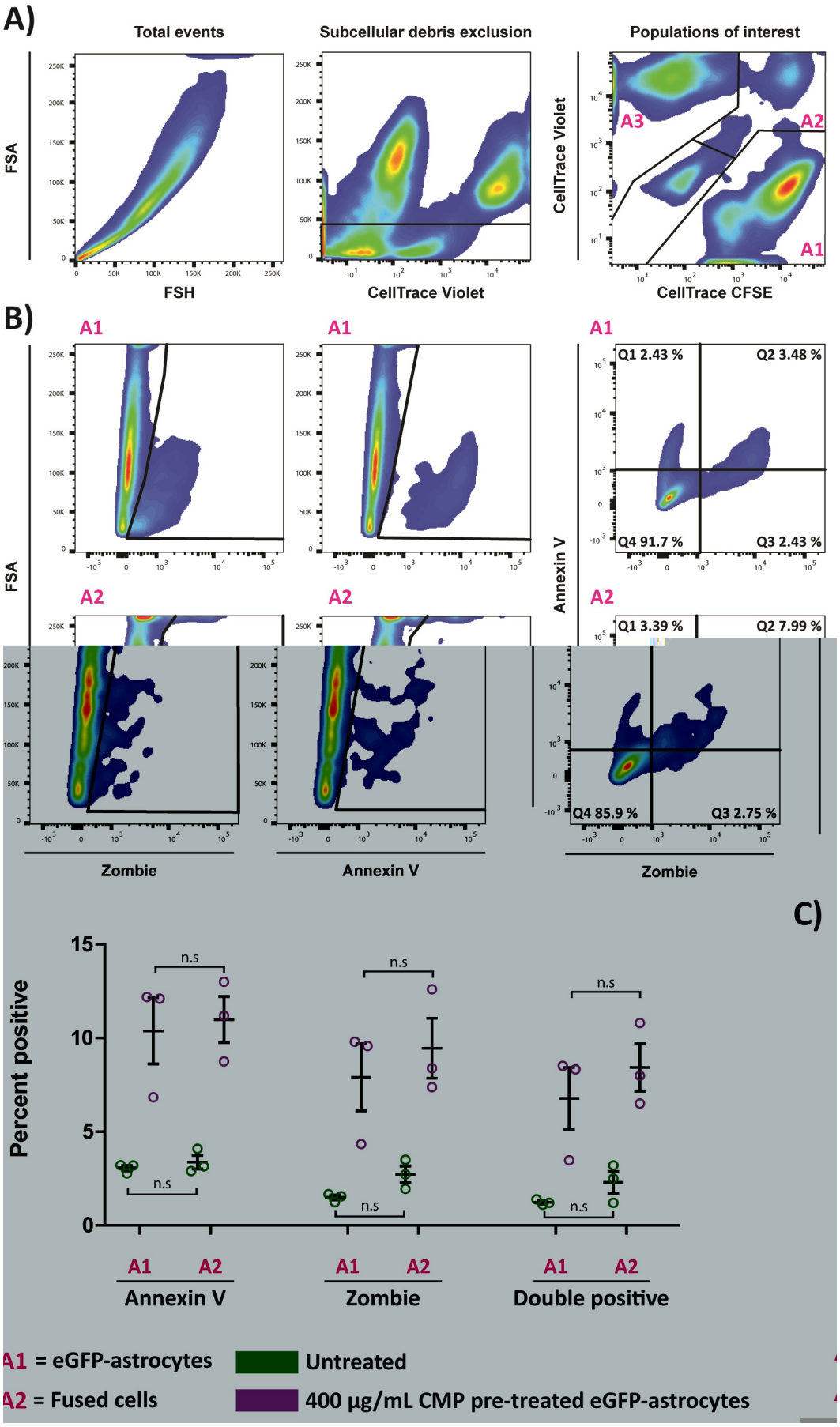
A)
Total events
Subcellular debris exclusion
Populations of interest
FSA
FSH
CellTrace Violet
CellTrace CFSE
A1
A2
A3
B)
Q1 2.43 %
Q2 3.48 %
Q4 91.7 %
Q3 2.43 %
Q1 3.39 %
Q2 7.99 %
Q4 85.9 %
Q3 2.75 %
Annexin V
Zombie
C)
Percent positive
n.s
Double positive
A1 = eGFP-astrocytes
A2 = Fused cells
Untreated
400 µg/mL CMP pre-treated eGFP-astrocytes

In **Figure 6.3.5B**, the FSA vs annexin V or Zombie NIR™ axis was gated for positive events, based on unstained controls. This enabled identification of singular, or fused eGFP-astrocytes which had externalised phosphatidyl serine, or those which were permeable and likely dead. A set of quadrants were also placed on the annexin V vs Zombie axis, to identify double positive events.

In **Figure 6.3.5C**, summary results for these experiments are presented as a scatter plot. For each stain, a significant difference was detected between untreated, and cells treated with CMP before co-culture. This indicated that an injury effect was still measurable in the co-culture 24 h following removal of CMP from the medium. When fused vs singular cells were compared, the proportions of cells positive for either stain was not significantly different. This indicated that engagement in cell fusion did not significantly improve the ability of the most severely affected eGFP-astrocytes to survive the CMP injury. Equal proportions of singular and fused cells died or entered early apoptosis as a result of CMP treatment.

6.3.2 IMT in eGFP-astrocyte/primary pericyte co-cultures – The effect of chloramphenicol on IMT

Treatment with CMP at 400 µg/mL for a 48 h period was sufficient to alter the growth characteristics, metabolism and level of apoptosis in a population of eGFP-astrocytes. Importantly, approximately 65% of the population was not yet pushed into early apoptosis with the treatment. This level of injury was suitable to test the hypothesis that acute cellular injury may enhance IMT: would CMP injury enhance uptake of mitochondria from untreated primary pericytes?

To test this, eGFP-astrocytes were pre-treated with CMP for 48 h or left as vehicle only untreated controls. The cells were then stained with CellTrace Yellow™, and co-cultures established on glass coverslips with DIV8 P2 primary pericytes. The co-cultures were then incubated for 72 h to allow for potential IMT to occur. After fixation, mtDNA_9461G targeted RCA was performed. The presence of mtDNA_9461G in an eGFP-astrocyte segment indicates mtDNA transferred through IMT. Approximately 600-700 image fields from each sample were collected by automated HTCM, from two technical replicate areas of RCA reaction. The images were then processed via the analysis pipeline developed in chapter 4. **Table 15** summarises the total number of objects successfully extracted from three independent biological replicate experiments, denoted as image sets 1, 2 and 3.

Table 15. Summary counts for Image analysis of chloramphenicol eGFP-astrocyte/primary pericyte co-cultures

Image set	Count cytoplasmic segments (cells) detected	Count RCP signals (mtDNA) detected
Untreated eGFP-astrocyte/primary pericyte set 1	1456	2046
Untreated eGFP-astrocyte/primary pericyte set 2	1339	2987
Untreated eGFP-astrocyte/primary pericyte set 3	4864	4492
Chloramphenicol eGFP-astrocyte/primary pericyte set 1	2268	1175
Chloramphenicol eGFP-astrocyte/primary pericyte set 2	581	2092
Chloramphenicol eGFP-astrocyte/primary pericyte set 3	3287	2806

Within each segment, the RCP count was determined. A correction was applied to the raw data to account for false-positive ligation events, based on the frequencies determined in chapter 4. This enabled population level comparisons between the CSP treated and untreated vehicle only control conditions as presented in **Figure 6.3.6.**

In **Figure 6.3.6A**, a heatmap summarises these data. eGFP-astrocyte segments with each RCP count, from 0 RCPs to 20 RCPs per segment, are represented by each row in the heatmap. The frequency of segments with each RCP count is indicated by the intensity of shading, from most frequent (yellow) to least frequent (blue). The most frequent observation was for segments with an RCP count of 0, seen in the first row of the heatmap. This indicated that most eGFP-astrocyte cells had not engaged in IMT. An exception to this is in image set 2, where the frequency of segments with RCP counts of 0 was reduced compared to set 1 and 3.

Given segments with an RCP count of 0 had not engaged in IMT, and segments with ≥1 RCP had engaged in IMT, the frequency of all segments with RCP counts >1 were summed. This represents the total frequency at which IMT occurred in the whole population.

A scatter plot presented in **Figure 6.3.6B** depicts the mean total frequency of IMT determined at the population level. Each point on the plot represents the sum frequency of IMT, for each set of images. No statistically significant difference was found in the mean sum frequency between treated and untreated cells, however a large degree of variability was present between image sets. This variability was most pronounced in the CMP treated image set 2, accounted for by the increased frequency of segments detected with RCP counts ≥1. When the individual data points are considered, two replicate experiments with CMP treated eGFP-astrocytes had similar frequencies of IMT of approximately 20%, while IMT in the remaining replicate was detected at approximately 60%, or 3x the frequency. The untreated image sets were less variable than CMP treated, but the total frequency of IMT in the population still ranged from approximately 25 to 45 %.

Figure 6.3.6. Chloramphenicol did not alter the total frequency of eGFP-astrocytes engaged in IMT after co-culture with primary pericytes

Three hundred thousand eGFP-astrocytes were injured with 400 µg/mL CMP, or left as vehicle only untreated controls for 48 h. The cells were stained with CellTrace™ Yellow and co-cultured with primary pericytes. After 72 h in co-culture, *in situ* RCA targeted to mtDNA_9461G was performed to detect mtDNA of pericyte origin. Images were collected by HTCM and analysis was performed as described in chapter 4. Data are presented from three independent image sets from paired treatment condition/control co-cultures. **(A)** The frequencies at which eGFP-astrocyte segments were detected with each count of mtDNA_9461G RCP between 0 and 20, visualised as a heat map. Each image set is presented independently. **(B)** The sum frequency of segments detected with ≥1 mtDNA_9461G RCPs (i.e cells which took up pericyte mtDNA) are presented as a scatter plot. Results are presented as the mean ± SEM from three replicate experiments. An unpaired students t-test indicated no significant difference between groups at $p \leq 0.05$.

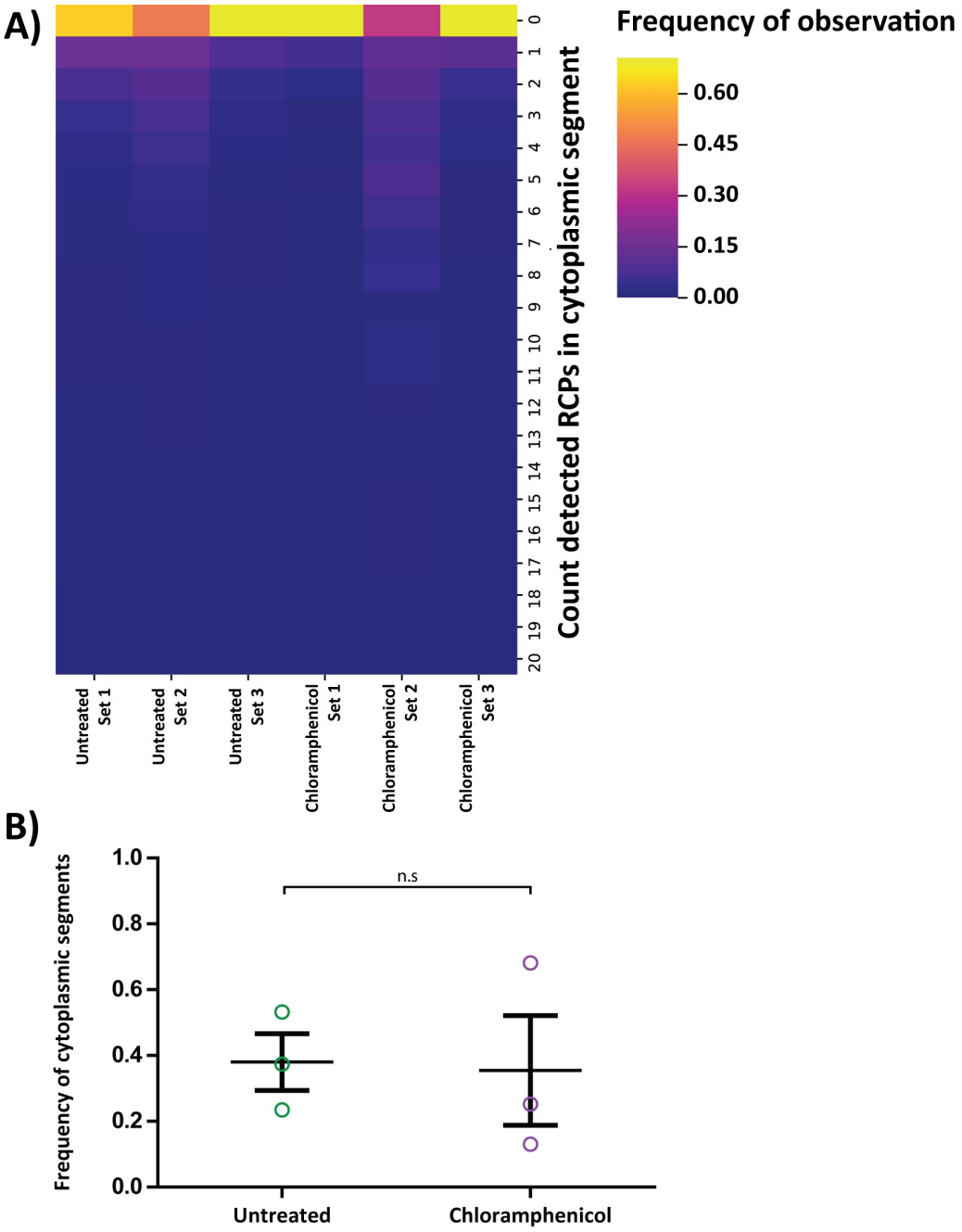
A)
Frequency of observation
0.60
0.45
0.30
0.15
0.00
Count detected RCPs in cytoplasmic segment
0
1
2
3
4
5
6
7
8
9
10
11
12
13
14
15
16
17
18
19
20
Untreated Set 1
Untreated Set 2
Untreated Set 3
Chloramphenicol Set 1
Chloramphenicol Set 2
Chloramphenicol Set 3
B)
Frequency of cytoplasmic segments
1.0
0.8
0.6
0.4
0.2
0.0
n.s
Untreated
Chloramphenicol

Next, only the segments that had IMT were examined (RCP ≥1), to determine if treatment altered the number of mtDNA detected per cell. In **Figure 6.3.7A**, Most segments had between 1 and 7 RCPs, and the frequency of observations decreased rapidly for segments with >7 RCPs.

Rather than comparing each image set by condition as in **Figure 6.3.6A**, the data here are presented as paired, untreated/CMP treated conditions. Each CMP treated image set more closely resembled its paired, untreated control. This is readily visible within the heatmap by shade intensity.

In **Figure 6.3.7B**, the difference in frequency of segments at each RCP count is presented as a scatter plot, for each paired treated/untreated control. Here, each data point represents a specific RCP count, and is plotted as the change in frequency with treatment, relative to untreated control. This allowed the comparison of variable replicates, and would highlight whether treatments favoured segments with specific RCP counts. From these, it was seen that for the majority of RCP counts, the frequency of segments was either the same as, or varied by only 0-3% of the control value. No significant difference in the mean change in frequency for each count of RCP was identified. This suggests that on average, treatment did not significantly alter the frequency of segments with specific RCP counts. Individual RCP count values with segment frequencies that deviated to a greater extent from their paired control value, were readily identified in this plot. While the means did not change significantly, these values indicate that each image set does contain subtle differences in how the segment frequencies were distributed.

Figure 6.3.7. Chloramphenicol did not alter the count of detected mtDNA molecules transferred into individual eGFP-astrocytes, where IMT had occurred
(A) The frequencies at which eGFP-astrocyte segments were detected for all counts of ≥1 RCP, visualised as a heat map. Each CMP treated image set is presented alongside its paired, vehicle only untreated control. **(B)** For each count of detected RCP, the frequency of detected segments was compared to the equivalent count of RCP in its paired control. This allowed segments with specific levels of IMT to be compared directly. Results are presented as the mean change in frequency ± SEM at each RCP count ≥1, normalised to each paired control. Paired students t-tests were performed to compare each count of RCP between control and treated samples, indicated no significant difference between image sets at $p \leq 0.05$. **(C)** Because various counts of RCP indicate a different extent of IMT occurrence in a given segment, the frequency value for each segment was multiplied by the RCP count, to produce a relative measure of total transferred mtDNAs at each RCP count. This value is displayed as a scatter plot of the mean at each RCP count, with the mean determined for each treatment condition ± SEM. This value reflects the total relative number of mtDNAs transferred into eGFP-astrocytes, between conditions. A Wilcoxon matched-pairs signed rank test indicated no significant difference between treatment conditions at $p \leq 0.05$.

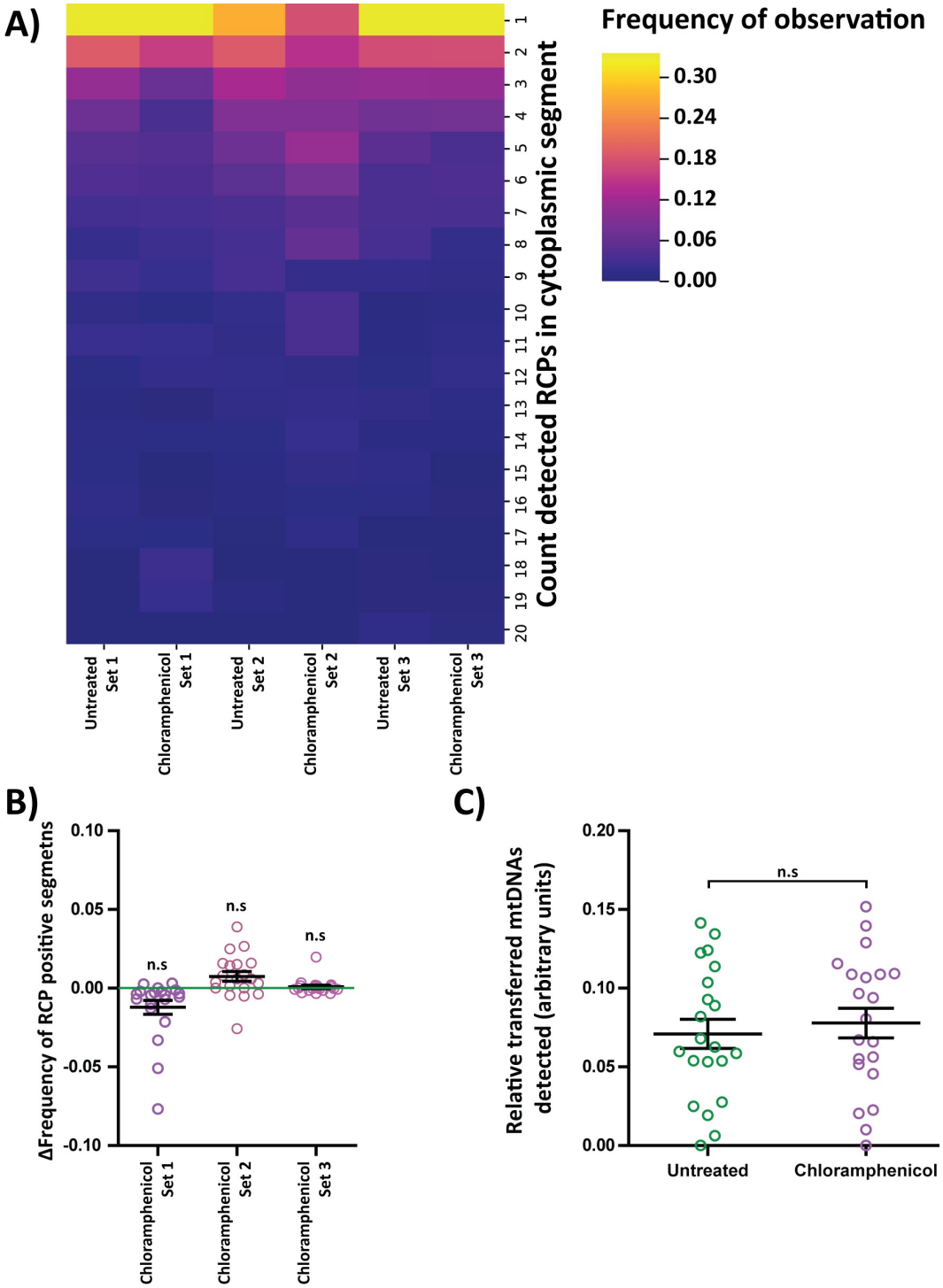
A)
Frequency of observation
0.30
0.24
0.18
0.12
0.06
0.00
Count detected RCPs in cytoplasmic segment
1
2
3
4
5
6
7
8
9
10
11
12
13
14
15
16
17
18
19
20
Untreated Set 1
Chloramphenicol Set 1
Untreated Set 2
Chloramphenicol Set 2
Untreated Set 3
Chloramphenicol Set 3
B)
ΔFrequency of RCP positive segmetns
0.10
0.05
0.00
-0.05
-0.10
n.s
n.s
n.s
Chloramphenicol Set 1
Chloramphenicol Set 2
Chloramphenicol Set 3
C)
Relative transferred mtDNAs detected (arbitrary units)
0.20
0.15
0.10
0.05
0.00
n.s
Untreated
Chloramphenicol

Biologically, the RCP count of a segment correlates with the number of mtDNA molecules transferred into an individual cell. By extension, segments with different RCP counts have different intensities of IMT, or mtDNAs transferred. It was possible to examine this relationship, by scaling the frequency of segments by the intensity of the IMT within them. This value represented the relative quantity of mtDNAs transferred by IMT at each given RCP count.

In **Figure 6.3.7C**, the mean relative quantity of mtDNA transferred into IMT positive segments is presented as a scatter plot. Here, each data point represents the mean intensity of IMT at each RCP count, averaged across the three replicate image sets. By examining the data this way, low frequency segments with unusually high or low RCP counts are accounted for, as they represent very few of the total mtDNAs transferred in the co-culture. The intensity of IMT from segments with each count of detected RCP were compared pair-wise. No significant difference was identified between CMP treated and untreated segments.

6.3.3 Cisplatin as an acute cellular injury

To use CSP as an acute injury in IMT experiments, the effects of the compound were first evaluated in eGFP-astrocytes. Like CMP, I aimed to determine a suitable concentration at which to treat the cells for 48 h, to push the population into a state of stress. The treatment time of 48 h established with CMP was maintained for CSP treatments, to enable these, and future co-culture experiments to be performed in parallel with CMP treatments.

To begin characterisation of the injury effect, eGFP-astrocytes were treated with CSP, or PBS as an untreated, vehicle only control. After 48 h, apoptotic cell death was quantified by annexin V and live/dead staining by Zombie NIR™, assessed by flow cytometry. The results of these experiments, alongside the gating strategy used in analysis, are presented in **Figure 6.3.8**.

In **Figure 6.3.8A,** A representative sample of untreated, vehicle only and 500 ng/mL CSP treated eGFP-astrocytes are depicted, to demonstrate the gating strategy used in this analysis. Events which corresponded to intact cells were first gated away from debris on a FSA/FSH axis. Next, each of annexin V **(B)** and Zombie NIR™ **(C)** stains were quantified against FSA, by placement of gates based on unstained controls (annexin V), or the high/low stained population of the untreated sample. An additional quadrant gate was placed on the annexin V/Zombie fluorescence axes to quantify events positive for both stains (**Q2**).

In **Figure 6.3.8E**, a series of scatter plots for each of annexin V positive, Zombie NIR™ positive and double positive events are presented to summarise data collected from these experiments. When eGFP-astrocytes were treated with CSP, the proportion of cells positive for annexin V was found to increase in a concentration dependent manner. At the lowest concentration of 31.25 ng/mL CSP, no significant increase in the proportion of annexin V stained events was detected when compared to vehicle only, untreated control. For concentrations of 125 and 250 ng/mL CSP, the cultures demonstrated an increase in the proportion of positively stained annexin V events. At 500 and 1000 ng/mL, a large increase in the proportion of annexin V positive events was detected. Interestingly, the data appears to describe a step-wise response between these three groups.

Similarly to annexin V, the Zombie NIR™ positively stained events were also found to increase in a concentration dependent manner. Concentrations of 0, 31.25, 125 and 250 ng/mL did not demonstrate an increased proportion of positively stained events. Concentrations of 500 and 1000 ng/mL demonstrated an increase in the proportion of events positive for Zombie NIR™. Interestingly, the variation amongst samples treated with 250 ng/mL was greater than all other conditions.

Events detected as double positive for Zombie NIR™ and annexin V closely resemble the values determined for Zombie NIR™ at all concentrations of CSP. This relationship was not maintained when double positive events were compared to events stained with annexin V alone. The frequency of cells positive for both stains was lower at all concentrations. This indicated that pre-apoptotic or early apoptotic cells were present within the populations 48 h after treatment. It is likely that these cells would proceed into late stage apoptosis and eventual cell death, if the cultures were examined at a later time point.

Taken together, these results indicated that CSP induced concentration dependent apoptotic cell death, though not in a strictly linear manner. It appeared certain threshold concentrations were required to push cells into death within 48 h, however many additional cells were pre-apoptotic or in early apoptosis at this point in time. These additional cells would likely proceed through apoptosis if measurements were conducted at a later time period; an important consideration if cells were to be placed into co-culture after drug treatment. Both the 250 and 500 ng/mL CSP concentrations were selected for further characterisations. These data suggested that a concentration of 250 ng/mL was likely to push a proportion of cells into a state of stress, but not completely into cell death. The 500 ng/mL concentration was perhaps too severe for future IMT experiments, as >50% of cells demonstrated annexin V positivity and would likely die in the following days if the cultures were extended. Nevertheless, either 250 ng/mL, or a concentration upwards of 250 but no greater than 500 ng/mL, was likely appropriate for the intended co-culture studies.

Figure 6.3.8. Acute cisplatin exposure induces apoptotic cell death in eGFP-astrocytes

Three hundred thousand eGFP-astrocytes in T75 flasks were treated with a series of CSP concentrations, or vehicle only untreated controls. Annexin V positive cells and dead cells were quantified by flow cytometry after 48 h of treatment. To demonstrate the gating strategy applied in this experiment, a representative untreated and CSP treated sample are depicted in the panels A, B and C. **(A)** Samples were first gated by FSA/FSH to separate cells away from debris. **(B)** An annexin V positive gate was set, based on unstained controls. **(C)** A Zombie positive gate was defined by Zombie NIR™ highly and lowly stained cells. **(D)** Quadrant gates were placed to identify double positive events. **(E)** Scatter plot of cells detected positive for either stain, or positive for both, in treated or vehicle only untreated control samples. Results are presented as the mean ±SEM from three independent experiments.

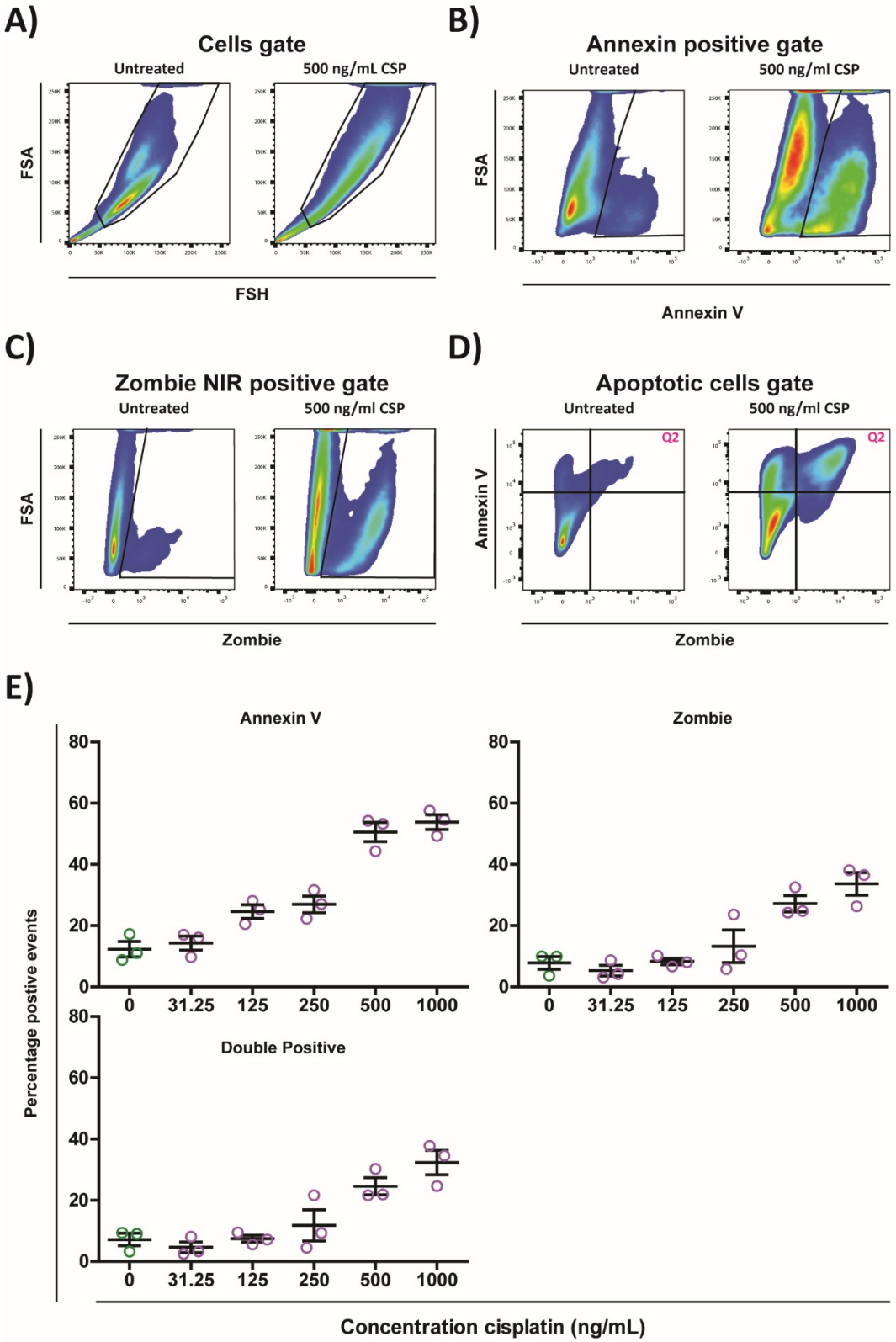
A)
Cells gate
Untreated
500 ng/mL CSP
FSA
FSH
B)
Annexin positive gate
Untreated
500 ng/ml CSP
FSA
Annexin V
C)
Zombie NIR positive gate
Untreated
500 ng/ml CSP
FSA
Zombie
D)
Apoptotic cells gate
Untreated
500 ng/ml CSP
Q2
Q2
Annexin V
Zombie
E)
Annexin V
Zombie
Double Positive
Percentage postive events
0
20
40
60
80
0
31.25
125
250
500
1000
Concentration cisplatin (ng/mL)

To gain insight into how the preliminary concentrations of CSP impacted on the eGFP-astrocyte culture, culture density monitoring was performed using an Incucyte S3™ live-cell imaging incubator. eGFP-astrocytes treated with either 250 or 500 ng/mL CSP were assayed alongside vehicle only, untreated controls and culture density by surface area was monitored for 70 h. The growth curve data generated in these experiments are presented in **Figure 6.3.9.** After 70 h growth time, both 250 and 500 ng/mL CSP were found to significantly inhibit the expansion of the eGFP-astrocyte cultures. The effect of the CSP treatments on population expansion began to emerge at approximately 20 h of culture time. By 70 h, cells treated with 250 ng/mL CSP reached approximately 62% density by area, while at 500 ng/mL, approximately just 37% of the surface area was covered in cells. In this same period of time, untreated cells reached 100% density. A relatively linear relationship is seen after 40 h for both CSP treated conditions. This suggests that a large number of cells in the culture are either dying off, or are not replicating at the same rate as the untreated eGFP-astrocytes. This is consistent with the increased proportion of annexin V positive events detected by flow cytometry in **Figure 6.3.8,** which indicated that the injury effect would continue past the 48 h time point.

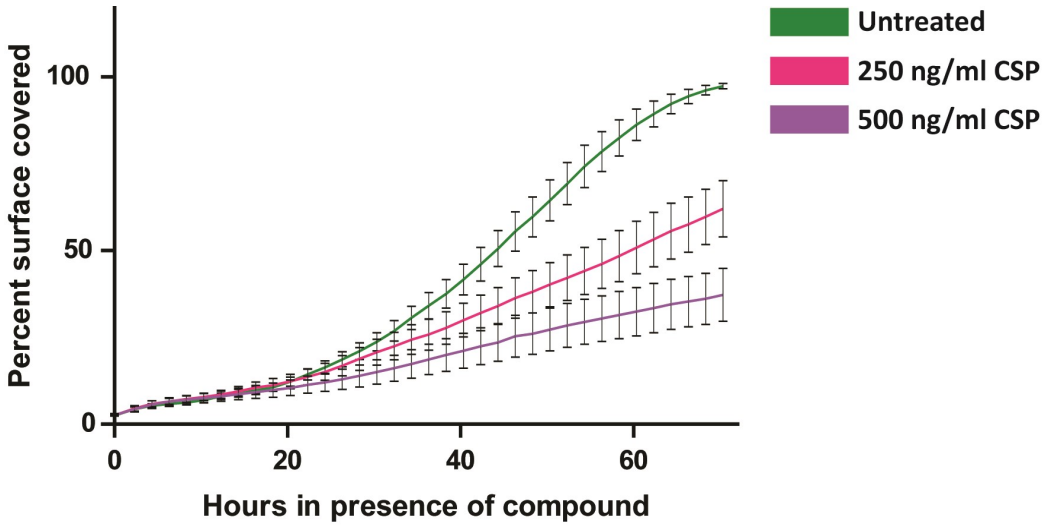

Figure 6.3.9. The growth rate of eGFP-astrocytes is inhibited by acute exposure to cisplatin

Fifty thousand eGFP-astrocytes were seeded into each well of a six-well plate, in medium which contained either 200 or 500 ng/mL CSP, or vehicle only untreated medium. The cells were monitored by collection of 32 images every two h, in an Incucyte S3™ imaging incubator. The percent of the vessel surface covered by cell area was determined for each image. Data are presented for 70 h incubation, whereby vehicle only untreated control samples reach complete coverage of the available growth area. Vehicle only untreated control data are equivalent to those presented in **Figure 6.3.2** as these assays were performed in parallel. Data are presented as the mean ± SEM from 4 independent biological replicates.

With effects on growth rate and apoptotic cell death established, I was interested in how CSP treatment impacted mitochondrial function in the eGFP-astrocytes. As a DNA damaging agent with an mtDNA selective component, I hypothesised that CSP would alter mitochondrial transcription, or the cells' ability to produce full length transcript.

To test this hypothesis, eGFP-astrocytes were treated with 250 and 500 ng/mL CSP alongside vehicle only, untreated controls. After 48 h, RNA was extracted and particular care was taken to ensure gDNA contamination was eliminated by a rigorous DNAse treatment. This was essential as mtDNA transcripts are polycistronic, thus amplify equivalently from residual mtDNA as from cDNA, as primers cannot be designed to span introns; a strategy used regularly when targeting transcripts encoded by nuclear DNA. Quantitative RT-PCR was performed to determine the relative abundance of specific mtDNA target transcripts.

In **Figure 6.3.10A**, a schematic which describes simplified transcription from the heavy and light strands of mtDNA is presented. The two arrows represent the approximate length of complete pre-mRNA transcribed from the heavy (inner arrow) or light (outer arrow) strands of mtDNA. The first target consisted of sequence from the D-loop region, transcribed immediately after the initiation of transcription from the light strand (outer, 1). Two further target sequences, Cox1 and CytB are transcribed from the heavy mtDNA strand approximately 50% of the way through (inner, 1), and at the 3' end (inner, 2) of the pre-mRNA respectively. As mitochondrial transcripts are polycistronic, an assumption was made that changes in the abundance of the three selected transcripts, when considered together, would reflect changes occurring for all mRNA species encoded by mtDNA.

In **Figure 6.3.10B**, the results of qRT-PCR for each of the target transcripts are summarised by scatter plot. After normalisation to 18s, data are presented as the mean abundance, as a proportion of the untreated control. With 250 ng/mL treatment, an approximate average 8% increase, 8% decrease and 15% decrease were detected for each of the D-Loop, Cox1 and CytB transcripts respectively. While a small effect size, these data indicate mitochondrial transcription was impacted in cells treated with 250 ng/mL CSP. Curiously, abundance of D-loop transcript was either unaltered, or marginally positive compared to the untreated control. At a concentration of 500 ng/mL, an approximate average 34% decrease, 51% decrease and 53% decrease were detected for each of the D-Loop, Cox1 and CytB transcripts respectively. This indicated that at 500 ng/mL CSP, mitochondrial transcription was impacted more severely than at 250 ng/mL. This is consistent with the concentration dependent relationship observed in growth rates and apoptotic cell death. A significant difference in the relative abundance of D-loop transcript and both Cox1 and

CytB was detected, for each concentration of CSP. This is consistent with the hypothesis that CSP induced mtDNA damage would impact full length transcript abundance and suggests early terminations of transcription, under the assumption that turnover rates and cellular demand for each transcript are similar.

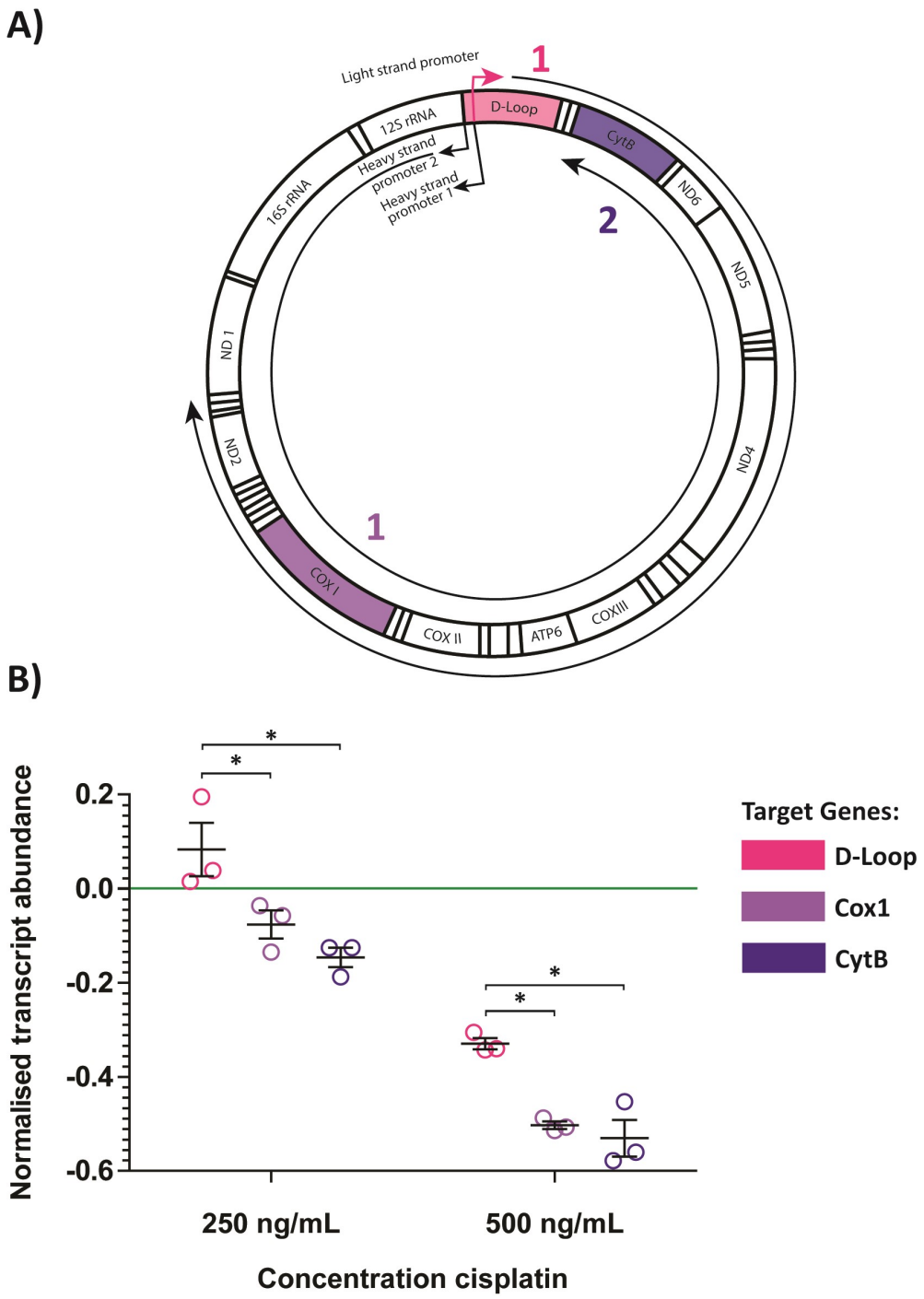

Figure 6.3.10. Acute exposure of eGFP-astrocytes to cisplatin reduces the abundance of transcripts produced from mtDNA

Three hundred thousand eGFP-astrocytes in T75 flasks were exposed to CSP, or vehicle only untreated control for 48 h. Transcripts for the D-loop, Cox1 and CytB were then quantified by RT-qPCR. **(A)** Schematic of simplified mitochondrial transcription from mtDNA. Mitochondrial mRNA are produced from polycistronic precursor transcript initiated from either the light strand, or heavy strand promoters. Sequence for Cox1 is transcribed before CytB in the precursor RNA, from the heavy strand promotors. Transcription of sequence within the D-loop is initiated from the light strand promotor. **(B)** Scatter plot of transcript abundance for each of D-Loop, Cox1 and CytB in CSP treated cells, relative to vehicle only untreated control cells. Data were normalised to 18s rRNA, to control for differences in RNA input. Data are presented as the mean ± SEM of three independent experiments. An unpaired students t-test was used to compare the difference in expression of each target transcript at $p \leq 0.05$.

Though transcript abundance does not translate directly to protein levels, it was plausible that eGFP-astrocytes treated with CSP could have a reduced capacity to maintain functional respiratory complexes as a consequence of the reduction in mitochondrial transcripts. In addition to the global cellular response to injury, a loss of functional respiratory complexes could alter the metabolic phenotype of the cells.

To test this, eGFP-astrocytes treated with 250 ng/mL CSP for 48 h, or untreated vehicle only controls were subject to a glycolytic rate assay performed with a Seahorse XFe96 flux analyser. The ECAR and OCR was determined for these cells in basal, rot/AA challenged and 2-DG challenged metabolic states and are presented in **Figure 6.3.11**.

In **Figure 6.3.11A**, the ECAR for treated and untreated eGFP-astrocytes are presented in a line plot, as a function of time. Here, the basal ECAR of untreated control cells was almost 3 times higher than that of the treated cells. When challenged with rot/AA, the ECAR of both treated and untreated cells was found to increase. When further challenged with 2-DG, the ECAR of both treated and untreated cells decreased, consistent with the expected inhibition of glycolysis by 2-DG.

In **Figure 6.3.11B**, the OCR for treated and untreated eGFP-astrocytes are presented in a line plot, as a function of time. Similarly to the CMP treated cells in **Figure 6.3.4B**, the basal OCR of CSP treated eGFP-astrocytes was considerably depressed compared to untreated, vehicle only control cells. After inhibition of complexes I and III by rot/AA, oxygen consumption was found to decrease for both the untreated and treated cells. The OCR and thus, overall mitochondrial respiration was reduced to a low level, consistent with non-mitochondrial oxygen consumption. Subsequent challenge with 2-DG did not further alter the OCR of either treatment condition.

Taken together, these results describe an altered metabolic state in eGFP-astrocytes treated with CSP, compared to untreated cells. Unlike CMP treated cells in **Figure 6.3.4A,** the small increase in ECAR after addition of rot/AA indicates that the CSP treated astrocytes retained some spare glycolytic capacity, though to a lesser degree than untreated cells. Additional glycolytic capacity was engaged in both treated and untreated cells to compensate for loss of mitochondrial ATP upon inhibition of complexes 1 and 3. This indicates that CSP treated cells remain able to derive ATP from oxidative phosphorylation, and did not become completely reliant on glycolytic ATP at this level of CSP treatment. The overall reduced ECAR and OCR in CSP treated cells indicates an altered metabolic state has been induced. A 48 h treatment with 250 ng/mL CSP was an adequate cellular injury to induce an altered metabolic phenotype.

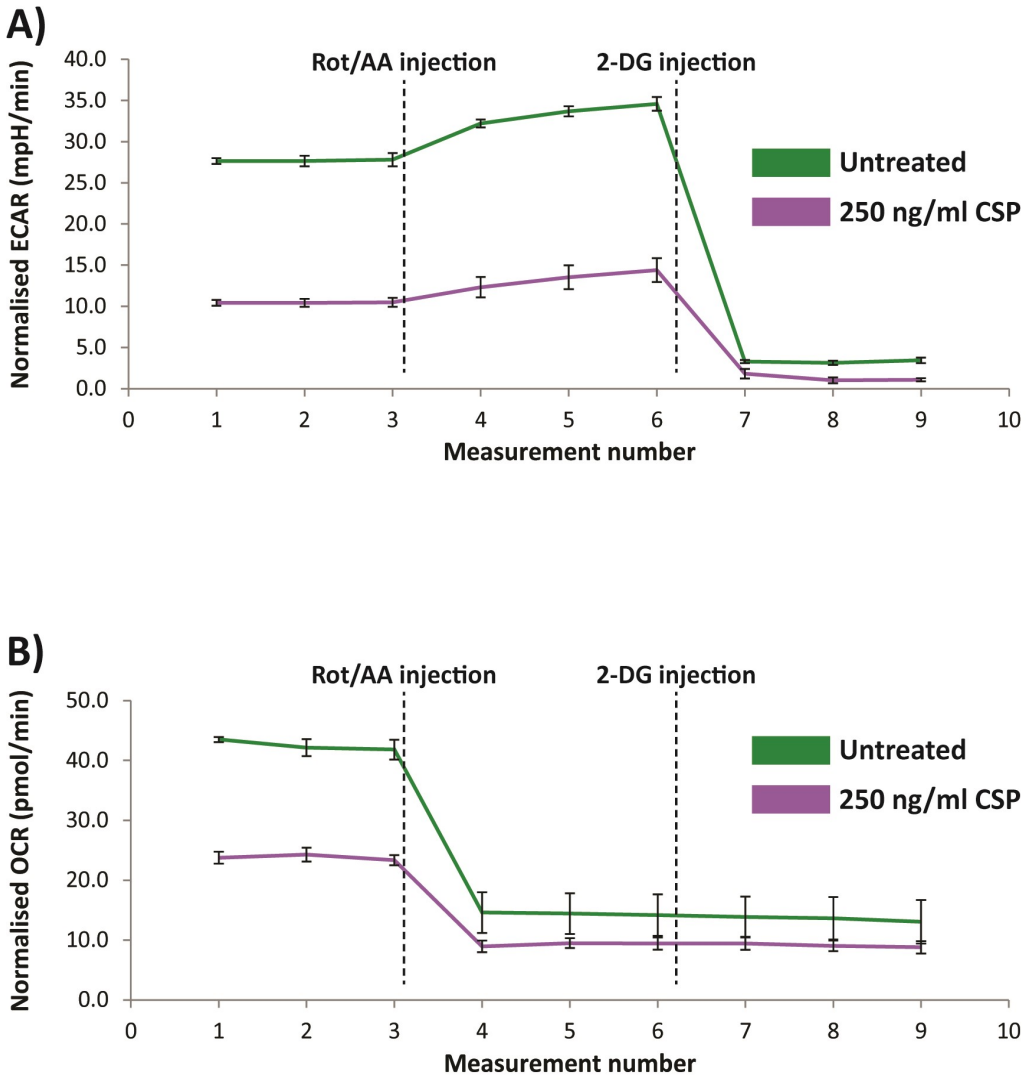

Figure 6.3.11. Acute cisplatin exposure induces mitochondrial respiratory deficiency in eGFP-astrocytes

The extracellular acidification rate and oxygen consumption rate of eGFP-astrocytes treated with 250 ng/mL CSP for 48 h, or vehicle only untreated control cells, were measured by Seahorse XFe96 Glycolytic Rate Assay. Rotenone/antimycin A or 2-deoxyglucose were injected into the medium at specific time points, to inhibit oxidative phosphorylation and glycolysis respectively. **(A)** The extracellular acidification rate recorded every 6.5 min over approximately 1 h. **(B)** The oxygen consumption rate recorded every 6.5 min over approximately 1 h. Data are normalised as described in the methods. Untreated vehicle only untreated control data are equivalent to those presented in **Figure 6.3.4** as these assays were performed in parallel. Results are presented as the mean ± SEM from three independent biological replicates.

6.3.4 IMT in eGFP-astrocyte/primary pericyte co-cultures – The effect of cisplatin on IMT

Treatment with CSP at 250 ng/mL for 48 h proved adequate to induce changes in the growth characteristics, mitochondrial transcript abundance, metabolism, and level of apoptotic cell death in eGFP-astrocytes. With this established, it was possible to test the hypothesis that cellular injury by CSP may alter IMT between injured eGFP-astrocytes and primary pericytes.

eGFP-astrocytes were treated with CSP for 48 h or left as vehicle only untreated controls. After staining with CellTrace Yellow™, co-cultures were established with DIV8 P2 primary pericytes on glass coverslips. The co-cultures were then incubated for 72 h to allow for potential IMT to occur. After fixation, mtDNA_9461G targeted RCA was performed. Approximately 600-700 image fields from each sample were collected by automated HTCM, from two technical replicate areas of RCA reaction. The images were then processed via the analysis pipeline developed in chapter 4. **Table 16** summarises the total number of objects successfully extracted from three independent biological replicate experiments, denoted as image sets 1, 2 and 3.

Table 16. Summary counts for Image analysis of cisplatin eGFP-astrocyte/primary pericyte co-cultures

Image set	Count cytoplasmic segments (cells) detected	Count RCP signals (mtDNA) detected
Untreated eGFP-astrocyte/primary pericyte set 1	1456	2046
Untreated eGFP-astrocyte/primary pericyte set 2	1339	2987
Untreated eGFP-astrocyte/primary pericyte set 3	4864	4492
Cisplatin eGFP-astrocyte/primary pericyte set 1	2308	4481
Cisplatin eGFP-astrocyte/primary pericyte set 2	96	92
Cisplatin eGFP-astrocyte/primary pericyte set 3	369	200

Note: The image sets which correspond to untreated eGFP-astrocyte/primary pericyte co-cultures are equivalent to those which appear in **Table 15**.

Within each segment, the RCP count was determined. As in **section 6.3.2**, a correction was applied to the raw data to account for false-positive ligation events, based on the frequencies determined in chapter 4.

In **Figure 6.3.12A**, a heatmap summarises these data. As for CMP in **Figure 6.3.6**, eGFP-astrocyte segments with each RCP count, from 0 RCP to 20 RCP per segment, are represented by each row in the heatmap. The most frequent observation was for segments with an RCP count of 0 (yellow shades), seen in the first row of the heatmap. This indicated that most eGFP-astrocyte cells had not engaged in IMT.

Given segments with an RCP count of 0 had not engaged in IMT, and segments with ≥1 RCP had engaged in IMT, the frequency of all segments with RCP counts >1 were summed. This represents the total frequency at which IMT occurred in the whole population.

A scatter plot presented in **Figure 6.3.12B** depicts the mean total frequency of IMT determined at the population level. Each point on the plot represents the sum frequency of IMT, for each set of images. No statistically significant difference was determined in the mean frequency of IMT positive segments. Curiously, and in contrast to the CMP treated image sets described in **Figure 6.3.6B**, CSP treated samples showed less variability compared to the untreated control.

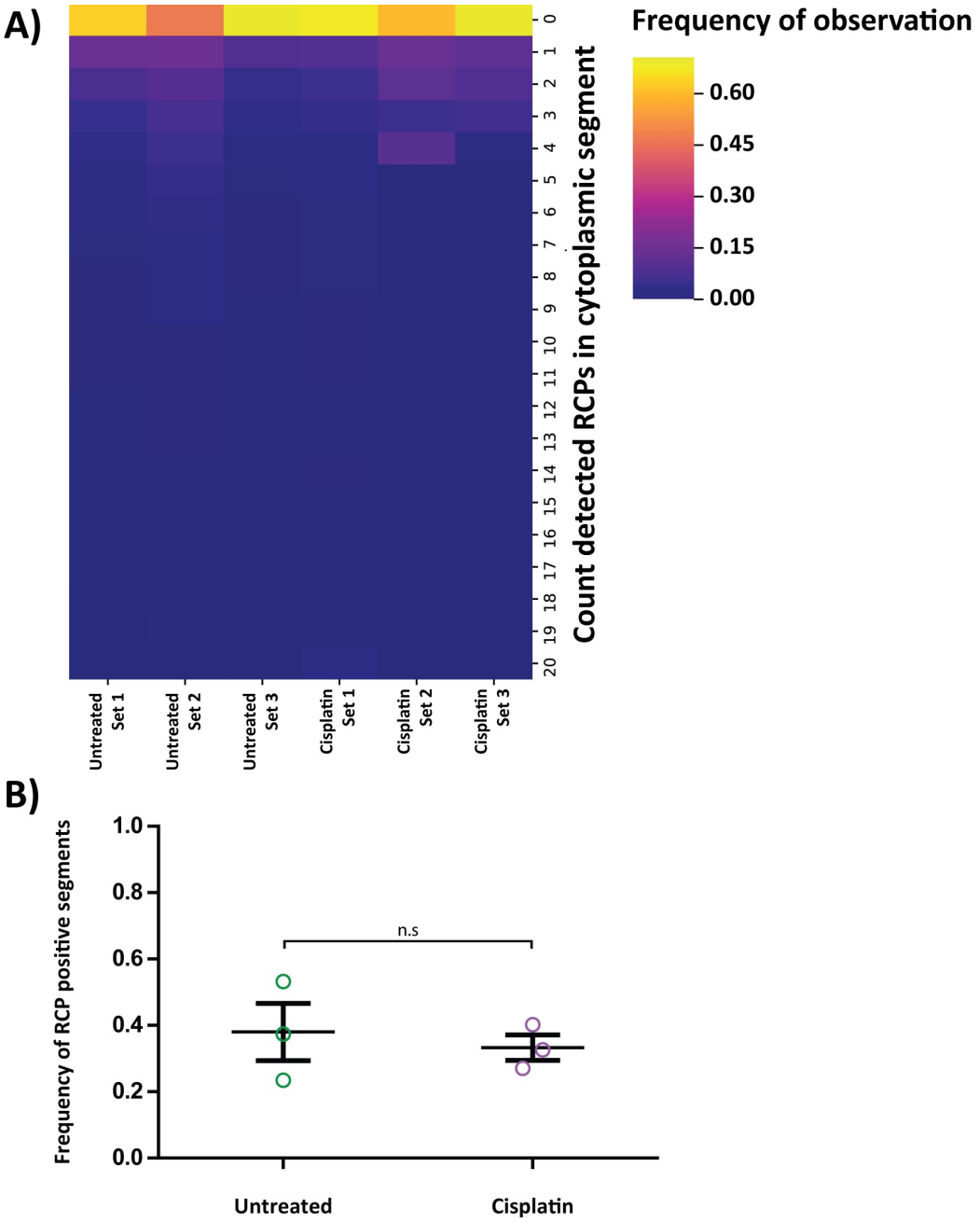

Figure 6.3.12. Cisplatin exposure did not alter the total frequency of eGFP-astrocytes engaged in IMT after co-culture with primary pericytes

Three hundred thousand eGFP-astrocytes were injured with 250 ng/mL CSP, or left as vehicle only untreated controls for 48 h. The cells were stained with CellTrace™ Yellow and co-cultured with primary pericytes. After 72 h in co-culture, in situ RCA targeted to mtDNA_9461G was performed to detect mtDNA of pericyte origin. Images were collected by HTCM and analysis performed as described in chapter 4. Data are presented from three independent image sets from paired treatment condition/control co-cultures. The frequency of false-positive ligation events determined experimentally in chapter 4 was applied as a correction to these data to account for false positive RCPs. (A) The frequency at which segments were detected with each particular count of mtDNA_9461G RCP between 0 and 20, visualised as a heat map. Each image set is presented independently. (B) The sum frequency of segments detected with ≥1 mtDNA_9461G RCPs (i.e cells which took up pericyte mtDNA) are presented as a scatter plot. Results are presented as the mean ± SEM from three replicate experiments. An unpaired students t-test indicated no significant difference between groups at $p \leq 0.05$.

Next, only the segments where IMT was detected were examined (RCP ≥1), to determine if treatment with CSP had altered the number of mtDNA detected per cell. In **Figure 6.3.13A**, each CSP treated image set is displayed adjacent to its paired, untreated control in a heatmap, which summarises the frequency of eGFP-astrocyte segments detected with each count of RCP ≥1.

In **Figure 6.3.13B**, the difference between frequencies of segments at each RCP count are presented as a scatter plot, for each paired treated/untreated control. Here, each data point represents a specific RCP count, and is plotted as the change in frequency with treatment, relative to untreated control. From these data, it is possible to see that for segments at the majority of RCP counts, the frequency of segments observed was either the same as, or varied by only 0-3% of the control value. No significant difference in the mean change in frequency between each count of RCP was identified, evaluated by a paired student's t test. This suggests that on average, treatment did not significantly alter the average frequency of segments with specific RCP counts.

Figure 6.3.13. Cisplatin altered the count of detected mtDNA molecules transferred into individual eGFP-astrocytes, where IMT had occurred

(A) The frequencies at which eGFP-astrocyte segments were detected for all counts of ≥1 RCP, visualised as a heat map. Each CSP treated image set is presented alongside its paired, vehicle only untreated control. **(B)** For each count of RCP, the frequency of detected segments was compared to the equivalent count of RCP in its paired control. This allowed segments with each individual level of IMT to be compared fairly. Results are presented as the mean change in frequency ± SEM for each RCP count of ≥1, normalised to each paired control. Paired students t-tests were performed to compare each count of RCP between control and treated samples, indicated no significant difference between image sets at $p \leq 0.05$. **(C)** Because various counts of RCP indicate a different extent of IMT occurrence in a given segment, the frequency value for each segment was multiplied by the RCP count, to produce a relative measure of total transferred mtDNAs at each RCP count. This value is displayed as a scatter plot of the mean at each RCP count, with the mean determined for each treatment condition ± SEM. This value reflects the total relative number of mtDNAs transferred into eGFP-astrocytes, between conditions. A Wilcoxon matched-pairs signed rank test was used to recognise a difference between treatment conditions $p \leq 0.05$.

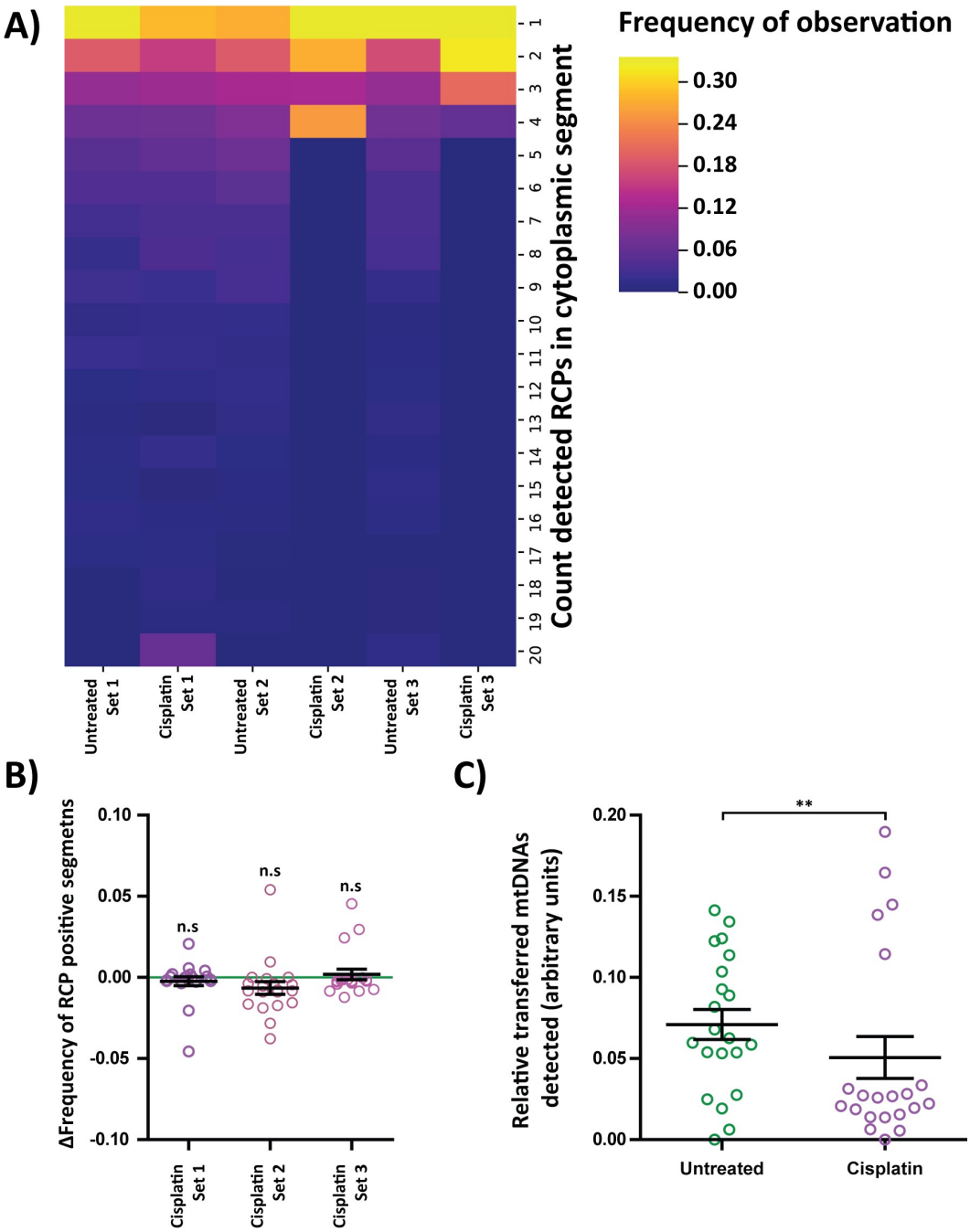
A)
Frequency of observation
0.30
0.24
0.18
0.12
0.06
0.00
Count detected RCPs in cytoplasmic segment
1
2
3
4
5
6
7
8
9
10
11
12
13
14
15
16
17
18
19
20
Untreated Set 1
Cisplatin Set 1
Untreated Set 2
Cisplatin Set 2
Untreated Set 3
Cisplatin Set 3
B)
ΔFrequency of RCP positive segmetns
0.10
0.05
0.00
-0.05
-0.10
n.s
n.s
n.s
Cisplatin Set 1
Cisplatin Set 2
Cisplatin Set 3
C)
Relative transferred mtDNAs detected (arbitrary units)
0.20
0.15
0.10
0.05
0.00
**
Untreated
Cisplatin

As described for **Figure 6.3.7** for the CMP treated cells, the RCP count of a segment correlates with the number of mtDNA molecules transferred into a cell. By extension, segments with different RCP counts have different intensities of IMT, or mtDNAs transferred. By scaling the frequency of segments by the counts of RCPs within them, the relative quantity of mtDNAs transferred through IMT was determined.

Figure 6.3.13A C, the mean relative quantity of mtDNAs transferred at each RCP count presented as a scatter plot. Here, each data point represents the mean intensity of IMT at each RCP count, averaged across the three replicate image sets. By examining the data this way, low frequency segments with unusually high or low RCP counts are accounted for, as they represent very few of the total mtDNAs transferred. The intensity of IMT from segments with each count of detected RCP were compared pair-wise. A significant difference was identified between CSP treated and untreated cells. Cells which were positive for IMT were found to contain less transferred mtDNA molecules on average after treatment with CSP.

6.4 Summary: Acute cellular injury and IMT

In this section, acute cellular injury by CMP and CSP was characterised in eGFP-astrocytes. This was necessary to determine a concentration of each drug which would push the population of cells towards a stress phenotype. Importantly, it was necessary to determine a level of injury caused by each compound which would be conducive to further experimentation with these cells.

In CMP treated cells, a significant effect on the growth, metabolic state and level of apoptotic cell death was found when cells were treated for 48 h at 400 µg/mL. In CSP treated cells, a significant effect on the growth, metabolic state, abundance of specific mitochondrial transcripts and level of apoptotic cell death in the population was observed when treated with 250 ng/mL for 48 h. At these concentrations of either compound, the level of cell death in the population was not severe, however the percentages of early apoptotic/pre-apoptotic cells were significantly increased above basal conditions. This was deemed an appropriate level of injury to explore an overarching question of this thesis; would these acute injuries alter the level of IMT occurring in co-culture, from primary pericytes into eGFP-astrocytes?

After eGFP-astrocytes were first pushed into this state, co-cultures were established with primary pericytes. Here, *in situ* RCA targeted to mtDNA_9461G enabled direct visualisation of SNVs in mtDNA of pericyte origin, within the eGFP-astrocytes. Many hundreds of images were collected by HTCM and occurrences of IMT analysed without human bias.

For each compound, no significant differences were found in the overall frequency of cells which engaged in IMT, however data collected from each replicate experiment was variable. By comparing IMT positive cells within each treated image set to those in each paired untreated control, an interesting relationship was revealed. Chloramphenicol did not significantly alter the total number of mtDNAs transferred into cells which had engaged in IMT. Conversely, CSP was found to decrease the total number of mtDNAs transferred into cells which had engaged in IMT.

6.5 Results: Chronic cellular injury and IMT

6.5.1 ρ^0-eGFP-astrocytes as a model of chronic mitochondrial injury

To test the hypothesis that a chronic mitochondrial deficiency may alter the rate of IMT, ρ^0-eGFP astrocytes were used. When pyruvate/uridine is removed from the culture medium, this cell line is no longer viable [262]. Restriction of pyruvate/uridine models chronic metabolic injury. Before ρ^0-eGFP-astrocyte/primary pericyte co-cultures were established, it was essential to confirm these cells were auxotrophic for pyruvate/uridine, and would in fact model the desired chronic injury.

To test this, growth inhibition by removal of pyruvate/uridine was assessed using an Incucyte S3™ live-cell imaging incubator. ρ^0-eGFP-astrocytes were seeded in complete medium, or in restrictive medium which lacked pyruvate and uridine. The growth curve data generated in these experiments are presented in **Figure 6.5.1**. After an extended culture time of 192 h, ρ^0-eGFP-astrocytes with pyruvate/uridine supplemented medium reached a plateau in density at approximately 50% coverage by surface area. Density of culture was seen to increase steadily over the first 100 h of growth. As the medium was not refreshed at any point in the 192 h period, it came as no surprise that a growth plateau was reached. This was likely due to depletion of nutrients, or accumulation of lactic acid in the medium.

Conversely, ρ^0-eGFP-astrocyte cultures in restrictive medium which lacked pyruvate/uridine did not demonstrate a detectable increase in density. The growth curve generated for these cells consisted of a horizontal line, unchanged over the 192 h period.

Taken together, these results indicate that the mitochondrial defect present in ρ^0-eGFP astrocytes is sufficient to completely inhibit growth, in medium which lacks pyruvate and uridine. This suggests the cells fail to overcome the bioenergetic crisis induced by removal of these essential biomolecules. This data establishes that removal of pyruvate/uridine from the medium of ρ^0-eGFP-astrocytes serves as a chronic metabolic injury.

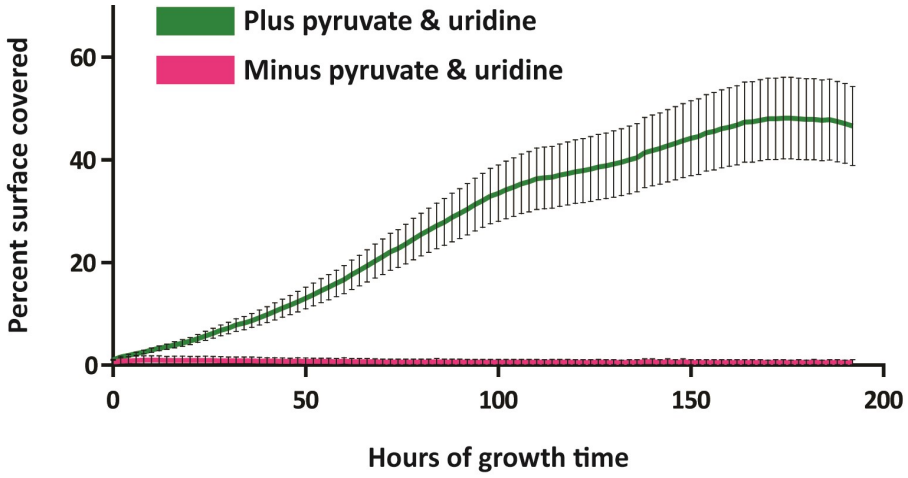

Figure 6.5.1. ρ^0-eGFP astrocytes do not expand when deprived of pyruvate and uridine

Fifty thousand ρ^0-eGFP-astrocytes were seeded into each well of a six-well plate, in complete medium, or in restricted medium lacking pyruvate and uridine. The cells were monitored by collection of 32 images every 2 h, in an Incucyte S3™ imaging incubator. The percent of the vessel surface covered by cell area was determined for each image. Data are presented for 192 h incubation. Data are presented as the mean ± SEM from 3 independent biological replicates.

6.5.2 IMT in ρ^0-eGFP-astrocyte/primary pericyte co-cultures – The effect of pyruvate and uridine deprivation on IMT.

With complete growth inhibition by removal of pyruvate/uridine confirmed in ρ^0-eGFP-astrocytes, co-cultures were established with primary pericytes to test whether or not an induced chronic injury would alter the rate of IMT. ρ^0-eGFP-astrocytes were stained with CellTrace Yellow™ and co-cultures established on glass coverslips with DIV8 P2 primary pericytes in either complete, or restrictive medium which lacked pyruvate and uridine. The co-cultures were then incubated for 72 h to allow for potential IMT to occur.

In **Figure 6.5.2**, representative images are presented of ρ^0-eGFP-astrocytes after 72 h in co-culture with primary pericytes. *In situ* RCA targeted to mtDNA_9461G revealed the presence of many mtDNA molecules of pericyte origin within the CellTrace Yellow™ stained ρ^0-eGFP-astrocytes. As the ρ^0-eGFP-astrocytes lack mtDNA, false positive events caused by non-specific ligation of PDPs do not occur in this reaction. All RCPs which were generated in these cells were templated exclusively by pericyte mtDNA sequence.

Both complete medium **(top)** and restrictive medium **(bottom)** conditions resulted in multiple mtDNA_9461G RCP products detected in ρ^0-eGFP-astrocytes. As in the enlarged panels (I. II.), multiple mtDNAs were detected in some ρ^0-eGFP-astrocytes, however other cells in the culture were void of transferred mtDNAs. This suggests IMT occurs in the ρ^0-eGFP-astrocyte/primary pericyte co-culture, independently of pyruvate/uridine restriction. This was not surprising, given the primary pericytes are capable of IMT with the parental, mitochondrial competent eGFP-astrocyte cell line.

Figure 6.5.2. ρ^0-eGFP-astrocytes receive mtDNA from primary pericytes as detected by mtDNA_9461G targeted *in situ* RCA
ρ^0-eGFP-astrocytes were co-cultured with primary pericytes, in both complete medium and medium void of pyruvate and uridine. After 72 h in co-culture, the cells were fixed and mtDNA_9461G targeted *in situ* RCA performed. From each representative image, a panel is enlarged which depicts one or more ρ^0-eGFP-astrocyte(s) which have acquired exogenous mitochondrial DNA (yellow). **(Top)** ρ^0-eGFP-astrocytes (magenta) co-cultured with primary pericytes (non-fluorescent) in complete medium. **(Bottom)** ρ^0-eGFP-astrocytes (magenta) co-cultured with primary pericytes (unlabelled) in restricted medium lacking pyruvate and uridine. Images were collected by LSCM at 600 x magnification. CellTrace Yellow™ = magenta, ATTO647 mtDNA_9461G RCPs = Yellow.

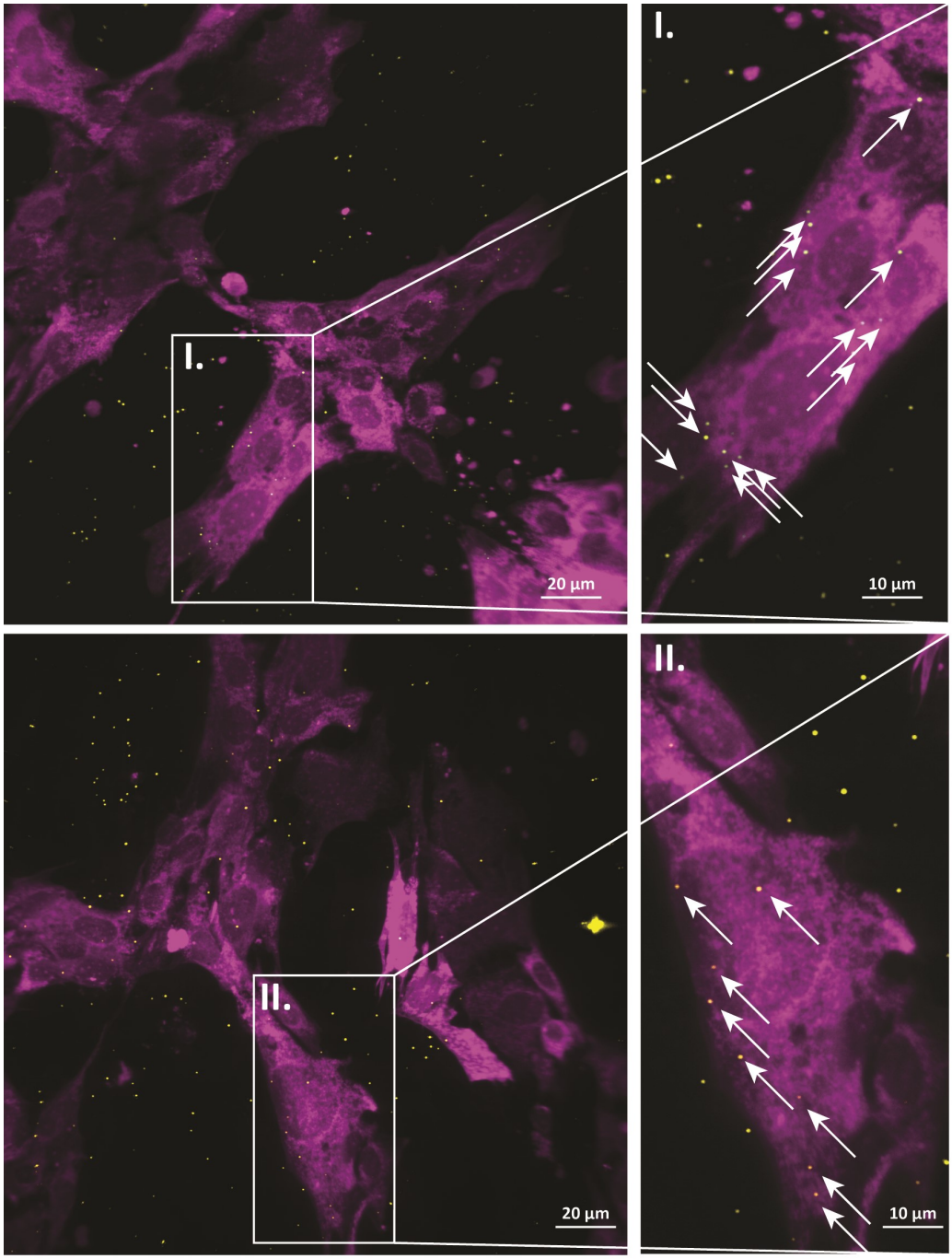
I.
I.
20 µm
10 µm
II.
II.
20 µm
10 µm

To assess whether or not ρ^0-eGFP-astrocytes pushed into a state of stress due to chronic mitochondrial DNA deficit would increase rates of IMT in these co-cultures, approximately 600-700 image fields from each sample were collected by automated HTCM, from two technical replicate areas of RCA reaction. The images were then processed via the analysis pipeline developed in chapter 4. **Table 17** summarises the total number of objects successfully extracted from three independent biological replicate experiments, denoted as image sets 1, 2 and 3.

Table 17. Summary counts for Image analysis of ρ^0-eGFP-astrocyte/primary pericyte co-cultures

Image set	Count cytoplasmic segments (cells) detected	Count RCP signals (mtDNA) detected
ρ^0-eGFP-astrocyte/primary pericyte plus pyruvate/uridine set 1	863	828
ρ^0-eGFP-astrocyte/primary pericyte plus pyruvate/uridine set 2	186	51
ρ^0-eGFP-astrocyte/primary pericyte plus pyruvate/uridine set 3	2262	4609
ρ^0-eGFP-astrocyte/primary pericyte minus pyruvate/uridine set 1	1027	899
ρ^0-eGFP-astrocyte/primary pericyte minus pyruvate/uridine set 2	192	223
ρ^0-eGFP-astrocyte/primary pericyte minus pyruvate/uridine set 3	606	115

For each detected ρ^0-eGFP-astrocyte segment, the count of RCPs was determined. A correction was applied to the raw data to account for false-positive ligation events, based on the frequencies determined in chapter 4. This enabled population level comparisons between the pyruvate/uridine supplemented or deprived conditions as presented in **Figure 6.5.3.**

In **Figure 6.5.3A**, a heatmap summarises these data. ρ^o-eGFP-astrocyte segments with each RCP count, from 0 RCP to 20+ RCP per segment, are represented by each row in the heatmap. The frequency of segments with each RCP count is indicated by the intensity of shading, from most frequent (yellow) to least frequent (blue). The most frequent observation was for segments with an RCP count of 0, seen in the first row of the heatmap. This indicated that most ρ^o-eGFP-astrocyte cells had not engaged in IMT, regardless of pyruvate/uridine status in the medium.

Because segments with ≥1 RCP were considered to have engaged in transfer, the sum frequency of positive segments represents the frequency of IMT in the whole population. In **Figure 6.5.3B,** the mean total frequency of IMT positive segments is represented by scatter plot, for each of pyruvate/uridine plus or minus conditions from the three replicate image sets. No statistically significant difference was found in the mean frequency of IMT in the population. It was immediately apparent that the population level frequency of IMT was highly variable, independent of pyruvate/uridine supplementation.

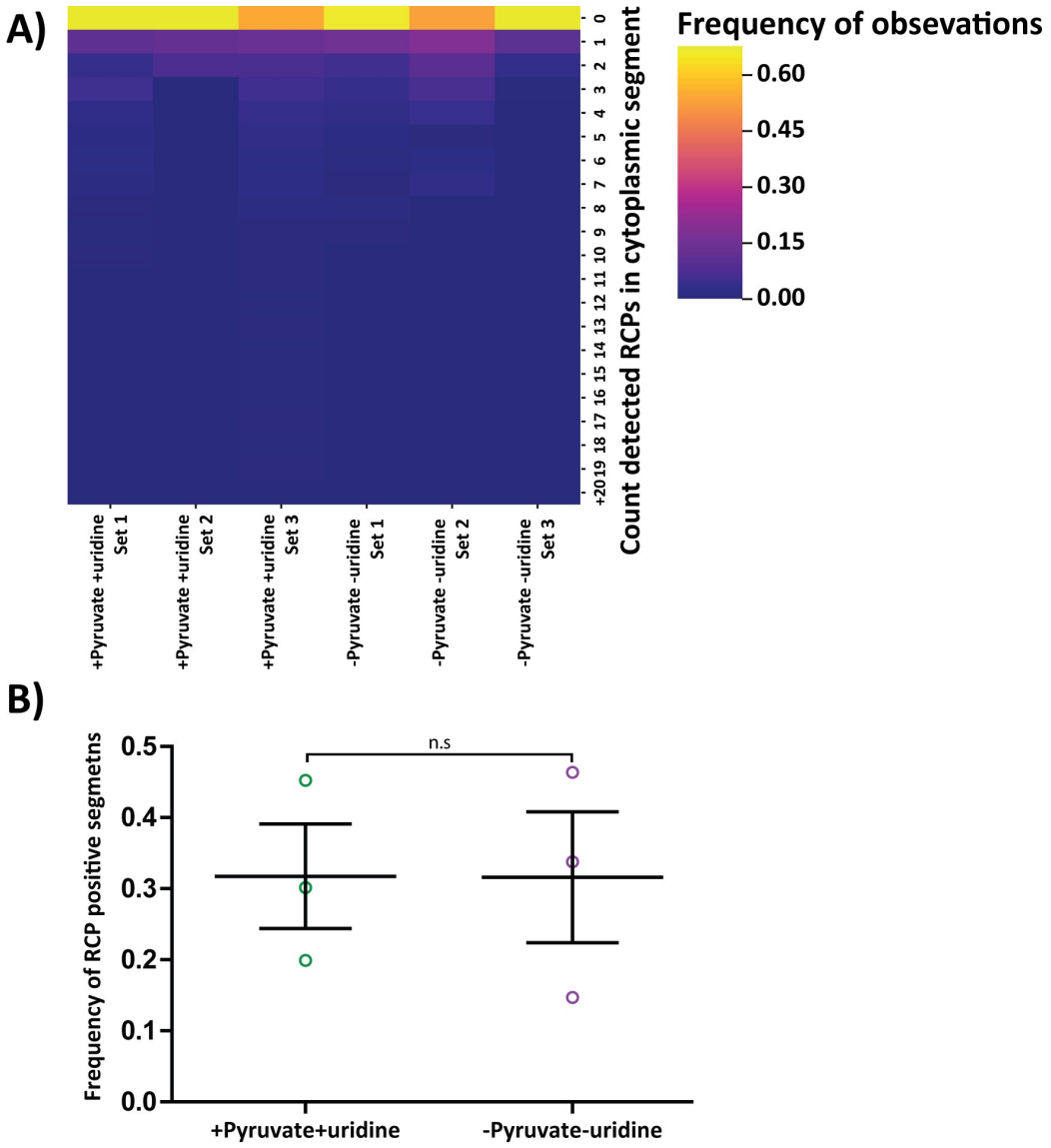

Figure 6.5.3. Deprivation of pyruvate and uridine did not affect the total frequency of eGFP-astrocytes engaged in IMT after co-culture with primary pericytes
Three hundred thousand ρ^0-eGFP-astrocytes were cultured in medium which either contained, or was deficient in pyruvate and uridine. After 48 h, the cells were stained with CellTrace™ Yellow and co-cultured with primary pericytes. After 72 h in co-culture, *in situ* RCA targeted to mtDNA_9461G was performed to detect mtDNA of pericyte origin. Images were collected by HTCM and analysis was performed as described in chapter 4. Data are presented from three independent image sets of paired +/+ and -/- pyruvate/uridine medium conditions. **(A)** The frequencies at which ρ^0-eGFP-astrocyte segments were detected with each count of mtDNA_9461G RCP between 0 and 20+, visualised as a heat map. Each image set is presented here independently. **(B)** The sum frequency of segments detected with ≥1 mtDNA_9461G RCPs (i.e cells which took up pericyte mtDNA) are presented as a scatter plot. Results are presented as the mean ± SEM from three replicate experiments. An unpaired students t-test indicated no significant difference between groups at $p \leq 0.05$.

Next, only the segments where IMT was detected were examined (RCP ≥1), to determine if removal of pyruvate and uridine from the culture medium of ρ^0-eGFP-astrocytes in co-culture had altered the number of mtDNA detected in cells that had engaged in IMT.

In **Figure 6.5.4A**, a heat map summarises the frequency of ρ^0-eGFP-astrocyte segments detected with each count of RCP ≥1. The data here are presented as paired, plus pyruvate/uridine and minus pyruvate/uridine medium conditions. It is possible to see that the paired medium conditions from image set 1 appear more similar to each other, than the respective paired medium conditions in image sets 2 and 3.

In **Figure 6.5.4B**, the average frequency of RCP positive segments between conditions are presented as a scatter plot. Here, each data point represents a specific RCP count. From these data, it is possible to see that the distribution segment frequencies is on average, very similar between each medium condition. The outlier values correspond to segments occurring with 1, 2, or 3 RCPs; the RCP count for most detected segments. No significant difference in the mean frequency between each count of RCP was identified. This suggests that on average, removal of pyruvate/uridine from the medium did not significantly alter the distribution segments with specific RCP counts.

The RCP count of a segment correlates with the number of mtDNA molecules transferred into a cell. By extension, segments with different RCP counts have different intensities of IMT, or mtDNAs transferred into the cell. By scaling the frequency of a segment's occurrence by each specific RCP count, it was possible to examine the relationship between intensity, or extent of mtDNA transfer within segments, and status of pyruvate/uridine in the medium.

In **Figure 6.5.4C**, the mean relative quantity of mtDNA transferred into IMT positive segments is presented as a scatter plot. Here, each data point represents the mean intensity of IMT at each RCP count, averaged across the three replicate image sets. Through this analysis, low frequency segments with unusually high or low RCP counts were accounted for, as they represented very few of the total mtDNAs transferred. When the intensity of IMT from segments with each RCP count were compared between medium conditions, a significant difference was detected in the total average RCP count. ρ^0-eGFP-astrocytes co-cultured in conditions that lacked pyruvate and uridine were found on average to contain fewer total transferred mtDNAs.

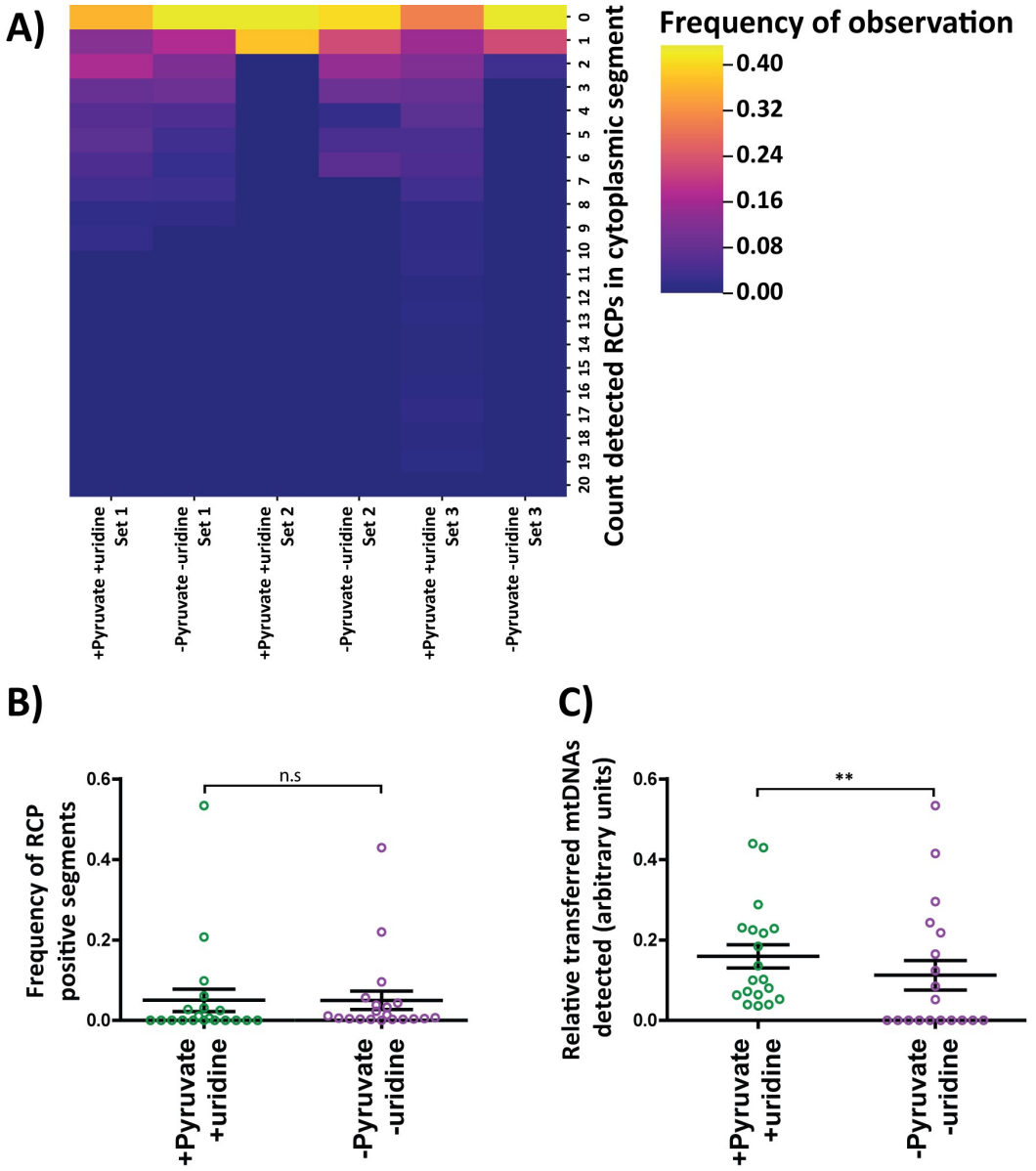

Figure 6.5.4. Deprivation of pyruvate and uridine altered the count of detected mtDNA molecules transferred into individual ρ^0-eGFP-astrocytes, where IMT had occurred

(A) The frequencies at which ρ^0-eGFP-astrocyte segments were detected for all counts of RCP ≥1, visualised as a heat map. Each CMP treated image set is presented alongside its paired, vehicle only untreated control. **(B)** For each count of detected RCP, the frequency of detected segments was compared to the equivalent count of RCP in its paired control. This allowed segments with each individual level of IMT to be compared fairly. Results are presented as the mean change in frequency ± SEM for each RCP count ≥1, normalised to each paired control. Paired students t-tests performed to compare each count of RCP between control and treated samples, indicated no significant difference between image sets at $p \leq 0.05$. **(C)** Because various counts of RCP indicate a different extent of IMT occurrence in a given segment, the frequency value for each segment was multiplied by the RCP count, to produce a relative measure of total transferred mtDNAs for each RCP count. This value is displayed as a scatter plot of the mean for each RCP count, with the mean determined for each treatment condition ± SEM. This value reflects the total relative number of mtDNAs transferred into ρ^0-eGFP-astrocytes, between conditions. A Wilcoxon matched-pairs signed rank test was used to recognise a difference between treatment conditions at $p \leq 0.05$.

6.5.3 Recovery of mitochondrial competence in ρ^0-eGFP-astrocytes after acquisition of mtDNA from primary pericytes by IMT.

A major driver for research in this thesis was the hypothesis that IMT represents a potential mechanism for cells to overcome critical mitochondrial damage, and survive the effects of therapy. After IMT was observed from pericytes into ρ^0-eGFP-astrocytes, I was interested in mitochondrial recovery in these cells over an extended period of time. The glass coverslips used to produce the data presented in section **Figure 6.5.2** were carefully extracted from the ρ^0-eGFP-astrocyte/primary pericyte cultures, keeping the cells which remained sterile. This enabled maintenance of extended ρ^0-eGFP-astrocyte/pericyte cultures in medium which lacked pyruvate and uridine. The cultures were passaged each time 80% density by surface area was reached. The growth rate of the primary pericytes slowed over time. This was likely the result of senescence and/or differentiation *in vitro* as commonly occurs with primary cells. Slow growing colonies of ρ^0-eGFP-astrocytes persisted, interspersed by residual primary cells. In **Figure 6.5.5**, a culture maintained for 21 days was examined by EtBr stain and mtDNA_9461G targeted RCA to evaluate the presence or absence of mitochondrial networks (EtBr) and/or mtDNA (RCA) in the ρ^0-eGFP-astrocytes.

Depicted in **Figure 6.5.5A**, a representative field of EtBr stained cells from this culture is presented. In the top left of the field, a GFP negative, residual primary cell is partially observed. In this cell, EtBr stain revealed reticular mitochondrial networks characteristic of healthy, functional mitochondria. Towards the center of the image are GFP positive (magenta) ρ^0-eGFP-astrocytes. In contrast to the residual primary cells, the ρ^0-eGFP-astrocytes did not display punctate or extended structures in the cytoplasm, consistent with mitochondrial networks. Only the nucleolar regions appear distinctly stained, as expected with EtBr. This suggests that 19-21 days after initial IMT events had occurred (in the culture overall), normal mitochondrial network morphology had not yet been re-established in these cells.

Figure 6.5.5B, mtDNA_9461G targeted RCA was performed to examine whether or not pericyte mtDNA could be detected inside the ρ^0-eGFP-astrocytes 21 days after the initial co-culture was initiated. A representative image field depicts a colony of ρ^0-eGFP-astrocytes. Rolling circle products were detected in the cytoplasm of almost every cell. Curiously, the count of these was low – typically just a single RCP per cytoplasm. This indicates that at 21 days, pericyte mtDNA is still present in ρ^0-eGFP astrocytes. It is not possible to determine from these data if these were recent IMT events which had continued to occur from residual primary cells, or are early events from which mtDNA was maintained.

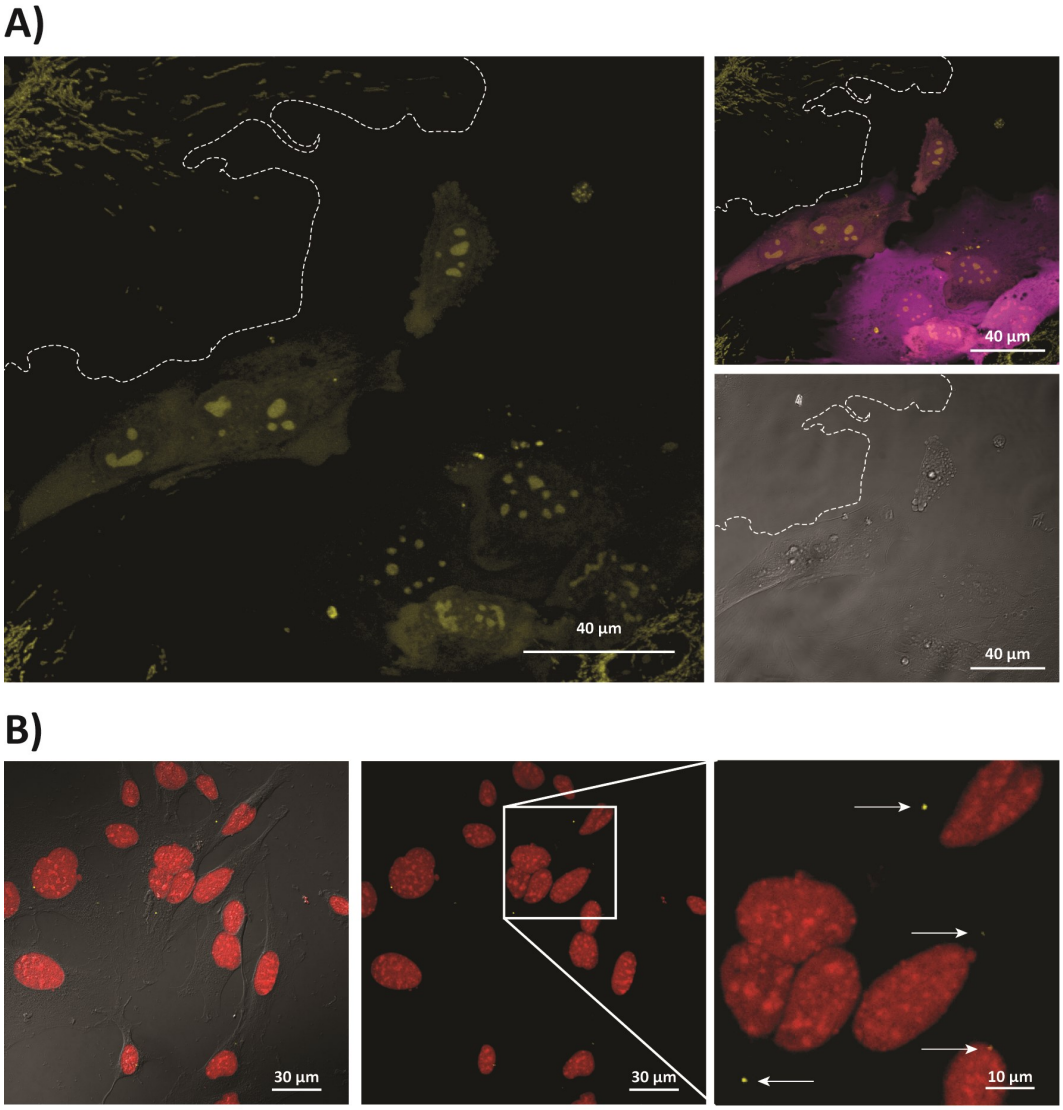

Figure 6.5.5. Recovery of mitochondrial networks in ρ^0-eGFP-astrocytes after co-culture with primary pericytes did not occur within 21 days
ρ^0-eGFP-astrocyte/primary pericyte co-cultures were maintained for an extended period in medium lacking pyruvate and uridine. At 21 days post-co-culture, samples were prepared for live-cell LSCM with EtBr staining **(A)**, and for mtDNA_9461G targeted *in situ* RCA **(B)**. Each field presented is representative of ρ^0-eGFP-astrocyte/pericyte co-cultures approximately 7 passages after the initial co-cultures were established. In **(top),** eGFP = magenta, EtBr = yellow. The periphery of an unlabelled pericyte membrane has been demarcated with a dashed line. In **(bottom)**, ATTO647 mtDNA_9461G RCPs = Yellow, PI = red. The area within the white square has been enlarged **(right)** to visualise individual RCPs. Images were collected by LSCM at 600 x magnification.

Maintenance of the extended co-cultures, in medium lacking pyruvate and uridine, was continued and the ρ^0-eGFP-astrocytes continued to replicate. Though data was not collected, the level of residual primary cells continued to decrease over time. Concurrently, the growth rate of the ρ^0-eGFP-astrocyte component of the culture appeared to increase.

In **Figure 6.5.6**, a co-culture maintained for 43 days was examined by EtBr stain and *in situ* RCA performed to evaluate the presence or absence of mitochondrial networks (EtBr) and/or mtDNA (RCA) in the ρ^0-eGFP-astrocytes. This was the same culture as that presented in **Figure 6.5.5,** after an additional 22 days.

In **Figure 6.5.6A**, a representative field of EtBr stained cells from this culture is presented. This time and somewhat surprisingly, punctate EtBr stain was present throughout the cell body of the ρ^0-eGFP-astrocytes. Two individual cells have been enlarged to provide an enhanced view. The observed pattern was consistent with the appearance of mitochondrial networks by EtBr stain. The networks were not well reticulated, instead appearing as fragmented areas of stain. This suggested that completely normal mitochondrial morphology had not yet been fully established in these cells.

Somewhat concerned that the culture had simply become contaminated by the parental eGFP-astrocyte cell line, *in situ* RCA targeted to both mtDNA_9461G and mtDNA_9348G was performed. In **Figure 6.5.6A**, a representative field from this experiment is presented. High counts of mtDNA_9461G were detected within all cells examined. Rolling circle products generated from mtDNA_9348G were detected at a very low level, consistent with non-specific ligation events. Taken together, and given very few pericyte derived cells remained in culture at this point in time, this was strong evidence that the ρ^0-eGFP-astrocytes had regained autonomous replication of mitochondrial DNA, by 43 days after the start of the co-culture.

The culture was sorted by FACS in an effort to deplete all remaining GFP negative cells from the population, to enhance downstream experiments on the now mtDNA recovered-ρ^0-eGFP-astrocytes.

Figure 6.5.6. Recovered ρ^0-eGFP-astrocytes demonstrate mitochondrial networks and abundant mtDNAs by *in situ* RCA after an extended period in culture

ρ^0-eGFP-astrocyte/primary pericyte co-cultures were maintained for an extended period in medium which lacked pyruvate and uridine. Forty three days after establishment of the initial co-cultures, samples were prepared for live-cell LSCM with EtBr staining **(A)**, and for mtDNA_9461G targeted *in situ* RCA **(B).** Each field presented is representative of ρ^0-eGFP-astrocyte/pericyte co-cultures approximately 14 passages after the initial co-cultures were established. In **(top),** eGFP = magenta, EtBr = green. The mitochondrial networks of two individual cells have been enlarged to provide detail **(I,II)**. In **(bottom)**, ATTO647 mtDNA_9461G RCPs = yellow, PI = red. Images were collected by LSCM at 600 x magnification.

A)

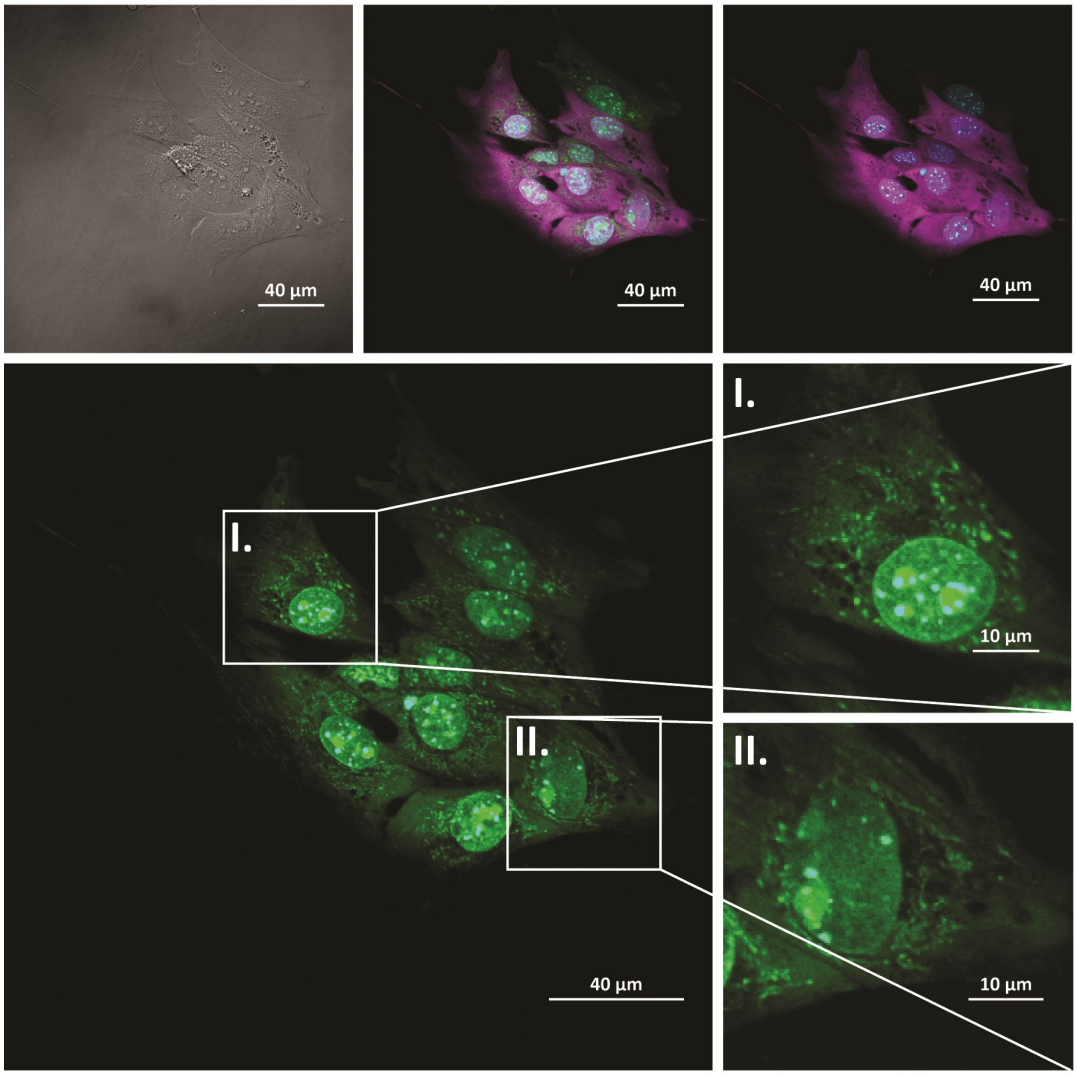

B)

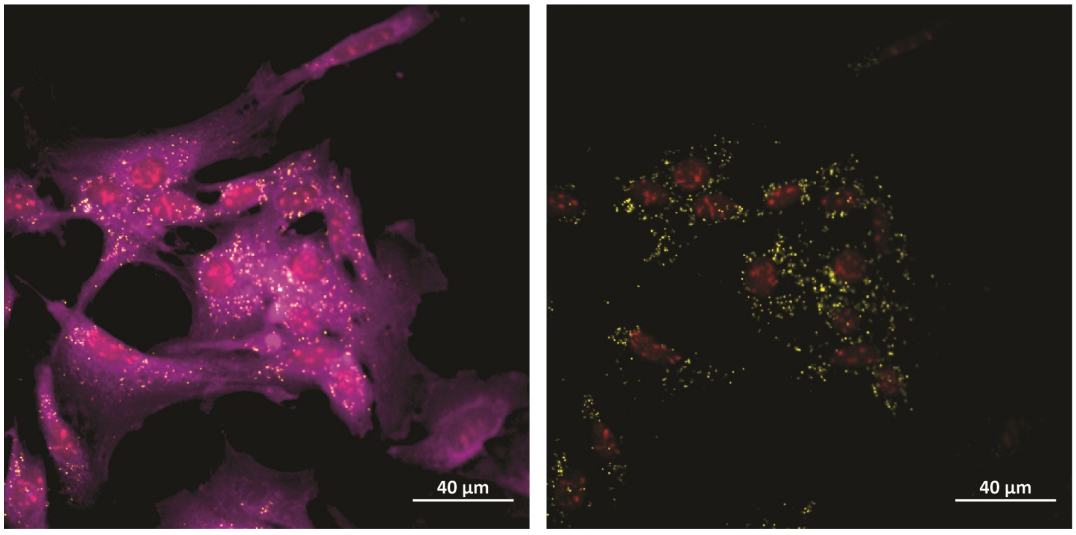

While the *in situ* RCA of recovered-ρ^0-eGFP-astrocytes was an effective means to genotype the mtDNA_9461 locus of these cells and confirm it matched the mtDNA of primary pericytes, it did not provide insight into the sequence present at other mtDNA identifying polymorphisms of interest. The recovered ρ^0 cell line described in **Figure 6.5.5** and **Figure 6.5.6**, and a second long term culture of a recovered ρ^0 line derived in the same fashion, were subject to sequencing of the mtDNA. Parental eGFP-astrocytes from which the ρ^0 line was derived by RTS were sequenced in parallel.

In **Figure 6.5.7**, representative mtDNA sequence alignments from each of the two independently derived, recovered-ρ^0-eGFP-astrocyte lines are presented, at the three polymorphic regions of interest: mtDNA9348, 9461 and the Poly-A tract. The parental eGFP-astrocytes carried the sequence G, T, 8A for mtDNA9348, 9461 and the Poly-A tract respectively, while both recovered ρ^0-eGFP-astrocyte lines carried the sequence A, C, 9A. This is consistent with the mtDNA sequences carried by a BALB/cByJ mouse; the source of tissue for the primary pericytes.

Taken together in addition to the observations made in **Figure 6.5.5** and **Figure 6.5.6**, these results confirmed that ρ^0-eGFP-astrocytes took up mtDNA, likely as complete mitochondria, from primary pericytes and had regained capacity to replicate mtDNA.

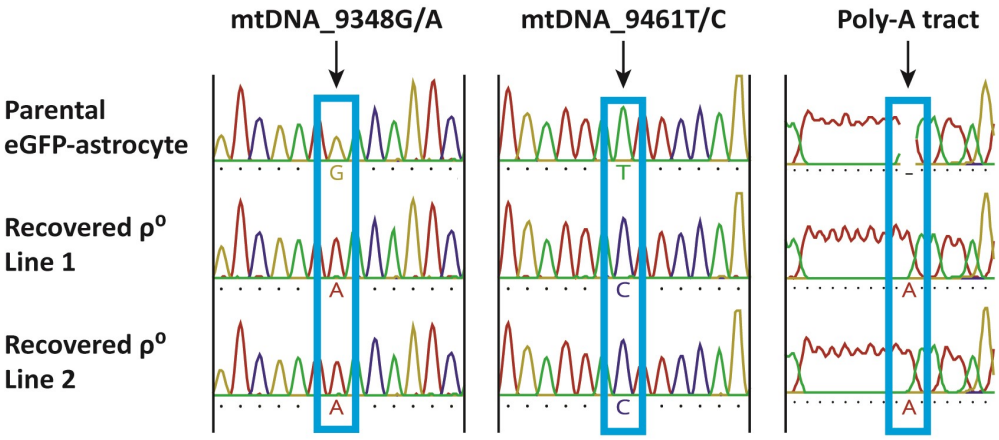

Figure 6.5.7. The mtDNA recovered ρ^0-eGFP-astrocyte lines carry mtDNA polymorphisms unlike the parental eGFP-astrocyte line

gDNA isolated from eGFP-astrocytes, and gDNA from ρ^0-eGFP astrocytes isolated from two independent long term ρ^0-eGFP-astrocyte/pericyte co-cultures, was PCR amplified and subject to sequencing at the tRNA-Arg locus, as described in the methods. Representative alignments of the mtDNA9348, 9461 and Poly-A tract polymorphisms are presented and describe the consensus sequence identified in three independent gDNA preparations of each sample. Sequencing was targeted to both the forward and reverse strands of the PCR product.

Recovery of both mtDNA and mitochondrial network morphology were strong indicators that IMT may allow cells to overcome chronic mitochondrial defects related to mtDNA, such as the ρ^0 phenotype. The abundance of mtDNA within the recovered ρ^0 cells suggested replicative capacity was restored. This did not however, indicate whether or not the mtDNA was now transcriptionally active. I was interested in whether these cells produced mitochondrial transcripts from the newly recovered mtDNA, and how the abundance of these compared to the parental eGFP-astrocytes.

To answer this question, qRT-PCR was performed to determine the relative abundance of D-loop, Cox1 and CytB mtDNA transcripts. Recovered-ρ^0, or parental eGFP-astrocyte cells were seeded into T75 flasks and cultured for 48 h. RNA was then extracted and again, care taken to eliminate gDNA through DNase treatment. In **Figure 6.5.8**, a scatter plot depicts the abundance of D-loop, Cox1 and CytB mitochondrial transcripts, as the ΔCt, relative to 18s. As reaction efficiencies were close to 100% for each primer set, a ΔCt of 1 cycle indicates double the target transcript.

The D-loop transcript was found to reach amplification threshold approximately 2 cycles earlier than 18s on average from the parental eGFP-cells. The amplification threshold was reached on average approximately 2.1 cycles later than 18s for recovered ρ^0 cells. This difference of 4.1 cycles indicates D-loop transcript was approximately 17.15 times more abundant in the parental cell line, than the recovered ρ^0 cells. Cox1 transcript was found to amplify approximately 7.8 cycles earlier than 18s on average from the parental eGFP-cells, while from recovered ρ^0 cells, an average of approximately 3.2 cycles earlier than 18s was detected. This difference of 4.6 cycles indicates Cox1 transcript was approximately 24.25 times more abundant in the parental cell line, than recovered ρ^0 cells. Similarly, CytB transcript was found to amplify approximately 8 cycles earlier than 18s on average from the parental eGFP-cells, while from recovered ρ^0 cells, an average of approximately 3 cycles earlier than 18s was detected. This difference of 5 cycles indicates CytB transcript was approximately 32 times more abundant in the parental cell line, than the recovered ρ^0 cells.

Taken together, these results provide two important insights into the transcriptional state of the recovered ρ^0-cells. The simple presence of the three measured mitochondrial transcripts confirms that the acquired mtDNA was transcriptionally active in these cells. Additionally, each of these transcripts were present in significantly lower abundance than the parental eGFP-astrocytes. This suggests that a combination of the rate of transcription, requirement for transcript, or turnover of mitochondrial transcripts remained altered in the ρ^0-eGFP astrocytes.

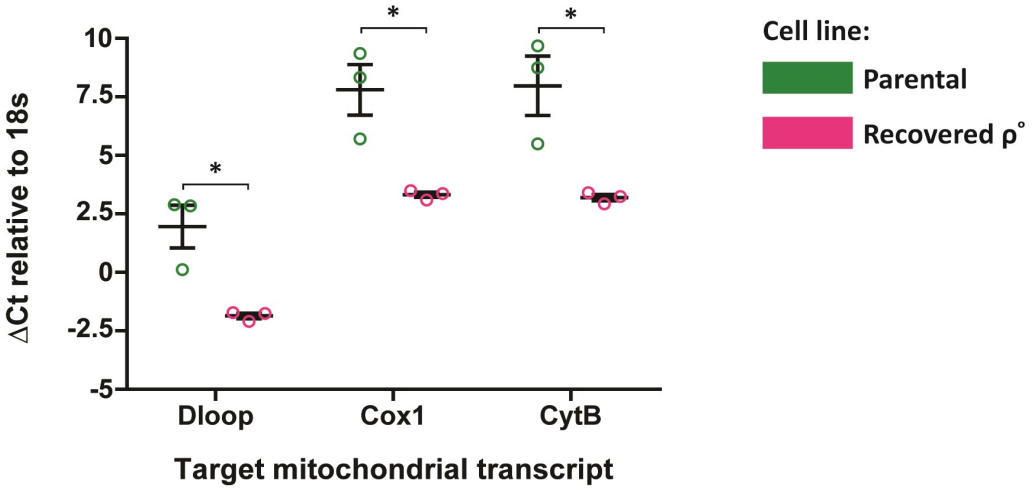

Figure 6.5.8. The mtDNA recovered ρ^0-eGFP-astrocytes have altered presence of mtDNA encoded transcripts

Three hundred thousand parental eGFP-astrocytes or mtDNA recovered ρ^0-eGFP-astrocytes were seeded into T75 flasks and cultured for 48 h before harvest. Basal levels of the D-loop, Cox1 and CytB target transcripts were then quantified by RT-qPCR. Expression data are presented as the difference in cycle threshold between target gene and 18s rRNA amplification, from three independent experiments. An unpaired students t-test was used to compare the difference in expression of each target transcript at $p \leq 0.05$.

With evidence in support of mitochondrial recovery at the mtDNA and transcriptional level, it was important to establish that this translated into cellular function. I was interested to find out if the recovered-ρ^0-eGFP-astrocytes would demonstrate mitochondrial respiration, and how the metabolic phenotype of these cells compared to the parental ρ^0-eGFP-astrocytes. To test this the parental eGFP-astrocytes, their ρ^0 derivative and the recovered-ρ^0 derivative cell lines were subject to a glycolytic rate assay performed with a Seahorse XFe96 instrument. The ECAR and OCR was determined for these cells in basal, rot/AA challenged and 2-DG challenged conditions. These are presented in **Figure 6.5.9** as line plots which depict the mean rates as a function of time, from three independent replicate experiments.

In **Figure 6.5.9A**, the ECAR for each cell line is presented. Here, the ECAR of the parental eGFP-astrocytes was approximately 1.6 x greater than the recovered-ρ^0 line, and approximately 3.7 x greater than the ρ^0 line. When challenged with rot/AA, the ECAR of the parental line and ρ^0 lines were found to increase, however only marginally for the ρ^0 line. The ECAR of the recovered-ρ^0 was unresponsive to rot/AA challenge. When challenged with 2-DG, the ECAR all three lines was strongly decreased, consistent with glycolytic inhibition by 2-DG.

In **Figure 6.5.9B**, the basal OCR of the parental eGFP-astrocytes was considerably higher than both the recovered-ρ^0 line and the ρ^0 line. This suggests a greater basal requirement for mitochondrial derived ATP in the parental cells, and the respiratory capacity to meet this requirement. The ρ^0 cell line was found to consume oxygen at a very low rate, barely distinguished from background levels. This was consistent with a lack of aerobic respiration. The OCR of the recovered ρ^0 was approximately half the rate of the parental cell line, indicative of a reduced basal requirement for mitochondrial ATP, or a lack of spare respiratory capacity. After rot/AA injection, OCR was found to decrease for both the parental and recovered-ρ^0 cell lines, consistent with inhibition of mitochondrial respiration at respiratory complexes I and III. No decrease was discernible for the ρ^0 line, as the OCR for ρ^0 was already at the lower limit of assay sensitivity. Sequential challenge with 2-DG did not further alter the OCR for any of the three cell lines.

Taken together, these results demonstrate that there are differences in the metabolic phenotype each eGFP-astrocyte derivative. Importantly, mitochondrial respiration was restored in the recovered-ρ^0 line, however not to the same extent as the parental eGFP-astrocytes, suggesting the recovered cells remained bio-energetically impaired overall. Challenge with rot/AA did not increase ECAR in the recovered-ρ^0 line, suggestive of a lack of spare glycolytic capacity. In contrast, the parental eGFP-astrocytes were capable of

an increased glycolytic rate, after inhibition of mitochondrial respiration. As expected, ρ^0 cells were solely reliant on glycolytic ATP production.

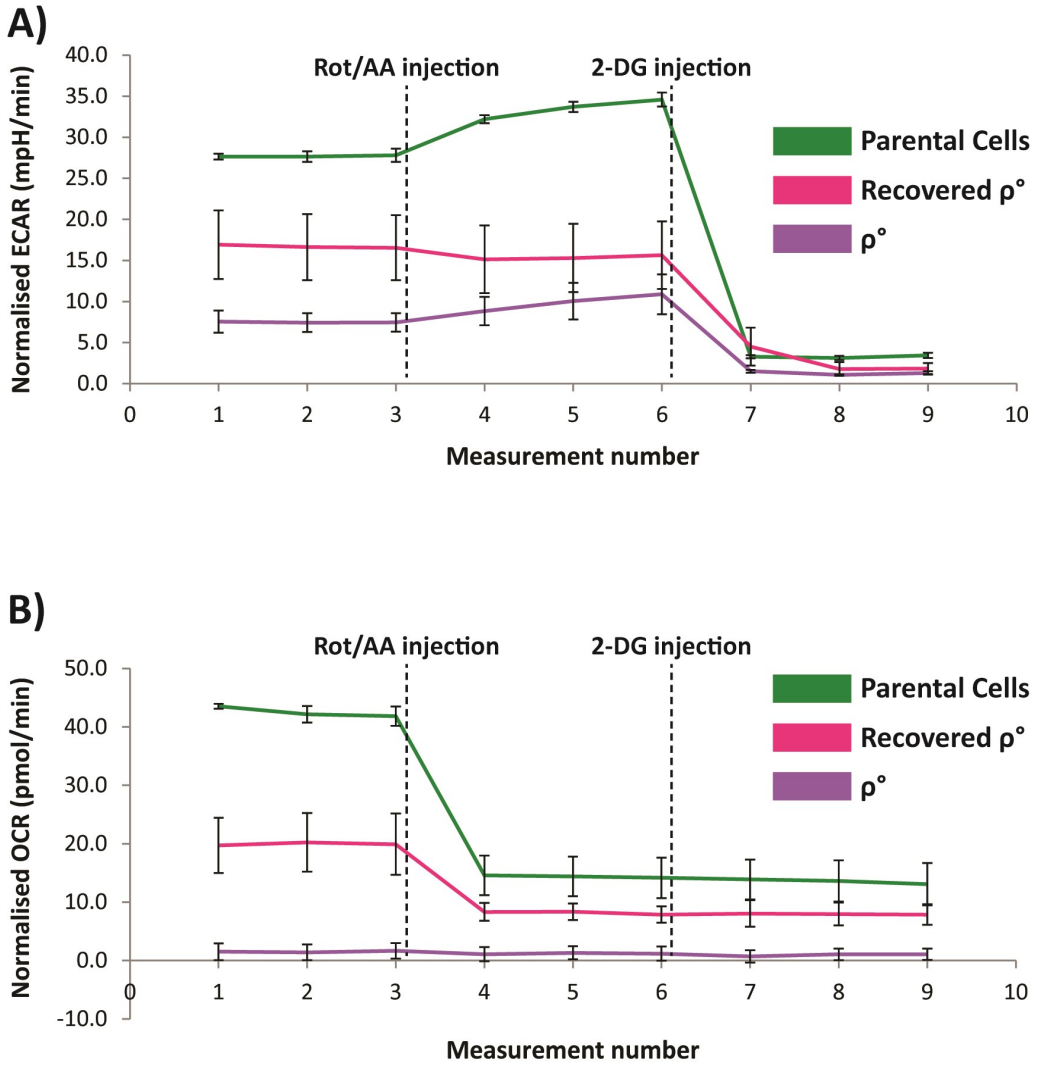

Figure 6.5.9. The mitochondrial respiratory function of mtDNA recovered ρ^0-eGFP-astrocytes remains impaired

The extracellular acidification rate and oxygen consumption rate of parental eGFP-astrocytes, mtDNA recovered p°-eGFP-astrocytes and ρ^0-eGFP-astrocytes were measured by Seahorse XFe96 Glycolytic Rate Assay. Rotenone/antimycin A or 2-deoxyglucose were injected into the medium at specific time points, to inhibit oxidative phosphorylation and glycolysis respectively. **(A)** The extracellular acidification rate recorded every 6.5 min over approximately 1 h. **(B)** The oxygen consumption rate recorded every 6.5 min over approximately 1 h. Data are normalised as described in the methods. The parental cells data are equivalent to the untreated vehicle only control sample presented in **Figure 6.3.4** as these assays were performed in parallel. Results are presented as the mean ± SEM from three independent biological replicates.

As a final test to determine whether or not the recovered ρ^0-eGFP-astrocytes had in fact regained complete mitochondrial respiratory function, recovered cells were subject to culture in restrictive medium which lacked pyruvate and uridine. The parental, recovered-ρ^0 derivative and ρ^0-eGFP-astrocyte derivatives were seeded in medium which either contained, or lacked pyruvate and uridine supplementation. Population density by surface area covered was captured once more using an Incucyte S3™ live-cell imaging incubator. A non-linear regression was calculated for the exponential phase of growth, to determine a population doubling time for each cell line.

In **Figure 6.5.10**, a scatter plot is presented which depicts the average doubling time in hours determined for each line, for both plus and minus pyruvate/uridine medium conditions. In medium which contained pyruvate and uridine, the parental eGFP-astrocytes required approximately 16.9 h to cover double the surface area of the vessel. While somewhat more variable, under the same medium conditions the recovered-ρ^0 and ρ^0-eGFP-astrocyte derivatives required an average of approximately 32.3 and 30.8 h to double in surface area covered. This was significantly more time than required by the parental eGFP-astrocytes.

In medium which lacked pyruvate and uridine, the parental eGFP-astrocytes required no additional time to double in surface area coverage compared to medium which contained pyruvate/uridine. The recovered-ρ^0-eGFP-astrocytes required an average of approximately 37 h to double in area covered. This was significantly slower than the parental eGFP-astrocytes, but not significantly slower than when these cells were cultured in medium which contained pyruvate and uridine. In medium which lacked pyruvate and uridine, the ρ^0 derivative cells were unable grow, thus no doubling time could be modelled. This is consistent with the data described in **Figure 6.5.1**.

Taken together, these results confirm that while the growth rate of the recovered ρ^0-eGFP-astrocytes remained decreased relative to parental eGFP-astrocytes, pyruvate and uridine auxotrophy was overcome entirely. This indicates that complete mitochondrial respiration, inclusive of normal electron transport chain function was restored in the recovered-ρ^0 cells.

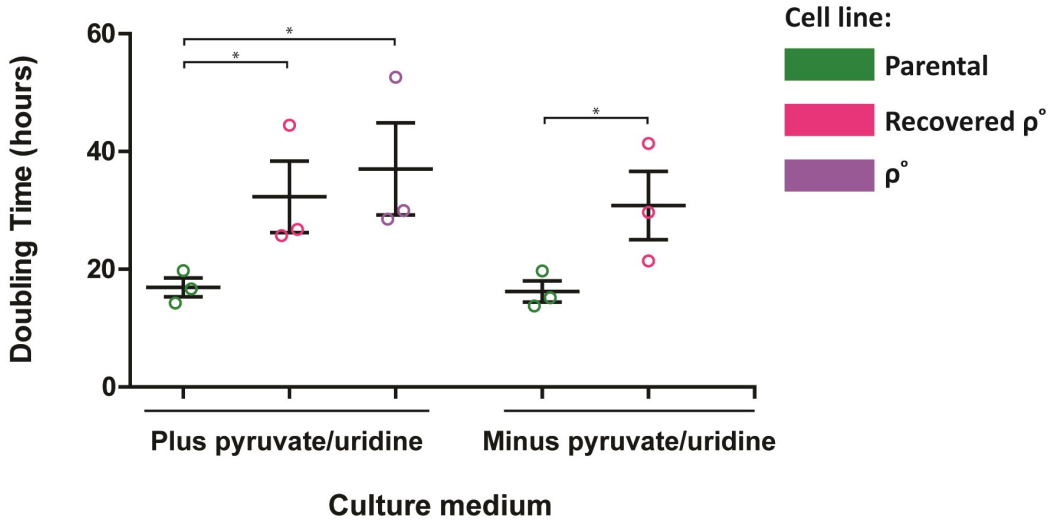

Figure 6.5.10. The mtDNA recovered ρ^0-eGFP-astrocytes are no longer auxotrophic for pyruvate and uridine

Fifty thousand parental eGFP-astrocytes, mtDNA recovered ρ^0-eGFP astrocytes, or ρ^0-eGFP-astrocytes were seeded into each well of a six-well plate, in complete medium, or in medium lacking pyruvate and uridine. The cells were monitored by collection of 32 images every 2 h, in an Incucyte S3™ imaging incubator. The percent of the vessel surface covered by cell area was determined for each image. A non-linear regression was modelled on the exponential growth phase to determine a population doubling rate. Data are presented as the mean ± SEM from 3 independent biological replicates. Note: ρ^0-eGFP-astrocytes are not displayed for the minus pyruvate/uridine condition, as no culture growth was observed in this condition due to auxotrophy.

6.6 Summary: Chronic cellular injury and IMT

In this section, ρ^0-eGFP-astrocytes were used to model a state of chronic mitochondrial injury. By removing pyruvate and uridine supplementation from the culture medium, ρ^0 cells were shown to be non-proliferative, likely due to metabolic crisis. The stress phenotype associated with this state enabled investigation into whether or not this type of chronic metabolic injury would enhance IMT activity, when co-cultured with primary pericytes.

When placed into co-culture, mtDNA of pericyte origin was readily detected in the ρ^0-eGFP-astrocytes. This occurred independently of whether the cells were supplemented with, or deprived of pyruvate/uridine.

No significant difference was found in the frequency of cells which engaged in IMT between either medium condition, however population level frequency of IMT from the three replicate experiments was highly variable. When the intensity of IMT was examined in those individual cells positive for transfer, cells deprived of pyruvate and uridine demonstrated a reduction in the total number of RCPs detected. This indicated that fewer total mtDNAs were taken up from the primary pericytes via IMT under those conditions.

Co-cultures of ρ^0-eGFP-astrocyte/pericytes were maintained for an extended period of time. During this time, the number of primary cells gradually decreased. After 21 days, the ρ^0-eGFP-astrocytes had not developed normal mitochondrial network morphology, however low levels of mtDNA_9461G RCPs detected suggested pericyte mtDNA remained inside these cells. After 43 days, mitochondrial networks had been re-established. The cells were subject to *in situ* single molecule genotyping once more, which revealed abundant mtDNA with the mtDNA_9461G SNV, consistent with that of the primary pericytes. This was confirmed by Sanger sequencing, where all three SNVs of interest were found to match that of the primary pericytes.

Next, mitochondrial transcription, auxotrophy and the metabolic phenotype of the recovered-ρ^0-eGFP-astrocytes was examined by RT-qPCR, Incucyte S3 and Seahorse glycolytic rate assay respectively. In each of these assays, the recovered-ρ^0-eGFP-astrocytes demonstrated a partially restored phenotype consistent with the parental eGFP-astrocytes as opposed to the mtDNA deficient ρ^0-eGFP-astrocytes. Full functional capacity was however, not entirely restored.

6.7 Discussion

The predominant research question of this thesis; "does cellular injury enhance the rate of IMT *in vitro*?" first required the capacity to push cells into an injured state. Only once this injury state was established, could co-cultures to study the effect on IMT be carried out. Given the IMT phenomenon itself was the variable of interest in these studies, I decided on three very simple injury models through which to examine the impact on IMT. Each means to induce injury was selected for specific effects as described in the literature, however the primary focus of this work was to examine the downstream effect on IMT after injury.

To induce acute cellular injury in eGFP-astrocytes, two compounds with distinct mechanisms of action were explored in this chapter. Disruption of the mtR with CMP acted to introduce a deficiency in mitochondrial function, through a targeted inhibition which acted directly inside the mitochondria [347, 353, 372-374]. While the abundance of various proteins synthesised at the mtR (e.g. ETC components) was not assessed directly in this work, multiple phenotypic outcomes of this inhibition were clearly demonstrated. Treatment with CSP is well known to induce DNA damage, inclusive of a selective mtDNA damage component [365, 367, 375, 376]. Again, the direct effect of this agent on DNA was not assessed in this study and instead the downstream effects were evaluated. Rather than to provide in depth characterisations of the injuries effect themselves, these experiments sought only to establish parameters for each injury, suitable for the downstream IMT experiments.

To model stress through a chronic mitochondrial defect, ρ^0-eGFP-astrocytes were deprived of pyruvate and uridine. This forced the mitochondrially deficient cells into a state of extreme metabolic stress. Without a functional ETC in the mitochondria, and without additional uridine, ρ^0 cells are unable to carry out pyrimidine biosynthesis. Furthermore, in the absence of externally provided pyruvate, the amount of pyruvate in ρ^0 cells is insufficient to recycle sufficient NADH to NAD^+ to sustain glycolysis, in addition to provision of acetyl-CoA to the TCA cycle. This results in a lack of critical biosynthetic intermediates and insufficient glycolytic ATP production to sustain cell proliferation.

In this study, ρ^0-eGFP-astrocytes were provided with medium supplemented with or deprived of pyruvate/uridine. The pyruvate/uridine deprived ρ^0-eGFP-astrocytes model metabolic stress. I hypothesised that this would promote IMT activity in co-culture with primary pericytes.

By pushing the cells into these acute or chronic states of stress, particularly due to the mitochondrial component of the injuries, I hypothesised that acute injuries in the eGFP-astrocytes, and the chronic injury in ρ^0-eGFP astrocytes would increase the rate of IMT from primary pericytes. This would implicate IMT as a mechanism for enhanced cell survival, and provide further insight into the purpose of the phenomenon.

The results presented in this chapter describe treatment schedules for each of CMP and CSP which would adequately prepare cells to conduct the experiments necessary to confirm or reject the proposed hypotheses. Despite the differences in mechanism of action, both compounds produced somewhat similar effects in the individual assays shared between treatments, when used at the concentration and duration chosen for each. This was a curious observation. At a treatment intensity that was sub-lethal to the majority of cells, CSP caused a similar global phenotype as CMP in the shared assays. This may suggest that CSP induced damage included similar disruption to mitochondrial function as CMP; the targeted mitochondrial injury. This was particularly evident through the Seahorse glycolytic rate assay results.

Co-cultures established between primary pericytes and both the acute or chronic injury models provided the context to study changes in the rate of IMT. Presented in this chapter is the first known application of *in situ* single molecule imaging to quantify the transfer of mtDNAs between cells. Independent of the cell biology studied, the data presented here demonstrate successful implementation of the approach, from cell culture to image analysis and data output.

To a certain extent, the measurement outputs from this approach took on the form of an entirely unfamiliar and novel data structure. Through the *in situ* single molecule imaging approach used in this work, I have derived metrics to describe the proportions of cells positive for IMT, in addition to the intensity of mtDNA transfer within any given cell. A significant amount of time was required to establish how to best interpret, visualise and extract conclusions from this form of data.

The data collected from *in situ* single molecule imaging and HTCM of the injured/uninjured co-culture experiments did not indicate that these specific injuries increased the rate of IMT in the total population of either the parental or ρ^0-eGFP-astrocytes. Contrary to the hypotheses, no change was identified in the mean frequency of IMT in the total population for any of CSP, CMP or the chronic metabolic injury (deprived ρ^0 cells) at the chosen concentration and time. Because of the variation seen between image sets from both treated and untreated conditions for each of the three injuries, the mean

frequency of IMT, it is somewhat inappropriate to draw a strong conclusion about the population level frequency of IMT in these particular datasets.

In contrast, a significant difference was detected in the total mtDNA molecules transferred within IMT positive cells treated with CSP. Here, the CSP injury was found to reduce the mean total number of mtDNAs transferred into cells that had engaged in IMT. A second difference was identified in the total number of mtDNAs transferred into ρ^0-eGFP-astrocytes when the cells were deprived of pyruvate/uridine. Under these conditions, the total number of mtDNAs transferred in the ρ^0-eGFP-astrocytes was again, reduced. This was an unexpected result, as it was hypothesised that injury would increase the rate of IMT. While this appears to disagree with a general consensus in the literature that cellular injury can increase the rate of IMT, it is important to consider that no prior studies have examined what occurs at the level of mtDNA specifically in IMT; existing methods have been limited exclusively to monitoring at the whole organelle level.

A number of caveats must be acknowledged when considering the strength of these conclusions. At the population level, a high degree of variation in the frequency of IMT was seen between replicate experiments; the largest of these varying by up to 55.09% from a mean of 35.46% for the CMP treated image sets. This variation was present in both treated and untreated data sets, which indicates it was not likely introduced by the treatments themselves. Because of this, no significant increase or decrease in frequency was identified between conditions. This however, does not indicate that the total frequency of IMT in each condition was equivalent. Curiously, the mean frequency for IMT positive cells for each of CSP, CMP and deprived ρ^0-eGFP-astrocytes were all highly similar to the paired uninjured control of each, despite the large degree of variation between replicates.

In contrast, conclusions regarding the intensity of transfer in individual segments are more robust. Within each set of paired untreated/treated conditions, and between replicate experiments, the distribution of RCP counts were similar. It is important to consider that the causes of variation in the population IMT frequency, as opposed to the intensity of IMT in individual segments, are likely to be from independent sources. It is possible that the reduced variation in the IMT transfer intensity data represents an underlying biological factor; perhaps transfer mtDNA occurs within a smaller minimum and maximum range of mtDNAs donated. This is sensible, given the cell involved in donation does not have an unlimited number of mitochondria (and/or other cellular resources).

One possibility as a major source of variation between replicate experiments could originate in the cell cultures themselves. The co-cultures produced for these studies required multiple elements to function in concert; each a potential source of variation. The primary

pericyte cultures had a degree of phenotypic variation between replicates, detailed by the immunophenotyping presented in **Figure 5.3.10**. It is possible that subtle differences in the IMT donor cell population contributed significantly to variation in the final co-cultures. Likewise, the complexity added in a co-culture system which requires cells from multiple sources likely to have introduced variation.

Alternatively, a technical aspect of the method may be a major source of variation. In **Table 15**, **Table 16 and Table 17**, it is readily apparent that different numbers of objects were successfully extracted from each set of collected HTCM images. This occurred based on reduced cell counts per surface area (particularly for treated samples), or due to differences in the number of images removed from the dataset for quality issues. It is possible that identification of more objects was required to accurately represent the cell population. This should be addressed in future experiments, or by further optimisations made in the image analysis pipeline, to improve data extraction from the existing image sets.

It is also important to consider that only cells which are relatively intact and adhered to the glass substrate will become adequately fixed prior to the RCA reactions. Because of this, cells which are mostly strongly affected by the compounds (i.e dead or dying and thus prone to detachment), are likely to be lost from the final analysis. It is possible that the *in situ* RCA approach used in this study loses some representation from these cells in the final datasets. Perhaps if these cells were included, an effect of treatment may have been more pronounced in the population frequency of IMT data.

In this study, a single concentration of CSP and CMP was used to pre-treat the eGFP-astrocyte cells, and co-cultures were established at a single time point. To improve the strength of the conclusions from this work, collection of data from a range of pre-treatment concentrations and/or time points would be desirable. If the rate of IMT is responsive to injury by these agents, it is possible that a concentration dependent effect would be observed. Additionally, the use of just two agents to induce injuries permits only a narrow window of investigation into how injury alters the rate of IMT. It is possible that specific signaling pathways must be invoked in either the donor or recipient cell, to engage in or enhance the rate of IMT. The specific mechanism of the chosen drugs action might strongly influence the outcome of experiments in this case.

When ρ^0-eGFP-astrocytes were co-cultured with primary pericytes, IMT was identified in both pyruvate/uridine supplemented, or deprived conditions. The mean intensity of IMT was however, found to decrease in pyruvate and uridine deprived conditions. A potential means to explain this data for this involves the ρ^0 cells immediate requirement to resolve

bioenergetic crisis. One may speculate that mitochondria and other cellular resources transferred from the 'donor' population are repurposed toward immediate restoration of depleted biosynthetic precursors. This would allow the cells to, at minimum, stabilise the injury state while in co-culture. If co-localisation of exogenous mitochondria with lysosomes in the starved ρ^0 cells could be established in further experimental work, this may provide support for this hypothesis.

Regardless, the long-term recovery of ρ^0-eGFP-astrocytes after co-culture with primary pericytes demonstrated in this chapter evidences that at some point in time, mitochondria (with functional mtDNA) were present inside the ρ^0 cells. At 21 days, the ρ^0 cells did not however, demonstrate normalised mitochondrial network morphology or mtDNA levels. Only low levels of detectable pericyte mtDNA were evident in the ρ^0-eGFP-astrocytes at this time. Given these observations, it was not likely that full mitochondrial function had been restored within 21 days in this extended co-culture, yet by some means, at an unknown time after initial co-culture, autonomous recycling of NADH and pyrimidine biosynthesis must have been re-established via ETC activity. This was evidenced by the persistence of recovered-ρ^0 cells, even as the residual primary cells were steadily depleted. The loss of primary cells over time is likely to correlate with diminished paracrine support availability in the form of pericyte derived metabolites. It is plausible that only a marginal level of restored mitochondrial function was required to support cell survival in the ρ^0 cells, while this exogenous support was reduced over time.

Complete mitochondrial function requires concerted activity from both the mitochondrial and nuclear genomes, to produce all the necessary protein components of the organelle, with appropriate stoichiometry for the cell's current energy and anabolic demands. To choreograph this under normal circumstances, crosstalk between mitochondrial and nuclear genomes occurs in the form of extensive retrograde and anti-retrograde signalling. Reactive oxygen species, calcium flux, $NADH/NAD^+$ ratio, ATP/AMP ratio, mitochondrial unfolded protein response activity, membrane potential [377-382] and more recently mito-peptides [33-36], have all been implicated in the modulation of signalling pathways. The ρ^0 cells have not had respiratory capacity for an extended time and thus have lacked certain elements of mitochondrial/nuclear crosstalk. In addition, the new mitochondria are pericyte-derived, a different cell type from astrocytes with potentially different crosstalk priorities. It is therefore no surprise that at 21 days, the ρ^0 cells did not display normalised mtDNA levels or network morphology. It is possible that these cells needed to undergo extensive retraining in communication between nucleus and mitochondria, in order to re-engage a transcriptional program for maintain mitochondrial function similar to the parental cell line.

Despite this challenge, the ρ^0 cells were found to have recovered mtDNA levels and partially recovered network morphology at some point in time between 21 days and 43 days after the initial co-cultures. Mitochondrial respiration was partially restored and thus, auxotrophy for pyruvate and uridine was completely ablated. The cells were shown to have reduced mitochondrial transcription, ECAR, OCR and overall growth phenotypes when compared to the parental eGFP-astrocyte line. It is unclear whether this is because the cells have been unable to completely recover, or if this represents an effect of clonality in cell culture.

An extensive selection pressure was placed on the eGFP-astrocytes treated with EtBr during generation of the ρ^0 line by RTS of the McConnell laboratory [262]. In addition, this mtDNA depletion process was likely to have introduced a degree of nuclear DNA damage as EtBr also intercalates with the nuclear genome; particularly for regions with high transcriptional activity. After maintenance for some time as a ρ^0 line, the ρ^0-eGFP-astrocytes have undergone another extensive selective bottleneck in co-culture, while deprived of pyruvate and uridine. While recovered-ρ^0-eGFP-astrocytes were isolated from 3 independent extended co-cultures, a complete characterisation of each line was not carried out. It would be informative to complete these experiments in future, to determine whether the diminished function in the line examined in detail was a consistent property for all recovered-ρ^0, or simply an effect of clonality. In addition, the time until recovery for different ρ^0 lines/repeats may also be informative to determine if a clonal effect alters the final phenotype of the recovered cells. It would be valuable to monitor the recovery of mtDNA/network morphology with higher temporal resolution, to gain further insights into how functional recovery of mitochondria occurs after IMT, and whether the time until recovery is subject to clonal effects.

7 Final Discussion

At its initiation, this project grew from potent experimental data produced in the Berridge laboratory [167, 172]. In these studies, ρ^0-B16 metastatic melanoma and ρ^0-4T1 metastatic triple negative breast carcinoma cells, were injected subcutaneously into mice; these formed tumors after a 2-3 week delay compared to the parental B16 and 4T1 lines. Cells isolated from both the primary tumor and sites of metastasis (lungs) demonstrated recovered mtDNA and mitochondrial respiration. The mtDNA sequence carried by these recovered ρ^0 cells corresponded to that of the host animal, not the parental B16 or 4T1 lines as evidenced by their specific mtDNA polymorphisms. This proved that mtDNA had been restored by IMT [167, 172]; the first reports of this phenomenon contributing to tumourigenesis *in vivo*.

Confident that IMT does occur *in vivo*, we intended to determine whether or not IMT rescued injured cells. This was explored in two ways; first was the functional outcome for individual injured cells after IMT. The second was the rate of IMT between cells under normal or injured conditions. If the purpose of the phenomenon was to aid injured cells, we hypothesised that injury may increase the frequency of IMT in the co-culture. If the level of IMT in co-culture was increased by an injury state, this would implicate IMT as an active component of cell survival.

After exploring the use of MitoTracker® dyes in various co-culture models, the discovery that in extended co-culture experiments, dye would leak out of stained cells into the mitochondria. These findings were reason enough to interpret with reservation, all published reports of IMT which had used these dyes. Conclusions based almost exclusively on data generated with these dyes must be evaluated with caution [204, 263]. Even now, MitoTracker® dyes still appear as primary evidence for IMT in the most recent publications [207, 383-385].

Instead we adopted mitochondrial targeted fluorescent protein (mito-FPs) strategies, to be certain that any IMT observed in our models would not simply be an artefact of direct MitoTracker® dye leakage. With mito-FPs, IMT was still not readily apparent. Were the cell types we were interested in not actually capable of interacting through IMT or were the culture conditions simply unsuitable? As described in the literature, MSCs appeared to readily donate mitochondria even under basal conditions [175, 176, 186, 188, 195, 196, 199-203, 205, 207, 208, 212, 213]. Perhaps an injury or stress state was required to induce IMT for certain other cell types?

After exploring a number of co-culture models, I had detected discrete extracellular vesicles loaded with mito-FPs from multiple cell lines. Accurate localisation of the vesicles was difficult with the available microscopy equipment, and certainly not at the throughput level required to generate quantitative data on IMT.

The fluorescent proteins approach was most successful in the WI-38/SH-SY5Y co-culture model. In this model, uptake of whole mitochondrial networks into SH-SY5Y was observed. However, concerns that plasmids encoded with mito-FPs were transferred directly into the unlabeled SH-SY5Y meant quantitative studies were not pursued using this model. In hindsight, it is entirely possible that these interactions were genuine examples of IMT which had occurred through partial or complete cell fusion. Cell fusion is not readily identified unless an experiment is designed specifically to look for this phenomenon and at the time, was not an anticipated mechanism for IMT.

Nevertheless, concerns, confusion and complications brought about through the limitations of existing techniques highlighted an opportunity to improve the quality, interpretability and robustness of methodologies used in the IMT field. This would improve not only the research quality produced in our own lab, but would advance the field as a whole.

To address this, I set out to develop and implement a radically new approach to study IMT. Rather than attempt to observe movement of whole mitochondrial organelles, I pursued mtDNA itself as a targetable sub-component to act as a proxy for transfer events. Prior to the work in this thesis, the presence of transferred mtDNA had been verified by PCR and Sanger sequencing to confirm IMT in [167, 172, 176, 195, 200, 203, 208, 228, 386]. Unfortunately, provision of data on transferred mtDNA is not standard in the field for two reasons: an inability to physically separate IMT 'donor' from 'recipient' with absolute precision prevents isolation of DNA from the target population alone; and the presence of a pre-existing endogenous complement of mtDNA in the recipient population of normal cells. This is why molecular confirmation has been limited to ρ^0 models which lack an endogenous mtDNA complement, or human/mouse xenograft or xeno-co-culture models where mtDNA can be successfully amplified via species specific sequence differences. Just two recent studies have used molecular confirmation of IMT by a deep-sequencing approach [384, 387]. These investigators should be commended for the methodological progress these studies represent for the field. In our own hands, cell separation of neural cell types was not adequate for direct analysis of 'recipient' DNA. For these reasons, the ability to carry out molecular analysis of mtDNA, without cell separation would be both advantageous and unique as an approach to study IMT. After scouring the literature for *in situ* techniques for the analysis of nucleic acids, padlock probes (PDPs) were discovered. These probes are used mainly to detect target nucleic acids in a diagnostic

capacity, or to demonstrate and quantify the abundance and location of specific RNA/DNA species of interest [284, 288-290, 388-394]. Recent developments in PDP technologies have focused on use of these probes for multi-plexed protein detection and spatially resolved transcriptomics *in situ* [395-401].

Because PDP reactions are enzyme assisted, the reaction fidelity is superior to direct target hybridisation techniques. The exquisite selectivity of the Taq HIFI Ligase™ used to circularize PDPs in this investigation enabled not only the detection of the target mtDNA, but discrimination between molecules by sequence. The use of this particular ligase was novel in its own right, as it has yet to be reported when used in combination with PDPs. The data presented in this thesis has demonstrated that Taq HIFI Ligase™ functioned equally to, or better than Ampligase™ for ligation of a PDP across the mtDNA_9461G locus. Further work should be carried out in future to establish if this is consistent across other ligation junction types, as Taq HIFI Ligase™ should also perform better than Ampligase™ against these, based on the work of Lohman et al. [286]. If this were to be the case, other researchers may also find Taq HIFI Ligase™ useful for high fidelity ligation of PDPs.

To my knowledge, no other report on IMT has provided spatial localisation data which demonstrates exogenous mtDNA within an IMT 'recipient' cell, as presented in this thesis. Likewise, this represents the first known use of PDPs as a tool to explore unknown biology, as opposed to a routine detection/sequencing application. While single molecule genotyping *in situ* was incredibly powerful, the limitations of the method must be acknowledged when applying the approach to study IMT.

1. Single nucleotide variants must be present between the mtDNAs of cell lines in co-culture, or between tissue types for *in vivo* models. This is relatively straightforward to address during the experimental design.

2. Reaction selectivity must be considered; in this study the rate of mis-ligation for PDPs targeted to the mtDNA_9461G was determined experimentally. This allowed false positive ligation events to be accounted for in the analysis of the downstream quantitative experiments. Researchers who wish to use this approach to study IMT should similarly determine the specific rate of false positives.

3. Reaction efficiency of target-primed RCA. In these studies, more mtDNA nucleoids were detected by SYBR Green I stain than were detected by mtDNA_9461G targeted RCA. This was expected, given not all mtDNA molecules will be accessed successfully *in situ* by the enzymes and oligonucleotides required to prepare and amplify the mtDNA template. This approach relies on the assumption

that the likelihood of reaction failure is equal for any given mtDNA molecule. Under this assumption, the ratio of true positive to false positive RCPs generated is constant, thus detected molecules are a representative sample of the total mtDNA population, provided enough images are collected. The approach under-reports the true count of transferred mtDNAs, which limits analysis to comparisons of event frequencies. This type of analysis was suitable to investigate the hypotheses of this thesis, however may not be suitable for other biological questions related to IMT.

The image analysis strategy is as equally important as any of molecular and cell biology. For this thesis, I established a pipeline to extract rudimentary data from these experiments, while minimising the influence of artefacts. The datasets collected in these studies contain more potentially valuable information about IMT in the explored contexts, and could be reanalysed in future when an improved pipeline is available.

Single molecule genotyping *in situ* was an extremely effective means of identifying IMT in new biological contexts. After RCA targeted to mtDNA_9461G and 9348G was optimised, I was able to effectively 'screen' for new instances of IMT in many new cell lines. Flexibility in the molecular design of the RCA reaction itself allowed an array of potential IMT 'donor/recipient' pairs to be tested rapidly for transfer of mtDNA between cells. This embodied part of the design philosophy, that the strategy would be widely applicable to different mouse models. This is because the inbred common laboratory mouse strains and cell lines will carry similar SNVs to be leveraged by these designs, regardless of laboratory. By shifting the focus of my project to mouse *in vitro* models as opposed to co-cultures of human cells (which will require custom PDP designs for unique sequences), the techniques designed in this thesis can now be used by other investigators with little to no required customisation or optimisation.

MSCs represent the IMT 'donor' cell type in the overwhelming majority of studies, however other cell types have been reported as capable of IMT. Among these are fibroblastic, glial, neuronal, myeloid, endothelial, epithelial, and even breast or lung cancer cells [175, 185, 198, 211, 384, 385, 387, 402-412]. This suggests that cell types other than MSCs do have access to the cellular machinery required to engage in IMT. Whether this occurs *in vivo* in primary cells of the same types, or only because the cell lines are immortalized, is yet to be determined. While some of the molecular components involved in IMT are beginning to be identified, the field as a whole is yet to elucidate what makes an effective IMT 'donor'. To identify new donor cell types for IMT, I first followed a semi-targeted approach. The murine cell lines placed into 'multi-cultures' met one or more of the following criteria: were available in the McConnell/Berridge labs; had mitochondrial SNVs which were targetable; were neural in origin; have known 'stem-like' properties; or were of

a cell type with a precedent for IMT in previously published reports. As a first approach to identifying a suitable combination for the injury studies, identification of IMT in specific cell combinations was never intended. Instead, the *in situ* RCA identified co-culture pairs where IMT was prevalent, and thus the model best suited for downstream study.

In parallel with identification of IMT interactions by the 'multi-culture' approach, this thesis also explored primary murine pericytes as a capable mitochondrial 'donor' cell type. In contrast to the semi-targeted approach, IMT 'donor' activity by these cells was identified *in vitro* through highly targeted, hypothesis driven experiments. I hypothesised that pericytes may as potential 'MSC-like' cells in IMT based on phenotypic markers and their presence within the brain micro-environment [302, 306-314, 321]. Fortuitously, a paper was published at the time these experiments were under consideration by Dieriks et al. which demonstrated transfer of mutant A53T-α-synuclein between both SH-SY5Y cells and primary human pericytes from Parkinson's disease patients *in vitro* [331]. It was possible that A53T-α-synuclein aggregates were transferred in the studies of Dieriks et al. in association with mitochondria. If this were true, a shared cellular machinery could be/was implicated for the processes of both IMT and the spread of α-synuclein between cells. If pericytes were capable of transferring A53T-α-synuclein aggregates, it was important that I assessed their ability to act as an IMT 'donor' *in vitro.* And indeed, after co-culture with eGFP-astrocytes, the capacity for pericytes to act as an IMT 'donor' cell was demonstrated experimentally in **Figure 5.3.11**.

It has long been recognised that multiple neuropathologies present with a characteristic spreading degeneration, mediated in part by toxic protein aggregates [413-421]. Transcellular movement of these proteins *in vitro*, or the spreading between interconnected brain regions *in vivo* is mediated by contact dependent mechanisms (which include TNTs), or contact independent mechanisms (including exosomes), (summarised by Chung et al [422]). Protein aggregates such as amyloid-β, amyloid precursor protein, α-synuclein, tau and mutant huntingtin protein all cause mitochondrial dysfunction as a component of the disease phenotype [422, 423]. Each protein species interacts directly with the mitochondria through distinct mechanisms to induce mitochondrial dysfunction, yet all lead to inevitable cell death by opening of the mitochondrial permeability transition pore [424]. It is possible that mitochondria laden with damaged or misfolded proteins are exported from cells via IMT, and these could well be detected alongside the spread of toxic proteins in neurodegenerative pathologies. Indeed such an activity was reported by Davis et al. who demonstrated that retinal ganglion cells transferred axonal mitochondria into the astrocytes of the optic nerve head to be recycled; a process dubbed transmitophagy [211].

The idea that the spread of toxic proteins could potentially be mediated by IMT, highlights a conflicted notion of what IMT may actually represent for cellular survival. Intercellular mitochondrial transfer is a phrase which describes the movement of mitochondrial organelles between cells, yet published reports rarely acknowledge that this in all likelihood, occurs concomitantly with numerous other biomolecules. We noticed a disturbing trend in the literature, where for injured cells placed into co-culture, reversal of the injury phenotype is immediately attributed to IMT. When healthy cells are introduced to an injured population as in a co-culture model, a completely new paracrine environment is established. It is possible that free, contact-mediated or vesicle-mediated secreted factors which include proteins, metabolites and micro or messenger RNAs are made available to injured cells and influence the injury phenotype [227, 425-430]. For these reasons, the rescue effect in itself comes as no surprise at all. What is of concern, is how little focus is placed on these numerous other potential mechanisms.

The complexity of attributing any observed cellular recovery directly to the transfer of mitochondria alone, outside of ρ^0 cell models, is a challenge for the field. Attenuation of the enhanced recovery effect seen in co-culture, correlated with IMT, has been demonstrated in various reports. Notable examples of these are siRNA knockdown of the Rieske iron-sulfur protein of complex III in the respiratory chain [186, 431], inhibition of complex I by rotenone [217], or depletion of mtDNA with EtBr [386], to induce mitochondrial dysfunction in MSC 'donor' cells prior to co-culture with injured cells. These types of experiment are the closest evidence we have in support of the hypothesis that cellular recovery from injury may be mediated by mitochondria received through IMT. Unfortunately, these experiments require an injury to the 'donor' cell population in the form of mitochondrial dysfunction. It is possible that damage induced in the 'donor' cell may compromise the recovery effect of co-culture for 'recipient' cells, rather than loss of functionality from the donated mitochondria.

For this reason, I chose not to pursue monitoring recovery from injury in co-cultures with mitochondrial replete eGFP-astrocytes. Instead, the quantitative studies presented in this thesis sought only to understand if injury altered the <u>rate</u> of IMT; a conservative, attributable and now measurable outcome, enabled by *in situ* RCA.

7.1 Future directions

The major contribution of this thesis is a new approach to study IMT, fundamentally different from all prior methods used in the field. The research presented here demonstrates the functionality of this approach, exclusively in novel models of IMT *in vitro*. It is essential that this research be applied to an established model of IMT. Reconstructing the model in our own lab, or applying the strategy to samples produced by others with published reports of IMT would demonstrate functionality of the approach, and simultaneously improve our understanding of IMT in those previously known contexts.

The source of variability seen in the population level frequency of IMT in primary pericyte/eGFP-astrocyte co-cultures remains to be identified. To improve the quality of these experiments, it would be valuable to determine whether a biological (e.g. consistency of pericyte phenotype) or technical (e.g. sample preparation or image analysis pipeline) aspect of the approach contributed to this variability. If the most influential variable(s) could be identified, the strength of the conclusions regarding if injury alters the rate of IMT in these models would be vastly improved. Replicate experiments would be informative to discovery of the major source(s) of variability.

During development of the *in situ* RCA approach to study IMT, the false-positive detection rate of mtDNA_9461G RCPs was determined in a cell line which does not carry this target SNV within its endogenous mtDNA. The false-positive detection rate for mtDNA_9348G could not be determined in this thesis, for reasons described in chapter 4. It would be valuable to determine this rate, and for additional probes targeted to mtDNA_9461C and 9348C (the alternative SNV target at each site), to validate the flexibility of this approach for models with differing mitochondrial genetics. Probes targeted to mtDNA_9461C and 9348C were designed and used since the initial development of this approach and are functional, however the reaction fidelity/efficiency remain to be addressed.

All examples of *in situ* RCA presented in this were applied to *in vitro* co-cultures. A powerful utility of the *in situ* RCA approach to study IMT is the ability to study mtDNAs which may be transferred between cells, *in vivo*. Studies of IMT *in vivo* have been limited by a lack of appropriate tools or methods at this point in time, outside of ρ^0 models. The approach developed in this thesis could be adapted to the research models of any group interested in detecting IMT *in vivo*, and thus act as a powerful enabler for these researchers. Here, primary pericytes were identified as capable IMT donor cells *in vitro*. By implanting pericytes intracranially [432, 433], a model with mtDNA SNV differences between host and pericyte could be established. This would be valuable confirm whether or not pericytes can engage in IMT *in vivo*, enabled by the *in situ* RCA approach. If found to act as IMT

donors, it would be possible to identify the cell types the pericyte may interact with through IMT *in vivo*, by combining immunofluorescence markers for various cell types in the brain micro-environment.

Unfortunately for patients, cancerous cells survive therapy. Disease recurs from residual cancer cells which have survived surgical resection, radiation and chemotherapy. How or why cells are able to do this is multifaceted and complex. It is likely that a symphony of interactions between multiple cell-survival mechanisms enables this devastating outcome. One of these mechanisms is indefinite cell cycle arrest; cells enter a state of senescence in response to damage which is otherwise lethal. An emergent area of cancer research focuses on the transition of cancer cells into therapy induced senescence, and the occasional return of a cell to a proliferative state [434-440]. Cells described by this mechanism could conceivably be involved in disease recurrence after therapy. Therapy induced injury often includes compromised mitochondrial function. The compounds CMP and CSP used in chapter 6 of this thesis have been reported to induce senescence or a senescence-like phenotype in various cell types [352, 353, 441-445]. Is damage to mitochondrial function or mtDNA as a component of therapy involved in the development of a senescence phenotype? Do cells recover from this phenotype, partially by recovery of mitochondrial function? Could IMT be linked to a return to the proliferative state for these cells?

These questions are challenging to address, but we do have a tool that is potentially useful for these investigations. The ρ^0 cell is not like any other in mammalian biology, where cells that completely lack mtDNA do not exist naturally outside of erythrocytes. Recovery of ρ^0 cells after IMT is therefore highly unlikely to accurately model a real physiological event. It is possible however, that ρ^0 cells could recapitulate molecular programs upon reacquisition of mtDNA, similar to those required in a therapy induced senescent cell's return to a proliferative state. Recovery of mitochondrial function in the ρ^0 cell may share fundamental biology with the recovery of senescent cells severely damaged by therapy. One could begin to explore these big picture ideas by looking at IMT into injured cells, whilst simultaneous monitoring known senescence biomarkers. If these ideas were biological truths, I hypothesise that cells in therapy-induced senescence would return to proliferative states at an enhanced rate, after co-culture and receipt of functional mitochondria, from cells that act as IMT donors. Given the severity of the consequence for patients when disease recurs from highly resistant sub-populations of cells, this is a valuable line of enquiry for future research.

References

1. Brocks, J.J., et al., *Archean Molecular Fossils and the Early Rise of Eukaryotes.* Science, 1999. **285**(5430): p. 1033.

2. Wang, M., et al., *A universal molecular clock of protein folds and its power in tracing the early history of aerobic metabolism and planet oxygenation.* Molecular Biology and Evolution, 2011. **28**(1): p. 567.

3. Soo, R.M., et al., *On the origins of oxygenic photosynthesis and aerobic respiration in Cyanobacteria.* Science, 2017. **355**(6332): p. 1436.

4. Lyons, T.W., C.T. Reinhard, and N.J. Planavsky, *The rise of oxygen in Earth's early ocean and atmosphere.* Nature, 2014. **506**: p. 307.

5. Bekker, A., et al., *Dating the rise of atmospheric oxygen.* Nature, 2004. **427**(6970): p. 117.

6. Scott, C., et al., *Tracing the stepwise oxygenation of the Proterozoic ocean.* Nature, 2008. **452**(7186): p. 456.

7. Canfield, D.E., S.W. Poulton, and G.M. Narbonne, *Late-Neoproterozoic Deep-Ocean Oxygenation and the Rise of Animal Life.* Science, 2007. **315**(5808): p. 92.

8. Fike, D.A., et al., *Oxidation of the Ediacaran Ocean.* Nature, 2006. **444**(7120): p. 744.

9. Schäfer, G., M. Engelhard, and V. Müller, *Bioenergetics of the Archaea.* Microbiology and Molecular Biology Reviews, 1999. **63**(3): p. 570.

10. Huber, G., et al., *Growth by Aerobic Oxidation of Molecular Hydrogen in Archaea —a Metabolic Property so far Unknown for this Domain.* Systematic and Applied Microbiology, 1992. **15**(4): p. 502.

11. Sagan, L., *On the origin of mitosing cells.* Journal of Theoretical Biology, 1967. **14**(3): p. 255.

12. Martin, W.F., S. Garg, and V. Zimorski, *Endosymbiotic theories for eukaryote origin.* Philosophical Transactions of the Royal Society London Series B Biological Sciences, 2015. **370**(1678): p. 20140330.

13. Bogenhagen, D.F., *Mitochondrial DNA nucleoid structure.* Biochimica et Biophysica Acta, 2012. **1819**(9-10): p. 914.

14. Robin, E.D. and R. Wong, *Mitochondrial DNA molecules and virtual number of mitochondria per cell in mammalian cells.* Journal of Cellular Physiology, 1988. **136**(3): p. 507.

15. Kukat, C., et al., *Super-resolution microscopy reveals that mammalian mitochondrial nucleoids have a uniform size and frequently contain a single copy of mtDNA.* Proceedings of the National Academy of Sciences of the United States of America, 2011. **108**(33): p. 13534.

16. Veltri, K.L., M. Espiritu, and G. Singh, *Distinct genomic copy number in mitochondria of different mammalian organs.* Journal of Cellular Physiology, 1990. **143**(1): p. 160.

17. Youle, R.J. and A.M. van der Bliek, *Mitochondrial fission, fusion, and stress.* Science, 2012. **337**(6098): p. 1062.

18. Wai, T. and T. Langer, *Mitochondrial Dynamics and Metabolic Regulation.* Trends in Endocrinology and Metabolism, 2016. **27**(2): p. 105.

19. Cole, L.W., *The Evolution of Per-cell Organelle Number.* Frontiers in Cell and Developmental Biology, 2016. **4**(85).

20. Posakony, J.W., J.M. England, and G. Attardi, *Mitochondrial growth and division during the cell cycle in HeLa cells.* The Journal of Cell Biology, 1977. **74**(2): p. 468.

21. Martínez-Diez, M., et al., *Biogenesis and dynamics of mitochondria during the cell cycle: significance of 3′ UTRs.* PLoS ONE, 2006. **1**(1): p. e107.

22. Palade, G.E., *The fine structure of mitochondria.* The Anatomical Record, 1952. **114**(3): p. 427.

23. Frey, T.G. and C.A. Mannella, *The internal structure of mitochondria.* Trends in Biochemical Sciences, 2000. **25**(7): p. 319.

24. Jourdain, A.A., et al., *GRSF1 regulates RNA processing in mitochondrial RNA granules.* Cell Metabolism, 2013. **17**(3): p. 399.

25. Antonicka, H., et al., *The mitochondrial RNA-binding protein GRSF1 localizes to RNA granules and is required for posttranscriptional mitochondrial gene expression.* Cell Metabolism, 2013. **17**(3): p. 386.

26. Kühlbrandt, W., *Structure and function of mitochondrial membrane protein complexes.* BMC Biology, 2015. **13**(1): p. 89.

27. Ahn, C.S. and C.M. Metallo, *Mitochondria as biosynthetic factories for cancer proliferation.* Cancer Metabolism, 2015. **3**(1): p. 1.

28. Lee, S.-Y., et al., *Architecture Mapping of the Inner Mitochondrial Membrane Proteome by Chemical Tools in Live Cells.* Journal of the American Chemical Society, 2017. **139**(10): p. 3651.

29. Llopis, J., et al., *Measurement of cytosolic, mitochondrial, and Golgi pH in single living cells with green fluorescent proteins.* Proceedings of the National Academy of Sciences of the United States of America, 1998. **95**(12): p. 6803.

30. Davies, K.M., et al., *Macromolecular organization of ATP synthase and complex I in whole mitochondria.* Proceedings of the National Academy of Sciences of the United States of America, 2011. **108**(34): p. 14121.

31. Berk, A.J. and D.A. Clayton, *Mechanism of mitochondrial DNA replication in mouse L-cells: asynchronous replication of strands, segregation of circular daughter molecules, aspects of topology and turnover of an initiation sequence.* Journal of Molecular Biology, 1974. **86**(4): p. 801.

32. Gustafsson, C.M., M. Falkenberg, and N.G. Larsson, *Maintenance and Expression of Mammalian Mitochondrial DNA.* Annual Review of Biochemistry, 2016. **85**: p. 133.

33. Lee, C., et al., *The mitochondrial-derived peptide MOTS-c promotes metabolic homeostasis and reduces obesity and insulin resistance.* Cell Metabolism, 2015. **21**(3): p. 443.

34. Hashimoto, Y., et al., *A rescue factor abolishing neuronal cell death by a wide spectrum of familial Alzheimer's disease genes and Abeta.* Proceedings of the National Academy of Sciences of the United States of America, 2001. **98**(11): p. 6336.

35. Kim, S.J., et al., *Mitochondrially derived peptides as novel regulators of metabolism.* Journal of Physiology, 2017. **595**(21): p. 6613.

36. Cobb, L.J., et al., *Naturally occurring mitochondrial-derived peptides are age-dependent regulators of apoptosis, insulin sensitivity, and inflammatory markers.* Aging (Albany NY), 2016. **8**(4): p. 796.

37. Calvo, S.E., K.R. Clauser, and V.K. Mootha, *MitoCarta2.0: an updated inventory of mammalian mitochondrial proteins.* Nucleic Acids Research, 2016. **44**(D1): p. D1251.

38. Burr, S.P., M. Pezet, and P.F. Chinnery, *Mitochondrial DNA Heteroplasmy and Purifying Selection in the Mammalian Female Germ Line.* Development, Growth & Differentiation, 2018. **60**(1): p. 21.

39. Dayama, G., et al., *The genomic landscape of polymorphic human nuclear mitochondrial insertions.* Nucleic Acids Research, 2014. **42**(20): p. 12640.

40. Singh, K.K., A.R. Choudhury, and H.K. Tiwari, *Numtogenesis as a mechanism for development of cancer.* Seminars in Cancer Biology, 2017. **47**: p. 101.

41. Calabrese, F.M., D. Simone, and M. Attimonelli, *Primates and mouse NumtS in the UCSC Genome Browser.* BMC Bioinformatics, 2012. **13 Suppl 4**: p. S15.

42. Kukat, C., et al., *Cross-strand binding of TFAM to a single mtDNA molecule forms the mitochondrial nucleoid.* Proceedings of the National Academy of Sciences of the United States of America, 2015. **112**(36): p. 11288.

43. Sasaki, T., et al., *Live imaging reveals the dynamics and regulation of mitochondrial nucleoids during the cell cycle in Fucci2-HeLa cells.* Scientific Reports, 2017. **7**(1): p. 11257.

44. Brown, T.A., et al., *Superresolution fluorescence imaging of mitochondrial nucleoids reveals their spatial range, limits, and membrane interaction.* Molecular and Cellular Biology, 2011. **31**(24): p. 4994.

45. Hayashi, J., et al., *Introduction of disease-related mitochondrial DNA deletions into HeLa cells lacking mitochondrial DNA results in mitochondrial dysfunction.* Proceedings of the National Academy of Sciences of the United States of America, 1991. **88**(23): p. 10614.

46. Larsson, N.G. and D.A. Clayton, *Molecular genetic aspects of human mitochondrial disorders.* Annual Review of Genetics, 1995. **29**: p. 151.

47. Gorman, G.S., et al., *Mitochondrial diseases.* Nature reviews Disease primers, 2016. **2**: p. 16080.

48. Stewart, J.B., et al., *Strong purifying selection in transmission of mammalian mitochondrial DNA.* PLoS Biology, 2008. **6**(1): p. e10.

49. Amorim, A., T. Fernandes, and N. Taveira, *Mitochondrial DNA in human identification: a review.* PeerJ, 2019. **7**: p. e7314.

50. Mitchell, S.L., et al., *Characterization of mitochondrial haplogroups in a large population-based sample from the United States.* Human Genetics, 2014. **133**(7): p. 861.

51. Shutt, T.E. and M.W. Gray, *Bacteriophage origins of mitochondrial replication and transcription proteins.* Trends in Genetics, 2006. **22**(2): p. 90.

52. Magnusson, J., et al., *Replication of mitochondrial DNA occurs throughout the mitochondria of cultured human cells.* Experimental Cell Research, 2003. **289**(1): p. 133.

53. Fan, L., et al., *A novel processive mechanism for DNA synthesis revealed by structure, modeling and mutagenesis of the accessory subunit of human mitochondrial DNA polymerase.* Journal of Molecular Biology, 2006. **358**(5): p. 1229.

54. Yakubovskaya, E., et al., *Functional human mitochondrial DNA polymerase gamma forms a heterotrimer.* Journal of Biological Chemistry, 2006. **281**(1): p. 374.

55. Gray, H. and T.W. Wong, *Purification and identification of subunit structure of the human mitochondrial DNA polymerase.* Journal of Biological Chemistry, 1992. **267**(9): p. 5835.

56. Garcia-Gomez, S., et al., *PrimPol, an archaic primase/polymerase operating in human cells.* Molecular and Cellular Biology, 2013. **52**(4): p. 541.

57. Sykora, P., et al., *DNA Polymerase Beta Participates in Mitochondrial DNA Repair.* Molecular and Cellular Biology, 2017. **37**(16).

58. Wisnovsky, S., S.R. Jean, and S.O. Kelley, *Mitochondrial DNA repair and replication proteins revealed by targeted chemical probes.* Nature Chemical Biology, 2016. **12**(7): p. 567.

59. Singh, B., et al., *Human REV3 DNA Polymerase Zeta Localizes to Mitochondria and Protects the Mitochondrial Genome.* PLoS ONE, 2015. **10**(10): p. e0140409.

60. Longley, M.J., et al., *The fidelity of human DNA polymerase gamma with and without exonucleolytic proofreading and the p55 accessory subunit.* Journal of Biological Chemistry, 2001. **276**(42): p. 38555.

61. Robberson, D.L., H. Kasamatsu, and J. Vinograd, *Replication of mitochondrial DNA. Circular replicative intermediates in mouse L cells.* Proceedings of the National Academy of Sciences of the United States of America, 1972. **69**(3): p. 737.

62. Spelbrink, J.N., et al., *Human mitochondrial DNA deletions associated with mutations in the gene encoding Twinkle, a phage T7 gene 4-like protein localized in mitochondria.* Nature Genetics, 2001. **28**(3): p. 223.

63. Korhonen, J.A., M. Gaspari, and M. Falkenberg, *TWINKLE Has 5' -> 3' DNA helicase activity and is specifically stimulated by mitochondrial single-stranded DNA-binding protein.* Journal of Biological Chemistry, 2003. **278**(49): p. 48627.

64. Korhonen, J.A., et al., *Structure-function defects of the TWINKLE linker region in progressive external ophthalmoplegia.* Journal of Molecular Biology, 2008. **377**(3): p. 691.

65. Mignotte, B., M. Barat, and J.C. Mounolou, *Characterization of a mitochondrial protein binding to single-stranded DNA.* Nucleic Acids Reserach, 1985. **13**(5): p. 1703.

66. Tiranti, V., et al., *Cloning of human and rat cDNAs encoding the mitochondrial single-stranded DNA-binding protein (SSB).* Gene, 1993. **126**(2): p. 219.

67. Wanrooij, S., et al., *Human mitochondrial RNA polymerase primes lagging-strand DNA synthesis in vitro.* Proceedings of the National Academy of Sciences of the United States of America, 2008. **105**(32): p. 11122.

68. Falkenberg, M., *Mitochondrial DNA replication in mammalian cells: overview of the pathway.* Essays in Biochemistry, 2018. **62**(3): p. 287.

69. Shokolenko, I.N. and M.F. Alexeyev, *Mitochondrial transcription in mammalian cells.* Frontiers in Bioscience (Landmark edition), 2017. **22**: p. 835.

70. Shutt, T.E., M. Bestwick, and G.S. Shadel, *The core human mitochondrial transcription initiation complex: It only takes two to tango.* Transcription, 2011. **2**(2): p. 55.

71. Wang, J., et al., *Dilated cardiomyopathy and atrioventricular conduction blocks induced by heart-specific inactivation of mitochondrial DNA gene expression.* Nature Genetics, 1999. **21**(1): p. 133.

72. Larsson, N.G., et al., *Mitochondrial transcription factor A is necessary for mtDNA maintenance and embryogenesis in mice.* Nature Genetics, 1998. **18**(3): p. 231.

73. Litonin, D., et al., *Human mitochondrial transcription revisited: only TFAM and TFB2M are required for transcription of the mitochondrial genes in vitro.* Journal of Biological Chemistry, 2010. **285**(24): p. 18129.

74. Ojala, D., J. Montoya, and G. Attardi, *tRNA punctuation model of RNA processing in human mitochondria.* Nature, 1981. **290**(5806): p. 470.

75. Gelfand, R. and G. Attardi, *Synthesis and turnover of mitochondrial ribonucleic acid in HeLa cells: the mature ribosomal and messenger ribonucleic acid species are metabolically unstable.* Molecular and Cellular Biology, 1981. **1**(6): p. 497.

76. Martin, M., et al., *Termination factor-mediated DNA loop between termination and initiation sites drives mitochondrial rRNA synthesis.* Cell, 2005. **123**(7): p. 1227.

77. Agaronyan, K., et al., *Mitochondrial biology. Replication-transcription switch in human mitochondria.* Science, 2015. **347**(6221): p. 548.

78. Posse, V., et al., *TEFM is a potent stimulator of mitochondrial transcription elongation in vitro.* Nucleic Acids Research, 2015. **43**(5): p. 2615.

79. Antonicka, H. and Eric A. Shoubridge, *Mitochondrial RNA Granules Are Centers for Posttranscriptional RNA Processing and Ribosome Biogenesis.* Cell Reports, 2015. **10**(6): p. 920.

80. Van Haute, L., et al., *Mitochondrial transcript maturation and its disorders.* Journal of Inherited Metabolic Disorders, 2015. **38**(4): p. 655.

81. Amunts, A., et al., *Ribosome. The structure of the human mitochondrial ribosome.* Science, 2015. **348**(6230): p. 95.

82. Kaushal, P.S., et al., *Cryo-EM structure of the small subunit of the mammalian mitochondrial ribosome.* Proceedings of the National Academy of Sciences of the United States of America, 2014. **111**(20): p. 7284.

83. Greber, B.J., et al., *Ribosome. The complete structure of the 55S mammalian mitochondrial ribosome.* Science, 2015. **348**(6232): p. 303.

84. Brown, A., et al., *Structure of the large ribosomal subunit from human mitochondria.* Science, 2014. **346**(6210): p. 718.

85. Suzuki, T. and T. Suzuki, *A complete landscape of post-transcriptional modifications in mammalian mitochondrial tRNAs.* Nucleic Acids Research, 2014. **42**(11): p. 7346.

86. Mai, N., Z.M.A. Chrzanowska-Lightowlers, and R.N. Lightowlers, *The process of mammalian mitochondrial protein synthesis.* Cell and Tissue Research, 2017. **367**(1): p. 5.

87. Lin, J., et al., *Ribosome-Targeting Antibiotics: Modes of Action, Mechanisms of Resistance, and Implications for Drug Design.* Annual Review of Biochemistry, 2018. **87**: p. 451.

88. Signes, A. and E. Fernandez-Vizarra, *Assembly of mammalian oxidative phosphorylation complexes I-V and supercomplexes.* Essays in Biochemistry, 2018. **62**(3): p. 255.

89. Moreno-Lastres, D., et al., *Mitochondrial complex I plays an essential role in human respirasome assembly.* Cell Metabolism, 2012. **15**(3): p. 324.

90. Milenkovic, D., et al., *The Enigma of the Respiratory Chain Supercomplex.* Cell Metabolism, 2017. **25**(4): p. 765.

91. Cogliati, S., et al., *Mitochondrial Cristae Shape Determines Respiratory Chain Supercomplexes Assembly and Respiratory Efficiency.* Cell, 2013. **155**(1): p. 160.

92. Meyerhof, O. and P. Oesper, *The mechanism of the oxidative reaction in fermentation.* Journal of Biological Chemistry, 1947. **170**(1): p. 1.

93. Meyerhof, O., *The origin of the reaction of Harden and Young in cell-free alcoholic fermentation.* Journal of Biological Chemistry, 1945. **157**(1): p. 105.

94. Meyerhof, O. and R. Junowicz-Kocholaty, *The equilibria of isomerase and aldolase, and the problem of the phosphorylation of glyceraldehyde phosphate.* Journal of Biological Chemistry, 1943. **149**(1): p. 71.

95. Bonora, M., et al., *ATP synthesis and storage.* Purinergic signalling, 2012. **8**(3): p. 343.

96. Mailloux, R.J., *Teaching the fundamentals of electron transfer reactions in mitochondria and the production and detection of reactive oxygen species.* Redox Biology, 2015. **4**: p. 381.

97. Owen, O.E., S.C. Kalhan, and R.W. Hanson, *The Key Role of Anaplerosis and Cataplerosis for Citric Acid Cycle Function.* Journal of Biological Chemistry, 2002. **277**(34): p. 30409.

98. Baradaran, R., et al., *Crystal structure of the entire respiratory complex I.* Nature, 2013. **494**: p. 443.

99. Cecchini, G., *Function and Structure of Complex II of the Respiratory Chain.* Annual Review of Biochemistry, 2003. **72**(1): p. 77.

100. Crofts, A.R., et al., *The Q-cycle reviewed: How well does a monomeric mechanism of the bc(1) complex account for the function of a dimeric complex?* Biochimica et Biophysica Acta, 2008. **1777**(7-8): p. 1001.

101. Chen, Q., et al., *Production of reactive oxygen species by mitochondria - Central role of complex III.* Journal of Biological Chemistry, 2003. **278**(38): p. 36027.

102. Turrens, J.F., A. Alexandre, and A.L. Lehninger, *Ubisemiquinone is the electron-donor for superoxide formation by complex III of heart-mitochondria.* Archives of Biochemistry and Biophysics, 1985. **237**(2): p. 408.

103. Tsukihara, T., et al., *The whole structure of the 13-subunit oxidized cytochrome c oxidase at 2.8 A.* Science, 1996. **272**(5265): p. 1136.

104. Junge, W. and N. Nelson, *ATP Synthase.* Annual Review of Biochemistry, 2015. **84**(1): p. 631-657.

105. Jonckheere, A.I., J.A. Smeitink, and R.J. Rodenburg, *Mitochondrial ATP synthase: architecture, function and pathology.* Journal of Inherited Metabolic Disorders, 2012. **35**(2): p. 211.

106. Duncan, T.M., et al., *Rotation of subunits during catalysis by Escherichia coli F1-ATPase.* Proceedings of the National Academy of Sciences of the United States of America, 1995. **92**(24): p. 10964.

107. Mookerjee, S.A., et al., *Quantifying intracellular rates of glycolytic and oxidative ATP production and consumption using extracellular flux measurements.* Journal of Biological Chemistry, 2017. **292**(17): p. 7189.

108. Hill, B.G., et al., *Integration of cellular bioenergetics with mitochondrial quality control and autophagy.* Biological Chemistry, 2012. **393**(12): p. 1485.

109. Brand, M.D. and D.G. Nicholls, *Assessing mitochondrial dysfunction in cells.* The Biochemical journal, 2011. **435**(2): p. 297.

110. Dranka, B.P., et al., *Assessing bioenergetic function in response to oxidative stress by metabolic profiling.* Free Radical Biology and Medicine, 2011. **51**(9): p. 1621.

111. Wu, M., et al., *Multiparameter metabolic analysis reveals a close link between attenuated mitochondrial bioenergetic function and enhanced glycolysis dependency in human tumor cells.* American Journal of Physiology and Cell Physiology, 2007. **292**(1): p. C125.

112. Mookerjee, S.A., D.G. Nicholls, and M.D. Brand, *Determining Maximum Glycolytic Capacity Using Extracellular Flux Measurements.* PLoS ONE, 2016. **11**(3): p. e0152016.

113. King, M. and G. Attardi, *Human cells lacking mtDNA: repopulation with exogenous mitochondria by complementation.* Science, 1989. **246**(4929): p. 500.

114. Leibowitz, R.D., *The effect of ethidium bromide on mitochondrial DNA synthesis and mitochondrial DNA structure in HeLa cells.* The Journal of Cell Biology, 1971. **51**(1): p. 116.

115. Kai, Y., et al., *Rapid and random turnover of mitochondrial DNA in rat hepatocytes of primary culture.* Mitochondrion, 2006. **6**(6): p. 299.

116. Kao, L.P., D. Ovchinnikov, and E. Wolvetang, *The effect of ethidium bromide and chloramphenicol on mitochondrial biogenesis in primary human fibroblasts.* Toxicology and Applied Pharmacology, 2012. **261**(1): p. 42.

117. Yu, M., et al., *Depletion of mitochondrial DNA by ethidium bromide treatment inhibits the proliferation and tumorigenesis of T47D human breast cancer cells.* Toxicology Letters, 2007. **170**(1): p. 83.

118. Spadafora, D., et al., *Methods for Efficient Elimination of Mitochondrial DNA from Cultured Cells.* PLoS ONE, 2016. **11**(5): p. e0154684.

119. Shokolenko, I.N., G.L. Wilson, and M.F. Alexeyev, *Persistent damage induces mitochondrial DNA degradation.* DNA repair, 2013. **12**(7): p. 488.

120. Kukat, A., et al., *Generation of rho0 cells utilizing a mitochondrially targeted restriction endonuclease and comparative analyses.* Nucleic Acids Research, 2008. **36**(7): p. e44.

121. Löffler, M., et al., *Dihydroorotat-ubiquinone oxidoreductase links mitochondria in the biosynthesis of pyrimidine nucleotides.* Molecular and Cellular Biochemistry, 1997. **174**(1-2): p. 125.

122. Loffler, M., et al., *Pyrimidine pathways in health and disease.* Trends in Molecular Medicine, 2005. **11**(9): p. 430.

123. Jones, M.E., *Pyrimidine nucleotide biosynthesis in animals: genes, enzymes, and regulation of UMP biosynthesis.* Annual Review of Biochemistry, 1980. **49**: p. 253.

124. Lane, A.N. and T.W.-M. Fan, *Regulation of mammalian nucleotide metabolism and biosynthesis.* Nucleic Acids Research, 2015. **43**(4): p. 2466.

125. Bajzikova, M., et al., *Reactivation of Dihydroorotate Dehydrogenase-Driven Pyrimidine Biosynthesis Restores Tumor Growth of Respiration-Deficient Cancer Cells.* Cell Metabolism, 2019. **29**(2): p. 399.

126. Gregoire, M., et al., *On auxotrophy for pyrimidines of respiration-deficient chick embryo cells.* European Journal of Biochemistry, 1984. **142**(1): p. 49.

127. Murphy, E., et al., *Mitochondrial Function, Biology, and Role in Disease.* Circulation Research, 2016. **118**(12): p. 1960.

128. Wallace, D.C., *A mitochondrial bioenergetic etiology of disease.* The Journal of Clinical Investigation, 2013. **123**(4): p. 1405.

129. Mattson, M.P., M. Gleichmann, and A. Cheng, *Mitochondria in neuroplasticity and neurological disorders.* Neuron, 2008. **60**(5): p. 748.

130. Arun, S., L. Liu, and G. Donmez, *Mitochondrial Biology and Neurological Diseases.* Current Neuropharmacology, 2016. **14**(2): p. 143.

131. Rusecka, J., et al., *Nuclear genes involved in mitochondrial diseases caused by instability of mitochondrial DNA.* Journal of Applied Genetics, 2018. **59**(1): p. 43.

132. Coskun, P., et al., *A mitochondrial etiology of Alzheimer and Parkinson disease.* Biochimica et Biophysica Acta, 2012. **1820**(5): p. 553.

133. Horton, T.M., et al., *Marked increase in mitochondrial DNA deletion levels in the cerebral cortex of Huntington's disease patients.* Neurology, 1995. **45**(10): p. 1879.

134. Coskun, P.E., et al., *Systemic mitochondrial dysfunction and the etiology of Alzheimer's disease and down syndrome dementia.* Journal of Alzheimer's disease, 2010. **20 Suppl 2**: p. S293.

135. Coskun, P.E., M.F. Beal, and D.C. Wallace, *Alzheimer's brains harbor somatic mtDNA control-region mutations that suppress mitochondrial transcription and replication.* Proceedings of the National Academy of Sciences of the United States of America, 2004. **101**(29): p. 10726.

136. Corral-Debrinski, M., et al., *Marked changes in mitochondrial DNA deletion levels in Alzheimer brains.* Genomics, 1994. **23**(2): p. 471.

137. Wallace, D.C., *Mitochondrial genetic medicine.* Nature Genetics, 2018. **50**(12): p. 1642.

138. Bauer, D.E., et al., *Cytokine stimulation of aerobic glycolysis in hematopoietic cells exceeds proliferative demand.* Federation of American Societies for Experimental Biology, 2004. **18**(11): p. 1303.

139. Zhou, W., et al., *HIF1alpha induced switch from bivalent to exclusively glycolytic metabolism during ESC-to-EpiSC/hESC transition.* The EMBO journal, 2012. **31**(9): p. 2103.

140. Folmes, C.D., et al., *Somatic oxidative bioenergetics transitions into pluripotency-dependent glycolysis to facilitate nuclear reprogramming.* Cell Metabolism, 2011. **14**(2): p. 264.

141. Simsek, T., et al., *The distinct metabolic profile of hematopoietic stem cells reflects their location in a hypoxic niche.* Cell Stem Cell, 2010. **7**(3): p. 380.

142. Zheng, X., et al., *Metabolic reprogramming during neuronal differentiation from aerobic glycolysis to neuronal oxidative phosphorylation.* Elife, 2016. **5**.

143. Takubo, K., et al., *Regulation of glycolysis by Pdk functions as a metabolic checkpoint for cell cycle quiescence in hematopoietic stem cells.* Cell stem cell, 2013. **12**(1): p. 49.

144. Chen, C.T., et al., *Coordinated changes of mitochondrial biogenesis and antioxidant enzymes during osteogenic differentiation of human mesenchymal stem cells.* Stem Cells, 2008. **26**(4): p. 960.

145. Hanahan, D. and Robert A. Weinberg, *Hallmarks of Cancer: The Next Generation.* Cell, 2011. **144**(5): p. 646.

146. Papa, S., P.M. Choy, and C. Bubici, *The ERK and JNK pathways in the regulation of metabolic reprogramming.* Oncogene, 2019. **38**(13): p. 2223.

147. Rosenzweig, A., J. Blenis, and A.P. Gomes, *Beyond the Warburg Effect: How Do Cancer Cells Regulate One-Carbon Metabolism?* Frontiers in Cell and Developmental Biology, 2018. **6**(90).

148. Salmond, R.J., *mTOR Regulation of Glycolytic Metabolism in T Cells.* Frontiers in Cell and Developmental Biology, 2018. **6**: p. 122.

149. Warburg, O., *On the origin of cancer cells.* Science, 1956. **123**(3191): p. 309.

150. DeBerardinis, R.J., et al., *The Biology of Cancer: Metabolic Reprogramming Fuels Cell Growth and Proliferation.* Cell Metabolism, 2008. **7**(1): p. 11.

151. Pavlova, N.N. and C.B. Thompson, *The Emerging Hallmarks of Cancer Metabolism.* Cell Metabolism, 2016. **23**(1): p. 27.

152. Finkel, T. and N.J. Holbrook, *Oxidants, oxidative stress and the biology of ageing.* Nature, 2000. **408**(6809): p. 239.

153. Hosios, A.M. and M.G. Vander Heiden, *The redox requirements of proliferating mammalian cells.* Journal of Biological Chemistry, 2018. **293**(20): p. 7490.

154. Christofk, H.R., et al., *Pyruvate kinase M2 is a phosphotyrosine-binding protein.* Nature, 2008. **452**(7184): p. 181.

155. Christofk, H.R., et al., *The M2 splice isoform of pyruvate kinase is important for cancer metabolism and tumour growth.* Nature, 2008. **452**(7184): p. 230.

156. Hitosugi, T., et al., *Tyrosine phosphorylation inhibits PKM2 to promote the Warburg effect and tumor growth.* Science Signaling, 2009. **2**(97): p. ra73.

157. Anastasiou, D., et al., *Pyruvate kinase M2 activators promote tetramer formation and suppress tumorigenesis.* Nature Chemical Biology, 2012. **8**(10): p. 839.

158. Israelsen, W.J., et al., *PKM2 isoform-specific deletion reveals a differential requirement for pyruvate kinase in tumor cells.* Cell, 2013. **155**(2): p. 397.

159. Lunt, S.Y., et al., *Pyruvate kinase isoform expression alters nucleotide synthesis to impact cell proliferation.* Molecular Cell, 2015. **57**(1): p. 95.

160. Cortes-Cros, M., et al., *M2 isoform of pyruvate kinase is dispensable for tumor maintenance and growth.* Proceedings of the National Academy of Sciences of the United States of America, 2013. **110**(2): p. 489.

161. Pfeiffer, T., S. Schuster, and S. Bonhoeffer, *Cooperation and competition in the evolution of ATP-producing pathways.* Science, 2001. **292**(5516): p. 504.

162. Lunt, S.Y. and M.G. Vander Heiden, *Aerobic glycolysis: meeting the metabolic requirements of cell proliferation.* Annual Review of Cell and Developmental Biology, 2011. **27**: p. 441.

163. Locasale, J.W. and L.C. Cantley, *Metabolic flux and the regulation of mammalian cell growth.* Cell Metabolism, 2011. **14**(4): p. 443.

164. Sullivan, L.B. and N.S. Chandel, *Mitochondrial reactive oxygen species and cancer.* Cancer and Metabolism, 2014. **2**: p. 17.

165. Tan, A.S., J.W. Baty, and M.V. Berridge, *The role of mitochondrial electron transport in tumorigenesis and metastasis.* Biochimica et Biophysica Acta (BBA) - General Subjects, 2014. **1840**(4): p. 1454.

166. Berridge, M.V., C. Crasso, and J. Neuzil, *Mitochondrial Genome Transfer to Tumor Cells Breaks The Rules and Establishes a New Precedent in Cancer Biology.* Molecular Cell Oncology, 2018. **5**(5): p. e1023929.

167. Tan, An S., et al., *Mitochondrial Genome Acquisition Restores Respiratory Function and Tumorigenic Potential of Cancer Cells without Mitochondrial DNA.* Cell Metabolism, 2015. **21**(1): p. 81.

168. Weinberg, F., et al., *Mitochondrial metabolism and ROS generation are essential for Kras-mediated tumorigenicity.* Proceedings of the National Academy of Sciences of the United States of America, 2010. **107**(19): p. 8788.

169. Cavalli, L., M. Varella-Garcia, and B. Liang, *Diminished tumorigenic phenotype after depletion of mitochondrial DNA.* Cell Growth and Differentiation, 1997. **8**(11): p. 1189.

170. Morais, R., et al., *Tumor-forming ability in athymic nude mice of human cell lines devoid of mitochondrial DNA.* Cancer Research, 1994. **54**(14): p. 3889.

171. Magda, D., et al., *mtDNA depletion confers specific gene expression profiles in human cells grown in culture and in xenograft.* BMC Genomics, 2008. **9**: p. 521.

172. Dong, L.-F., et al., *Horizontal transfer of whole mitochondria restores tumorigenic potential in mitochondrial DNA-deficient cancer cells.* eLife, 2017. **6**.

173. Rustom, A., et al., *Nanotubular Highways for Intercellular Organelle Transport.* Science, 2004. **303**(5660): p. 1007.

174. Onfelt, B., et al., *Cutting edge: Membrane nanotubes connect immune cells.* Journal of Immunology, 2004. **173**(3): p. 1511.

175. Spees, J.L., et al., *Mitochondrial transfer between cells can rescue aerobic respiration.* Proceedings of the National Academy of Sciences, 2006. **103**(5): p. 1283.

176. Cho, Y.M., et al., *Mesenchymal stem cells transfer mitochondria to the cells with virtually no mitochondrial function but not with pathogenic mtDNA mutations.* PLoS ONE, 2012. **7**(3).

177. Gerdes, H.H. and R.N. Carvalho, *Intercellular transfer mediated by tunneling nanotubes.* Current Opinons in Cell Biology, 2008. **20**(4): p. 470.

178. Gurke, S., J.F.V. Barroso, and H.-H. Gerdes, *The art of cellular communication: tunneling nanotubes bridge the divide.* Histochemistry and Cell Biology, 2008. **129**(5): p. 539.

179. Koyanagi, M., et al., *Cell-to-cell connection of endothelial progenitor cells with cardiac myocytes by nanotubes: A novel mechanism for cell fate changes?* Circulation Research, 2005. **96**(10): p. 1039.

180. Önfelt, B., et al., *Structurally distinct membrane nanotubes between human macrophages support long-distance vesicular traffic or surfing of bacteria.* Journal of Immunology, 2006. **177**(12): p. 8476.

181. Otsu, K., et al., *Concentration-dependent inhibition of angiogenesis by mesenchymal stem cells.* Blood, 2009. **113**(18): p. 4197.

182. Plotnikov, E.Y., et al., *Cell-to-cell cross-talk between mesenchymal stem cells and cardiomyocytes in co-culture.* Journal of Cellular and Molecular Medicine, 2008. **12**(5A): p. 1622.

183. Plotnikov, E.Y., et al., *Cytoplasm and organelle transfer between mesenchymal multipotent stromal cells and renal tubular cells in co-culture.* Experimental Cell Research, 2010. **316**(15): p. 2447.

184. Yasuda, K., et al., *Adriamycin nephropathy: a failure of endothelial progenitor cell-induced repair.* The American journal of pathology, 2010. **176**(4): p. 1685.

185. He, K.M., et al., *Long-distance intercellular connectivity between cardiomyocytes and cardiofibroblasts mediated by membrane nanotubes.* Cardiovascular Research, 2011. **92**(1): p. 39.

186. Islam, M.N., et al., *Mitochondrial transfer from bone-marrow-derived stromal cells to pulmonary alveoli protects against acute lung injury.* Nature Medicine, 2012. **18**(5): p. 759.

187. Domhan, S., et al., *Intercellular communication by exchange of cytoplasmic material via tunneling nano-tube like structures in primary human renal epithelial cells.* PLoS ONE, 2011. **6**(6).

188. Acquistapace, A., et al., *Human mesenchymal stem cells reprogram adult cardiomyocytes toward a progenitor-like state through partial cell fusion and mitochondria transfer.* Stem Cells, 2011. **29**(5): p. 812.

189. Wang, Y., et al., *Tunneling-nanotube development in astrocytes depends on p53 activation.* Cell Death and Differentiation, 2011. **18**(4): p. 732.

190. Vallabhaneni, K.C., H. Haller, and I. Dumler, *Vascular smooth muscle cells initiate proliferation of mesenchymal stem cells by mitochondrial transfer via tunneling nanotubes.* Stem Cells and Development, 2012. **21**(17): p. 3104.

191. Wittig, D., et al., *Multi-level communication of human retinal pigment epithelial cells via tunneling nanotubes.* PLoS ONE, 2012. **7**(3).

192. Lou, E., et al., *Tunneling Nanotubes Provide a Unique Conduit for Intercellular Transfer of Cellular Contents in Human Malignant Pleural Mesothelioma.* PLoS ONE, 2012. **7**(3): p. e33093.

193. Rogers, R.S. and J. Bhattacharya, *When cells become organelle donors.* Physiology (Bethesda), 2013. **28**(6): p. 414.

194. Caicedo, A., et al., *MitoCeption as a new tool to assess the effects of mesenchymal stem/stromal cell mitochondria on cancer cell metabolism and function.* Scientific Reports, 2015. **5**.

195. Lin, H.Y., et al., *Mitochondrial transfer from Wharton's jelly-derived mesenchymal stem cells to mitochondria-defective cells recaptures impaired mitochondrial function.* Mitochondrion, 2015. **22**: p. 31.

196. Phinney, D.G., et al., *Mesenchymal stem cells use extracellular vesicles to outsource mitophagy and shuttle microRNAs.* Nature Communication, 2015. **6**: p. 8472.

197. Wang, X. and H.-H. Gerdes, *Transfer of mitochondria via tunneling nanotubes rescues apoptotic PC12 cells.* Cell Death and Differentiation, 2015. **22**(7): p. 1181.

198. Hayakawa, K., et al., *Transfer of mitochondria from astrocytes to neurons after stroke.* Nature, 2016. **535**(7613): p. 551.

199. Jiang, D., et al., *Mitochondrial transfer of mesenchymal stem cells effectively protects corneal epithelial cells from mitochondrial damage.* Cell Death and Disease, 2016. **7**(11): p. e2467.

200. Moschoi, R., et al., *Protective mitochondrial transfer from bone marrow stromal cells to acute myeloid leukemic cells during chemotherapy.* Blood, 2016. **128**(2): p. 253.

201. Yang, H., et al., *Biochip-based study of unidirectional mitochondrial transfer from stem cells to myocytes via tunneling nanotubes.* Biofabrication, 2016. **8**(1).

202. Zhang, Y., et al., *iPSC-MSCs with High Intrinsic MIRO1 and Sensitivity to TNF-α Yield Efficacious Mitochondrial Transfer to Rescue Anthracycline-Induced Cardiomyopathy.* Stem Cell Reports, 2016. **7**(4): p. 749.

203. Marlein, C.R., et al., *NADPH oxidase-2 derived superoxide drives mitochondrial transfer from bone marrow stromal cells to leukemic blasts.* Blood, 2017. **130**(14): p. 1649.

204. Berridge, M.V., et al., *Mitochondrial transfer between cells: Methodological constraints in cell culture and animal models.* Analytical Biochemistry, 2018. **552**: p. 75.

205. Boukelmoune, N., et al., *Mitochondrial transfer from mesenchymal stem cells to neural stem cells protects against the neurotoxic effects of cisplatin.* Acta Neuropathologica Communications, 2018. **6**(1): p. 139.

206. Guo, R., D. Davis, and Y. Fang, *Intercellular transfer of mitochondria rescues virus-induced cell death but facilitates cell-to-cell spreading of porcine reproductive and respiratory syndrome virus.* Virology, 2018.

207. Wang, J., et al., *Cell adhesion-mediated mitochondria transfer contributes to mesenchymal stem cell-induced chemoresistance on T cell acute lymphoblastic leukemia cells.* Journal of Hematological Oncology, 2018. **11**(1): p. 11.

208. Marlein, C.R., et al., *CD38-Driven Mitochondrial Trafficking Promotes Bioenergetic Plasticity in Multiple Myeloma.* Cancer Research, 2019. **79**(9): p. 2285.

209. Chang, J.C., et al., *Allogeneic/xenogeneic transplantation of peptide-labeled mitochondria in Parkinson's disease: Restoration of mitochondria functions and attenuation of 6-hydroxydopamine-induced neurotoxicity.* Translational Research, 2016. **170**: p. 40.

210. Rocca, C.J., et al., *Transplantation of wild-type mouse hematopoietic stem and progenitor cells ameliorates deficits in a mouse model of Friedreich's ataxia.* Science Translational Medicine, 2017. **9**(413).

211. Davis, C.H.O., et al., *Transcellular degradation of axonal mitochondria.* Proceedings of the National Academy of Sciences of the United States of America, 2014. **111**(26): p. 9633.

212. Liu, K., et al., *Mesenchymal stem cells rescue injured endothelial cells in an in vitro ischemia–reperfusion model via tunneling nanotube like structure-mediated mitochondrial transfer.* Microvascular Research, 2014. **92**: p. 10.

213. Ahmad, T., et al., *Miro1 regulates intercellular mitochondrial transport & enhances mesenchymal stem cell rescue efficacy.* EMBO Journal, 2014. **33**(9): p. 994.

214. Gerdes, H.-H., N.V. Bukoreshtliev, and J.F. Barroso, *Tunneling nanotubes: a new route for the exchange of components between animal cells.* FEBS letters, 2007. **581**(11): p. 2194.

215. Bukoreshtliev, N.V., et al., *Selective block of tunneling nanotube (TNT) formation inhibits intercellular organelle transfer between PC12 cells.* FEBS Letters, 2009. **583**(9): p. 1481.

216. Wang, X., N.V. Bukoreshtliev, and H.-H. Gerdes, *Developing Neurons Form Transient Nanotubes Facilitating Electrical Coupling and Calcium Signaling with Distant Astrocytes.* PLoS ONE, 2012. **7**(10): p. e47429.

217. Ahmad, T., et al., *Miro1 regulates intercellular mitochondrial transport & enhances mesenchymal stem cell rescue efficacy.* The EMBO journal, 2014. **33**(9): p. 994.

218. Fransson, S., A. Ruusala, and P. Aspenstrom, *The atypical Rho GTPases Miro-1 and Miro-2 have essential roles in mitochondrial trafficking.* Biochemical and Biophysical Research Communications, 2006. **344**(2): p. 500.

219. Stowers, R.S., et al., *Axonal transport of mitochondria to synapses depends on milton, a novel Drosophila protein.* Neuron, 2002. **36**(6): p. 1063.

220. Glater, E.E., et al., *Axonal transport of mitochondria requires milton to recruit kinesin heavy chain and is light chain independent.* Journal of Cell Biology, 2006. **173**(4): p. 545.

221. Bohil, A.B., B.W. Robertson, and R.E. Cheney, *Myosin-X is a molecular motor that functions in filopodia formation.* Proceedings of the National Academy of Sciences of the United States of America, 2006. **103**(33): p. 12411.

222. Falnikar, A., S. Tole, and P.W. Baas, *Kinesin-5, a mitotic microtubule-associated motor protein, modulates neuronal migration.* Molecular Biology of the Cell, 2011. **22**(9): p. 1561.

223. Nawaz, M. and F. Fatima, *Extracellular Vesicles, Tunneling Nanotubes, and Cellular Interplay: Synergies and Missing Links.* Frontiers in Molecular Bioscience, 2017. **4**: p. 50.

224. Hase, K., et al., *M-Sec promotes membrane nanotube formation by interacting with Ral and the exocyst complex.* Nature Cell Biology, 2009. **11**(12): p. 1427.

225. Omsland, M., et al., *Inhibition of Tunneling Nanotube (TNT) Formation and Human T-cell Leukemia Virus Type 1 (HTLV-1) Transmission by Cytarabine.* Scientific Reports, 2018. **8**(1): p. 11118.

226. Hashimoto, M., et al., *Potential Role of the Formation of Tunneling Nanotubes in HIV-1 Spread in Macrophages.* Journal of Immunology, 2016. **196**(4): p. 1832.

227. van Niel, G., G. D'Angelo, and G. Raposo, *Shedding light on the cell biology of extracellular vesicles.* Nature Reviews Molecular Cell Biology, 2018. **19**(4): p. 213.

228. Caicedo, A., et al., *MitoCeption as a new tool to assess the effects of mesenchymal stem/stromal cell mitochondria on cancer cell metabolism and function.* Scientific Reports, 2015. **5**: p. 9073.

229. Nzigou Mombo, B., et al., *MitoCeption: Transferring Isolated Human MSC Mitochondria to Glioblastoma Stem Cells.* Journal of Visualized Experiments (JoVE), 2017(120).

230. Cabrera, F., et al., *Primary allogeneic mitochondrial mix (PAMM) transfer/transplant by MitoCeption to address damage in PBMCs caused by ultraviolet radiation.* BMC Biotechnology, 2019. **19**(1): p. 42.

231. Masuzawa, A., et al., *Transplantation of autologously derived mitochondria protects the heart from ischemia-reperfusion injury.* American Journal of Physiology. Heart and Circulatory Physiology, 2013. **304**(7): p. H966.

232. Ramirez-Barbieri, G., et al., *Alloreactivity and allorecognition of syngeneic and allogeneic mitochondria.* Mitochondrion, 2019. **46**: p. 103.

233. Cowan, D.B., et al., *Transit and integration of extracellular mitochondria in human heart cells.* Scientific Reports, 2017. **7**(1): p. 17450.

234. Cowan, D.B., et al., *Intracoronary Delivery of Mitochondria to the Ischemic Heart for Cardioprotection.* PLoS ONE, 2016. **11**(8): p. e0160889.

235. Ogle, B.M., M. Cascalho, and J.L. Platt, *Biological implications of cell fusion.* Nature Reviews Molecular Cell Biology, 2005. **6**(7): p. 567.

236. Harris, H. and J.F. Watkins, *Hybrid Cells Derived from Mouse and Man : Artificial Heterokaryons of Mammalian Cells from Different Species.* Nature, 1965. **205**(4972): p. 640.

237. Weimann, J.M., et al., *Stable reprogrammed heterokaryons form spontaneously in Purkinje neurons after bone marrow transplant.* Nature Cell Biology, 2003. **5**(11): p. 959.

238. Alvarez-Dolado, M., et al., *Fusion of bone-marrow-derived cells with Purkinje neurons, cardiomyocytes and hepatocytes.* Nature, 2003. **425**(6961): p. 968.

239. Bae, J.S., et al., *Neurodegeneration augments the ability of bone marrow-derived mesenchymal stem cells to fuse with Purkinje neurons in Niemann-Pick type C mice.* Human Gene Therapy, 2005. **16**(8): p. 1006.

240. Giordano-Santini, R., C. Linton, and M.A. Hilliard, *Cell-cell fusion in the nervous system: Alternative mechanisms of development, injury, and repair.* Seminars in Cell and Developmental Biology, 2016. **60**: p. 146.

241. Mandel, K., et al., *Mesenchymal stem cells directly interact with breast cancer cells and promote tumor cell growth in vitro and in vivo.* Stem Cells and Development, 2013. **22**(23): p. 3114.

242. Yang, Y., A. Otte, and R. Hass, *Human mesenchymal stroma/stem cells exchange membrane proteins and alter functionality during interaction with different tumor cell lines.* Stem Cells and Development, 2015. **24**(10): p. 1205.

243. Wei, H.J., et al., *FOXF1 mediates mesenchymal stem cell fusion-induced reprogramming of lung cancer cells.* Oncotarget, 2014. **5**(19): p. 9514.

244. Xue, J., et al., *Tumorigenic hybrids between mesenchymal stem cells and gastric cancer cells enhanced cancer proliferation, migration and stemness.* BMC Cancer, 2015. **15**: p. 793.

245. Terada, N., et al., *Bone marrow cells adopt the phenotype of other cells by spontaneous cell fusion.* Nature, 2002. **416**(6880): p. 542.

246. Osswald, M., et al., *A malignant cellular network in gliomas: potential clinical implications.* Neuro-oncology, 2016. **18**(4): p. 479.

247. Osswald, M., et al., *Brain tumour cells interconnect to a functional and resistant network.* Nature, 2015. **528**(7580): p. 93.

248. Venkataramani, V., et al., *Glutamatergic synaptic input to glioma cells drives brain tumour progression.* Nature, 2019. **573**(7775): p. 532.

249. Venkatesh, H.S., et al., *Electrical and synaptic integration of glioma into neural circuits.* Nature, 2019. **573**(7775): p. 539.

250. Zeng, Q., et al., *Synaptic proximity enables NMDAR signalling to promote brain metastasis.* Nature, 2019. **573**(7775): p. 526.

251. Kemp, K., et al., *Fusion between human mesenchymal stem cells and rodent cerebellar Purkinje cells.* Neuropathology and Applied Neurobiology, 2011. **37**(2): p. 166.

252. Nygren, J.M., et al., *Myeloid and lymphoid contribution to non-haematopoietic lineages through irradiation-induced heterotypic cell fusion.* Nature Cell Biology, 2008. **10**(5): p. 584.

253. Johansson, C.B., et al., *Extensive fusion of haematopoietic cells with Purkinje neurons in response to chronic inflammation.* Nature Cell Biology, 2008. **10**(5): p. 575.

254. Okabe, M., et al., *'Green mice' as a source of ubiquitous green cells.* FEBS Lett, 1997. **407**(3): p. 313.

255. Hasuwa, H., et al., *Transgenic mouse sperm that have green acrosome and red mitochondria allow visualization of sperm and their acrosome reaction in vivo.* Experimental Animals, 2010. **59**(1): p. 105.

256. Minamikawa, T., et al., *Chloromethyl-X-rosamine (MitoTracker Red) photosensitises mitochondria and induces apoptosis in intact human cells.* Journal of Cell Science, 1999. **112 (Pt 14)**: p. 2419.

257. Icha, J., et al., *Phototoxicity in live fluorescence microscopy, and how to avoid it.* BioEssays, 2017. **39**(8): p. 1700003.

258. Buckman, J.F., et al., *MitoTracker labeling in primary neuronal and astrocytic cultures: influence of mitochondrial membrane potential and oxidants.* Journal of Neuroscience Methods, 2001. **104**(2): p. 165.

259. Appelhans, T. and K.B. Busch, *Dynamic imaging of mitochondrial membrane proteins in specific sub-organelle membrane locations.* Biophysical Reviews, 2017. **9**(4): p. 345.

260. Brazelton, T.R. and H.M. Blau, *Optimizing Techniques for Tracking Transplanted Stem Cells In Vivo.* STEM CELLS, 2005. **23**(9): p. 1251.

261. Friedman, J.R., et al., *ER tubules mark sites of mitochondrial division.* Science, 2011. **334**(6054): p. 358-62.

262. Schneider, R., *Intercellular mitochondrial transfer in neural cells*. Doctoral thesis. 2017, Victoria University of Wellington: Wellington, New Zealand. Retrieved from http://researcharchive.vuw.ac.nz/handle/10063/6977.

263. Cselenyák, A., et al., *Live-cell fluorescent imaging of membrane or mitochondrion transfer between connected cells in culture.* Microscopy: Science, Technology, Applications and Education, 2010. **1**: p. 764.

264. Hayflick, L. and P.S. Moorhead, *The serial cultivation of human diploid cell strains.* Experimental Cell Research, 1961. **25**(3): p. 585.

265. Grégoire, M., et al., *On auxotrophy for pyrimidines of respiration-deficient chick embryo cells.* European Journal of Biochemistry, 1984. **142**(1): p. 49.

266. Morlan, J., J. Baker, and D. Sinicropi, *Mutation Detection by Real-Time PCR: A Simple, Robust and Highly Selective Method.* PLoS ONE, 2009. **4**(2): p. e4584.

267. Latorra, D., et al., *Enhanced allele-specific PCR discrimination in SNP genotyping using 3' locked nucleic acid (LNA) primers.* Human Mutation, 2003. **22**(1): p. 79.

268. Kwok, S., et al., *Effects of primer-template mismatches on the polymerase chain reaction: Human immunodeficiency virus type 1 model studies.* Nucleic Acids Research, 1990. **18**(4): p. 999.

269. Ikuta, S., et al., *Dissociation kinetics of 19 base paired oligonucleotide-DNA duplexes containing different single mismatched base pairs.* Nucleic Acids Research, 1987. **15**(2): p. 797.

270. Robin, E.D. and R. Wong, *Mitochondrial DNA molecules and virtual number of mitochondria per cell in mammalian cells.* Journal of Cellular Physiology, 1988. **136**.

271. Reznik, E., et al., *Mitochondrial DNA copy number variation across human cancers.* eLife, 2016. **5**.

272. Dickinson, A., et al., *The regulation of mitochondrial DNA copy number in glioblastoma cells.* Cell Death and Differention, 2013. **20**(12): p. 1644.

273. John, H.A., M.L. Birnstiel, and K.W. Jones, *RNA-DNA Hybrids at the Cytological Level.* Nature, 1969. **223**(5206): p. 582.

274. Pardue, M.L. and J.G. Gall, *Molecular hybridization of radioactive DNA to the DNA of cytological preparations.* Proceedings of the National Academy of Sciences, 1969. **64**(2): p. 600.

275. Buongiorno-Nardelli, M. and F. Amaldi, *Autoradiographic Detection of Molecular Hybrids between rRNA and DNA in Tissue Sections.* Nature, 1970. **225**(5236): p. 946.

276. Femino, A.M., *Visualization of Single RNA Transcripts in Situ.* Science, 1998. **280**(5363): p. 585.

277. Raj, A., et al., *Imaging individual mRNA molecules using multiple singly labeled probes.* Nature Methods, 2008. **5**(10): p. 877.

278. Levesque, M.J., et al., *Visualizing SNVs to quantify allele-specific expression in single cells.* Nature Methods, 2013. **10**(9): p. 865.

279. Hansen, C.H. and A. Van Oudenaarden, *Allele-specific detection of single mRNA molecules in situ.* Nature Methods, 2013. **10**(9): p. 869.

280. Ginart, P., et al., *Visualizing allele-specific expression in single cells reveals epigenetic mosaicism in an H19 loss-of-imprinting mutant.* Genes and Development, 2016. **30**(5): p. 567.

281. Nilsson, M., et al., *Padlock probes: circularizing oligonucleotides for localized DNA detection.* Science, 1994. **265**(5181): p. 2085.

282. Lizardi, P.M., et al., *Mutation detection and single-molecule counting using isothermal rolling-circle amplification.* Nature Genetics, 1998. **19**(3): p. 225.

283. Christian, A.T., et al., *Detection of DNA point mutations and mRNA expression levels by rolling circle amplification in individual cells.* Proceedings of the National Academy of Sciences, 2001. **98**(25): p. 14238.

284. Larsson, C., et al., *In situ genotyping individual DNA molecules by target-primed rolling-circle amplification of padlock probes.* Nature Methods, 2004. **1**(3): p. 227.

285. Liu, P., *DNA ligases ensure fidelity by interrogating minor groove contacts.* Nucleic Acids Research, 2004. **32**(15): p. 4503.

286. Lohman, G.J., et al., *A high-throughput assay for the comprehensive profiling of DNA ligase fidelity.* Nucleic Acids Research, 2016. **44**(2): p. e14.

287. Akhras, M.S., et al., *Connector Inversion Probe Technology: A Powerful One-Primer Multiplex DNA Amplification System for Numerous Scientific Applications.* PLoS ONE, 2007. **2**(9): p. e915.

288. Hardenbol, P., et al., *Multiplexed genotyping with sequence-tagged molecular inversion probes.* Nature Biotechnology, 2003. **21**(6): p. 673.

289. Mignardi, M., et al., *Oligonucleotide gap-fill ligation for mutation detection and sequencing in situ.* Nucleic Acids Research, 2015. **43**(22): p. e151.

290. Blab, G.A., T. Schmidt, and M. Nilsson, *Homogeneous detection of single rolling circle replication products.* Analytical Chemistry, 2004. **76**(2): p. 495.

291. Brutlag, D. and A. Kornberg, *A proofreading function for the 3'-5' exonuclease activity in deoxyribonucleic acid polymerases.* Journal of Biological Chemistry, 1972. **247**: p. 241.

292. Blacker, T.S. and M.R. Duchen, *Investigating mitochondrial redox state using NADH and NADPH autofluorescence.* Free Radical Biology and Medicine, 2016. **100**: p. 53.

293. Clausson, C.-M., et al., *Compaction of rolling circle amplification products increases signal integrity and signal-to-noise ratio.* Scientific Reports, 2015. **5**(1): p. 12317.

294. Collins, T.J., et al., *Mitochondria are morphologically and functionally heterogeneous within cells.* The EMBO journal, 2002. **21**(7): p. 1616.

295. Carpenter, A.E., et al., Genome Biology, 2006. **7**(10): p. R100.

296. Kamentsky, L., et al., *Improved structure, function and compatibility for CellProfiler: modular high-throughput image analysis software.* Bioinformatics, 2011. **27**(8): p. 1179.

297. Lamprecht, M.R., D.M. Sabatini, and A.E. Carpenter, *CellProfiler: free, versatile software for automated biological image analysis.* Biotechniques, 2007. **42**(1): p. 71.

298. Otsu, N., *A Threshold Selection Method from Gray-Level Histograms.* IEEE Transactions on Systems, Man, and Cybernetics, 1979. **9**(1): p. 62.

299. Bray, M.-A. and A.E. Carpenter, *Quality Control for High-Throughput Imaging Experiments Using Machine Learning in Cellprofiler.* Methods in Molecular Biology (Clifton, N.J.), 2018. **1683**: p. 89.

300. Jones, T.R., et al., *CellProfiler Analyst: data exploration and analysis software for complex image-based screens.* BMC Bioinformatics, 2008. **9**(1): p. 482.

301. Sharpless, T., et al., *Flow cytofluorimetry: discrimination between single cells and cell aggregates by direct size measurements.* Acta Cytologica, 1975. **19**(6): p. 577.

302. Dore-Duffy, P., *Isolation and Characterization of Cerebral Microvascular Pericytes*, in *The Blood-Brain Barrier: Biology and Research Protocols*, S. Nag, Editor. 2003, Humana Press: Totowa, NJ. p. 375.

303. Helms, H.C. and B. Brodin, *Generation of primary cultures of bovine brain endothelial cells and setup of cocultures with rat astrocytes.* Methods in Molecular Biology, 2014. **1135**: p. 365.

304. Zhou, L., F. Sohet, and R. Daneman, *Purification of endothelial cells from rodent brain by immunopanning.* Cold Spring Harbor Protocols, 2014. **2014**(1): p. 65.

305. Zhou, L., F. Sohet, and R. Daneman, *Purification and culture of central nervous system pericytes.* Cold Spring Harb Protocols, 2014. **2014**(6): p. 581.

306. Gama Sosa, M.A., et al., *Interactions of primary neuroepithelial progenitor and brain endothelial cells: distinct effect on neural progenitor maintenance and differentiation by soluble factors and direct contact.* Cell Research, 2007. **17**(7): p. 619.

307. Zhang, Y., et al., *An RNA-sequencing transcriptome and splicing database of glia, neurons, and vascular cells of the cerebral cortex.* The Journal of neuroscience : the official journal of the Society for Neuroscience, 2014. **34**(36): p. 11929.

308. Hutter-Schmid, B. and C. Humpel, *Primary mouse brain pericytes isolated from transgenic Alzheimer mice spontaneously differentiate into a CD11b(+) microglial-like cell type in vitro.* Experimental Gerontology, 2018. **112**: p. 30.

309. Winkler, E.A., R.D. Bell, and B.V. Zlokovic, *Pericyte-specific expression of PDGF beta receptor in mouse models with normal and deficient PDGF beta receptor signaling.* Molecular Neurodegeneration, 2010. **5**: p. 32.

310. Smyth, L.C.D., et al., *Markers for human brain pericytes and smooth muscle cells.* Journal of Chemical Neuroanatomy, 2018. **92**: p. 48.

311. Jung, B., et al., *Visualization of vascular mural cells in developing brain using genetically labeled transgenic reporter mice.* Journal of Cerebral Blood Flow and Metabolism, 2018. **38**(3): p. 456.

312. Armulik, A., et al., *Pericytes regulate the blood-brain barrier.* Nature, 2010. **468**(7323): p. 557.

313. Hartmann, D.A., et al., *Pericyte structure and distribution in the cerebral cortex revealed by high-resolution imaging of transgenic mice.* Neurophotonics, 2015. **2**(4): p. 041402.

314. Chen, J., et al., *CD146 coordinates brain endothelial cell-pericyte communication for blood-brain barrier development.* Proceedings of the National Academy of Sciences of the United States of America, 2017. **114**(36): p. E7622.

315. Grant, R.I., et al., *Organizational hierarchy and structural diversity of microvascular pericytes in adult mouse cortex.* Journal of Cerebral Blood Flow and Metabolism, 2019. **39**(3): p. 411.

316. Kisler, K., et al., *Cerebral blood flow regulation and neurovascular dysfunction in Alzheimer disease.* Nature Reviews Neuroscience, 2017. **18**(7): p. 419.

317. Attwell, D., et al., *What is a pericyte?* Journal of Cerebral Blood Flow and Metabolism, 2016. **36**(2): p. 451.

318. Sweeney, M.D., S. Ayyadurai, and B.V. Zlokovic, *Pericytes of the neurovascular unit: key functions and signaling pathways.* Nature Neuroscience, 2016. **19**(6): p. 771.

319. Vanlandewijck, M., et al., *A molecular atlas of cell types and zonation in the brain vasculature.* Nature, 2018. **554**(7693): p. 475.

320. Etchevers, H.C., et al., *The cephalic neural crest provides pericytes and smooth muscle cells to all blood vessels of the face and forebrain.* Development, 2001. **128**(7): p. 1059.

321. Dominici, M., et al., *Minimal criteria for defining multipotent mesenchymal stromal cells. The International Society for Cellular Therapy position statement.* Cytotherapy, 2006. **8**(4): p. 315.

322. Dore-Duffy, P., et al., *CNS microvascular pericytes exhibit multipotential stem cell activity.* Journal of Cerebral Blood Flow and Metabolism, 2006. **26**(5): p. 613.

323. Guimaraes-Camboa, N., et al., *Pericytes of Multiple Organs Do Not Behave as Mesenchymal Stem Cells In Vivo.* Cell Stem Cell, 2017. **20**(3): p. 345.e5.

324. Dore-Duffy, P., et al., *Pericyte migration from the vascular wall in response to traumatic brain injury.* Microvascular Research, 2000. **60**(1): p. 55.

325. Klement, W., et al., *Seizure progression and inflammatory mediators promote pericytosis and pericyte-microglia clustering at the cerebrovasculature.* Neurobiology of Disease, 2018. **113**: p. 70.

326. Fernandez-Klett, F., et al., *Early loss of pericytes and perivascular stromal cell-induced scar formation after stroke.* Journal of Cerebral Blood Flow and Metabolism, 2013. **33**(3): p. 428.

327. Milesi, S., et al., *Redistribution of PDGFRbeta cells and NG2DsRed pericytes at the cerebrovasculature after status epilepticus.* Neurobiology of Disease, 2014. **71**: p. 151.

328. Sakuma, R., et al., *Brain pericytes serve as microglia-generating multipotent vascular stem cells following ischemic stroke.* Journal of Neuroinflammation, 2016. **13**(1): p. 57.

329. Dias, D.O., et al., *Reducing Pericyte-Derived Scarring Promotes Recovery after Spinal Cord Injury.* Cell, 2018. **173**(1): p. 153.e22.

330. Goritz, C., et al., *A pericyte origin of spinal cord scar tissue.* Science, 2011. **333**(6039): p. 238.

331. Dieriks, B.V., et al., *α-synuclein transfer through tunneling nanotubes occurs in SH-SY5Y cells and primary brain pericytes from Parkinson's disease patients.* Scientific Reports, 2017. **7**: p. 42984.

332. Ruan, L., et al., *Cytosolic proteostasis through importing of misfolded proteins into mitochondria.* Nature, 2017. **543**(7645): p. 443.

333. Devi, L., et al., *Mitochondrial import and accumulation of alpha-synuclein impair complex I in human dopaminergic neuronal cultures and Parkinson disease brain.* Journal of Biological Chemistry, 2008. **283**(14): p. 9089.

334. Bartz, Q.R., *Isolation and characterization of chloromycetin.* Journal of Biological Chemistry, 1948. **172**(2): p. 445.

335. Controulis, J., M.C. Rebstock, and H.M. Crooks, *Chloramphenicol (Chloromycetin).1 V. Synthesis.* Journal of the American Chemical Society, 1949. **71**(7): p. 2463.

336. Long, L.M. and H.D. Troutman, *Chloramphenicol1 (Chloromycetin). VI. A Synthetic Approach.* Journal of the American Chemical Society, 1949. **71**(7): p. 2469.

337. Cundliffe, E. and K. McQuillen, *Bacterial protein synthesis: The effects of antibiotics.* Journal of Molecular Biology, 1967. **30**(1): p. 137.

338. Borovinskaya, M.A., et al., *Structural basis for aminoglycoside inhibition of bacterial ribosome recycling.* Nature Structural & Molecular Biology, 2007. **14**(8): p. 727.

339. Hammett-Stabler, C.A. and T. Johns, *Laboratory guidelines for monitoring of antimicrobial drugs. National Academy of Clinical Biochemistry.* Clinical Chemistry, 1998. **44**(5): p. 1129.

340. Holt, D., D. Harvey, and R. Hurley, *Chloramphenicol toxicity.* Adverse Drug Reactions and Toxicological Reviews, 1993. **12**(2): p. 83.

341. Winternitz, C., *Fatal aplastic anemia following chloramphenicol (chloromycetin) therapy.* California Medicine, 1952. **77**(5): p. 335.

342. Volini, I.F., et al., *Hemopoietic changes during administration of chloramphenicol (chloromycetin).* Journal of the American Medical Association, 1950. **142**(17): p. 1333.

343. Sutherland, J.M., *Fatal cardiovascular collapse of infants receiving large amounts of chloramphenicol.* American Medical Association Journal of Diseases of Children, 1959. **97**(6): p. 761.

344. Rich, M.L., R.J. Ritterhoff, and R.J. Hoffmann, *A fatal case of aplastic anemia following chloramphenicol (chloromycetin) therapy.* Annals of Internal Medicine, 1950. **33**(6): p. 1459.

345. Kroon, A. and C. Van den Bogert, *Antibacterial drugs and their interference with the biogenesis of mitochondria in animal and human cells.* Pharmaceutisch weekblad, 1983. **5**(3): p. 81.

346. Riesbeck, K., A. Bredberg, and A. Forsgren, *Ciprofloxacin does not inhibit mitochondrial functions but other antibiotics do.* Antimicrobial Agents and Chemotherapy, 1990. **34**(1): p. 167.

347. Duewelhenke, N., O. Krut, and P. Eysel, *Influence on mitochondria and cytotoxicity of different antibiotics administered in high concentrations on primary human osteoblasts and cell lines.* Antimicrobial Agents and Chemotherapy, 2007. **51**(1): p. 54.

348. Karbowski, M., et al., *Cycloheximide and 4-OH-TEMPO suppress chloramphenicol-induced apoptosis in RL-34 cells via the suppression of the formation of megamitochondria.* Biochimica et Biophysica Acta (BBA)-Molecular Cell Research, 1999. **1449**(1): p. 25.

349. Robbana-Barnat, S., et al., *Use of human lymphoblastoid cells to detect the toxic effect of chloramphenicol and metabolites possibly involved in aplastic anemia in man.* Drug and Chemical Toxicology, 1997. **20**(3): p. 239.

350. Lafarge-Frayssinet, C., et al., *Cytotoxicity and DNA damaging potency of chloramphenicol and six metabolites: a new evaluation in human lymphocytes and Raji cells.* Mutation Research/Genetic Toxicology, 1994. **320**(3): p. 207.

351. Goldstein, S. and L.B. Korczack, *Status of mitochondria in living human fibroblasts during growth and senescence in vitro: use of the laser dye rhodamine 123.* Journal of Cell Biology, 1981. **91**(2 Pt 1): p. 392.

352. Li, C.H., *Chloramphenicol-induced Mitochondrial Stress Increases p21 Expression and Prevents Cell Apoptosis through a p21-dependent Pathway.* The Journal of Biological Chemistry, 2005. **280**(28): p. 26193.

353. Li, C.H., et al., *Chloramphenicol Causes Mitochondrial Stress, Decreases ATP Biosynthesis, Induces Matrix Metalloproteinase-13 Expression, and Solid-Tumor Cell Invasion.* Toxicological sciences, 2010. **116**(1): p. 140.

354. Rosenberg, B., et al., *Platinum-induced filamentous growth in Escherichia coli.* Journal of Bacteriology, 1967. **93**(2): p. 716.

355. Rosenberg, B., et al., *The Inhibition of Growth or Cell Division in Escherichia coli by Different Ionic Species of Platinum(IV) Complexes.* Journal of Biological Chemistry, 1967. **242**(6): p. 1347.

356. Rosenberg, B., L. Van Camp, and T. Krigas, *Inhibition of Cell Division in Escherichia coli by Electrolysis Products from a Platinum Electrode.* Nature, 1965. **205**(4972): p. 698.

357. Rosenberg, B., et al., *Platinum compounds: a new class of potent antitumour agents.* Nature, 1969. **222**(5191): p. 385.

358. Kelland, L., *The resurgence of platinum-based cancer chemotherapy.* Nature Reviews Cancer, 2007. **7**(8): p. 573.

359. Dasari, S. and P.B. Tchounwou, *Cisplatin in cancer therapy: molecular mechanisms of action.* European Journal of Pharmacology, 2014. **740**: p. 364.

360. Beck, D.J. and R.R. Brubaker, *Effect of cis-platinum(II)diamminodichloride on wild type and deoxyribonucleic acid repair deficient mutants of Escherichia coli.* Journal of Bacteriology, 1973. **116**(3): p. 1247.

361. Fraval, H.N., C.J. Rawlings, and J.J. Roberts, *Increased sensitivity of UV-repair-deficient human cells to DNA bound platinum products which unlike thymine dimers are not recognized by an endonuclease extracted from Micrococcus luteus.* Mutation Research, 1978. **51**(1): p. 121.

362. Santos, N.A., et al., *Cisplatin-induced nephrotoxicity is associated with oxidative stress, redox state unbalance, impairment of energetic metabolism and apoptosis in rat kidney mitochondria.* Archives of Toxicology, 2007. **81**(7): p. 495.

363. Dehne, N., et al., *Cisplatin ototoxicity: involvement of iron and enhanced formation of superoxide anion radicals.* Toxicology and Applied Pharmacology, 2001. **174**(1): p. 27.

364. Jiang, Y., et al., *Implications of apurinic/apyrimidinic endonuclease in reactive oxygen signaling response after cisplatin treatment of dorsal root ganglion neurons.* Cancer Research, 2008. **68**(15): p. 6425.

365. Marullo, R., et al., *Cisplatin Induces a Mitochondrial-ROS Response That Contributes to Cytotoxicity Depending on Mitochondrial Redox Status and Bioenergetic Functions.* PLoS ONE, 2013. **8**(11): p. e81162.

366. Olivero, O.A., et al., *Preferential formation and decreased removal of cisplatin-DNA adducts in Chinese hamster ovary cell mitochondrial DNA as compared to nuclear DNA.* Mutation Research, 1997. **391**(1-2): p. 79.

367. Yang, Z., et al., *Cisplatin preferentially binds mitochondrial DNA and voltage-dependent anion channel protein in the mitochondrial membrane of head and neck squamous cell carcinoma: possible role in apoptosis.* Clinical Cancer Research, 2006. **12**(19): p. 5817.

368. Podratz, J.L., et al., *Cisplatin induced mitochondrial DNA damage in dorsal root ganglion neurons.* Neurobiology of Disease, 2011. **41**(3): p. 661.

369. Kukat, A., et al., *Generation of rho0 cells utilizing a mitochondrially targeted restriction endonuclease and comparative analyses.* Nucleic Acids Research, 2008. **36**(7): p. e44.

370. Yang, Y. and A.A. Sauve, *NAD(+) metabolism: Bioenergetics, signaling and manipulation for therapy.* Biochimica et Biophysica Acta, 2016. **1864**(12): p. 1787.

371. Fang, J., et al., *Dihydro-orotate dehydrogenase is physically associated with the respiratory complex and its loss leads to mitochondrial dysfunction.* Bioscience Reports, 2013. **33**(2): p. e00021.

372. Holt, D., et al., *The myelotoxicity of chloramphenicol: in vitro and in vivo studies: I. In vitro effects on cells in culture.* Human & Experimental Toxicology, 1997. **16**(10): p. 570.

373. Leiter, L.M., et al., *Chloramphenicol-induced mitochondrial dysfunction is associated with decreased transferrin receptor expression and ferritin synthesis in K562 cells and is unrelated to IRE-IRP interactions.* Journal of Cellular Physiology, 1999. **180**(3): p. 334.

374. Tian, F., et al., *The antibiotic chloramphenicol may be an effective new agent for inhibiting the growth of multiple myeloma.* Oncotarget, 2016. **7**(32): p. 51934.

375. Lomeli, N., et al., *Cisplatin-induced mitochondrial dysfunction is associated with impaired cognitive function in rats.* Free Radical Biology & Medicine, 2017. **102**: p. 274.

376. Marrache, S., R.K. Pathak, and S. Dhar, *Detouring of cisplatin to access mitochondrial genome for overcoming resistance.* Proceedings of the National Academy of Sciences, 2014. **111**(29): p. 10444.

377. Jones, A.W., et al., *PGC-1 family coactivators and cell fate: roles in cancer, neurodegeneration, cardiovascular disease and retrograde mitochondria-nucleus signalling.* Mitochondrion, 2012. **12**(1): p. 86.

378. Jazwinski, S.M., *The retrograde response: when mitochondrial quality control is not enough.* Biochimica et Biophysica Acta, 2013. **1833**(2): p. 400.

379. Mottis, A., V. Jovaisaite, and J. Auwerx, *The mitochondrial unfolded protein response in mammalian physiology.* Mammalian Genome, 2014. **25**(9-10): p. 424.

380. Cagin, U. and J.A. Enriquez, *The complex crosstalk between mitochondria and the nucleus: What goes in between?* The International Journal of Biochemistry and Cell Biology, 2015. **63**: p. 10.

381. Jornayvaz, F.R. and G.I. Shulman, *Regulation of mitochondrial biogenesis.* Essays in Biochemistry, 2010. **47**: p. 69.

382. Sabharwal, S.S. and P.T. Schumacker, *Mitochondrial ROS in cancer: initiators, amplifiers or an Achilles' heel?* Nature Reviews Cancer, 2014. **14**(11): p. 709.

383. Jin, S. and N. Cordes, *ATM controls DNA repair and mitochondria transfer between neighboring cells.* Cell Communication and Signaling, 2019. **17**(1): p. 144.

384. Sun, C., et al., *Endocytosis-mediated mitochondrial transplantation: Transferring normal human astrocytic mitochondria into glioma cells rescues aerobic respiration and enhances radiosensitivity.* Theranostics, 2019. **9**(12): p. 3595.

385. Ippolito, L., et al., *Cancer-associated fibroblasts promote prostate cancer malignancy via metabolic rewiring and mitochondrial transfer.* Oncogene, 2019. **38**(27): p. 5339.

386. Liu, K., et al., *Mesenchymal stem cells rescue injured endothelial cells in an in vitro ischemia-reperfusion model via tunneling nanotube like structure-mediated mitochondrial transfer.* Microvascular Research, 2014. **92**: p. 10.

387. Jayaprakash, A.D., et al., *Stable heteroplasmy at the single-cell level is facilitated by intercellular exchange of mtDNA.* Nucleic Acids Research, 2015. **43**(4): p. 2177.

388. Nilsson, M., *Lock and roll: single-molecule genotyping in situ using padlock probes and rolling-circle amplification.* Histochemistry and Cell Biology, 2006. **126**(2): p. 159.

389. Antson, D.-O., et al., *PCR-generated padlock probes detect single nucleotide variation in genomic DNA.* Nucleic Acids Research, 2000. **28**(12): p. e58.

390. Prins, T.W., et al., *Towards a multiplex cereal traceability tool using padlock probe ligation on genomic DNA.* Food Chemistry, 2010. **118**(4): p. 966.

391. Jonstrup, S.P., J. Koch, and J. Kjems, *A microRNA detection system based on padlock probes and rolling circle amplification.* RNA, 2006. **12**(9): p. 1747.

392. Nilsson, M., et al., *Enhanced detection and distinction of RNA by enzymatic probe ligation.* Nature Biotechnology, 2000. **18**(7): p. 791.

393. Baner, J., et al., *Signal amplification of padlock probes by rolling circle replication.* Nucleic Acids Research, 1998. **26**(22): p. 5073.

394. Melin, J., et al., *Homogeneous amplified single-molecule detection: Characterization of key parameters.* Analytical Biochemistry, 2007. **368**(2): p. 230.

395. Zieba, A., et al., *In situ protein detection with enhanced specificity using DNA-conjugated antibodies and proximity ligation.* Modern Pathology, 2018. **31**(2): p. 253.

396. Ke, R., et al., *In situ sequencing for RNA analysis in preserved tissue and cells.* Nature Methods, 2013. **10**(9): p. 857.

397. Maïno, N., et al., *A microfluidic platform towards automated multiplexed in situ sequencing.* Scientific Reports, 2019. **9**(1): p. 3542.

398. Soderberg, O., et al., *Direct observation of individual endogenous protein complexes in situ by proximity ligation.* Nature Methods, 2006. **3**(12): p. 995.

399. Qian, X., et al., *Probabilistic cell typing enables fine mapping of closely related cell types in situ.* Nature Methods, 2019.

400. Partel, G., et al., *Identification of spatial compartments in tissue from from in situ sequencing data.* bioRxiv, 2019: p. 765842.

401. Svedlund, J., et al., *Generation of in situ sequencing based OncoMaps to spatially resolve gene expression profiles of diagnostic and prognostic markers in breast cancer.* EBioMedicine, 2019. **48**: p. 212.

402. Gao, L., et al., *Mitochondria Are Dynamically Transferring Between Human Neural Cells and Alexander Disease-Associated GFAP Mutations Impair the Astrocytic Transfer.* Frontiers in Cellular Neuroscience, 2019. **13**(316).

403. Falchi, A.M., et al., *Astrocytes shed large membrane vesicles that contain mitochondria, lipid droplets and ATP.* Histochemistry and Cell Biology, 2013. **139**(2): p. 221.

404. Wang, X. and H.H. Gerdes, *Transfer of mitochondria via tunneling nanotubes rescues apoptotic PC12 cells.* Cell Death and Differentiation, 2015. **22**(7): p. 1181.

405. Zhu, L., et al., *Mitochondrial transplantation attenuates hypoxic pulmonary hypertension.* Oncotarget, 2016. **7**(31): p. 48925.

406. Hough, K.P., et al., *Exosomal transfer of mitochondria from airway myeloid-derived regulatory cells to T cells.* Redox Biology, 2018. **18**: p. 54.

407. Pasquier, J., et al., *Preferential transfer of mitochondria from endothelial to cancer cells through tunneling nanotubes modulates chemoresistance.* Journal of Translational Medicine, 2013. **11**: p. 94.

408. Rostami, J., et al., *Human Astrocytes Transfer Aggregated Alpha-Synuclein via Tunneling Nanotubes.* Journal of Neuroscience, 2017. **37**(49): p. 11835.

409. Patel, D., et al., *Macropinocytic entry of isolated mitochondria in epidermal growth factor-activated human osteosarcoma cells.* Scientific Reports, 2017. **7**(1): p. 12886.

410. Wittig, D., et al., *Multi-level communication of human retinal pigment epithelial cells via tunneling nanotubes.* PLoS ONE, 2012. **7**(3): p. e33195.

411. Pankotai, E., et al., *The role of mitochondria in direct cell-to-cell connection dependent rescue of postischemic cardiomyoblasts.* Mitochondrion, 2012. **12**(2): p. 352.

412. Lou, E., et al., *Tunneling nanotubes provide a unique conduit for intercellular transfer of cellular contents in human malignant pleural mesothelioma.* PLoS ONE, 2012. **7**(3).

413. Desplats, P., et al., *Inclusion formation and neuronal cell death through neuron-to-neuron transmission of alpha-synuclein.* Proceedings of the National Academy of Sciences of the United States of America, 2009. **106**(31): p. 13010.

414. Luk, K.C., et al., *Intracerebral inoculation of pathological alpha-synuclein initiates a rapidly progressive neurodegenerative alpha-synucleinopathy in mice.* Journal of Experimental Medicine, 2012. **209**(5): p. 975.

415. Masuda-Suzukake, M., et al., *Prion-like spreading of pathological alpha-synuclein in brain.* Brain, 2013. **136**(Pt 4): p. 1128.

416. Liu, L., et al., *Trans-synaptic spread of tau pathology in vivo.* PLoS ONE, 2012. **7**(2): p. e31302.

417. Kane, M.D., et al., *Evidence for seeding of beta -amyloid by intracerebral infusion of Alzheimer brain extracts in beta -amyloid precursor protein-transgenic mice.* Journal of Neuroscience, 2000. **20**(10): p. 3606.

418. Ye, L., et al., *Progression of Seed-Induced Abeta Deposition within the Limbic Connectome.* Brain Pathology, 2015. **25**(6): p. 743.

419. Masuda-Suzukake, M., et al., *Pathological alpha-synuclein propagates through neural networks.* Acta Neuropathologica Communications, 2014. **2**: p. 88.

420. Iba, M., et al., *Tau pathology spread in PS19 tau transgenic mice following locus coeruleus (LC) injections of synthetic tau fibrils is determined by the LC's afferent and efferent connections.* Acta Neuropathology, 2015. **130**(3): p. 349.

421. Luk, K.C., et al., *Pathological alpha-synuclein transmission initiates Parkinson-like neurodegeneration in nontransgenic mice.* Science, 2012. **338**(6109): p. 949.

422. Chung, C.G., H. Lee, and S.B. Lee, *Mechanisms of protein toxicity in neurodegenerative diseases.* Cellular and Molecular Life Sciences, 2018. **75**(17): p. 3159.

423. Cheng, Y. and F. Bai, *The Association of Tau With Mitochondrial Dysfunction in Alzheimer's Disease.* Frontiers in Neuroscience, 2018. **12**: p. 163.

424. Abramov, A.Y., et al., *Interaction of misfolded proteins and mitochondria in neurodegenerative disorders.* Biochemical Society Transactions, 2017. **45**(4): p. 1025.

425. Colombo, M., G. Raposo, and C. Thery, *Biogenesis, secretion, and intercellular interactions of exosomes and other extracellular vesicles.* Annual Review of Cell and Developmental Biology, 2014. **30**: p. 255.

426. Shin, J., et al., *Comparative analysis of differentially secreted proteins in serum-free and serum-containing media by using BONCAT and pulsed SILAC.* Scientific Reports, 2019. **9**(1): p. 3096.

427. Majety, M., et al., *Fibroblasts Influence Survival and Therapeutic Response in a 3D Co-Culture Model.* PLoS ONE, 2015. **10**(6): p. e0127948.

428. Long, X., et al., *Cancer-associated fibroblasts promote cisplatin resistance in bladder cancer cells by increasing IGF-1/ERβ/Bcl-2 signalling.* Cell Death and Disease, 2019. **10**(5): p. 375.

429. O'Brien, J., et al., *Overview of MicroRNA Biogenesis, Mechanisms of Actions, and Circulation.* Frontiers in Endocrinology, 2018. **9**: p. 402.

430. Tkach, M. and C. Thery, *Communication by Extracellular Vesicles: Where We Are and Where We Need to Go.* Cell, 2016. **164**(6): p. 1226.

431. Guzy, R.D., et al., *Mitochondrial complex III is required for hypoxia-induced ROS production and cellular oxygen sensing.* Cell Metabolism, 2005. **1**(6): p. 401.

432. Cai, W., et al., *Pericytes in Brain Injury and Repair After Ischemic Stroke.* Translational Stroke Research, 2017. **8**(2): p. 107-121.

433. Tachibana, M., et al., *Pericyte implantation in the brain enhances cerebral blood flow and reduces amyloid-beta pathology in amyloid model mice.* Experimental Neurology, 2018. **300**: p. 13.

434. Feringa, F.M., et al., *Persistent repair intermediates induce senescence.* Nature Communications, 2018. **9**(1): p. 3923.

435. Ewald, J.A., et al., *Therapy-induced senescence in cancer.* Journal of the National Cancer Institute, 2010. **102**(20): p. 1536.

436. Wiley, C.D., et al., *Mitochondrial Dysfunction Induces Senescence with a Distinct Secretory Phenotype.* Cell Metabolism, 2016. **23**(2): p. 303.

437. Tominaga, K., *The emerging role of senescent cells in tissue homeostasis and pathophysiology.* Pathobiology of Aging and Age-related Diseases, 2015. **5**(1): p. 27743.

438. Fujimaki, K. and G. Yao, *Crack the state of silence: Tune the depth of cellular quiescence for cancer therapy.* Molecular and Cellular Oncology, 2018. **5**(1): p. e1403531.

439. Becker, W., *A wake-up call to quiescent cancer cells – potential use of DYRK1B inhibitors in cancer therapy.* The FEBS Journal, 2018. **285**(7): p. 1203.

440. Chen, W., et al., *Cancer Stem Cell Quiescence and Plasticity as Major Challenges in Cancer Therapy.* Stem Cells International, 2016. **2016**: p. 1740936.

441. Zhao, W., Z.X. Lin, and Z.Q. Zhang, *Cisplatin-induced premature senescence with concomitant reduction of gap junctions in human fibroblasts.* Cell Research, 2004. **14**(1): p. 60.

442. Li, W., et al., *Cisplatin-induced senescence in ovarian cancer cells is mediated by GRP78.* Oncology Reports, 2014. **31**(6): p. 2525.

443. Li, C., et al., *N-acetylcysteine ameliorates cisplatin-induced renal senescence and renal interstitial fibrosis through sirtuin1 activation and p53 deacetylation.* Free Radical Biology and Medicine, 2019. **130**: p. 512.

444. Demaria, M., et al., *Cellular Senescence Promotes Adverse Effects of Chemotherapy and Cancer Relapse.* Cancer Discovery, 2017. **7**(2): p. 165.

445. Petrova, N.V., et al., *Small molecule compounds that induce cellular senescence.* Aging Cell, 2016. **15**(6): p. 999.